


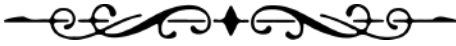


Universitat Autònoma de Barcelona

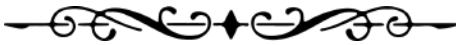
**ADVERTIMENT.** L'accés als continguts d'aquesta tesi queda condicionat a l'acceptació de les condicions d'ús establertes per la següent llicència Creative Commons:  [http://cat.creativecommons.org/?page\\_id=184](http://cat.creativecommons.org/?page_id=184)

**ADVERTENCIA.** El acceso a los contenidos de esta tesis queda condicionado a la aceptación de las condiciones de uso establecidas por la siguiente licencia Creative Commons:  <http://es.creativecommons.org/blog/licencias/>

**WARNING.** The access to the contents of this doctoral thesis it is limited to the acceptance of the use conditions set by the following Creative Commons license:  <https://creativecommons.org/licenses/?lang=en>



UNDERSTANDING THE TEMPERATURE AND  
PRESSURE DEPENDENCE OF THE  
OPTOELECTRONIC AND STRUCTURAL PROPERTIES  
OF  $\text{FA}_x\text{MA}_{1-x}\text{PbI}_3$  PEROVSKITE SOLID SOLUTIONS



PhD Thesis by  
Adrian Francisco López

Supervisors: \_\_\_\_\_  
Alejandro R. Goñi

\_\_\_\_\_  
Mariano Campy Quiles

\_\_\_\_\_  
M. Isabel Alonso

Tutor: \_\_\_\_\_  
Gemma Garcia Alonso

**UAB**  
Universitat Autònoma de Barcelona  
Facultat de Ciències  
Departament de Física

**ICMAB**  
INSTITUT DE CIÈNCIA DE MATERIALS DE BARCELONA  
 EXCELENCIA  
SEVERO  
OCHOA  **CSIC**  
CONSEJO SUPERIOR DE INVESTIGACIONES CIENTÍFICAS

Marzo 2020



A mis padres,  
Mi hermano,  
Y mi tía Dolores.

## Acknowledgments

To my parents, for their unconditional support.

To my supervisor, A. R. Goñi, for shedding light before my doctoral steps, and for doing his best in making an intimidating, crooked path look shorter and straight. I learned very valuable lessons from him, and also I made a good friend.

To my supervisor Mariano, for his continuous efforts to being there for everybody in the group, providing wisdom, knowledge and cohesion.

To my supervisor Isabel, who was always ready to help me whenever I needed it.

To the rest of the NanOpto group, for the good environment created, and special thanks to my office colleagues: Quique, Osnat, Alex, Bernhard, Valentina and Mariana, who made of this hard mountain climb looking sometimes like a wonderful trip on a sunny morning. Also to Mayte, Albert, and everyone who joined us in our Friday board game after-work sessions.

To my friends, Emilio, Héctor, Adrián, Yu, Nacho, Buko, Jon and Javi, who made a long trip to celebrate and support me while defending this thesis, and which no matter the distance I know I can count on them.

Also, to all the people who play an important role in my life, specially my friend Cristina, or Javi while he was living in Cerdanyola, because all of them are puzzle pieces necessary to build anything I can amount to, including this thesis.

And finally, to Scihub and Libgen, for holding open the doors of science for me.

## Abstract

Hybrid organic/inorganic perovskites have attracted a lot of attention since they were first introduced in a working photovoltaic device ten years ago, yielding an efficiency of around 3%. Since then, the efficiency of the perovskite solar cells has risen to almost stand toe to toe with that of commercial silicon photovoltaics. Besides, it allows the fabrication of flexible devices at an inexpensive cost. Due to its exceptionally good optoelectronic properties, there is also an intense research for different applications of this type of materials, such as sensors, lasers or light-emitting diodes. However, they still present some issues that need to be addressed, such as chemical or structural instabilities under ambient conditions. In order to better understand the structural stability, and the role played by the interaction between the organic cation and the inorganic framework, we studied the structural and optoelectronic properties of perovskites of the family  $\text{FA}_x\text{MA}_{1-x}\text{PbI}_3$  at different pressures (up to 15 GPa) and temperatures (10 to 385 K). We investigated this material by noninvasive optical spectroscopy means, such as photoluminescence (PL), Raman and ellipsometry.

In the articles here compiled, the first complete phase diagram of mixed cation (formamidinium and methylammonium) lead iodide perovskites is provided as a function of temperature and composition. This serves to assess the best relative concentration of the organic cations to stabilize the cubic phase with respect to temperature changes. These materials also present an atypical dependence of the bandgap with temperature, which in the literature is ascribed exclusively to a huge electron-phonon renormalization. However, here we show that thermal expansion effects also play a decisive role in the temperature behavior of the fundamental gap.

From all the combinations in the family of organometal halide perovskites,  $\text{MAPbI}_3$  is probably the most studied due to its outstanding optoelectronic properties. It is known that the interplay between the movement of the organic cations and the rigid inorganic cage has a decisive role in the crystalline structure of this material. For instance, due to the dynamic disorder of the methylammonia,  $\text{MAPbI}_3$  adopts a highly symmetric cubic phase at high temperatures. When cooling down, both the contraction of the lattice and the reduction of symmetry due to a transition to an orthorhombic phase lock the MA molecules in the cage voids. We are able to observe for the first time a similar effect but at room temperature, by applying hydrostatic pressure to the material. In both cases, the locking of the MA cations can be indirectly observed through a drastic reduction of the phonon linewidths in Raman experiments. We have shown, in this way, that it is possible to alter the vibrational properties of the material by applying a controlled hydrostatic pressure. Finally, the tuning of the bandgap and the variation of the band structure of the mixed-system  $\text{FA}_x\text{MA}_{1-x}\text{PbI}_3$  is evaluated as a function of FA composition with ellipsometry and photoluminescence.

# Nomenclature

## Abbreviations

ABX<sub>3</sub> – General formula for perovskite compounds

DFT – Density Functional Theory

DSSC – Dye-Sensitized Solar Cell

DW – Debye-Waller

FA – Formamidinium, (NH<sub>2</sub>)<sub>2</sub>CH<sup>+</sup>

FAPbI<sub>3</sub> – Formamidinium lead iodide (NH<sub>2</sub>)<sub>2</sub>CHPbI<sub>3</sub>

FA<sub>x</sub>MA<sub>1-x</sub>PbI<sub>3</sub> – Formamidinium/methylammonium lead iodide

FTO – Fluorine doped Tin Oxide.

I.I. – Integrated Intensity

MA – Methylammonium CH<sub>3</sub>NH<sub>3</sub><sup>+</sup>

MAPbI<sub>3</sub> – Methylammonium lead iodide CH<sub>3</sub>NH<sub>3</sub>PbI<sub>3</sub>

NCs – Nanocrystals

NREL – National Renewable Energy Laboratory (US)

OHP – Organometal Halide Perovskite

PCE – Power Conversion Efficiency

PL - Photoluminescence

PSC – Perovskite Solar Cell

PV – Photovoltaic

SE – Self-energy

TiO<sub>2</sub> – Titanium Oxide

## List of Figures

|   |    |
|---|----|
| <b>Figure 1.1</b> <i>Unit cell of the cubic phase of MAPbI<sub>3</sub></i>                                    | 1  |
| <b>Figure 1.2</b> <i>Example of perovskite crystals used</i>  | 2  |
| <b>Figure 1.3</b> <i>Dye-sensitized PV cell</i>   | 3  |
| <b>Figure 1.5</b> <i>Example of p-i-n heterojunction</i>  | 4  |
| <b>Figure 1.4</b> <i>NREL World record PV efficiencies chart</i>  | 4  |
| <b>Figure 1.6</b> <i>PL spectra of different FA<sub>x</sub>MA<sub>1-x</sub>PbI<sub>3</sub> compounds</i>      | 5  |
| <b>Figure 1.7</b> <i>Perfect cube and Goldschmidt factor</i>  | 7  |
| <b>Figure 1.8</b> <i>Molecular representation of cubic MAPbI<sub>3</sub>.</i>                                 | 7  |
| <b>Figure 1.9</b> <i>Crystalline MAPbI<sub>3</sub> structure in all its phases</i>                            | 9  |
| <b>Figure 1.10</b> <i>All possible types of point defects in MAPbI<sub>3</sub></i>                            | 11 |
| <b>Figure 1.11 to Figure 1.16</b> <i>Recombination mechanisms in semiconductors</i>                           | 12 |
| <b>Figure 1.14</b> <i>PL spectra of MAPbI<sub>3</sub> and FA<sub>0.5</sub>MA<sub>0.5</sub>PbI<sub>3</sub></i> | 12 |
| <b>Figure 2.1</b> <i>Magnification lenses to manually introduce the sample</i>                                | 17 |
| <b>Figure 2.2</b> <i>Example of MAPbI<sub>3</sub> single crystals</i>   | 17 |
| <b>Figure 2.3</b> <i>Picture of the Raman spectrometer</i>  | 18 |
| <b>Figure 2.4</b> <i>Light Scattering Processes</i>   | 19 |
| <b>Figure 2.5</b> <i>Insides of the Raman Spectrometer</i>  | 20 |
| <b>Figure 2.6</b> <i>Raman spectrum of MAPbI<sub>3</sub></i>  | 21 |
| <b>Figure 2.7</b> <i>PL spectrum of MAPbI<sub>3</sub> at 0.55 GPa</i>   | 22 |
| <b>Figure 2.8</b> <i>Monomolecular Recombination</i>  | 23 |
| <b>Figure 2.9</b> <i>Bimolecular Recombination</i>  | 23 |
| <b>Figure 2.10</b> <i>Reflection of the Electric Field</i>  | 24 |
| <b>Figure 2.11</b> <i>Path of light through the ellipsometer</i>  | 25 |
| <b>Figure 2.12</b> <i>Picture of a Diamond Anvil Cell</i>   | 27 |
| <b>Figure 2.14</b> <i>3D Representation of the diamonds and gasket</i>  | 27 |
| <b>Figure 2.13</b> <i>3D Cross-section of the diamonds and gasket</i>   | 28 |
| <b>Figure 2.15</b> <i>Picture of the cryostat</i>   | 29 |

|   |    |
|---|----|
| <b>Figure 3.1</b> <i>MAPbI<sub>3</sub> electronic band structure</i>        | 31 |
| <b>Figure 3.2</b> <i>Energy contribution of each phonon mode</i>            | 33 |
| <b>Figure 3.3</b> <i>Phonon band structure and DOS of FAPbI<sub>3</sub></i> | 33 |
| <b>Figure 3.4</b> <i>Phonon band structure and DOS of MAPbI<sub>3</sub></i> | 33 |
| <b>Figure 4.1</b> <i>Energy uncertainty in the electronic transitions</i>   | 35 |
| <b>Figure 4.2</b> <i>Direct observation of inhomogeneous broadening</i>     | 36 |
| <b>Figure 5.1</b> <i>Temperature dependence of the bandgap</i>              | 39 |
| <b>Figure 5.2</b> <i>Thermal Expansion</i>                                  | 40 |

## Motivation

A transition from conventional energy resources to clean and renewable ones is essential to stop and possibly revert climate change, aiming to have a healthier environment. Finding a cheap and efficient solar power alternative to fossil-based sources could be a critical step in this process. Hybrid halide perovskites are presented as promising candidates due to their inexpensive fabrication costs and remarkably high efficiencies. However, they are unstable at ambient conditions, and since it is a novel material, much is still unknown about the origin of such good performances. A better understanding is fundamental to overcome obstacles such as the instability, or to look for replacements of the lead atom for another less toxic element.

By applying pressure or varying the temperature, it is possible to study the optoelectronic properties of the material under different structural phase transitions, the dependence of its bandgap with pressure and temperature, as well as the effect of reducing the lattice parameters by a few percent in a controlled way.

This kind of experimental work gives us valuable information about the material. In particular, for hybrid perovskites, it shows the special interplay between the organic molecules and the inorganic frame, or the structural behavior depending on the cation concentration, among other things.

Our group has a long experience in optical characterization and fundamental studies of the optoelectronic properties of semiconductors, and it counts with the experimental setups needed to carry this kind of experiments in our laboratories.





## Organization of this thesis

This Doctoral thesis is presented as a compilation of research articles following the UAB (Universidad Aut3noma de Barcelona) regulations in this respect.

Apart from a general introduction and a detailed summary of the experimental techniques employed, three chapters more have been added with the intention of introducing the theoretical background used in the articles in an intuitive and simple way. In particular, the fundamentals of the electronic and vibrational properties of perovskite materials, the interaction between the organic cation and the inorganic matrix, and the bandgap dependence on temperature of this type of materials are explained. All of which are of relevance to fully understand the work summarized on the papers.

The articles included in this memoir and presented to the Doctoral committee are the following, sorted by chronological order:

- I. Pressure-induced locking of methylammonium cations versus amorphization in hybrid lead iodide perovskites. *Francisco-L3pez, A., Charles, B., Weber, O. J., Alonso, M. I., Garriga, M., Campoy-Quiles, M., Weller, M. T., & Goñi, A. R.* (2018). *The Journal of Physical Chemistry C*, 122, 22073-22082.
- II. Equal footing of thermal expansion and electron-phonon interaction in the temperature dependence of lead halide perovskite band gaps. *Francisco-L3pez, A., Charles, B., Weber, O. J., Alonso, M. I., Garriga, M., Campoy-Quiles, M., Weller, M. T., & Goñi, A. R.* (2019). *The Journal of Physical Chemistry Letters*, 10, 2971-2977.
- III. Spectroscopic ellipsometry study of FA<sub>x</sub>MA<sub>1-x</sub>PbI<sub>3</sub> hybrid perovskite single crystals. *Alonso, M. I., Charles, B., Francisco-L3pez, A., Garriga, M., Weller, M. T., & Goñi, A. R.* (2019). *Journal of Vacuum Science & Technology B* 37, 062901/1-7.
- IV. Phase diagram of methylammonium/formamidinium lead iodide perovskite solid solutions from temperature-dependent photoluminescence and Raman spectroscopies. *Francisco-L3pez, A., Charles, B., J., Alonso, M. I., Garriga, M., Campoy-Quiles, M., Weller, M. T., & Goñi, A. R.* (2020). *The Journal of Physical Chemistry C*. 124, 6, 3448-3458

Another article produced as a direct result of researching during this PhD thesis, but which is not included in this work because it is unrelated to the main research line is:

- I'. On the impact of the stress situation on the optical properties of  $WSe_2$  monolayers under high pressure. *Francisco-López, A., Han, B., Lagarde, D., Marie, X., Urbaszek, B., Robert, C., & Goñi, A.* (2019). *Papers in Physics*, 11, 110005-110005.

# Index

|          |  |           |
|----------|--|-----------|
| <b>1</b> | <b>Introduction</b>  | <b>1</b>  |
| 1.1      | Hybrid Perovskites $\text{FA}_x\text{MA}_{1-x}\text{PbI}_3$ .....  | 1         |
| 1.1.1    | Applications.....  | 3         |
| 1.1.2    | Tunability.....  | 4         |
| 1.1.3    | Structure.....   | 6         |
| 1.1.4    | Defect tolerance.....  | 10        |
| 1.1.5    | Stability.....   | 14        |
| <b>2</b> | <b>Experimental techniques</b>   | <b>17</b> |
| 2.1      | Sample Growth.....   | 17        |
| 2.2      | Raman.....   | 18        |
| 2.3      | Photoluminescence.....   | 22        |
| 2.4      | Ellipsometry.....  | 24        |
| 2.5      | High pressure and low temperatures.....  | 27        |
| 2.5.1    | High pressure.....   | 27        |
| 2.5.2    | Low temperatures.....  | 29        |
| <b>3</b> | <b>Vibrational and electronic structure in hybrid perovskites</b>  | <b>31</b> |
| 3.1      | Electronic band structure, spin orbit coupling (SOC), and band inversion... 31                                 |           |
| 3.2      | Vibrational properties.....  | 32        |
| <b>4</b> | <b>Homogeneous and inhomogeneous broadening in hybrid Perovskites</b>  | <b>35</b> |
| 4.1      | Homogeneous broadening.....  | 35        |
| 4.2      | Inhomogeneous broadening.....  | 36        |
| <b>5</b> | <b>Temperature dependence of the bandgap</b>   | <b>39</b> |
| 5.1      | Thermal expansion.....   | 39        |
| 5.2      | Electron-Phonon renormalization of the band gap.....   | 41        |
| <b>6</b> | <b>Published articles</b>  | <b>43</b> |
| I.       | Pressure-Induced Locking of Methylammonium Cations versus Amorphization in Hybrid Lead Iodide Perovskites..... | 45        |

|  |            |
|--|------------|
| <b>II.</b> Equal Footing of Thermal Expansion and Electron-Phonon Interaction in the Temperature Dependence of Lead Halide perovskite Band Gaps .....                      | 67         |
| <b>III.</b> Spectroscopic ellipsometry study of $\text{FA}_x\text{MA}_{1-x}\text{PbI}_3$ hybrid perovskite single crystals .....   | 87         |
| <b>IV</b> Phase Diagram of Methylammonium/Formamidinium Lead Iodide Perovskite Solid Solutions from Temperature-Dependent Photoluminescence and Raman Spectroscopies ..... | 115        |
| <b>7 Conclusions and perspectives</b>  | <b>153</b> |

# 1 Introduction

## 1.1 Hybrid Perovskites $\text{FA}_x\text{MA}_{1-x}\text{PbI}_3$

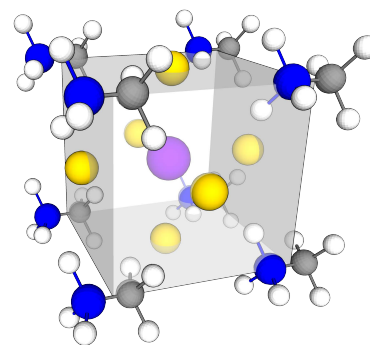
The name “perovskite” refers to the group of materials that share the same crystalline structure with the mineral  $\text{CaTiO}_3$ . It was first discovered by Gustav Rose in 1839, and was named after the Russian mineralogist Lev Perovski<sup>1</sup>.

Perovskite structure is characterized by the unit formula  $\text{ABX}_3$ . It can be represented geometrically as a cubic hexahedron with the B-site atoms, usually metal cations, in the middle of the cube. The A-site cations, which in the case of this thesis are organic molecules, are placed at the corners. Finally, the X anions, which typically belong to the halide family for photovoltaic applications, are located in the center of each of the six faces. This structure is schematically represented in Figure 1.1 for the particular case of methylammonium lead iodide perovskite,  $\text{CH}_3\text{NH}_3\text{PbI}_3$  ( $\text{MAPbI}_3$ ).

Several inorganic perovskite compounds have been intensively studied during the last decades due to their interesting physical properties such as ferroelectricity ( $\text{BaTiO}_3$ )<sup>2</sup>, ferromagnetism ( $\text{SrRuO}_3$ )<sup>3</sup>, superconductivity ( $\text{YBa}_2\text{Cu}_3\text{O}_7$ )<sup>4</sup> photoconductivity and magnetoresistance ( $\text{LaAlO}_3/\text{SrTiO}_3$  interfaces)<sup>5</sup> or low thermal conductivity ( $\text{LaCoO}_3$ )<sup>4</sup>.

However, there was an important breakthrough in the field of perovskite photovoltaics in 2009. A hybrid organic-inorganic compound,  $\text{MAPbI}_3$ , was first introduced by Kojima and coworkers as a light-harvester layer in a dye-sensitized cell<sup>6</sup>. The power conversion efficiency (PCE) of this early device was 3.6%. Such efficiency was promising but still not very high, as it was being hampered by the presence of a liquid electrolytic layer that degraded the perovskite material. In just three years, the reported efficiency rose rapidly to 9.7% by replacing the electrolyte with a solid-state hole transport layer<sup>7</sup>. Besides, due to the inherent ability of the perovskite material to separate charge carriers, the mesoporous titanium oxide scaffold was removed and planar perovskite p-i-n heterojunction architectures were introduced in solar cells. These devices were yielding efficiencies over 15% in less than four years of development in the field<sup>8</sup>.

Years later, in 2013, solar cells based on perovskite materials were given their own classification by the National Renewable Research Laboratory (NREL). This is a laboratory from the U.S. National Department of Energy that monitors and standardizes



**Figure 1.1** Unit cell of the cubic phase of  $\text{MAPbI}_3$ , which follows the perovskite  $\text{ABX}_3$  structure. Iodine ions (yellow) belong to the X-site, placed in the faces of the cube; lead (purple) corresponds to the B site, in the middle of the cube, and the methylammonium molecules (Blue for N, dark grey for C and white for H) are placed in the corners of the structure, occupying the A-sites. Notice the octahedra formed by the iodine atoms, which will be recurrent in the next figures.

[1] Rose, Gustav. (1840) “Ueber einige neue Mineralien des Urals.” *Journal für praktische Chemie* 19.1: 459-468.

[2] Von Hippel, A., (1950) “Ferroelectricity, domain structure, and phase transitions of barium titanate.” *Reviews of Modern Physics*, 22(3), p.221.

[3] Longo, J. M., et al. (1968). “Magnetic properties of  $\text{SrRuO}_3$  and  $\text{CaRuO}_3$ ”. *Journal of Applied Physics*, 39(2), 1327-1328.

[4] Pena, M. A., & Fierro, J. L. G. (2001). “Chemical structures and performance of perovskite oxides.” *Chemical reviews*, 101(7), 1981-2018.

[5] Tebano, Antonello, et al. (2012) “Room-temperature giant persistent photoconductivity in  $\text{SrTiO}_3/\text{LaAlO}_3$  heterostructures.” *Acs Nano* 6.2: 1278-1283.

[6] Kojima, A., et al. (2009). “Organometal halide perovskites as visible-light sensitizers for photovoltaic cells.” *Journal of the American Chemical Society*, 131(17), 6050-6051.



**Figure 1.2** Example of perovskite crystals used during this thesis. From left to right:  $\delta$ -phase of  $\text{FAPbI}_3$ ,  $\text{MAPbBr}_3$ , and  $\text{MAPbI}_3$  crystals synthesized by our colleagues in Bath.

[7] Kim, Hui-Seon, et al. (2012) "Lead iodide perovskite sensitized all-solid-state submicron thin film mesoscopic solar cell with efficiency exceeding 9%." *Scientific reports* 2: 591.

[8] Burschka, Julian, et al. (2013) "Sequential deposition as a route to high-performance perovskite-sensitized solar cells." *Nature* 499.7458: 316.

[9] Best Research-Cell Efficiency Chart (2019) | Photovoltaic Research | NREL <https://www.nrel.gov/pv/cell-efficiency.html>

[10] Gao, P., Grätzel, M., & Nazeeruddin, M. K. (2014). "Organohalide lead perovskites for photovoltaic applications." *Energy & Environmental Science*, 7(8), 2448-2463.

[11] Prasanna, Rohit, et al. (2017) "Band gap tuning via lattice contraction and octahedral tilting in perovskite materials for photovoltaics." *Journal of the American Chemical Society* 139.32: 11117-11124.

[12] Ball, James M., et al. (2013) "Low-temperature processed meso-structured to thin-film perovskite solar cells." *Energy & Environmental Science* 6.6: 1739-1743.

[13] Yang, Shida, et al. (2017) "Recent advances in perovskite solar cells: efficiency, stability and lead-free perovskite." *Journal of Materials Chemistry A* 5.23: 11462-11482.

photovoltaic (PV) efficiency records all over the world. According to them, the efficiency world record has risen up to 25% at the moment of writing this thesis<sup>9</sup>. The current high performance of perovskite technology is comparable with that of Si or GaAs photovoltaic cells, which nowadays dominate the market due to the good balance between high efficiency, great long-term stability and, in the case of silicon, moderate cost of the modules.

The number of advantages of these materials with respect to the inorganic PV is large; for instance the ability to tune the bandgap and the absorbed energy range by simply changing relative composition<sup>10,11</sup>, the reduced fabrication temperatures (<150 °C) in comparison to inorganic solar cells such as those made from Si, or GaAs<sup>12</sup> (that require temperatures higher than 1000 °C), the easier solution processability and crystallization, and the flexibility of the modules, which allows roll-to-roll production, reducing further production costs.

All of these advantages help to explain the sky-rocketing number of related publications and conferences on the matter in the last few years. However, before bursting into the market, some issues related to the long-term stability of the material such as chemical or structural stability need to be addressed. Its organic molecules are highly hygroscopic and moisture degrades the material irreversibly after just a few weeks exposed to ambient conditions. There is also UV light related degradation, and instability of the structural phase at operating temperatures of a PV device. Moreover, one of the main drawbacks of this technology is the toxicity of lead, which raises environmental concerns as well as poses a risk for the workers during fabrication. The latter is one of the main reasons why lately some efforts have been made to replace lead with other less toxic elements, such as tin or bismuth<sup>13</sup>.

In this introduction I will briefly focus on some of the optical and electronic properties which are related to the structural phase of the crystal. Besides, I will mention the tunable composition and its tolerance to defects, which plays a fundamental role in its notably good optoelectronic properties, and on some stability issues concerning these hybrid perovskites. In particular, I will discuss the structural stability and optoelectronic properties of hybrid perovskites of the formula  $\text{FA}_x\text{MA}_{1-x}\text{PbI}_3$  as a function of temperature and pressure.

### 1.1.1 Applications

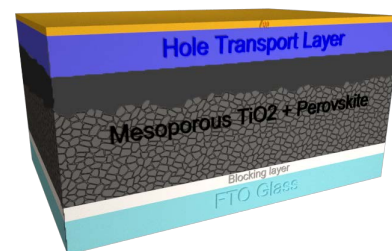
Hybrid halide perovskites are typically used as a photovoltaic material. However, they also show interesting properties for other applications, such as lasers, light-emitting diodes (LEDs) or thermoelectrics, the latter due to their ultra-low thermal conductivity<sup>14</sup>.

Figure 1.3 represents schematically the first reported architecture<sup>6</sup> employed in perovskite solar cells in 2009. It is a dye-sensitized solar cell (DSSC), and in this case the perovskite material was infiltrated in a mesoporous scaffold of titanium oxide ( $\text{TiO}_2$ ). The perovskite used as a light absorber was  $\text{MAPbI}_3$ , whereas the surface of the  $\text{TiO}_2$  scaffold favored the exciton dissociation. Later on, it was observed that this mesoporous structure was not necessary, as the perovskite already can generate free carriers due to the weak values of the exciton binding energy. Then, a less complicated planar *p-i-n* heterojunction architecture was adopted (see Figure 1.5). Currently, both types of solar cells exhibit good PV efficiencies.

Both generic types of structures present similar layers, apart from the mesoporous  $\text{TiO}_2$ . The top and bottom layers are the charge conducting electrodes, one of them being transparent, like FTO (fluorine-doped tin oxide) glass, to allow the light going through. Sandwiched in between is the light-absorbing layer, with two selective charge blocking layers on top and below it, allowing either electrons or holes to reach the electrodes, and blocking the opposite type of carrier.

Figure 1.4 is a partial reproduction of the record efficiency chart from the National Renewable Energy Laboratory. The yellow circles with the red stroke represent the evolution of perovskite solar cells. It is interesting to observe the steep, increasing tendency over time. Additionally, we can observe that they have reached record efficiency values close to that of Silicon solar cells (blue) in just a few years of development. Furthermore, the continuous progress made in film formation<sup>15,16</sup>, defect passivation<sup>17,18</sup> and contact engineering<sup>19,20</sup> suggest that perovskites will soon approach the maximum efficiency possible, according to the Shockley-Queisser limit.

Miller, Yablonovitch and Kurtz<sup>21</sup> spread the idea that a good solar cell needs to be a good light emitter, since highly efficient solar cells avoid trap-assisted recombination. If the deep-trap defect concentration is reduced, the main recombination pathway available is then radiative, making it suitable for light emission.



**Figure 1.3** Dye-sensitized PV cell. In this configuration the perovskite acts as dye (light absorber). The mesoporous  $\text{TiO}_2$  scaffold helps separate the charge carriers generated in the perovskite. Below, a hole blocking layer (typically  $\text{TiO}_2$  as well) only allows electrons to reach the transparent electrode (FTO glass). On the other side of the cell, a hole transport layer blocks only electrons, so the holes can reach the gold electrode.

[14] Pisoni, Andrea, et al. "Ultra-low thermal conductivity in organic-inorganic hybrid perovskite  $\text{CH}_3\text{NH}_3\text{PbI}_3$ ." *The journal of physical chemistry letters* 5.14 (2014): 2488-2492.

[15] Jeon, Nam Joong, et al. "Solvent engineering for high-performance inorganic-organic hybrid perovskite solar cells." *Nature materials* 13.9 (2014): 897.

[16] Eperon, Giles E., et al. "Morphological control for high performance, solution-processed planar heterojunction perovskite solar cells." *Advanced Functional Materials* 24.1 (2014): 151-157.

[17] Noel, Nakita K., et al. "Enhanced photoluminescence and solar cell performance via Lewis base passivation of organic-inorganic lead halide perovskites." *ACS nano* 8.10 (2014): 9815-9821.

[18] Shao, Yuchuan, et al. "Origin and elimination of photocurrent hysteresis by fullerene passivation in  $\text{CH}_3\text{NH}_3\text{PbI}_3$  planar heterojunction solar cells." *Nature communications* 5 (2014): 5784.

[19] Wojciechowski, Konrad, et al. Heterojunction modification for highly efficient organic-inorganic perovskite solar cells. *ACS nano* 8.12 (2014): 12701-12709.

[20] Zhou, Huanping, et al. Interface engineering of highly efficient perovskite solar cells. *Science* 345.6196 (2014): 542-546.



**Figure 1.5** Example of a p-i-n heterojunction architecture for a fully perovskite solar cell.

[21] Miller, O. D., Yablonovitch, E., & Kurtz, S. R. (2012). “Strong internal and external luminescence as solar cells approach the Shockley–Queisser limit.” *IEEE Journal of Photovoltaics*, 2(3), 303-311.

[22] Lin, Kebin, et al. (2018) “Perovskite light-emitting diodes with external quantum efficiency exceeding 20 per cent.” *Nature* 562.7726: 245.

[23] Yu, Jae Choul, et al. (2016) “High-performance perovskite light-emitting diodes via morphological control of perovskite films.” *Nanoscale* 8.13: 7036-7042.

[24] Tan, Zhi-Kuang, et al. (2014) “Bright light-emitting diodes based on organometal halide perovskite.” *Nature nanotechnology* 9.9: 687.

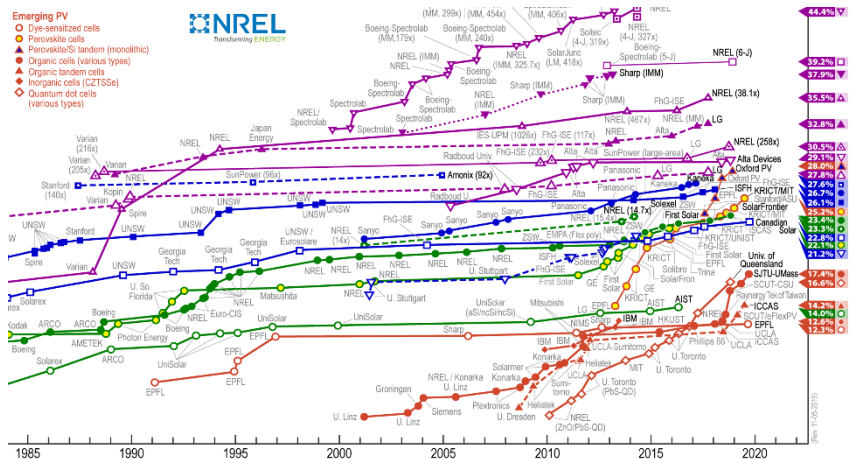
[25] Xing, Guichuan, et al. (2014) “Low-temperature solution-processed wavelength-tunable perovskites for lasing.” *Nature materials* 13.5: 476.

[26] Yuan, Mingjian, et al. (2016) “Perovskite energy funnels for efficient light-emitting diodes.” *Nature nanotechnology* 11.10: 872.

[27] Galkowski, Krzysztof, et al. (2016) “Determination of the exciton binding energy and effective masses for methylammonium and formamidinium lead tri-halide perovskite semiconductors.” *Energy & Environmental Science* 9.3: 962-970

[28] Xing, Guichuan, et al. (2013) “Long-range balanced electron-and hole-transport lengths in organic-inorganic CH<sub>3</sub>NH<sub>3</sub>PbI<sub>3</sub>.” *Science* 342.6156: 344-347

[29] Wehrenfennig, Christian, et al. (2014) “High charge carrier mobilities and lifetimes in organolead trihalide perovskites.” *Advanced materials* 26.10: 1584-1589.



**Figure 1.4** NREL World record PV efficiencies as a function of time. Chart trimmed for clarity, zoomed in to see the amazingly fast growing tendency of perovskite (red circles with yellow core), which has already almost caught up with silicon solar cells in efficiency. (Blue lines) GaAs and multijunction solar cells are showed in purple, and thin film technologies in green. Reproduced with permission of ref. [9]

Besides, most of the exceptionally good optoelectronic properties that make organometal perovskites very suitable materials for PV also make them good candidates for making light-emitting diodes and lasers in the visible range<sup>22,23,24,25,26</sup>. These properties are, for example, a direct bandgap, long charge carrier diffusion length and lifetime, high absorption coefficient and a low binding energy of ca. 15 meV on the photo-generated excitons<sup>27,28,29</sup>. Moreover, they present a tunable bandgap, high quantum efficiency, and the ability to be integrated into different optical resonators<sup>30,31</sup>.

It has been shown as well that hybrid perovskites present a low amplified stimulated emission carrier density threshold (which gives a hint about how easily it can obtain net gain), making them very promising candidates for lasing applications<sup>31,32,33</sup>.

Finally, due to the strong interaction of these materials with incident light, new photodetector devices have been designed to take advantage of the good optoelectronic properties of organometal perovskites<sup>34</sup>.

The field of applications is thus very broad, and more fundamental research for this type of materials that could lead to better understanding such good properties is necessary.

### 1.1.2 Tunability

A wide range of mixed compositional perovskites has been studied for their exceptionally good performance as solar cells<sup>35</sup>. This is probably one of the biggest advantages of hybrid perovskites: the good miscibility of the A-site cations and the halogen anions in



the  $ABX_3$  formula. It enables access to a wide range of combined properties, and moreover, to tune them towards optimum values.

Typically, for the A-site cation, the best optoelectronic properties are obtained employing organic molecules such as methylammonium (MA), formamidinium (FA), or even an inorganic element such as cesium (Cs) or rubidium (Rb). For the metal, the best performances are obtained with lead (Pb). Lead electrons present huge spin-orbit coupling, which directly affects the electronic band structure of lead-based perovskites<sup>36</sup>. However, as it is mentioned above, due to its toxicity new routes are being explored to substitute lead with other metals such as Sn<sup>37</sup>. Unfortunately, the PCEs obtained this way are remarkably lower. Finally, for the X-site ion, halides such as iodine (I), chlorine (Cl) and bromine (Br) are the most employed ones in the fabrication of perovskite solar cells. Interestingly, all of these are compositionally miscible with each other<sup>38</sup>.

The archetypal  $MAPbI_3$  is the most studied material of the family of organometal halide perovskites (OHP), but it is not the only one. Apart from  $MAPbI_3$  (PCE  $\sim 21.1\%$ )<sup>39</sup>, single-junction high power conversion efficiencies have been obtained for perovskites like  $FAPbI_3$  ( $\sim 20.2\%$ )<sup>40</sup>,  $FA_{0.92}MA_{0.08}PbI_3$  ( $\sim 20.8\%$ )<sup>41</sup>, and other

[30] Sutherland, Brandon R., and Edward H. Sargent. (2016) "Perovskite photonic sources." *Nature Photonics* 10.5: 295.

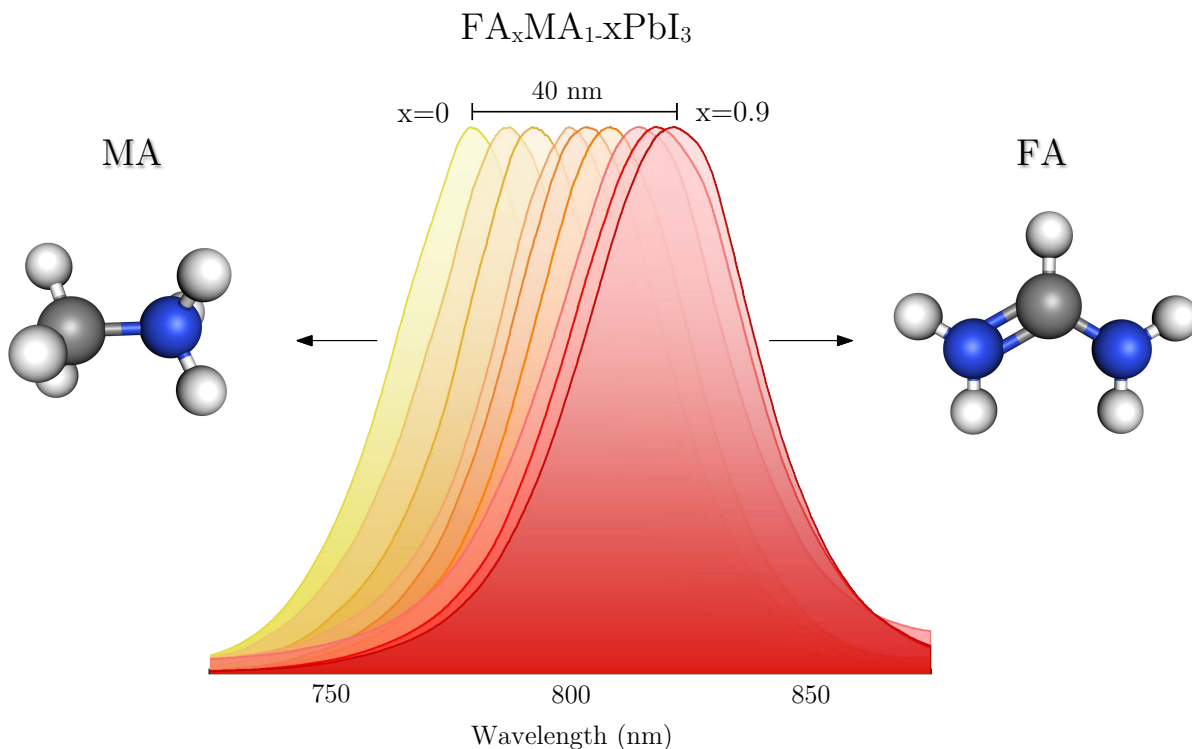
[31] Stylianakis, Minas M., et al. (2019) "Inorganic and hybrid perovskite based laser devices: A Review." *Materials* 12.6: 859.

[32] Deschler, Felix, et al. (2014) "High photoluminescence efficiency and optically pumped lasing in solution-processed mixed halide perovskite semiconductors." *J. Phys. Chem. Lett* 5.8: 1421-1426.

[33] Zhu, Haiming, et al. (2015) "Lead halide perovskite nanowire lasers with low lasing thresholds and high quality factors." *Nature materials* 14.6: 636.

[34] Dou, Letian, et al. (2014) Solution-processed hybrid perovskite photodetectors with high detectivity. *Nature communications* 5: 5404.

[35] Even, Jacky, et al. "Solid-state physics perspective on hybrid perovskite semiconductors." *The Journal of Physical Chemistry C* 119.19 (2015): 10161-10177.



**Figure 1.6** Normalized PL spectra of different  $FA_xMA_{1-x}PbI_3$  crystals, with  $x$  ranging from 0 to 0.9 in 0.1 steps. From this image we can conclude that the emission lines and the bandgap of the material can be tuned by changing the composition of its constituent parts.

[36] Even, Jacky, et al. “Importance of spin-orbit coupling in hybrid organic/inorganic perovskites for photovoltaic applications.” *The Journal of Physical Chemistry Letters* 4.17 (2013): 2999-3005.

[37] Koh, Teck Ming, et al. “Formamidinium tin-based perovskite with low E<sub>g</sub> for photovoltaic applications.” *Journal of Materials Chemistry A* 3.29 (2015): 14996-15000.

[38] Leijtens, Tomas, et al. (2015) “Stability of metal halide perovskite solar cells.” *Advanced Energy Materials* 5.20: 1500963.

[39] Chen, Zhaolai, et al. (2019) “Single-Crystal MAPbI<sub>3</sub> Perovskite Solar Cells Exceeding 21% Power Conversion Efficiency.” *ACS Energy Letters* 4: 1258-1259.

[40] Yang, Woon Seok, et al. (2015) “High-performance photovoltaic perovskite layers fabricated through intramolecular exchange.” *Science* 348.6240: 1234-1237.

[41] Shi, Pengju, et al. (2019) “Advanced partial nucleation for single-phase FA<sub>0.92</sub>MA<sub>0.08</sub>PbI<sub>3</sub>-based high-efficiency perovskite solar cells.” *Science China Materials*: 1-11.

[42] Saliba, Michael, et al. (2016) “Incorporation of rubidium cations into perovskite solar cells improves photovoltaic performance.” *Science* 354.6309: 206-209.

[43] Kulkarni, Sneha A., et al. (2014) “Band-gap tuning of lead halide perovskites using a sequential deposition process.” *Journal of Materials Chemistry A* 2.24: 9221-9225.

[44] Kong, Lingping, et al. (2016) “Simultaneous band-gap narrowing and carrier-lifetime prolongation of organic-inorganic trihalide perovskites.” *Proceedings of the National Academy of Sciences* 113.32: 8910-8915.

[45] Rühle, Sven. (2016) “Tabulated values of the Shockley-Queisser limit for single junction solar cells.” *Solar Energy* 130: 139-147.

more complex formulas such as  $\text{Rb}_{0.05}[\text{Cs}_{0.05}(\text{MA}_{0.17}\text{FA}_{0.83})_{0.95}]_{0.95}\text{Pb}(\text{I}_{0.83}\text{Br}_{0.17})_3$  (~21.6%)<sup>42</sup>.

Besides, the composition can be modified to tune the emission in all the visible spectral range (390-790 nm) by varying the cation, the halide, or the metal relative concentrations, or modifying the metal halide precursor concentrations during synthesis<sup>25,43</sup>.

Figure 1.6 shows almost the whole range of compositions for the formula  $\text{FA}_x\text{MA}_{1-x}\text{PbI}_3$ , with x ranging from 0 to 0.9 in steps of 0.1. We can observe that the PL shifts from that of pure  $\text{MAPbI}_3$  to that corresponding to  $\text{FAPbI}_3$ , at small steps for each solid solution. The bandgap changes accordingly with the PL, ranging from 1.41 to 1.53 eV, with the extreme values corresponding to the compositional ends  $\text{FAPbI}_3$  and  $\text{MAPbI}_3$ , respectively<sup>37,44</sup>. It is worth mentioning that both are remarkably close to the theoretical optimum bandgap value of 1.34 eV for a single-junction solar cell given by the Shockley-Queisser limit for the solar spectrum.<sup>45</sup>

Table 1 summarizes some of the best efficiencies obtained for perovskite solar cells so far<sup>46</sup>, and their stability as a function of the time necessary for its efficiency to drop by a 20% (T80).

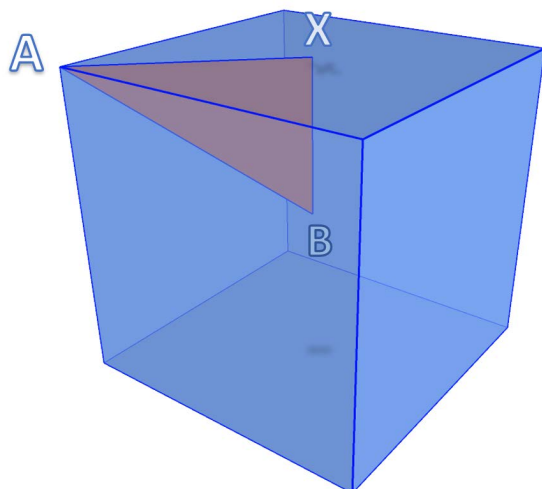
**Table 1** Power conversion efficiencies (PCE) of some of the most efficient perovskite solar cells. Notice that electron and hole transport layers are not specified here, however, they still play a fundamental role in obtaining high efficiencies. After references 40, 41 and 46.

| Composition  | PCE (%) | T80 (h) Stored | T80 (h) Illum. |
|--|---------|----------------|----------------|
| $\text{MAPbI}_3$   | 23.9    | 2200           | 650            |
| $\text{MAPbI}_{3-x}\text{Cl}_x$  | 19.3    | 24             | -              |
| $\text{FAPbI}_3$   | 20.2    | -              | -              |
| $(\text{CsMAFA})\text{Pb}(\text{I}_{0.85}\text{Br}_{0.15})_3$  | 21.5    | -              | 400            |
| $(\text{FAPbI}_3)_{0.95}(\text{MAPbBr}_3)_{0.05}$  | 22.3    | -              | 320            |
| $(\text{Cs}_{0.02}\text{FA}_{0.98}\text{PbI}_3)_{0.97}(\text{MAPbBr}_3)_{0.03}$  | 21.7    | 250            | 250            |
| $(\text{FA}_{0.83}\text{MA}_{0.17})_{0.95}\text{Cs}_{0.05}\text{Pb}(\text{I}_{0.9}\text{Br}_{0.1})_3$                            | 19.8    | -              | 1800           |
| $\text{Rb}_{0.05}[\text{Cs}_{0.05}(\text{MA}_{0.17}\text{FA}_{0.83})_{0.95}]_{0.95}\text{Pb}(\text{I}_{0.83}\text{Br}_{0.17})_3$ | 21.6    | -              | -              |

### 1.1.3 Structure

Perovskite structure, following the general  $\text{ABX}_3$  formula, can be visualized in its cubic form as a cube with the A atoms or molecules at the corners, the B atoms in the center of the structure

and the X sites in the middle of each of the six cube surfaces. This structure is represented in 3D in Figure 1.8



**Figure 1.7** Perfect cube, with one of the corners labelled A, the center in one of the faces named X, and the middle of the cube labelled B. The letters represent the  $ABX_3$  sites in a cubic perovskite.

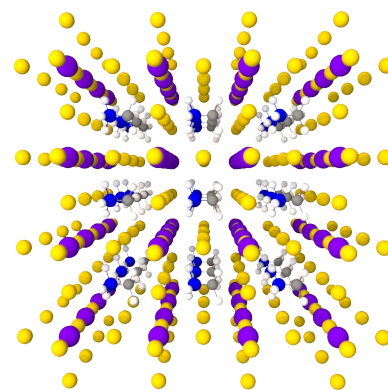
In a perfect cube, as the one shown in Figure 1.7, the distance between the X and A sites is  $\sqrt{2}$  times longer than the distance between X and B, as one could deduce by simple trigonometry. If we think of a perfectly packed cubic perovskite structure, the distance from X to A would be the radius of the cation A, say  $R_A$ , plus the radius of the anion X, i.e.  $R_X$ . Similarly,  $R_X + R_B$  would be equal to the distance from X to B. Then we obtain this relation:

$$(R_A + R_X) = \sqrt{2}(R_X + R_B)$$

Now if we assume that this relation is only nearly met in real cubic perovskites, we introduce the Goldsmith tolerance factor ( $t$ ) for perovskite structures:

$$t = \frac{(R_A + R_X)}{\sqrt{2}(R_X + R_B)} \quad (1.1)$$

One can expect the formation of a cubic phase at room temperature when  $t$  is close to 1. For  $MAPbI_3$ ,  $t = 0.955$ , and for  $FAPbI_3$ ,  $t = 1.036$ , according to the literature<sup>47</sup>. The former is lower than 1, and  $MAPbI_3$  exhibits a tetragonal phase at 298 K. The latter, on the other hand, is higher than 1 and the cubic structure of  $FAPbI_3$  is unstable, transforming into a hexagonal phase spontaneously at room temperature. Lower symmetry structures such as rhombohedral or orthorhombic can be observed<sup>38,48</sup> when  $t$  lies between 0.7 and 0.9.



**Figure 1.8** Atomic and molecular representation of cubic  $MAPbI_3$ . Iodine atoms (yellow) sit at the corners of an imaginary octahedron with lead (purple) in the core. MA molecules (blue, gray and white for nitrogen, carbon and hydrogen respectively) are then placed in the free space left among the octahedra. See Figure 1.9 for a representation with octahedra walls placed in the structure to better guide the eye.

[46] Urbina, A. (2019). “The balance between efficiency, stability and environmental impacts in perovskite solar cells: a review.” *Journal of Physics: Energy*.

[47] Charles, Bethan, et al. “Understanding the stability of mixed A-cation lead iodide perovskites.” *Journal of Materials Chemistry A* 5.43 (2017): 22495-22499.

[48] Li, Zhen, et al. (2015) “Stabilizing perovskite structures by tuning tolerance factor: formation of formamidinium and cesium lead iodide solid-state alloys.” *Chemistry of Materials* 28.1: 284-292.

[49] Yin, Wan-Jian, et al. (2015)  
“Halide perovskite materials for solar cells: a theoretical review.” *Journal of Materials Chemistry A*, vol. 3, no 17, p. 8926-8942.

[50] Leguy, Aurelien MA, et al. (2015)  
“The dynamics of methylammonium ions in hybrid organic–inorganic perovskite solar cells.” *Nature communications* 6: 7124.

[51] Leguy, Aurélien MA, et al. (2016)  
“Dynamic disorder, phonon lifetimes, and the assignment of modes to the vibrational spectra of methylammonium lead halide perovskites.” *Physical Chemistry Chemical Physics*, vol. 18, no 39, p. 27051-27066.

[52] Taylor, Victoria CA, et al. (2018)  
“Investigating the role of the organic cation in formamidinium lead iodide perovskite using ultrafast spectroscopy.” *The journal of physical chemistry letters* 9.4: 895-901.

[53] Mosconi, Edoardo, and Filippo De Angelis. (2016) “Mobile ions in organohalide perovskites: interplay of electronic structure and dynamics.” *ACS Energy Letters* 1.1: 182-188.

[54] Weber, Oliver J., et al. (2018)  
“Phase behavior and polymorphism of formamidinium lead iodide.” *Chemistry of Materials* 30.11: 3768-3778.

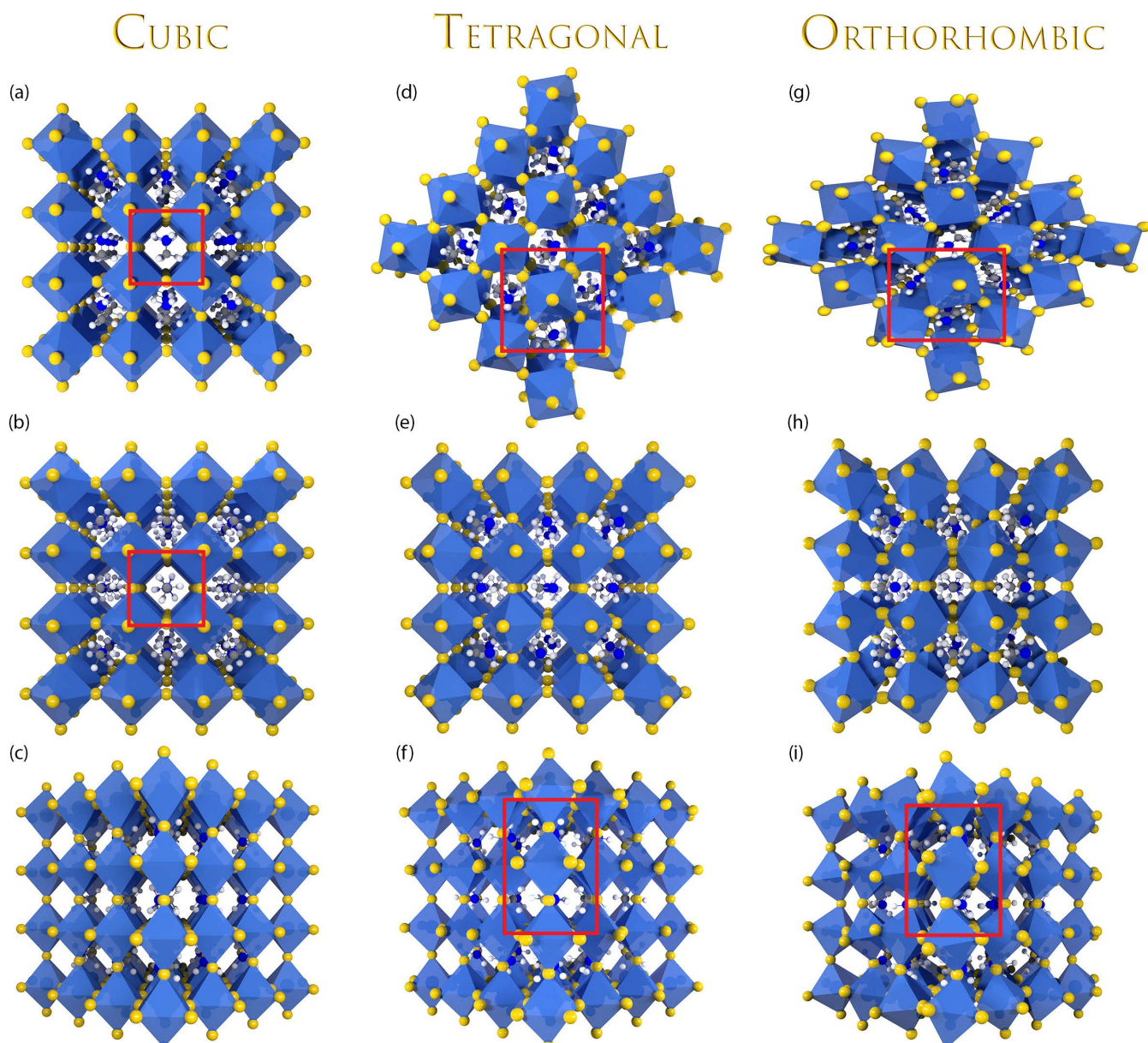
However, there is another very helpful way of visualizing this structure. The chemical bonds between the metal and the halide ions have a strong ionic and covalent dual nature<sup>49</sup> in hybrid perovskites such as the archetypal MAPbI<sub>3</sub>. These bonds form an inorganic lattice made of corner-sharing octahedra, with the halide sitting in the corners and the metal laying in their centers. This inorganic framework is rigid in comparison with the weaker hydrogen bonding of the methylammonium cation, which can move and reorient itself inside the inorganic cage, and whose main function is balancing the net charge in the crystal<sup>50</sup>.

When the temperature is high enough (usually around room temperature), the high dynamic disorder caused by a rotational and librational movement of the cation inside the inorganic cage, favors a highly symmetric cubic phase. This is common to most of the hybrid halide perovskites<sup>51,52,53</sup>. However, when temperature decreases below the first phase transition temperature (330 K in the case of MAPbI<sub>3</sub>), the octahedra tilt with respect to each other to reduce the volume of the crystal, undergoing a transition to a tetragonal phase. Another phase transition to an orthorhombic phase happens in this material when temperature decreases below 160 K<sup>51</sup>, with a further tilting of the octahedra, this time in a different plane than the previous one, leading to a volume reduction in the crystals. Moreover, the octahedra themselves experience an asymmetric reduction of its volume (Figure 1.9 (c)), reducing the symmetry of the crystal to orthorhombic. This phase has a very important peculiarity; the available space for the organic molecule is reduced, locking its movement inside the inorganic cage and affecting its optoelectronic properties<sup>51,1</sup>. All different phases observed in MAPbI<sub>3</sub> are represented in Figure 1.9.

However, in the case of FAPbI<sub>3</sub>, such reduction of the inorganic cage is not possible due to the bigger size and shape of the organic molecule, FA. Instead, a transition to another, more disordered tetragonal phase takes place<sup>54</sup>.

The organic cation, thus, even though it does not present a strong bonding to the inorganic framework, actually plays a fundamental role in the crystalline structure of organometal halide perovskites.

MAPbI<sub>3</sub>, despite its high efficiency in solar cells and other advantages previously mentioned, presents a phase transition at 330 K, which is just in the middle of the typical operating temperature of a photovoltaic device. This temperature ranges between 270-350 K, which accounts for colder conditions at night and hot peaks when the sun is perpendicular to the module. The crystalline material in the photovoltaic module would be forced to



**Figure 1.9** 3D representation of MAPbI<sub>3</sub> crystalline structure in its different structural phases. The first one is the cubic phase (a to c) This phase is present at temperatures higher than 330 K, and belongs to the  $Pm\bar{3}m$  space group. The tetragonal phase (d to f) lies in the range of temperatures between 163 and 330 K, and its space group is  $I4/mcm$ . Finally, the orthorhombic phase (g to i) can be found at temperatures below 163 K, and the space group is classified as  $Pnma$ . The top row of figures are oriented in the  $\langle 001 \rangle$  direction, the middle ones in the  $\langle 110 \rangle$ , and the bottom ones in the  $\langle 100 \rangle$

repeatedly undergo a structural phase transition. On the other hand, this phase transition is continuous, so cycling it may not be affecting the crystalline quality of the material after all. It has been shown, however, that the first-order low-temperature phase transition in MAPbI<sub>3</sub>, happening at around 150 K, from a tetragonal to an orthorhombic phase presents hysteresis, and cycling it could indeed induce permanent changes in the material properties<sup>55</sup>.

FAPbI<sub>3</sub>, on the other hand, presents a lower temperature phase transition at 280 K<sup>54</sup>, so it would be subject to much less cycling

[55] Oshero, Anna, et al. (2016) "The impact of phase retention on the structural and optoelectronic properties of metal halide perovskites." *Advanced Materials* 28.48: 10757-10763.



stress than MAPbI<sub>3</sub>. It presents, however, a different structural problem; its perovskite phase is unstable at room temperature; it spontaneously transforms into a non-perovskite hexagonal, yellow  $\delta$  phase, with no interest in PV due to its poor photovoltaic properties<sup>54</sup>. By mixing the organic cations, we can obtain compounds such as FA<sub>0.5</sub>MA<sub>0.5</sub>PbI<sub>3</sub>, a perovskite material which is both stable at operational temperatures for a photovoltaic device, and does not undergo a spontaneous transition into a non-perovskite phase<sup>47,IV</sup>.

Studying the structural stability of a material is then of fundamental importance to obtain good performing devices in the long time range. Reference IV, presented in this thesis, shows the first complete phase diagram for compounds of the formula FA<sub>x</sub>MA<sub>1-x</sub>PbI<sub>3</sub>. And reference I shows the phase transitions that MAPbI<sub>3</sub> undergoes under pressure, revealing for the first time a high-pressure phase not reported previously in the literature.

### 1.1.4 Defect tolerance

One attractive advantage of using perovskites as the active layer in photovoltaics is its easy solution processability, as well as the low temperature required during crystal growth. This makes it cheaper than its conventional inorganic competitors and compatible with large scale production at low cost. However, one should expect a high amount of defects from this fabrication process, so it is striking that the PV record efficiency for hybrid perovskites is already at 25.2%<sup>9</sup>, and increasing every year. Actually, it is approaching quickly the theoretical maximum efficiency for a semiconductor with a bandgap near 1.5 eV, which is around 33%<sup>56</sup>. Hybrid perovskites, such as the archetypal MAPbI<sub>3</sub>, must then present an extremely good defect tolerance<sup>57,58</sup>. Understanding why is that so could open the path to designing more robust or stable photovoltaic materials.

There are several types of defects in crystals, which involve one or more atoms<sup>59</sup>. If it only involves one atom they are called point defects; such as vacancies, interstitial or substitutions. A missing atom in the lattice is called a vacancy. An interstitial happens if an atom lies in between other crystalline positions. Finally, a substitution occurs when one of the atomic species of the crystal is occupying a different crystalline site other than its original structural position. If these point defects are related to elements that are not natural to the crystal, they are called impurities. These point defects are illustrated in Figure 1.10 for a perovskite

[56] Shockley, W., & Queisser, H. J. (1961). "Detailed balance limit of efficiency of p-n junction solar cells." *Journal of applied physics*, 32(3), 510-519.

[57] Meggiolaro, Daniele, et al. (2018) "Iodine chemistry determines the defect tolerance of lead-halide perovskites." *Energy & Environmental Science* 11.3: 702-713.

[58] Brandt, Riley E., et al. (2015) Identifying defect-tolerant semiconductors with high minority-carrier lifetimes: beyond hybrid lead halide perovskites. *Mrs Communications* 5.2: 265-275.

[59] Queisser, Hans J., and Haller, E. Eugene (1998) "Defects in semiconductors: some fatal, some vital." *Science* 281.5379: 945-950.

[60] Schmolke, Rüdiger, et al. (1999) "Observation of extremely low defect densities in silicon wafers." *Japanese journal of applied physics* 38.4R: 1852.

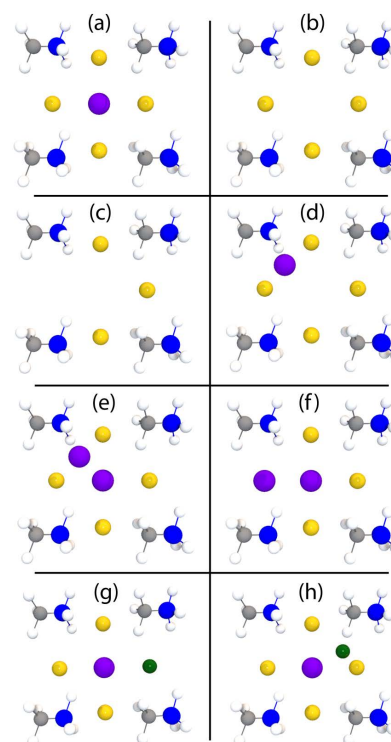
(MAPbI<sub>3</sub>) lattice. Defects may also involve higher dimensional structures; such as arrays of atoms (dislocations) or three dimensional defects (i.e. grain boundaries).

All crystalline materials of macroscopic proportions present defects, and the good quality of a crystal is related to a low number of these. This number can vary enormously: for example, the highest quality silicon wafers<sup>60</sup> have a density of defects on the order of  $10^4 \cdot \text{cm}^{-3}$ , which is impressive taking into account that the density of Si atoms in a crystal lattice is around  $\cdot 10^{22} \text{cm}^{-3}$ . Other crystalline materials grown at lower temperatures such as organometal halide perovskites have a density of defects twelve orders of magnitude higher<sup>61</sup>, around  $10^{16} \cdot \text{cm}^{-3}$ . This large amount of defects contrasts with the high efficiencies obtained in perovskite solar cells (PSC), which demonstrate their ability to tolerate defects without affecting its optoelectronic properties.

All of these defects are spatially localized, and often their energy levels lie within the bandgap of the material. These defects may affect the material optoelectronic properties when they interact with nearby charge carriers. If a charge carrier gets captured by a shallow defect, which are those whose energy levels lie near the band edges, it may escape the trap via phonon absorption, or it could recombine with a hole in the valence band emitting a photon (Figure 1.13 and Figure 1.15, respectively). If the defect, however, lies well within the bandgap, in what is called a deep trap, the radiative recombination process is unlikely, and it will most probably decay emitting phonons. When an electron gets trapped in a deep trap state, the lattice is distorted around the defect, producing lattice relaxation, due to the change in coulombic interaction between the defect and its surroundings. This process generates an oscillating movement around the defect which is not natural of the crystal, and it quickly decays in several phonons due to phonon-phonon interaction (see Figure 1.16). Lattice relaxation is thus the mechanism responsible of non-radiative recombination in deep trap states. However, it is not exclusive of this type of defects, and it can be present even in defects whose energy levels lie inside the conduction or valence band, even though this is less common.

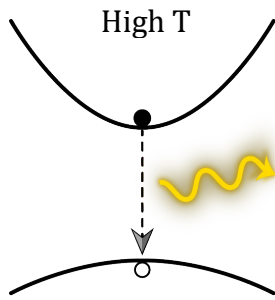
Figure 1.11 to Figure 1.16, at the sides of the next pages, summarize the recombination processes in semiconductors, mainly for excitonic processes such as the ones present in perovskites.

Since electron-hole recombination via deep trap states constitutes a common loss mechanism in photovoltaic devices<sup>62</sup>, the reduction of these type of non-radiative recombination routes is fundamental

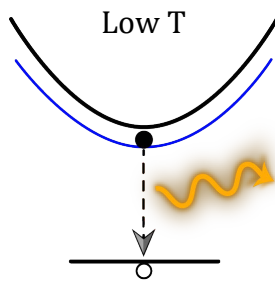


**Figure 1.10** Schematic representation of all possible types of point defects in MAPbI<sub>3</sub>. (a) Perfect lattice, (b) Vacancy, (c) Schottky defect (two vacancies from opposite charged ions), (d) Frenkel defect (An atom moves to an interstitial position, leaving a vacancy behind), (e) Interstitial, (f) Anti-site substitution, (g) Substitutional impurity and (h) Interstitial impurity.

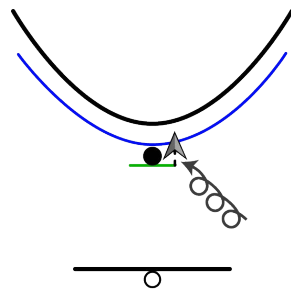
[61] Jiang, Minlin, et al. (2019) "Observation of lower defect density brought by excess PbI<sub>2</sub> in CH<sub>3</sub>NH<sub>3</sub>PbI<sub>3</sub> solar cells." *AIP Advances* 9.8: 085301.



**Figure 1.11** Energy vs wave vector “k” diagram of a band to band radiative recombination of an electron at the bottom of the conduction band with a hole at the top of the valence band



**Figure 1.12** Radiative recombination from an excitonic level. Coulombic interaction between the electron and hole decreases the energy difference between the excited and the relaxed state, represented here in total value.

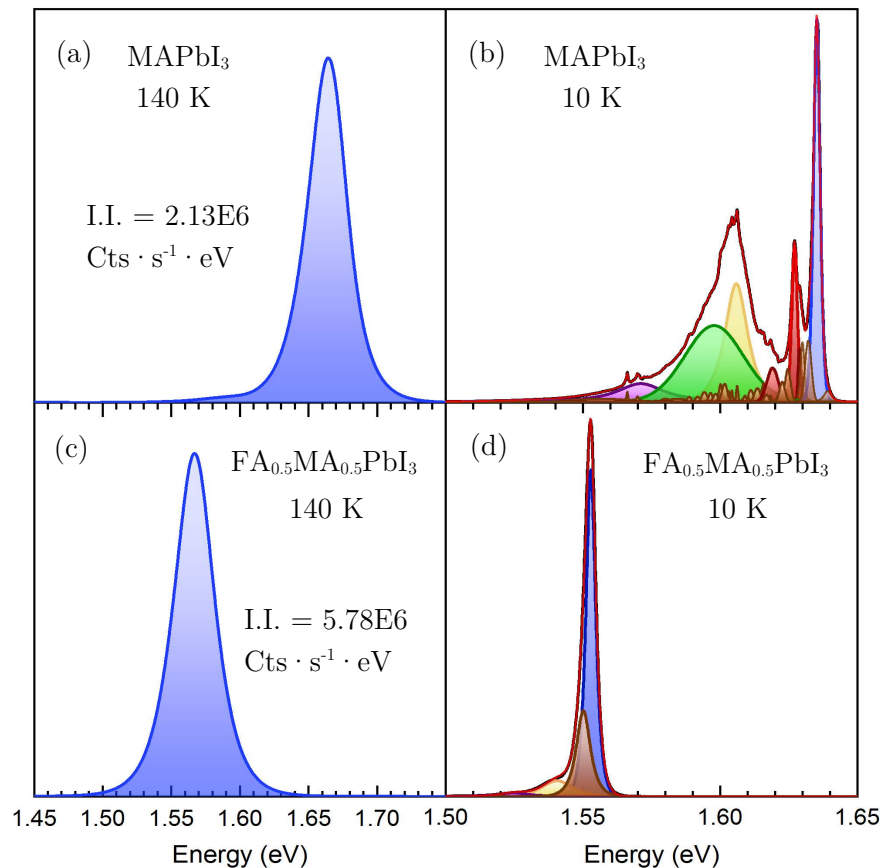


**Figure 1.13** Electron absorbing a phonon and hopping back to the exciton energy level from a shallow defect state. Here the temperature is high enough to have a populated density of phonons.

for obtaining high efficiencies in solar power conversion. Growing very high quality, low defect density crystals, usually increases the production costs. Hybrid perovskites, on the other hand, naturally do not present a high density of deep trap states, which is a great advantage.

Shallow defects usually have a formation energy lower than the thermal energy at room temperature. Then, it becomes easy for trapped charge carriers to be spontaneously detrapped by absorbing a phonon (Figure 1.13), in a process that typically occurs much faster than the recombination with a hole from the valence band. Radiative recombination from shallow defect states can be observed, however, upon photoexcitation when the temperature is low enough and there is a small phonon population (see Figure 1.14 and Figure 1.15).

Shallow defects thus have a much lower impact than deep traps on the performance of the device. They may, however,



**Figure 1.14** PL spectra of MAPbI<sub>3</sub> (a, b) and FA<sub>0.5</sub>MA<sub>0.5</sub>PbI<sub>3</sub> (c, d) both at 140 and 10 K. Both left panels show a single and well defined PL excitonic peak for the 140 K temperature, being the PL efficiency of the mixed formula considerably higher than that of MAPbI<sub>3</sub>. The right panels show the low temperature regime, where radiative recombination from the free exciton and also shallow defects can be observed. Notice that FA<sub>0.5</sub>MA<sub>0.5</sub>PbI<sub>3</sub> show almost no exciton complexes in comparison with the single cation MAPbI<sub>3</sub>.

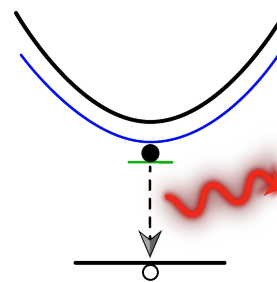
[62] Ball, James M., and Petrozza, Annamaria. (2016) “Defects in perovskite-halides and their effects in solar cells.” *Nature Energy* 1.11: 16149.



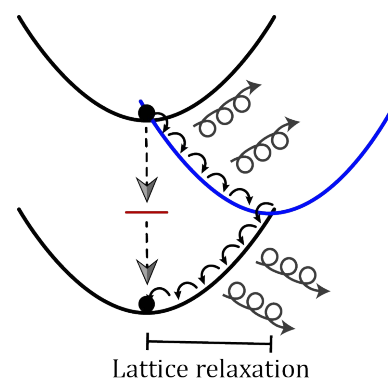
unintentionally dope the material. This can be avoided if there is compensation between the creation of donor and acceptor defects, and this way the performance of a PV device would not be strongly affected. Both type of defects, however, may also affect the charge transport in the device, especially if they are electrically charged, because they become scattering centers due to coulombic interactions.

Understanding the defect distribution and trying to minimize their number and impact is therefore of great importance in any material used in optoelectronic devices, as is the case for hybrid perovskites. This type of materials exhibit very bright photoluminescence (PL) at room temperature<sup>63</sup>. Figure 1.14 shows PL spectra of single crystals MAPbI<sub>3</sub> and FA<sub>0.5</sub>MA<sub>0.5</sub>PbI<sub>3</sub> obtained at 140 and 10 K for both materials, using a 633 nm excitation laser. This high intensity of the free-exciton PL peak (in blue) shows that non-radiative recombination via deep trap states does not dominate the relaxation processes in the material. On the other hand, looking at the spectra of MAPbI<sub>3</sub> at 10 K in Figure 1.14(b), we observe many defect-related peaks (different colors). They are now visible because due to the low temperature, the phonon population is reduced, so the phonon absorption represented in Figure 1.13 does not take place. It becomes more difficult for the electron to absorb a phonon and be promoted back to the excitonic energy levels, and, when the photoexcited charge carriers become trapped in these shallow defects, they tend instead to recombine radiatively directly from that level, emitting a lower energy photon. It is interesting, however, to observe that the mixed cation crystal with an even FA and MA concentration shows a much lower presence of shallow defects. Besides, the integrated intensity (I.I.) of the exciton in the mixed formula almost triplicate the intensity of the corresponding one in pure MAPbI<sub>3</sub> for the same temperature and laser power density. Thus, the radiative recombination is even more favored in FA<sub>0.5</sub>MA<sub>0.5</sub>PbI<sub>3</sub>.

This shows the importance of mixing cations in hybrid perovskites, and the relevance of the studies carried on them, such as the ones shown in Papers III and IV. It goes beyond the scope of this introduction to further analyze the nature of these defects or properly ascribe them to specific point defects in the material. However, I will just summarize the nature of defects found in the literature for MAPbI<sub>3</sub>. This material presents twelve possible native point defects. Three of them are the vacancies of any of its constituent parts (MA, Pb or I), another three are interstitials of these atoms, and finally, six correspond to all the anti-site possible



**Figure 1.15** When the temperature is low enough, the number of phonons in the system is reduced, and the electron which is trapped in a shallow defect cannot hop back to the excitonic level. Eventually, radiative recombination occurs from these lower energy states.



**Figure 1.16** Deep trap states acting as a recombination center. In this case, the x axis corresponds to the configurational coordinate  $q$ , a distance in real space. The energy loss of the electrons that get trapped is absorbed by an internal atomic movement, i.e. lattice relaxation, whose anharmonic vibrational mode decays quickly, emitting multiple phonons.

[63] Deschler, Felix, et al. "High photoluminescence efficiency and optically pumped lasing in solution-processed mixed halide perovskite semiconductors." *J. Phys. Chem. Lett* 5.8 (2014): 1421-1426.

- [64] Buin, Andrei, et al. "Halide-dependent electronic structure of organolead perovskite materials." *Chemistry of Materials* 27.12 (2015): 4405-4412.
- [65] Kim, Jongseob, et al. "The role of intrinsic defects in methylammonium lead iodide perovskite." *The journal of physical chemistry letters* 5.8 (2014): 1312-1317.
- [66] Yin, W. J., Shi, T., & Yan, Y. (2014). "Unusual defect physics in CH<sub>3</sub>NH<sub>3</sub>PbI<sub>3</sub> perovskite solar cell absorber." *Applied Physics Letters*, 104(6), 063903.
- [67] Walsh, Aron, et al. "Self-regulation mechanism for charged point defects in hybrid halide perovskites." *Angewandte Chemie International Edition* 54.6 (2015): 1791-1794.
- [68] Stranks, Samuel D., et al. "Recombination kinetics in organic-inorganic perovskites: excitons, free charge, and subgap states". *Physical Review Applied* 2.3 (2014): 034007.
- [69] Xiao, Zhengguo, et al. "Giant switchable photovoltaic effect in organometal trihalide perovskite devices". *Nature materials* 14.2 (2015): 193.
- [70] Leijtens, Tomas, et al. "Mapping Electric Field-Induced Switchable Poling and Structural Degradation in Hybrid Lead Halide Perovskite Thin Films". *Advanced Energy Materials* 5.20 (2015): 1500962.
- [71] Zhang, Ye, et al. "Charge selective contacts, mobile ions and anomalous hysteresis in organic-inorganic perovskite solar cells". *Materials Horizons* 2.3 (2015): 315-322.

combinations. Most of the theoretical approaches to calculate the formation energy of these defects so far have been done with density functional theory (DFT)<sup>62,64,65,66</sup>. They agree that the defects with lower formation energy, that is, the more probable to be present, are shallow defects. The deep trap states have higher formation energies, preventing them to dominate the electronic landscape of hybrid perovskites.

Shallow acceptor defects<sup>66</sup> are vacancies of MA ( $V_{MA}$ ),  $V_{Pb}$ , iodine interstitial ( $I_i$ ), and methylammonium substituting lead ( $MA_{Pb}$ ). On the other hand, shallow donor defects are  $MA_i$ ,  $MA_I$ , and  $V_I$ .

More importantly, when synthesizing MAPbI<sub>3</sub> in stoichiometric conditions, donor and acceptors defects are produced in equal numbers, thus leading to charge carrier compensation<sup>67</sup>.

### 1.1.5 Stability

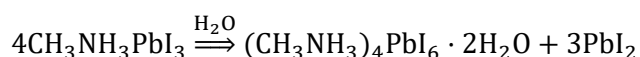
Power conversion efficiency is probably the most important parameter in photovoltaic applications. However, the stability of the material is also essential, because any type of degradation would generally affect negatively the efficiency.

The ions inside the perovskite crystal present high mobility, in particular halide vacancies or interstitials<sup>68,69</sup>. The fact that these ions move and create an internal electric field has diverse consequences for the optical and electrical properties of the material. On the one hand, this built-in electric field helps separating charges, and even in devices with no selective layers, charge can be extracted upon application of an external electric field<sup>70,71</sup>. On the other hand, perovskite solar cells can present great hysteresis when measuring current-voltage curves, due to ion movement<sup>72,73</sup>. This means that its photovoltaics parameters, including the efficiency, may change according to the voltage applied, or the power generated upon illumination may vary with time. Moreover, hysteresis should be avoided because due to its dependence on scan rate or direction, efficiencies may be over or under-estimated when characterizing the device.

However, this hysteresis can be greatly reduced by selecting a convenient solar cell architecture. For instance, the dye-sensitized solar cell with the perovskite infiltrated within the mesoporous TiO<sub>2</sub> matrix presents a smaller hysteresis than those that use an alumina scaffold, or those that employ the normal planar configuration<sup>15</sup>. This hysteresis is also reduced in "inverted" planar

heterojunctions, with an inverted *p-i-n* configuration and using organic compounds as selective layers<sup>74</sup>.

In fact, the biggest challenge for perovskite solar cells is probably overcoming the degradation happening due to the contact with water, or even with the humidity in the air. The organic cations present a very hygroscopic nature, and this hydration of the perovskite leads to degradation of the material. In the case of humidity, degradation can be reversed after drying the material<sup>75</sup>. However, if the sample gets in contact with liquid water it decomposes irreversibly into lead iodide (PbI<sub>2</sub>) and a non-perovskite sub-product following this chemical reaction<sup>76</sup>:



However, direct degradation with water is not the only concern. The combination of moisture with heat<sup>77</sup>, or a weak electric field<sup>70</sup>, produces an extremely fast degradation. Proper encapsulation of the device is thus fundamental in perovskite solar cells. Usually, the best insulating technique consists in attaching a glass surface to the device with an epoxy glue. Another option is using a plastic sealant, because it offers flexibility and a lower price, but it presents a certain degree of permeability to water.

Light soaking is another concern regarding the stability of organometal perovskites, in particular, the exposition to ultraviolet light. Recently, it was hinted that the cause of the degradation of perovskite solar cells upon UV irradiation was the presence of TiO<sub>2</sub> in contact with the perovskite material<sup>78</sup>, so the solution could be either adding a UV blocking layer to the device, or using non-metallic oxide contacts, which has already given good results<sup>74</sup>.

Apart from all the stability concerns already mentioned, long term structural stability is also necessary for making practical devices. MAPbI<sub>3</sub> and FAPbI<sub>3</sub> present astoundingly high efficiencies, however, they present serious structural instability problems that prevent them from being perfectly suitable for commercial photovoltaic applications. As it was stated above, the Goldschmidt tolerance factor of FAPbI<sub>3</sub> is 1.04, making the perovskite phase unstable and favoring a hexagonal, photoinactive,  $\delta$  phase. On the other hand, the MAPbI<sub>3</sub> tolerance factor is 0.95, which forces the crystal to adopt a tetragonal phase at room temperature, finally transitioning to the cubic phase at 330 K. By mixing both MA and FA, it is possible to access those tolerance factors between 0.95 and 1.04, getting thus closer to the ideal  $t = 1$  cubic perovskite value. In particular, a good value of

[72] Snaith, Henry J., et al. (2014) "Anomalous hysteresis in perovskite solar cells". *J. Phys. Chem. Lett* 5.9: 1511-1515.

[73] Unger, Eva Lisa, et al. (2014) "Hysteresis and transient behavior in current-voltage measurements of hybrid-perovskite absorber solar cells". *Energy & Environmental Science* 7.11: 3690-3698.

[74] Heo, Jin Hyuck, et al. (2015) "Hysteresis-less inverted CH<sub>3</sub>NH<sub>3</sub>PbI<sub>3</sub> planar perovskite hybrid solar cells with 18.1% power conversion efficiency". *Energy & Environmental Science* 8.5: 1602-1608.

[75] Leguy, Aurélien MA, et al. (2015) "Reversible hydration of CH<sub>3</sub>NH<sub>3</sub>PbI<sub>3</sub> in films, single crystals, and solar cells." *Chemistry of Materials* 27.9: 3397-3407.

[76] Zhao, Jiangtao, et al. (2016) "Investigation of the hydrolysis of perovskite organometallic halide CH<sub>3</sub>NH<sub>3</sub>PbI<sub>3</sub> in humidity environment". *Scientific reports* 6: 21976.

[77] Liu, Jiewei, et al. (2015) Employing PEDOT as the p-type charge collection layer in regular organic-inorganic perovskite solar cells. *The journal of physical chemistry letters* 6.9: 1666-1673.

[78] Weidmann, J., et al. (1999) "Influence of oxygen and water related surface defects on the dye sensitized TiO<sub>2</sub> solar cell." *Solar energy materials and solar cells* 56.2: 153-165.

the tolerance factor for these compounds to stabilize a cubic perovskite phase in room temperatures lie between 0.97 and 1.01, which corresponds to values of  $x$  ranging from 0.4 to 0.6 in the  $\text{FA}_x\text{MA}_{1-x}\text{PbI}_3$  formula<sup>47</sup>. Besides, mixed cation compounds, present both a slower polymorphism route than that of  $\text{FAPbI}_3$  to a hexagonal phase, and a slower decomposition due to moisture present in the air<sup>47</sup>.

## 2 Experimental techniques

All perovskite samples studied during this thesis were characterized using optical, non-invasive techniques, such as photoluminescence or Raman. Usually, these measurements were made as a function of temperature, pressure, or both at the same time.

In this section I will introduce the fundamental working principles of these techniques, trying to avoid repeating the details and specifications that are already present in the articles. I will focus, however, on some practical aspects and theoretical concepts that were not explained in detail in the papers.

### 2.1 Sample Growth

All the samples were provided by Bethan Charles, Oliver J. Weber and Mark T. Weller from Bath University. These samples were all single-crystal perovskites, in particular perovskites of the type  $\text{FA}_x\text{MA}_{1-x}\text{PbI}_3$ , with  $x$  ranging from 0 to 1 in 0.1 steps. Using single crystals allows us to better study the material intrinsic properties, compared with polycrystalline materials, whose grain boundaries may affect their optoelectronic and structural properties.

We obtained several batches, grown from 2016 to 2019. The size and crystalline quality of the samples improved after the first batch, leading to bigger crystallite sizes (between 1 to 5 mm in diameter), and improved quality in the PL and Raman spectra obtained. Most of our measurements were done on these latter high-quality single crystals (See Figure 2.2)

Crystal growth of the mixed cation samples was carried out according to the inverse solubility method developed by Saidaminov et al<sup>79</sup>. The compositional ends,  $\text{MAPbI}_3$ ,  $\text{FAPbI}_3$ , and  $\text{MAPbBr}_3$ , however, were grown via the precipitation from HI method by Poglitsch and Weber<sup>80</sup>. A slightly different method was employed with the very thin samples (30  $\mu\text{m}$  of thickness) needed for the experiments at high pressures. These samples were grown in between two glass slides, in a process further explained in reference I. More details about the growing techniques from our collaborators can be consulted elsewhere<sup>81</sup>.

Remarkably thin samples are necessary to fit in the narrow space available inside the metal gasket used in pressure experiments, as it will be explicitly shown in section 2.5, and the number of samples grown by the confined method at our disposal was



**Figure 2.1** The author of the present work, using magnification lenses to manually introduce a fragment of a sample (of only a few tens of micrometers in size), inside the 0.25 mm diameter hole of a metal gasket, used for pressure generation.



**Figure 2.2** Example of two of the  $\text{MAPbI}_3$  single crystals used in this thesis, grown at Bath University. A 1 cent coin is placed next to them for perspective.

[79] Saidaminov, Maksud I., et al. (2015) "High-quality bulk hybrid perovskite single crystals within minutes by inverse temperature crystallization." *Nature communications* 6: 7586.

[80] Poglitsch, A., & Weber, D. (1987). Dynamic disorder in methylammoniumtrihalogenoplumbates (II) observed by millimeter-wave spectroscopy. *The Journal of chemical physics*, 87(11), 6373-6378.

[81] Weber, O. J., B. Charles, and M. T. Weller. (2016) "Phase behaviour and composition in the formamidinium-methylammonium hybrid lead iodide perovskite solid solution." *Journal of Materials Chemistry A* 4.40: 15375-15382.

limited. Fortunately, we found a very simple but useful method to obtain thin samples from bigger perovskite crystals. In this method, we proceeded to crush millimeter-sized crystals, like the ones shown in Figure 2.2, between two glass slides. The crystals broke in a large number of small pieces, with a tendency to create thin, planar fragments, many of them of adequate size for the experiments.

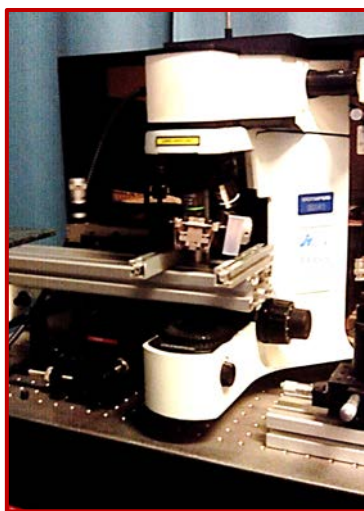
## 2.2 Raman

The Raman effect was discovered simultaneously by Raman and Krishnan<sup>[82]</sup>, and by Landsberg and Mandelstam<sup>[83]</sup> in 1928. It was Raman, however, who was awarded with a Nobel prize in 1930 for its discovery.

The effect consists in the shift in frequency of a small fraction of the light scattered by a sample. This shift is related to the vibrational states of the constituent atoms of the sample, and it can be regarded as a fingerprint of the material. The Raman signal is very weak in comparison to the intensity of the elastically scattered laser light. However, by filtering the latter, it is possible to resolve the Raman signal and characterize the sample, analyzing it quantitatively or qualitatively.

To understand the Raman effect, we have to introduce briefly the interaction taking place between the vibrations of the material and light. The vibrational state of a molecule composed by  $N$  atoms is completely defined by the temporal evolution of the three spatial coordinates for each of the atoms. Thus, in a classical approach, the solution is given by solving the  $3N$  Lagrange equations (one for each particle in each of the three dimensions); giving  $3N$  solutions. Three of them correspond to all the atoms moving in the same direction (translational movement), and another three correspond to rotations, in both cases with respect to each one of the axes. The rest of the solutions,  $3N-6$ , correspond to the normal vibrational modes, where the atoms vibrate in phase with each other.

Since light is an electromagnetic wave, it can interact with positive and negative charges in a molecule. Apart from the electrons, that may absorb a photon and be promoted from the valence band to the conduction band in a semiconductor, the vibrational state of the atomic core can also change by interacting with infra-red light, by absorbing a photon and emitting a phonon. However, when the frequency of the light is far away from the vibrational frequency



**Figure 2.3** Olympus BX41 microscope, integrated in the Jobin Yvon LABRAM HR 800 spectrometer used to measure Raman and photoluminescence during the work of this thesis.

[82] Raman, C. V., & Krishnan, K. S. (1928). "A new type of secondary radiation". *Nature*, 121(3048), 501-502.

[83] Landsberg, G., & Mandelstam, L. (1928). "A novel effect of light scattering in crystals. *Naturwissenschaften*", 16(5), 5.

of the molecule, the main process taking place is the electronically assisted scattering of the light.

In the following discussion I will present the classical approach to the Raman effect, however, the images at the side of this page represent the quantum interpretation, involving real and virtual energy states, which is easier to visualize.

The dipole moment of a molecule ( $\vec{P}$ ) can vary with an external electric field ( $\vec{E}$ ). The strength of this interaction depends on the polarizability ( $\vec{\alpha}$ ), according to the following equation:

$$\vec{P} = \vec{\alpha}\vec{E}$$

Here,  $\vec{E} = \vec{E}_0 \cos \omega_0 t$  is the external electric field, oscillating with an angular frequency  $\omega_0$ , and  $\vec{\alpha}$  is the polarizability of the molecule (a second rank tensor), which can be expanded to first order in a Taylor series as:

$$\vec{\alpha}(q) = \vec{\alpha}_0 + \left(\frac{\partial \vec{\alpha}}{\partial q}\right)_0 + \dots$$

Being  $q = q_0 \cos \omega t$  a generalized coordinate.

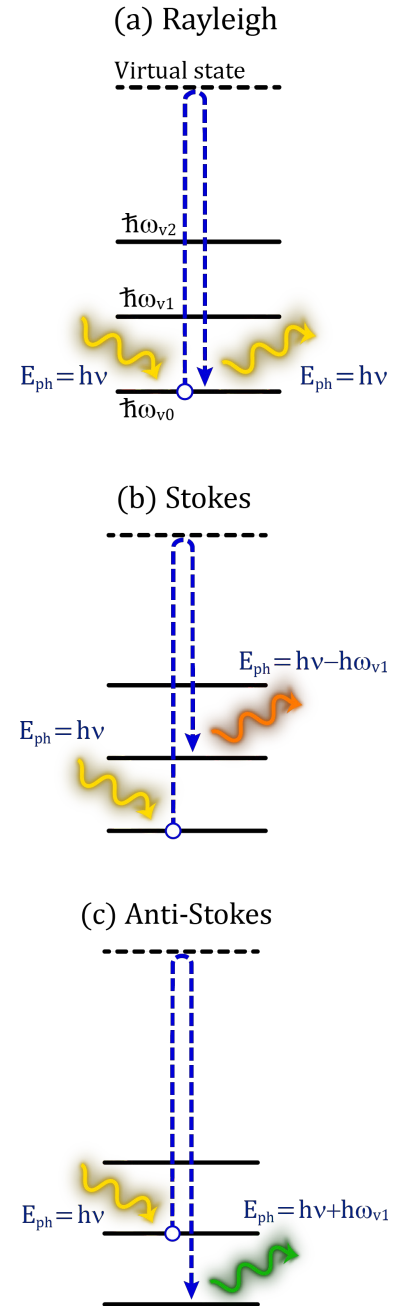
The induced dipole moment  $\vec{P}$ , proportional to the scattered electric field  $\vec{E}_s$ , is:

$$\vec{E}_s \approx \vec{P} = \vec{\alpha}_0 \vec{E}_0 \cos \omega_0 t + \left(\frac{\partial \vec{\alpha}}{\partial q}\right)_0 q_0 \vec{E}_0 \cos \omega_0 t \cos \omega t$$

Which, by applying the trigonometry relation  $2 \cos A \cos B = \cos(A + B) + \cos(A - B)$ , leads to:

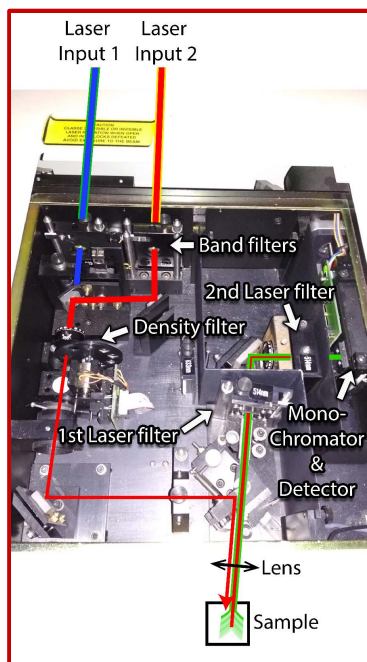
$$\vec{E}_s = \underbrace{\vec{\alpha}_0 \vec{E}_0 \cos \omega_0 t}_{\text{Rayleigh}} + \frac{1}{2} \left(\frac{\partial \vec{\alpha}}{\partial q}\right)_0 q_0 \vec{E}_0 \left[ \underbrace{\cos(\omega_0 - \omega)t}_{\text{Raman Stokes}} + \underbrace{\cos(\omega_0 + \omega)t}_{\text{R. Anti-Stokes}} \right]$$

The first term corresponds to the Rayleigh scattering, i.e. elastic scattering, where the scattered light frequency is unchanged. The second term, on the other hand, shows a shift in the frequency of the scattered light with respect to the incident one; this is the Raman effect. The scattered frequencies are  $(\omega_0 - \omega)$  and  $(\omega_0 + \omega)$ , corresponding to the so-called Stokes, and anti-Stokes processes, respectively. The latter presents a lower probability to happen than the former, because it requires an occupied excited state to take place (See Figure 2.4 (c)), which is more unlikely according to a Maxwell-Boltzmann distribution of states for a given temperature. Besides, in an anti-Stokes process a phonon is absorbed, so it also depends on the number of phonons available



**Figure 2.4** The three types of light scattering processes. (a), Rayleigh Scattering, (b) Raman Stokes and (c) Raman anti-Stokes. In Raman scattering, the energy of the scattered photon has increased (or decreased) a quantity equal to the difference in vibrational energy of the molecule after interacting with the excitation light (it absorbed or emitted a phonon in the process). The top energy level is a virtual state. However, in resonant Raman scattering this level would be either real or close to a real one.





**Figure 2.5** Insides of the spectrometer LABRAM HR 800. The light path is highlighted for clarity. There are two openings, to make it easier to change the excitation wavelength by just moving a mirror. In our laboratory we count with different lasers that allow us to use excitation wavelengths of 488 nm, 514 nm, 633 nm and 785 nm. It is possible also to couple the spectrometer to a super-continuum laser, but the maximum intensity available is greatly reduced.

[84]Barbillat, Jacques et al.  
 “Spectrométrie Raman” (1999)  
*Techniques de l'ingénieur - Traité  
 Analyse et caractérisation* P 2 865

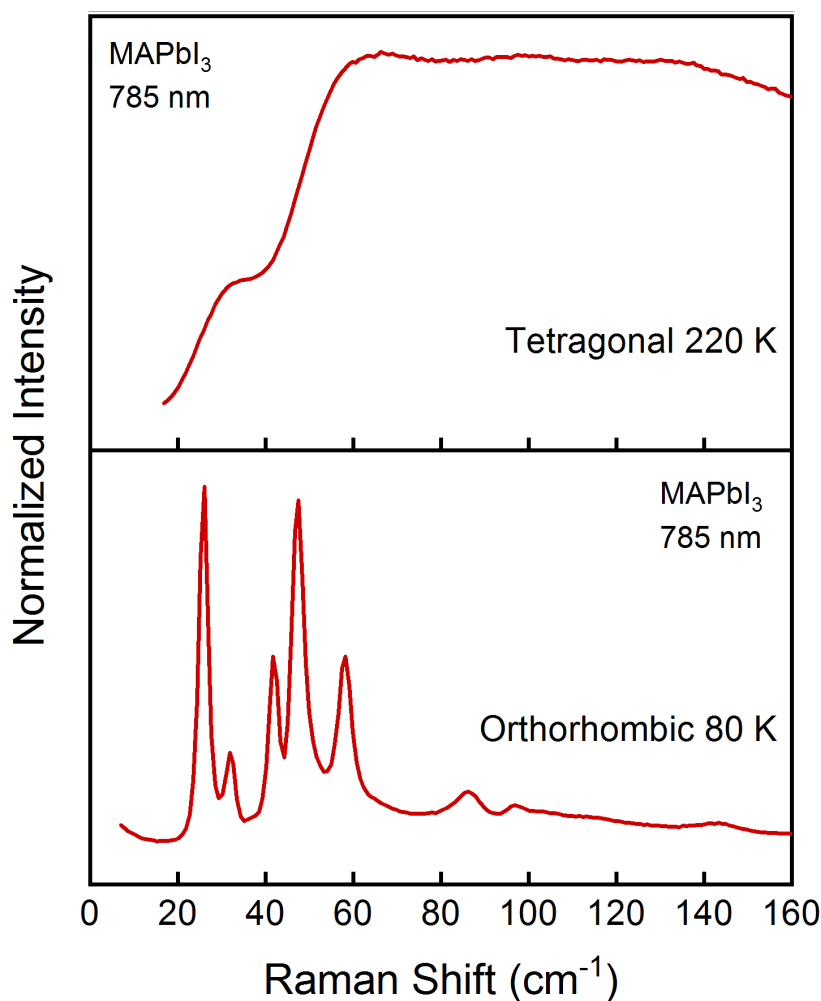
at that moment. Figure 2.4 illustrates the three different types of light scattering.

Also, it is important to note that the Raman effect needs the factor  $\left(\frac{\partial \bar{\alpha}}{\partial q}\right)_0$  to be different than zero. That is, only the vibrations that lead to a change in the polarizability of the molecule are Raman active. A useful tool to determine the activity of the vibrational modes is group theory. Each mode transforms according to irreducible representations of the symmetry group of the molecule (or the crystal), and, in order for any derivative  $\left(\frac{\partial \bar{\alpha}}{\partial q}\right)_0$  to be zero,  $\bar{\alpha}$  and  $q$  must belong to different symmetry classes<sup>84</sup>. So, a mode is Raman active only if its normal coordinate transforms in the same way of any of the  $\bar{\alpha}(q)$  matrix components. The number and symmetry of the active Raman modes in a crystal can be deduced thus by looking at the group symmetry character tables for a given crystal structure.

As mentioned above, typically the Raman signal is very weak compared to the elastically scattered light. However, this signal may be increased by up to 6 orders of magnitude in resonance conditions. Usually, as is shown in Figure 2.4, scattering happens promoting the molecule to a virtual energy state for a very short period of time. However, if the excitation light energy matches the energy of a real transition, such as the promotion of a valence band electron to the conduction band, then resonance happens and the Raman signal intensity is increased. For solids and liquids, however, the photoluminescence produced after the excitation of electronic states beyond the bandgap of the material may mask the Raman spectra, complicating its recognition.

Regarding our measurements, we mainly looked at the vibrational modes of the inorganic cage of the perovskites<sup>51</sup> ( $\sim 50$  to  $160$   $\text{cm}^{-1}$ ). The excitation wavelength was 785 nm, being near resonance at room temperature for all the samples due to the proximity in energy with the bandgap (785 nm is equivalent to 1.58 eV, whereas the bandgap of the  $\text{FA}_x\text{MA}_{1-x}\text{PbI}_3$  ranges from 1.41 to 1.53). At lower temperatures, the samples experienced different phase transitions, having associated a shift in the bandgap. In some cases, as in the low-temperature regime for concentrations of FA higher than 50%, the excitation energy approached too much that of the bandgap, and a very intense PL peak would appear in the spectra, masking completely the Raman signal. For the rest of the samples, the PL peak position was far enough from the excitation light energy, and the Raman could thus be easily resolved. We did not observe any influence of the orientation of





**Figure 2.6** Raman spectra of MAPbI<sub>3</sub> at 220 K and 80 K, in the tetragonal and orthorhombic phases, respectively. The excitation laser wavelength was 785 nm. As can be seen, there is a huge difference in the line shape of the Raman peaks between the two phases. The range 0 – 160 cm<sup>-1</sup> correspond to the inorganic cage modes.

the samples in the Raman signal obtained, even in the orthorhombic phase, and we did not use any polarizer, so it was not necessary in this case to take into account the selection rules.

Figure 2.3 shows the spectrometer (LABRAM HR 800) used during this thesis to measure most of the Raman and photoluminescence spectra. In this case, the sample was located inside a pressure cell. The scattered light from the sample is collected back again by the system (backscattering configuration), where the incident laser light is filtered, and the rest of the signal is spread in frequency by a diffraction grating, to be finally detected with a liquid nitrogen-cooled, charged coupled device (CCD) camera. See Figure 2.5 for further details of the working mechanism inside this optical device, and Figure 2.6 for an example of a Raman spectrum obtained measuring MAPbI<sub>3</sub>. The spectrum obtained in the tetragonal phase is qualitatively very different than the one obtained in the orthorhombic phase,

allowing us to determine unambiguously the phase transition temperature.

## 2.3 Photoluminescence

Luminescence is electromagnetic radiation (light) emitted from a material in a non-equilibrium state. That is, radiation different than the one emitted by a black body in thermodynamic equilibrium according to Planck's law.

In order to bring the system out of equilibrium, it is necessary to apply an external *excitation energy* to it. This energy may be provided by different means: Applying an electric field to the material (electroluminescence), directing an electron beam to it (cathodoluminescence), thermally exciting it (thermoluminescence), exciting it with sound waves (sonoluminescence), etc. In the case of photoluminescence, this excitation energy is electromagnetic radiation (light), typically from a laser.

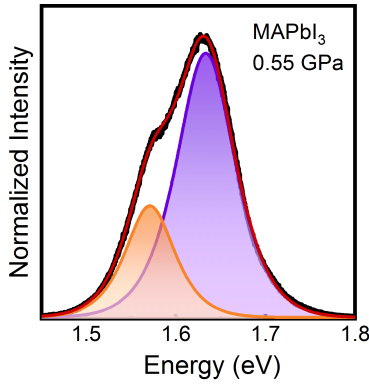
The difference with other processes such as reflection, or scattering, is that in a luminescence process, prior to emitting light, the energy is actually absorbed. This energy is employed to promote electrons to real excited energy states, and these electrons will finally emit light when they decay into lower energy electronic states.

If this luminescence comes from a perfect crystalline lattice in a solid, it is called *intrinsic luminescence*<sup>85</sup>. Band to band recombination, or recombination of an exciton (as is the case in hybrid perovskites<sup>86</sup>), are examples of intrinsic luminescence. However, if the origin lies in the presence of defects or impurities, then its nature is *extrinsic*, as can be observed in the photoluminescence of rubies.

The probability of an electron to decay to the ground state is the inverse of the lifetime  $\tau$ , and equals the sum of the probabilities of a radiative and a non-radiative transition:

$$\frac{1}{\tau} = \frac{1}{\tau_r} + \frac{1}{\tau_{nr}}$$

Here  $\tau_r$  is the radiative decay mean time and  $\tau_{nr}$  is the non-radiative one. The latter involves processes where the energy, instead of being radiated, is transferred to the crystal lattice in the form of heat.



**Figure 2.7** Example of a photoluminescence spectrum of MAPbI<sub>3</sub> measured with a 633 nm laser. This material presents a phase transition at 0.4 GPa, characterized by a sudden shift in the position of the PL peak. Between 0.4 and 0.7 GPa, however, there is coexistence of both phases, and both peaks can be resolved (orange and purple peaks in the figure)

[85] Pelant, Ivan & Valenta, Jan "Luminescence spectroscopy of Semiconductors" - Oxford University Press, 2012. ISBN-13: 9780199588336

[86] Pan, L., & Zhu, G. (Eds.). (2016) "Perovskite Materials" - Chapter 12: Photoexcitations and Emission Processes in Organometal Trihalide Perovskites - V. Michele Cadelano et al. ISBN: 978-953-51-2245-6

From a kinetic point of view, luminescence can be separated in two types of processes: monomolecular and bimolecular. A monomolecular process involves a localized luminescence center, and it is characteristic of defect/impurity mediated recombination (See Figure 2.8). It depends on the concentration of recombination centers ( $N(t)$ ), according to the relation

$$\frac{dN(t)}{dt} = G - \frac{N}{\tau} \approx \alpha I_{ex} - \frac{N}{\tau}$$

Where  $G$  is the generation term, that is, the number of photons absorbed per unit volume per unit time.  $G$  can roughly be described as the product of the absorption coefficient  $\alpha$ , times the excitation intensity  $I_{ex}$ .

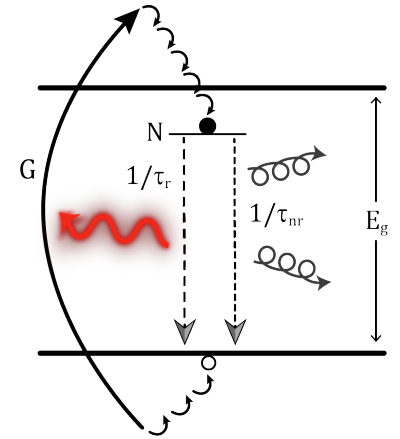
Bimolecular processes, on the other hand, are characteristic of free charge carriers (see Figure 2.9). They are, therefore, dependent on both the concentration of electrons,  $n$ , and holes,  $p$ . This is so because for an electron and a hole that are moving freely inside the crystal, in order to recombine radiatively, they must randomly encounter one another first. Therefore, the probability of this event increases when both the density of electrons and holes is larger. The equation that governs this process is:

$$\frac{dn(t)}{dt} = G - \beta np = \alpha I_{ex} - \beta n^2$$

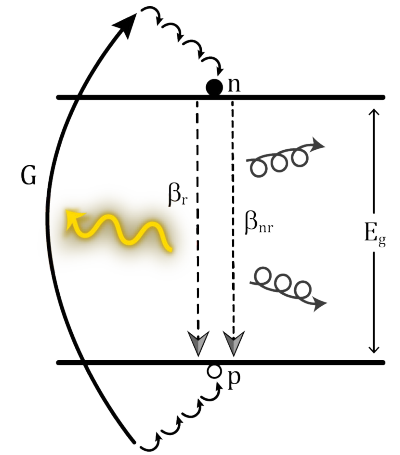
Where  $\beta$  is the bimolecular recombination coefficient, represented as the sum of the corresponding radiative and non-radiative coefficients  $\beta = \beta_r + \beta_{nr}$ . Also we consider, for simplicity, an intrinsic semiconductor where  $n = p$ .

When electron-hole pairs are photo-generated, they may recombine before charges are completely separated (i.e. before they are separated a distance larger than the Coulomb radius, which is the distance where the Coulomb energy is  $\sim K_B T$ ). In that case, called geminate recombination, the exciton recombination kinetics are monomolecular. On the other hand, if an exciton is formed from free electrons and holes, since the electron needs to randomly meet a hole before forming the bound electron-hole pair, the recombination process follows bimolecular kinetics.

It is typical to find both mono- and bi-molecular processes simultaneously. It is not in the scope of this brief introduction to photoluminescence spectroscopy to elaborate further on the equations that govern these processes, however, I just want to note that in our materials it is possible to see both processes happening at the same time when measuring at low temperatures



**Figure 2.8** Monomolecular recombination. The defect acts as a localized recombination center.



**Figure 2.9** Schematic representation of a bimolecular recombination process. Free charge carriers must come across another one of opposite charge to recombine. That is why the process is dependent both in the density of electrons and holes.

[87] Davies, Christopher L., et al. "Bimolecular recombination in methylammonium lead triiodide perovskite is an inverse absorption process." *Nature communications* 9.1 (2018): 293.

(see Figure 1.14). On the one hand, exciton recombination in hybrid perovskites presents a bimolecular character<sup>87</sup>, and on the other hand, when the temperature is low enough, we can also see luminescence from the defects, which, since they are spatially localized, must follow a monomolecular description of its recombination kinetics.

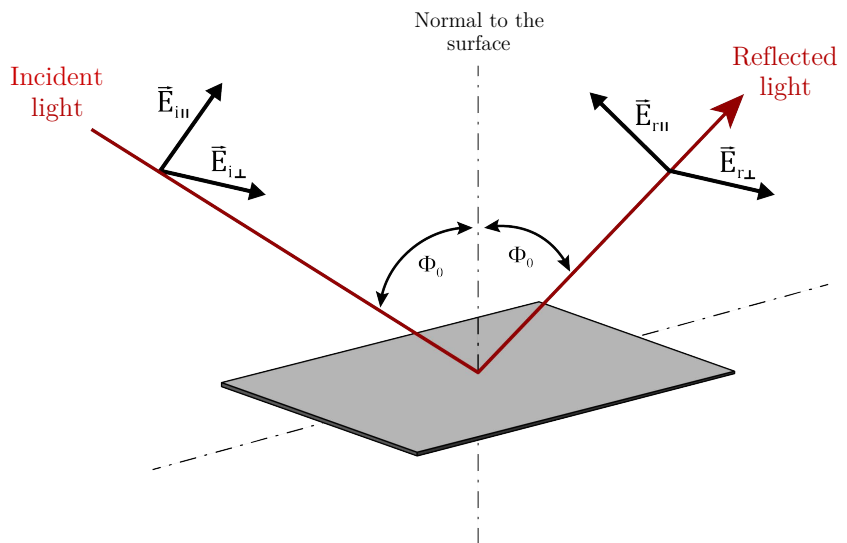
By looking at the shift of the photoluminescence peak with changing conditions, such as increasing pressure or decreasing temperature, we can extract the bandgap dependence on these parameters. This allows us to obtain information about the electronic band structure, or electron-phonon and thermal expansion effects on the bandgap (See ref. II). Also, sudden changes in the tendency or the position of these peaks, are indicative of structural phase transitions, as we note in ref. I and IV. Besides, valuable information about the quality of the crystal can be extracted from PL spectra. A representative spectrum is shown in Figure 2.7 for MAPbI<sub>3</sub> under mild pressure (0.55 GPa).

## 2.4 Ellipsometry

[88] Bernoux, Frank et al. (2003)  
 “Ellipsométrie” *Techniques de  
 l’ingénieur – Traité Mesures et  
 Contrôle*. R6490

Ellipsometry is also an optical, non-destructive characterization technique. It is based on the measurement of the change in polarization of the incident light upon reflection (or transmission) on a material surface.

Spectroscopic ellipsometry allows the determination of the complex refractive index of a material, and its thickness in the

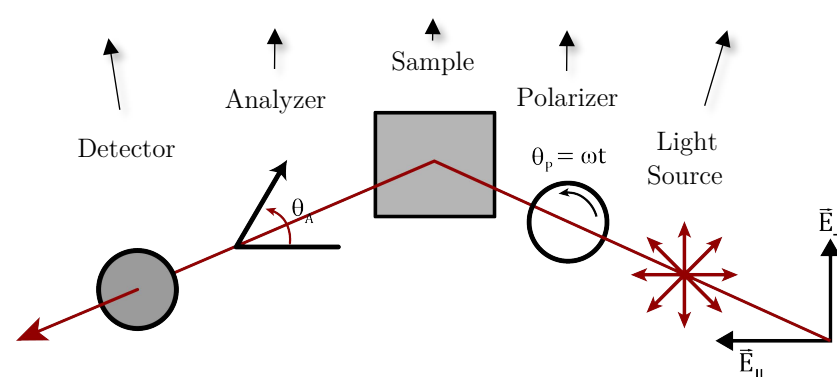


**Figure 2.10** Electric field being reflected on the surface of a material.  $\mathbf{E}_{i||}$  and  $\mathbf{E}_{r||}$  represent respectively the incident and reflected components of the field parallel to the plane of incidence.  $\mathbf{E}_{i\perp}$  and  $\mathbf{E}_{r\perp}$  correspond to the incident and reflected components perpendicular to the plane of incidence.  $\Phi_0$  is the angle of incidence.

case of a thin film. It is possible as well to study electronic transitions in the material, and the magnitude of the bandgap of a semiconductor, as it was done in ref. III with hybrid perovskites.

There are several types of ellipsometry techniques<sup>88</sup>; the zero method, the phase modulation method, the modulation by rotation method, etc. The latter method presents a rotatory element in the setup, which can be either the polarizer, the analyzer or a compensator. Below I will explain the fundamental working principles of ellipsometry with a rotatory polarizer, as this is the setup present in our laboratories.

If we decompose the electric field in its components relative to the plane of incidence; parallel ( $E_{\parallel}$ ) and perpendicular ( $E_{\perp}$ ) (See Figure 2.10), then the effect of each element of the setup on the polarization can be represented as a 2x2 matrix with complex coefficients.

$$\begin{bmatrix} E_{\parallel} \\ E_{\perp} \end{bmatrix} = \begin{bmatrix} \cos \theta_A & -\sin \theta_A \\ \sin \theta_A & \cos \theta_A \end{bmatrix} \begin{bmatrix} r_{\parallel} & 0 \\ 0 & r_{\perp} \end{bmatrix} \begin{bmatrix} \cos \theta_P & \sin \theta_P \\ -\sin \theta_P & \cos \theta_P \end{bmatrix} \begin{bmatrix} E_0 \\ E_0 \end{bmatrix}$$


**Figure 2.11** Path of the light from the source to the detector, with each element in the path associated with a transformation matrix.

The amplitude of the field on the detector is:

$$\mathbf{E}_d = \mathbf{A} \cdot \mathbf{R}(A) \cdot \mathbf{S} \cdot \mathbf{R}(-P) \cdot \mathbf{P} \cdot \mathbf{L} \quad (2.4-1)$$

Where  $\mathbf{P} = \mathbf{A} = \begin{pmatrix} 1 & 0 \\ 0 & 0 \end{pmatrix}$  corresponds to the polarizer and the analyzer matrices,  $\mathbf{R}(\theta) = \begin{pmatrix} \cos \theta & -\sin \theta \\ \sin \theta & \cos \theta \end{pmatrix}$  applies to the rotating elements,  $\mathbf{L} = \begin{pmatrix} E_0 \\ E_0 \end{pmatrix}$  is the isotropic field emitted from the light source, and  $\mathbf{S} = \begin{pmatrix} r_{\perp} & 0 \\ 0 & r_{\parallel} \end{pmatrix}$  represents the reflection on an optically isotropic sample, being  $r_{\perp}$  and  $r_{\parallel}$  the reflection coefficients for each of the polarizations, i.e. the relationship between the incident ( $E_i$ ) and reflected ( $E_r$ ) field:

$$r_{\perp} = \frac{E_{\perp r}}{E_{\perp i}} = |r_{\perp}| \exp(i\delta_{\perp})$$

$$r_{\parallel} = \frac{E_{\parallel r}}{E_{\parallel i}} = |r_{\parallel}| \exp(i\delta_{\parallel})$$

These coefficients are complex. The moduli  $|r_{\perp}|$  and  $|r_{\parallel}|$  represent the change in amplitude of the field after the reflection, and the phase  $\delta_{\perp}$  and  $\delta_{\parallel}$ , the phase shift introduced. Equation (2.4-1) can be visualized above, in Figure 2.11, where  $\theta_A$  is the angle of the analyzer, and  $\theta_P = \omega t$  the corresponding angle of the polarizer

We can define  $\rho$  as the relationship between the parallel and perpendicular reflection coefficients:

$$\rho = \frac{r_{\parallel}}{r_{\perp}} = \tan \Psi \exp(i\Delta)$$

With  $\tan \Psi = \frac{|r_{\parallel}|}{|r_{\perp}|}$ , and  $\Delta = \delta_{\parallel} + \delta_{\perp}$ .

For a bulk sample, the refractive index can be obtained with the following equation:

$$\frac{N_1}{N_0} = \sin \Phi_0 \sqrt{1 + \left(\frac{1-\rho}{1+\rho}\right)^2 \tan^2 \Phi_0} \quad (2.4-2)$$

Being  $N_1$  the complex refractive index of the measured sample ( $N_1 = n_1 + jk_1$ ), and  $N_0$  the refractive index of the medium in which the measurement is made ( $N_0 = 1$  in air). Also,  $\Phi_0$  is the angle of incidence.

To obtain the values of  $\tan \Psi$  and  $\Delta$ , which are necessary to calculate  $\rho$  and then the refractive index  $N_1$ , the intensity is measured as a function of the polarizer and analyzer angles. Solving equation 2.4-1, we obtain for the intensity:

$$I = |\vec{E}_d|^2 = \left( |r_{\parallel}|^2 \cos^2 \theta_A \cos^2 \theta_P + |r_{\perp}|^2 \sin^2 \theta_A \sin^2 \theta_P \right. \\ \left. + (r_{\parallel} r_{\perp}^* + r_{\parallel}^* r_{\perp}) \cos \theta_A \sin \theta_A \cos \theta_P \sin \theta_P \right) |\vec{E}_0|^2$$

The asterisk (\*) means complex conjugate. We can rewrite the above equation as:

$$I = I_0(1 + \alpha \cos 2\theta_P + \beta \sin 2\theta_P)$$

With

$$\alpha = \frac{\tan^2 \Psi - \tan^2 \theta_A}{\tan^2 \Psi + \tan^2 \theta_A}$$

$$\beta = 2 \cos \Delta \frac{\tan \Psi \tan \theta_A}{\tan^2 \Psi + \tan^2 \theta_A}$$

$$I_0 = \frac{|r_{\perp}|^2 |E_0|^2}{2} \cos^2 \theta_A (\tan^2 \Psi + \tan^2 \theta_A)$$

Finally, with  $\alpha$ ,  $\beta$  and  $\theta_A$  we can obtain  $\Psi$  and  $\Delta$ , and from them  $\rho$

$$\tan \Psi = \sqrt{\frac{1 + \alpha}{1 - \alpha}} |\tan \theta_A|$$

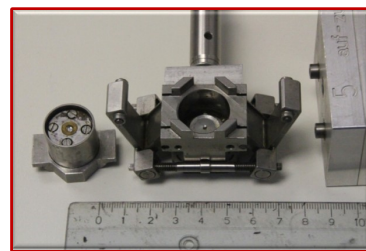
$$\cos \Delta = \frac{\beta}{\sqrt{1 - \alpha^2}}$$

## 2.5 High pressures and low temperatures

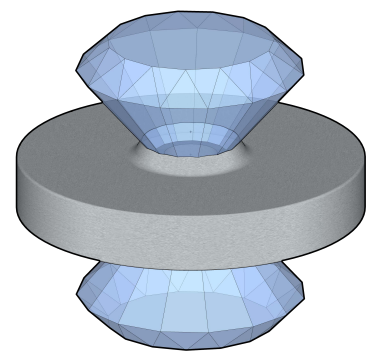
By studying the behavior of a material with changing conditions such as pressure or temperature, we can extract information about its structure or optoelectronic properties. Decreasing the temperature has different effects, such as a reduction in the population of phonons in the material, or the change in the lattice parameters. By applying pressure, it is possible to change the interatomic distances as well, but while keeping the temperature constant. Crystalline structure is dependent on both pressure and temperature, and by modifying these two in a controlled way, new properties may arise, or the previous ones can be better understood.

### 2.5.1 High pressures

The diamond anvil cell (DAC) employed in this work (Figure 2.12) was designed and made at the Planck Institute for Solid State Research, in Stuttgart. The pressure is exerted by tightening a pair of threaded rods that push a piston, with a diamond on it, towards the diamond placed in the DAC body. The sample is placed in the middle of the hole of a metal gasket, which is put between the diamonds, and which will act as lateral walls. Hydrostatic pressure is conveyed by filling the hole with a pressure transmitting medium, typically an alcohol, oil or He (liquid). The size of the hole used in our experiments ranged between 150 and 350  $\mu\text{m}$  in diameter, with a thickness around 80-130  $\mu\text{m}$ . However, the dimensions of the hole can be reduced to less than half its initial values as pressure is increased during the experiments. A schematic representation of the gasket and the diamonds is shown in Figure 2.13, and a cross-section is shown in Figure 2.14.



**Figure 2.12** Actual diamond anvil cell used for the high pressures experiments. The removable piston on the left has a diamond tip in the middle. Inside the cell there is another diamond, and both diamonds face each other when the piston is put into place (inside the open hole of the cell). Between the two diamonds is placed a metal gasket, to be sandwiched in between. This gasket has been previously indented and perforated, making a small hole (between 150 and 350  $\mu\text{m}$  in diameter) where the sample is put, together with a ruby for pressure calibration. Also, the small hole is filled with a liquid pressure transmitting media to transfer hydrostatically the pressure exerted by the diamonds to the sample and the ruby.



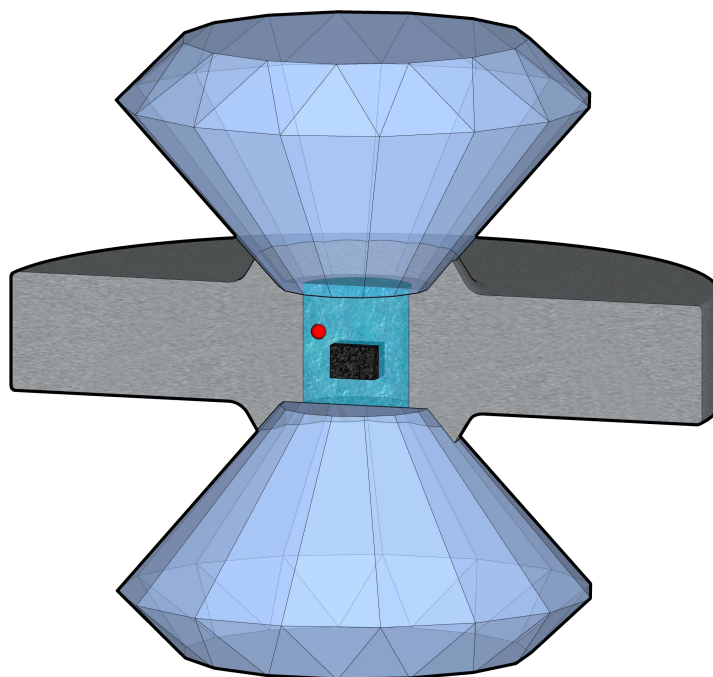
**Figure 2.13** 3D Image of the diamonds inside a DAC pressing against the metal gasket

[89] Tateiwa, Naoyuki, and Yoshinori Haga. (2010) "Appropriate pressure-transmitting media for cryogenic experiment in the diamond anvil cell up to 10 GPa." *Journal of Physics: Conference Series*. Vol. 215. No. 1. IOP Publishing,

[90] Takemura, K. (2001). "Evaluation of the hydrostaticity of a helium-pressure medium with powder X-ray diffraction techniques." *Journal of Applied Physics*, 89(1), 662-668.

PL and Raman measurements are carried out by illuminating the sample with a laser through the diamonds, and retrieving back the signal in a backscattering configuration.

Regarding our measurements, perovskites proved to be extremely sensitive to water (Ref. I), so the pressure medium chosen had to be completely anhydrous. Generally, we used propanol as the transmission medium, after thoroughly removing all traces of water with molecular sieves. Propanol did not affect our samples in any way, and it presents adequate hydrostaticity below 5 GPa<sup>89</sup>. For the experiments at low temperatures we used liquid helium as the pressure-transmitting medium, which ensures best hydrostatic conditions both at room temperature (up to 50 GPa<sup>90</sup>) and at low temperatures.



**Figure 2.14** 3D Representation of the working mechanism inside a DAC. The metal gasket is shown cut in half for clarity. The top diamond is attached to a piston which gets pushed down with screws, in a controlled way. The hole in the metal gasket acts as the lateral walls in the cavity where the liquid (pressure transmission media) is. The sample (in black) is placed inside the hole as well, together with a small ruby ball (red), whose PL peak position is calibrated for the whole range of pressures. Optical measurement is performed through the transparent diamonds.

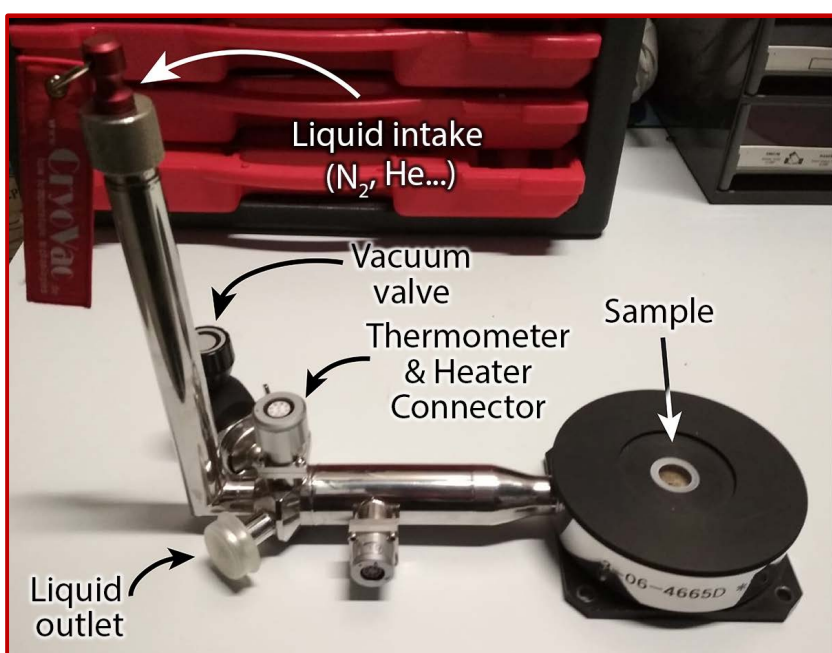


## 2.5.2 Low temperatures

Low temperatures were reached by cooling down with liquid nitrogen, or liquid helium, inside a vacuum isolated cryostat from CryoVac.

A glass window placed above the sample holder of the cryostat granted us optical access to the cooled sample. Again, PL and Raman measurements were performed with the same instrument, a LABRAM HR 800 spectrometer from Jobin Yvon.

Figure 2.15 below shows a picture of the real device employed during measurements.



**Figure 2.15** The cryostat used in this thesis. The black lid can be removed to paste or remove the samples inside. The glass window in the middle allows the optical characterization of the sample.



### 3 Vibrational and electronic structure in hybrid perovskites

In this section I briefly review the literature regarding the electronic and vibrational properties of hybrid halide perovskites. Understanding both is a necessary step in order to explain the behavior of the bandgap with temperature, or the origin of the Raman features observed experimentally during the realization of this thesis.

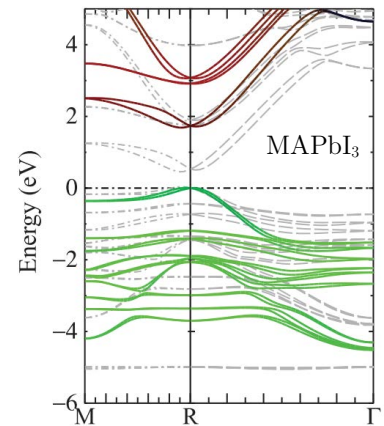
#### 3.1 Electronic band structure, spin-orbit coupling (SOC), and band inversion

The direct bandgap of the cubic phase of MAPbI<sub>3</sub> and FAPbI<sub>3</sub> is located at the R point  $(\frac{1}{2}, \frac{1}{2}, \frac{1}{2})$  in the Brillouin zone<sup>91</sup> (see Figure 3.1). Both the valence and conduction band consist of electronic states from the inorganic (PbI<sub>3</sub>) cage<sup>92</sup>, whereas the organic molecule (CH<sub>3</sub>NH<sub>3</sub>)<sup>+</sup> does not contribute to the density of states near the band edges. The organic cation compensates, however, the crystal net electric charge.

The electronic configuration of Pb<sup>2+</sup> is  $5d^{10}6s^26p^0$ , and for I<sup>-</sup> it is  $5p^6$ , so the valence band maximum consists of hybridized Pb *s* and I *p* orbitals, presenting a strong anti-bonding character<sup>49</sup>. The conduction band minimum, on the other hand, is composed primarily by Pb *p* orbitals. This makes the electronic configuration in hybrid perovskites inverted with respect to conventional semiconductors, where the conduction band minimum has *s* orbital character. This band inversion has an impact on the atypical dependence of the bandgap of hybrid perovskites with temperature and pressure as is explained further in ref. I and II.

Reflectivity measurements showed more than twenty years ago that the conduction band in hybrid halide perovskites was split in two due to a giant spin-orbit coupling (SOC)<sup>93</sup>. Later, in 2003, Tanaka et al. gave further experimental evidence of it through optical absorption measurements<sup>94</sup>.

The first computational studies of the electronic band structure of these materials ignored the spin-orbit coupling in their calculations<sup>95,96</sup>. Subsequent density functional theory (DFT) calculations<sup>36</sup> hinted that the spin-orbit coupling had indeed a huge effect on the bandgap, lowering its value in more than 1 eV. However, they underestimated the value of the bandgap with



**Figure 3.1** GW-SOC band structure for MAPbI<sub>3</sub> (Colored lines). Red lines correspond to Pb 6p orbitals, green lines depict I 5p, and blue lines Pb 6s. The blue lines overlap with the green ones, appearing dark green near 0 eV. Dashed grey lines correspond to local density approximation (LDA) of density functional theory (DFT). Reproduced with permission from ref. [92]

[91] Targhi, F. F., Jalili, Y. S., & Kanjouri, F. (2018). “MAPbI<sub>3</sub> and FAPbI<sub>3</sub> perovskites as solar cells: Case study on structural, electrical and optical properties.” *Results in Physics*, 10, 616-627.

[92] Brivio, F., Butler, K. T., Walsh, A., & Van Schilfgaarde, M. (2014). “Relativistic quasiparticle self-consistent electronic structure of hybrid halide perovskite photovoltaic absorbers.” *Physical Review B*, 89(15), 155204.

[93] Hirasawa, M., Ishihara, T., & Goto, T. (1994). “Exciton features in 0-, 2-, and 3-dimensional networks of [PbI<sub>6</sub>] 4-octahedra.” *Journal of the Physical Society of Japan*, 63(10), 3870-3879.

[94] Tanaka, Kenichiro, et al. (2003) “Comparative study on the excitons in lead-halide-based perovskite-type crystals CH<sub>3</sub>NH<sub>3</sub>PbBr<sub>3</sub> CH<sub>3</sub>NH<sub>3</sub>PbI<sub>3</sub>.” *Solid state communications* 127.9-10: 619-623.

[95] Borriello, I., et al. (2008). “Ab initio investigation of hybrid organic-inorganic perovskites based on tin halides.” *Physical Review B*, 77(23), 235214.

[96] Mosconi, Edoardo, et al. (2013)  
 “First-principles modeling of mixed  
 halide organometal perovskites for  
 photovoltaic applications.” *The Journal  
 of Physical Chemistry C* 117.27: 13902-  
 13913.

[97] Umari, P., et al. (2014).  
 “Relativistic GW calculations on  
 CH<sub>3</sub>NH<sub>3</sub>PbI<sub>3</sub> and CH<sub>3</sub>NH<sub>3</sub>SnI<sub>3</sub>  
 perovskites for solar cell applications.”  
*Scientific reports*, 4, 4467.

[98] Leguy, Aurélien MA, et al. (2016)  
 “Experimental and theoretical optical  
 properties of methylammonium lead  
 halide perovskites.” *Nanoscale* 8.12:  
 6317-6327.

(51) Leguy, Aurélien MA, et al.  
 (2016) “Dynamic disorder, phonon  
 lifetimes, and the assignment of modes  
 to the vibrational spectra of  
 methylammonium lead halide  
 perovskites.” *Physical Chemistry  
 Chemical Physics*, vol. 18, no 39, p.  
 27051-27066.

respect to the experimental results, by almost 1 eV as well. Brivio et al.<sup>92</sup> ascribed this discrepancy to the fact that DFT calculations ignore spatial nonlocality in the exchange-correlation potential. According to them, the valence band dispersion is described poorly with this computational method. They also studied the electronic structure of MAPbI<sub>3</sub>, in this case using quasiparticle self-consistent GW theory, where G stands for Green function and W refers to the screened Coulomb potential. Their results are reproduced in Figure 3.1. They obtained a rather close value of the bandgap (1.67 eV) with respect to the experimental number (1.61 eV). Similar results were obtained simultaneously by Umari et al.<sup>97</sup>, also employing GW calculations with SOC corrections, and by Leguy et al.<sup>98</sup>

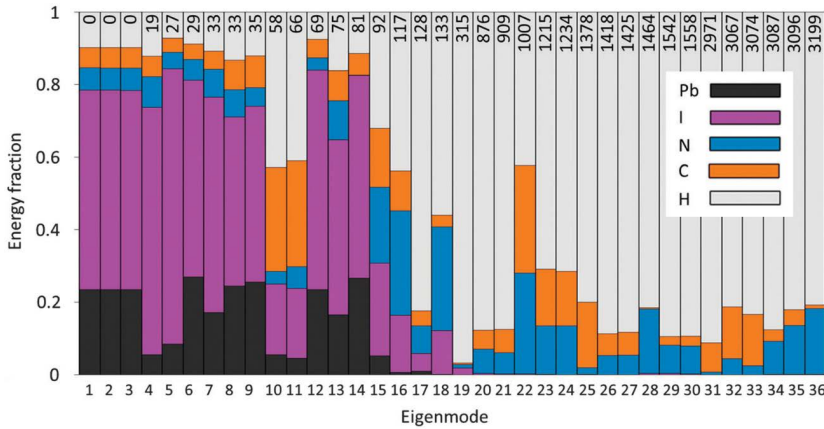
## 3.2 Vibrational properties

A complete description of the vibrational properties of hybrid halide perovskites (MAPbI<sub>3</sub>, MAPbCl<sub>3</sub> and MAPbBr<sub>3</sub>) was provided by Leguy and coworkers in ref. [51]. They calculated the vibrational frequencies of these materials using density functional theory, and compared the theoretical calculations with experimental results from Raman and infrared measurements.

All three compounds have 36 vibrational modes in the cubic phase. This number increases to 144 in the tetragonal and orthorhombic phases due to the increase in the unit cell size. The tilting of the octahedra and the concomitant reduction in symmetry, cause the phonon bands that were degenerated to split.

The vibrational modes in the cubic phase can be separated into two groups; one consists of a low-energy band (between 0 and 200 cm<sup>-1</sup>) comprising 18 eigenmodes of the inorganic cage, and the other set corresponds to 18 higher energy modes of the organic molecule, spreading between ~200 and 3300 cm<sup>-1</sup>. Figure 3.2 from ref. [51] shows the contribution of each atom to the total energy of a given vibrational mode, for the cubic phase of MAPbI<sub>3</sub>.

The first three vibrational modes correspond to the acoustic modes along the three spatial coordinates. Modes 4, 5 and 6 are related to twists of the octahedra by flexing the Pb-I-Pb bonds. The next three modes consist on a distortion of the octahedra characterized by a change in the angle of the I-Pb-I bonds. The rest of the low energy modes, 10 to 18, are coupled modes of the inorganic cage and the organic molecule. Of these, modes 12 to 15 present the strongest coupling, corresponding to steric interactions of the MA

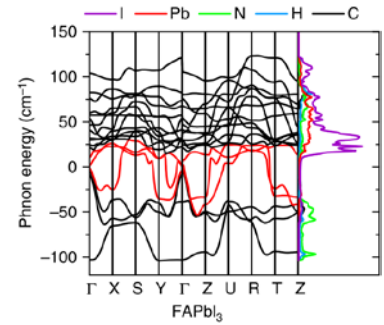


**Figure 3.2** Energy contribution of each atom to the vibrational states in MAPbI<sub>3</sub>. The color code is as follows: Black for lead, purple for iodine, blue for nitrogen, orange for carbon and grey for hydrogen. Reproduced with permission from ref. [51]

atoms with the inorganic framework, concomitantly changing the Pb-I bond lengths in the process. Modes 19 to 36 are modes corresponding to vibrations of the organic molecule. In particular, even though mode 19 is a torsional mode of the CH<sub>3</sub>NH<sub>3</sub><sup>+</sup> cation, to be spectroscopically active it needs to be coupled with the lattice.

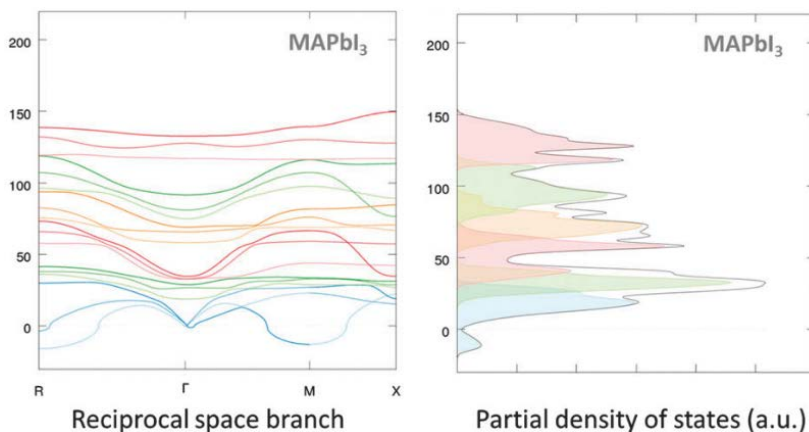
Figure 3.3, from ref. [99], and Figure 3.4 from ref. [51] show the phonon band diagram and density of states of FAPbI<sub>3</sub> and MAPbI<sub>3</sub> respectively, for the range of frequencies corresponding to the inorganic cage modes.

In our work we studied the low-frequency modes corresponding to the vibrations of the inorganic cage by Raman spectroscopy. At room temperature the spectra show very broad features, with the width being dominated by inhomogeneous broadening. This type of broadening is generated by the disorder induced by the

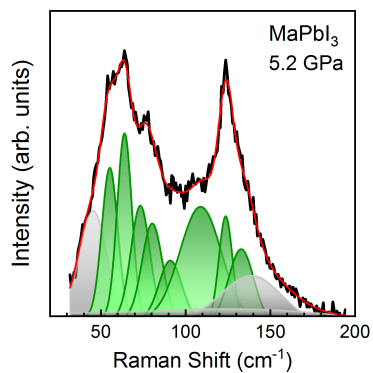


**Figure 3.3** Phonon dispersion and density of states for FAPbI<sub>3</sub> in the cubic phase at room temperature. The range of frequencies show the inorganic cage modes. Figure reproduced with permission from ref. [99]

[99] Yang, Jianfeng, et al. (2017)  
 “Acoustic-optical phonon up-conversion and hot-phonon bottleneck in lead-halide perovskites.” *Nature communications* vol. 8, no 1, p. 1-9.



**Figure 3.4** Phonon dispersion and density of states for MAPbI<sub>3</sub> in the cubic phase at room temperature. The range of frequencies show the inorganic cage modes. Figure reproduced with permission from ref. [51]



**Figure 3.5** Raman spectrum of MAPbI<sub>3</sub> at 5.2 GPa. The peaks observed (in green) correspond to some of the vibrational cage modes, (between 0 and 200 cm<sup>-1</sup>).

reorientation dynamics of the organic molecules inside of the inorganic cage, which creates a normal distribution of Pb-I bond lengths, spreading the range of frequencies for each mode. In the orthorhombic phase, however, the linewidth of the Raman peaks is greatly reduced, and their features are much better defined. This happens because the dynamic inhomogeneous broadening disappears with the locking of the methylammonium molecules inside the inorganic cage in the orthorhombic phase. Figure 3.5 shows a representative Raman spectrum of the orthorhombic phase of pure MAPbI<sub>3</sub> under high pressure, where the Raman peaks correspond to vibrations of the inorganic lattice.

## 4 Homogeneous and inhomogeneous broadening in Hybrid Perovskites

The lines resolved in emission or scattering spectra are never completely monochromatic. They always present a certain width, independently of the resolution of the spectrometer, which corresponds to a spectral distribution around a central frequency.

Breit and Wigner derived in 1936<sup>100</sup> a probability distribution for a particular physical process; the capture of slow neutrons. This distribution, in its non-relativistic form, can be applied to many physical processes as well, such as light emission or absorption. The broadening introduced in the measurements by this distribution is called natural line-width, or *homogeneous broadening*. On the other hand, if the system presents inhomogeneities that give rise to a distribution of energies for said physical process, the overall line shape is the sum of all the contributions, giving rise to an *inhomogeneous broadening* of the line shape.

### 4.1 Homogeneous broadening

This type of broadening is related to a finite lifetime of the state involved. The resulting spectral line shape follows a Lorentzian distribution, whose deduction can be found in several spectroscopy or solid-state books<sup>101,102,103</sup>. The Lorentzian line-shape can be written as:

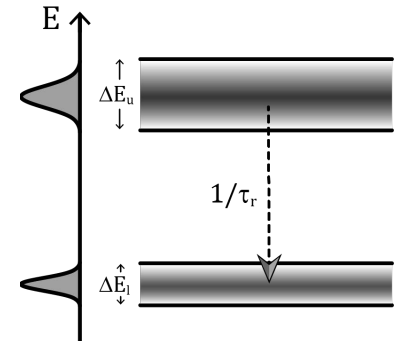
$$I(\omega) = I_0 \cdot \frac{\Gamma^2}{\Gamma^2 + (\omega - \omega_0)^2}$$

Here  $I_0$  is the height of the peak,  $\omega_0$  the central frequency, and  $\Gamma$  the half-width at half maximum (HWHM).

The linewidth  $\Gamma$  is related to the mean lifetime by the Heisenberg uncertainty principle  $\Delta E \cdot \Delta t \geq \hbar$  (See Figure 4.1). The uncertainty in the energy of the emitted radiation in a decay process is the sum of the uncertainties for the energies of the upper level ( $\Delta E_u$ ) and the lower level ( $\Delta E_l$ ), and is proportional to the inverse of the radiative decay time  $\tau_r$ .

$$\Delta E = \Delta E_u + \Delta E_l = \hbar \Delta \omega = \hbar \frac{1}{\tau_r}$$

[100] Breit, G., & Wigner, E. (1936). "Capture of slow neutrons." *Physical review*, 49(7), 519.

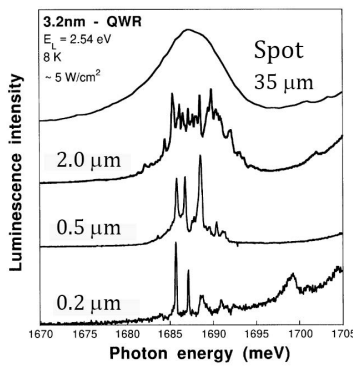


**Figure 4.1** Illustration of the relationship between the uncertainties in the energies of the upper and lower energy levels, and the radiative life time in the Heisenberg uncertainty principle.

[101] Merzbacher, E. (1998). "Quantum Mechanics" John Wiley & Sons. Inc., New York.

[102] Demtröder, W. (2014). "Laser spectroscopy 1: basic principles." Springer 5th ed. ISBN: 978-3-642-53858-2

[103] Powell, R. C. (1998). "Physics of solid-state laser materials" (Vol. 1). Springer Science & Business Media. 1st Ed. ISBN: 1-56396-658-1



**Figure 4.2** Direct observation of inhomogeneous broadening in GaAs/AlGaAs nanowires. For a wide spot (35  $\mu\text{m}$ ), the width of the line shape is dominated by inhomogeneous disorder, and it follows a Gaussian distribution function. For a reduced size of the spot, local uniformity gives rise to better defined Lorentzian emission line shapes. Reproduced with permission from reference [104]

[104] Vouilloz, F., et al. (1998) "Direct observation of localized excitons in quantum wires by spatially resolved photoluminescence." *Physica E: Low-dimensional Systems and Nanostructures* 2.1-4: 862-866.

The lifetime of an excited state is affected by the number of scattering processes per unit time, and since this number increases with temperature, the homogeneous broadening of the peak is temperature-dependent.

Regarding hybrid halide perovskites, Figure 4 (b) in reference IV shows the dependence on the line-width of the photoluminescence peak with temperature, which is related to the homogeneous broadening of the line shape.

## 4.2 Inhomogeneous broadening

Inhomogeneous broadening occurs when the emission or absorption process presents a normal distribution of frequencies, each one associated to a Lorentzian line shape. The final envelope function follows a Gaussian line shape:

$$I = I_0 \cdot \exp\left(-\ln(2) \cdot \frac{(\omega - \omega_0)^2}{\Gamma^2}\right)$$

Where  $I_0$  is the height of the peak,  $\omega_0$  the central frequency, and  $\Gamma$  the half-width at half maximum.

Inhomogeneities in a crystalline structure, such as defects, doping, or alloying give rise to a distribution of lattice constants, or different local microscopic strains. This generates a normal distribution in the energies of the emission or absorption processes, independent of its lifetime. The inhomogeneous broadening is then independent of the temperature.

The effect of interface disorder in the recombination of localized excitons, giving rise to inhomogeneous broadening is illustrated in Figure 4.2, after F. Vouilloz et al.<sup>104</sup> This effect of interface disorder, and alloy fluctuations in GaAs/AlGaAs quantum wires, produces a random distribution of Lorentzian peaks, whose sum follows a Gaussian line shape. When the size of the laser spot is reduced, the inhomogeneous broadening disappears, and the Lorentzian peaks corresponding to the recombination of excitons in isolated QD-like potential wells start being resolved in the spectra.

In the case of hybrid halide perovskites, the effect of mixing cations produces a static inhomogeneous broadening of the Raman peaks. For instance, the Raman peaks observed in pure MAPbI<sub>3</sub> in the orthorhombic phase are narrow and well defined, but they



gradually increase in width as FA is mixed with MA in the crystal lattice. (See Figure 2 of reference IV, included in this thesis).

Another example of inhomogeneous broadening in  $\text{MAPbI}_3$  can be observed in the cubic and tetragonal phases, in this case due to dynamic disorder. In these phases, the MA cation can rotate and rearrange freely inside the inorganic cage, interacting with the surrounding atoms and creating a random distribution of atomic distances in the  $\text{PbI}_3$  octahedra. The lifetime of the phonons is much shorter than the reorientation time of the organic molecules, so this dynamic disorder does not increase phonon-phonon scattering, neither affects the phonons lifetime. It creates, nonetheless, an inhomogeneous disorder based on the random orientation of the cations. Strikingly, this inhomogeneous broadening suddenly disappears in the transition to the orthorhombic phase. In this low symmetry phase, the volume available in the inorganic cage is reduced, and the movement of the organic cation is limited. The MA can no longer rotate or reorient, and thus the inhomogeneous contribution to the line width vanishes. This is illustrated clearly in Figure 1 of article IV, and Figure 2.6 above in the experimental section, where the Raman peaks greatly reduce their line width after the tetragonal to orthorhombic phase transition.



## 5 Temperature dependence of the bandgap

Most semiconductors, including the archetypal semiconductors Si, Ge, GaAs, etc. present a red shift in their bandgap energy with increasing temperature<sup>105,106</sup>. This temperature dependence is shown in Figure 5.1 for different materials.

There are two physical effects that contribute to the bandgap dependence on temperature: the thermal expansion and the renormalization of the band energies by electron-phonon coupling. The derivative of the gap over temperature includes, thus, these two terms:

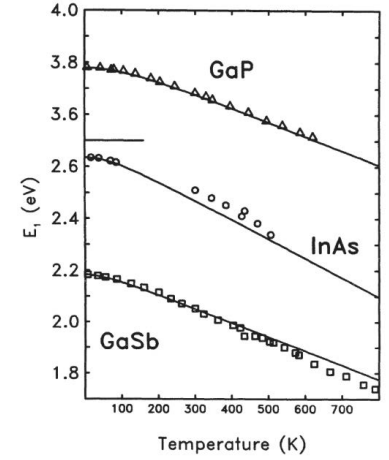
$$\frac{dE_g}{dT} = \left[ \frac{\partial E_g}{\partial T} \right]_{TE} + \left[ \frac{\partial E_g}{\partial T} \right]_{EP}$$

The thermal expansion component is linked to the change in the electronic band energies with volume, and experimentally it can be separated from the other term by measuring the pressure dependence of the bandgap isothermally<sup>107</sup>, as is shown below. The bandgap renormalization due to electron-phonon coupling, on the other hand, comes from a perturbative analysis of the electron self-energy up to second order in the atomic displacements<sup>108,109</sup> (i.e. phonon amplitudes). It is comprised of two components; the so-called Debye-Waller and the Fan (or self-energy) terms.

Regarding hybrid halide perovskites, an atypical dependence of the bandgap energy with temperature is observed. In their cubic and tetragonal I and II phases the tendency is inverted with respect to classical semiconductors, as the band gap energy increases monotonically with temperature. This atypical behavior is further explained in ref. II, later in this thesis. In the case of the orthorhombic and tetragonal III phases, the dependence is even more peculiar, as the derivative  $\frac{dE_g}{dT}$  changes linearly. Ongoing work is being carried out at the moment of writing this thesis regarding this shift observed for the band gap energy of  $FA_xMA_{1-x}PbI_3$  perovskites for the low temperature phases.

### 5.1 Thermal expansion

The harmonic approximation has proven to be very useful in quantum mechanics and solid-state physics<sup>110</sup>. Mainly because for the harmonic potential  $V = \frac{1}{2}m\omega^2x^2$ , where  $\omega$  is the vibrational



**Figure 5.1** Temperature dependence on the band gap energy for Gallium phosphide (GaP), Indium arsenide (InAs) and Gallium antimonide (GaSb). Reproduced with permission from ref. [106].

[105] Varshni, Y. P. (1967).

“Temperature dependence of the energy gap in semiconductors.” *Physica*, 34(1), 149-154.

[106] Cardona, M., & Gopalan, S. (1989). “Temperature Dependence of the Band Structure of Semiconductors: Electron-Phonon Interaction. In” *Progress in Electron Properties of Solids* (pp. 51-64). Springer, Dordrecht.

[107] Lautenschlager, P., Allen, P. B., & Cardona, M. (1985). “Temperature dependence of band gaps in Si and Ge”. *Physical Review B*, 31(4), 2163.

[108] Cardona, M. (2005). “Electron-phonon interaction in tetrahedral semiconductors.” *Solid State Communications*, 133(1), 3-18.

[109] Gopalan, S., Lautenschlager, P., & Cardona, M. (1987). “Temperature dependence of the shifts and broadenings of the critical points in GaAs.” *Physical Review B*, 35(11), 5577.

[110] Maradudin, Alexei A., et al. (1963) "Theory of lattice dynamics in the harmonic approximation". *New York: Academic press*. Vol. 3

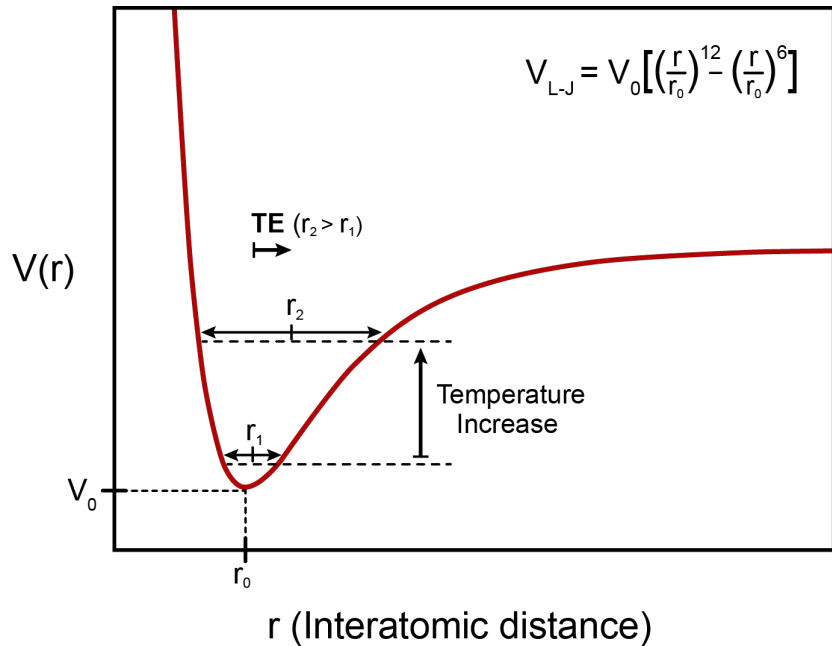
[111] Ashcroft, N. W. & ND Mermin (1976) *Solid state physics*. *Saunders College, Philadelphia*, vol. 120. pp.489

[112] Adnan Jaradat et al. (2018) "Evolution of Thermal Expansion due to Anharmonic Potential" *Int. J. of App. Eng. Res.* Vol. 13, N°12, pp. 10372-10375

frequency, one can find an exact solution to the time independent Schrödinger equation.

However, there are multiple physical processes that depend entirely on higher-order terms in the expansion of the lattice potential. One of these phenomena is the increase of volume in a crystalline solid with increasing temperature, also known as thermal expansion. That is, in a purely harmonic approximation, the size of the crystal lattice would not depend on temperature<sup>111</sup>. Due to the symmetry of the quadratic potential, the amplitude of the oscillation around the equilibrium position would not affect the distance between atoms<sup>112</sup>.

This can be intuitively understood by looking at the dependence on temperature in the vibrational amplitude of the atoms in a Lennard-Jones potential, an approximation for atomic bonding. As is shown in Figure 5.2, the asymmetry of the Lennard Jones potential produces an increase in the interatomic distance with temperature.



**Figure 5.2** Inter-atomic Lennard-Jones potential. An increase in temperature increases the amplitude of the oscillations, which, due to the asymmetric potential, gives rise to a thermal expansion.

To analyze the thermal expansion contribution, however, it is useful to use a quasiharmonic approximation, where the dependence on temperature of the gap is given by the dependence on temperature of the crystal parameters. The effect of thermal expansion on the band gap energy can be expressed with derivatives:

$$\left(\frac{\partial E_g}{\partial T}\right)_{TE} = \left(\frac{\partial \ln V}{\partial T}\right)_p \left(\frac{\partial P}{\partial \ln V}\right)_T \left(\frac{\partial E_g}{\partial P}\right)_{TE} = -\alpha_V \cdot B_0 \cdot \left(\frac{\partial E_g}{\partial P}\right)_{TE}$$

Where  $\alpha_V$  is the volumetric expansion coefficient and  $B_0$  is the bulk modulus. This allows us to obtain the differential thermal expansion shift using experimental values for  $\alpha_V$ ,  $B_0$  and  $\left(\frac{\partial E_g}{\partial P}\right)_{TE}$

## 5.2 Electron-Phonon renormalization of the bandgap

The fundamental theory that addresses the dependence of the bandgap energy on temperature was developed by Allen and Heine<sup>113</sup> in 1976. It included a thermal expansion term and the renormalization of the electronic energies due to electron-phonon interaction. The latter comprises both the Debye-Waller (DW) and self-energy (SE) terms, which are obtained by expanding the electron-phonon coupling in perturbation theory and keeping terms up to second order in phonon amplitudes<sup>114</sup>. The DW term is a first-order process in perturbation theory that comprises two phonons, and it accounts for the coupling between the lattice vibrations and the electronic band states through thermal fluctuations of the atoms around their equilibrium positions. The SE, on the other hand, corresponds to the second-order term in perturbation theory, being an iterated one-phonon event. The self-energy correction can be viewed as a change in the effective mass of valence and conduction electrons due to their interaction with the lattice vibrations. Higher order terms are not necessary to explain the experimental data obtained for the dependence on temperature of the gap<sup>114</sup>.

The energy shift of a given band state, with wave vector  $\mathbf{k}$  and band index  $n$ , can be expressed as the summation over the contribution of all phonon modes  $(\mathbf{Q}, j)$  of energy  $\hbar\omega_{\mathbf{Q}j}$ :

$$\Delta E_{\mathbf{k}n} = \sum_{\mathbf{Q}, j} \frac{\partial E_{\mathbf{k}n}}{\partial n_{\mathbf{Q}j}} \left[ n_{\mathbf{Q}j}(T) + \frac{1}{2} \right],$$

Here  $n_{\mathbf{Q}j} = e^{\frac{\hbar\omega_{\mathbf{Q}}}{k_B T}}$  is the Bose-Einstein occupation factor. The real part of the coefficient  $\frac{\partial E_{\mathbf{k}n}}{\partial n_{\mathbf{Q}j}}$  includes both the DW and SE terms, and in our work, we approximate it by a constant A which represents the amplitude of a single oscillator. The frequency  $\omega_0$  of this oscillator is obtained by averaging the frequencies of the

[113] Allen, P. B., & Heine, V. (1976). "Theory of the temperature dependence of electronic band structures." *Journal of Physics C: Solid State Physics*, 9(12), 2305.

[114] Zollner, S., Gopalan, S., & Cardona, M. (1991). "The temperature dependence of the band gaps in InP, InAs, InSb, and GaSb." *Solid state communications*, 77(7), 485-488.

inorganic cage modes, weighted by their DOS, since only the cage modes interact with the valence and conduction band electrons.

The electron-phonon correction to the bandgap shift, with a single oscillator frequency  $\omega_0$  then reads:

$$[\Delta E_g(T)]_{\text{EP}} = A \cdot \left( n_{B-E}(\omega_0, T) + \frac{1}{2} \right)$$

This approximation provides a good fit to our experimental data using the minimum number of parameters, with realistic values of the averaged phonon frequency.

## 6 Published articles

- I. Pressure-induced locking of methylammonium cations versus amorphization in hybrid lead iodide perovskites. *Francisco-López, A., Charles, B., Weber, O. J., Alonso, M. I., Garriga, M., Campoy-Quiles, M., Weller, M. T., & Goñi, A. R.* (2018). *The Journal of Physical Chemistry C*, 122, 22073-22082.
  
- II. Equal footing of thermal expansion and electron-phonon interaction in the temperature dependence of lead halide perovskite band gaps. *Francisco-López, A., Charles, B., Weber, O. J., Alonso, M. I., Garriga, M., Campoy-Quiles, M., Weller, M. T., & Goñi, A. R.* (2019). *The Journal of Physical Chemistry Letters*, 10, 2971-2977.
  
- III. Spectroscopic ellipsometry study of  $\text{FA}_x\text{MA}_{1-x}\text{PbI}_3$  hybrid perovskite single crystals. *Alonso, M. I., Charles, B., Francisco-López, A., Garriga, M., Weller, M. T., & Goñi, A. R.* (2019). *Journal of Vacuum Science & Technology B* 37, 062901/1-7.
  
- IV. Phase diagram of methylammonium/formamidinium lead iodide perovskite solid solutions from temperature-dependent photoluminescence and Raman spectroscopies. *Francisco-López, A., Charles, B., J., Alonso, M. I., Garriga, M., Campoy-Quiles, M., Weller, M. T., & Goñi, A. R.* (2020). *The Journal of Physical Chemistry C*. DOI: 10.1021/acs.jpcc.9b10185





# Pressure-Induced Locking of Methylammonium Cations versus Amorphization in Hybrid Lead Iodide Perovskites

Adrián Francisco-López,<sup>†</sup> Bethan Charles,<sup>‡</sup> Oliver J. Weber,<sup>‡</sup> M. Isabel Alonso,<sup>†</sup> Miquel Garriga,<sup>†</sup> Mariano Campoy-Quiles,<sup>†</sup> Mark T. Weller,<sup>‡,§</sup> and Alejandro R. Goñi<sup>\*,†,§</sup>

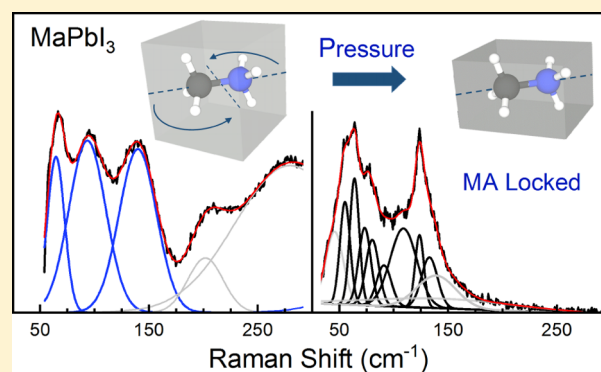
<sup>†</sup>Institut de Ciència de Materials de Barcelona (ICMAB-CSIC), Campus UAB, 08193 Bellaterra, Spain

<sup>‡</sup>Department of Chemistry & Centre for Sustainable Chemical Technologies, University of Bath, Claverton Down, Bath BA2 7AY, U.K.

<sup>§</sup>ICREA, Passeig Lluís Companys 23, 08010 Barcelona, Spain

## Supporting Information

**ABSTRACT:** The structural phase behavior of high-quality single crystals of methylammonium lead iodide ( $\text{CH}_3\text{NH}_3\text{PbI}_3$  or  $\text{MAPbI}_3$ ) was revisited by combining Raman scattering and photoluminescence (PL) measurements under high hydrostatic pressure up to ca. 10 GPa. The single crystals were specially grown with the final thickness needed for pressure experiments, retaining their high quality due to a less invasive preparation procedure, which avoids sample thinning. Both PL and Raman spectra show simultaneous changes in their profiles that indicate the occurrence of three phase transitions subsequently at around 0.4, 2.7, and 3.3 GPa. At the second phase transition, the Raman spectra exhibit a pronounced reduction in the line width of the phonon modes of the inorganic cage, similar to the changes observed at the tetragonal-to-orthorhombic phase transition occurring at around 160 K but ambient pressure. This behavior is interpreted as evidence for the locking of the organic cations in the cage voids above 2.7 GPa due to the reduced volume and symmetry of the unit cell. At the third phase transition, reported here for the first time, the PL is greatly affected, whereas the Raman spectrum experiences only subtle changes related to a splitting of some of the peaks. This behavior may indicate a change mostly in the electronic structure with little effect on the crystal structure. Strikingly, the sharp Raman features observed at high pressures do not support amorphization of  $\text{MAPbI}_3$  with onset at 3 GPa, as claimed by most of the high-pressure (X-ray) literature. We interpret this apparent discrepancy in terms of the degree of disorder introduced at different length scales in the perovskite lattice by the pressure-induced freeze-out of the methylammonium cation motion.



## INTRODUCTION

For all of the spectacular developments in lead halide-perovskite-based photovoltaics that catapulted solar-cell efficiency to values in excess of 22% in a few years,<sup>1</sup> there are still several fundamental physical questions that remain a matter of debate. For example, the existence and stability of bound electron–hole pairs (excitons) and their role in the optoelectronic properties of these materials<sup>2</sup> remain controversial. Another issue is the apparent contradiction of having strong optical absorption as for direct gap materials and simultaneously the long charge-carrier lifetimes typical of indirect semiconductors like Si. A possible explanation relies on a mixed nature of the fundamental band gap in methylammonium (MA,  $\text{CH}_3\text{NH}_3$ ) lead halide perovskites due to large spin–orbit coupling.<sup>3</sup> Furthermore, the great advantage of this family of materials of being solution-processable is somewhat counterbalanced by their mechanical softness<sup>4</sup> and the consequent low energetic barriers for point

defect formation and ion migration.<sup>5,6</sup> It is speculated that the photoinduced movement of ions and their accumulation at interfaces are the origin of large hysteresis in current–voltage characteristics<sup>7</sup> and transitory changes in the optical response of lead halide perovskites.<sup>8,9</sup> Probably the most prominent drawback of these perovskite materials, however, is the sensitivity to ambient conditions, in particular humidity,<sup>10,11</sup> which still hampers the improvement of their longtime stability. To address all of these open questions, a deeper understanding of different structure–property relationships appears necessary if not mandatory.

In this respect, high-pressure techniques offer the possibility to vary interatomic and intermolecular distances in condensed matter in a controlled way, having large impact on the

Received: May 30, 2018

Revised: August 21, 2018

Published: September 5, 2018

structural and consequently the electronic and optical properties of the solid. The incipient high-pressure work on hybrid halide perovskites has been recently reviewed regarding their power for assessing new properties or enlightening fundamental physical problems in this new class of photovoltaic materials.<sup>12,13</sup> Regarding the archetypal hybrid perovskite MAPbI<sub>3</sub>, most of the high-pressure work performed so far concerning the structural changes under compression relied mainly, but not exclusively, on X-ray diffraction methods. Reports span different forms of the perovskite material (powder,<sup>14,15</sup> single,<sup>14–17</sup> or polycrystals<sup>18</sup> and nanorods<sup>19</sup>) and different hydrostatic conditions regarding the pressure transmitting medium. The general picture that emerges for MAPbI<sub>3</sub> is that the material is relatively soft, mainly against the tilting of the PbI<sub>6</sub> octahedra, because it exhibits a first structural phase transition at a relatively low pressure in the range of 0.3–0.6 GPa. In addition, a second structural transformation takes place at around 3 GPa into a very disordered phase, at which the organic cations seem to play a role. The reports, however, differ in the phenomenology at higher pressures. For the high-pressure phase, after the first transition, an orthorhombic<sup>15,17,19</sup> as well as a cubic<sup>14,16,18</sup> symmetry was proposed. There is more consensus about the amorphous nature of the high-pressure phase after the second phase transition. The accurate determination of the structural changes in MAPbI<sub>3</sub> of Szafranski and Katrusiak<sup>16</sup> provides strong evidence that under hydrostatic pressure the phase changes are from tetragonal to cubic, followed by an isostructural transition to another cubic phase, which exhibits gradual amorphization with increasing pressure. Qualitatively, a similar phenomenology is found for other members of the hybrid halide perovskite family such as MAPbBr<sub>3</sub>,<sup>14,15</sup> MAPbCl<sub>3</sub>,<sup>20</sup> and FAPbBr<sub>3</sub>,<sup>21</sup> where FA stands for formamidinium (CH(NH<sub>2</sub>)<sub>2</sub>).

As pointed out by Postorino and Malavasi,<sup>12</sup> despite the fact that the application of high pressure is a particularly suitable means to study the interplay between degrees of freedom of the organic molecules and the inorganic cage, such kind of studies remain scarce. In recent temperature-dependent experiments, we have found in the Raman scattering signature of MAPbI<sub>3</sub> evidence of significant coupling between the vibrations of the anionic (PbI<sub>3</sub>)<sub>n</sub> network and the CH<sub>3</sub>NH<sub>3</sub><sup>+</sup> cations,<sup>22,23</sup> in spite of the supposedly weak hydrogen bonding between them. At around 160 K, MAPbI<sub>3</sub> undergoes a transition from the tetragonal, room-temperature phase into an orthorhombic one.<sup>24</sup> Neutron scattering measurements provided quantitative insight into the rotational dynamics and degree of order of the MA cations within the inorganic cage in the different phases.<sup>25,26</sup> Furthermore, time-resolved vibrational spectroscopy has identified fast librations (300 fs) and slow rotations (3 ps) of the MA molecule in the tetragonal phase.<sup>27</sup> These excitations dominate the dynamics of the MA molecules in the tetragonal phase because they are fully unlocked within the cage voids. As a consequence of the hydrogen-bonding-mediated interaction between the MA molecules and the halogen atoms of the inorganic cage, the vibrational modes of the latter exhibit a wide statistical distribution of frequencies, which in turn leads to a strong inhomogeneous broadening of the Raman peaks.<sup>22,23</sup> In contrast, in the low-temperature orthorhombic phase, the reduced volume and symmetry of the cage voids causes the locking of the organic cations, which become well oriented along high-symmetry directions of the perovskite crystal. The

result is a pronounced reduction of the inhomogeneous broadening, which is readily observed in low-temperature Raman spectra.<sup>22,23</sup> Although not proven, it is believed that such a strong coupling between organic and inorganic degrees of freedom is the origin of the extremely low thermal conductivity of MAPbI<sub>3</sub>.<sup>28,28</sup> This served as motivation to look for a similar effect induced through the application of pressure rather than by decreasing the temperature, eventually leading to control of thermal transport by strain.

In this work, we present a systematic study of the structural phase behavior of high-quality MAPbI<sub>3</sub> single crystals under compression by monitoring the pressure-induced changes in the fundamental band gap and vibrational spectrum, as observed in photoluminescence (PL) and Raman experiments, respectively. In the range up to ca. 10 GPa, we find three successive phase transitions characterized by sudden jumps in the energy position of the main PL emission peak, indicating abrupt changes in the fundamental band gap. A striking result is that we do not seem to observe pressure-induced amorphization of MAPbI<sub>3</sub> in the whole pressure range of the experiment, in contrast to what might be expected from the literature. On the contrary, at the second phase transition occurring at about 2.7 GPa, the Raman spectra exhibit a clear reduction of the peak widths. As explained below, this is taken as compelling evidence of a strong reduction of phonon inhomogeneous broadening due to the pressure-induced locking of the MA cations along certain directions within the inorganic cage voids. Our ansatz is that this freeze-out of the organic cation motion leads locally to an orthorhombic distortion of the crystal structure of MAPbI<sub>3</sub>, as probed by Raman scattering, whereas on a macroscopic scale, the different locked orientations and positions of the MA molecules disrupt the long-range order sensed by X-rays. The latter has been repeatedly interpreted as amorphization. Moreover, at the third phase transition, which takes place at ca. 3.3 GPa, only the emission properties are strongly affected, whereas the Raman spectra barely display a slight splitting of a couple of modes. We believe that this phenomenon is indicative of subtle structural changes at the phase transition, which despite their small magnitude can cause a partial folding of the Brillouin zone (BZ) in the high-pressure phase. As a consequence, the gap widens suddenly from 1.85 to 2.15 eV.

## ■ EXPERIMENTAL SECTION

**Preparation of Loading-Ready Hybrid Perovskite Single Crystals.** The methylammonium iodide (MAI) synthesis proceeds by adding dropwise 16.620 mL of HI (57 wt % aq + 1.5% H<sub>3</sub>PO<sub>2</sub> stabilizer) to 10.891 mL of methylamine (40 wt % aq) in 50 mL of isopropanol in an ice bath under stirring. The solvent is removed by rotary evaporation, and the crude product recrystallizes from hot ethanol, which is then washed with diethyl ether and dried at 100 °C. The space-confined on-substrate fabrication method of MAPbI<sub>3</sub> single crystals with adjustable thickness<sup>29</sup> consists first in dissolving 2.3050 g of PbI<sub>2</sub> (99%, Sigma) and 0.7948 g of MAI in 5 mL of dry  $\gamma$ -butyrolactone in a normal fume cupboard, affording a 1 mol/dm<sup>3</sup> solution. Then, 100  $\mu$ L of the solution is dropped onto a glass coverslip on a hotplate. Another glass coverslip is placed on top of the first, sandwiching the solution between. The hotplate is ramped to 100 °C at 10 °C/h and retained at 100 °C for 48 h, driving off the solvent and inducing crystallization of flat MAPbI<sub>3</sub> crystals. The thickness of the crystals was varied by application of

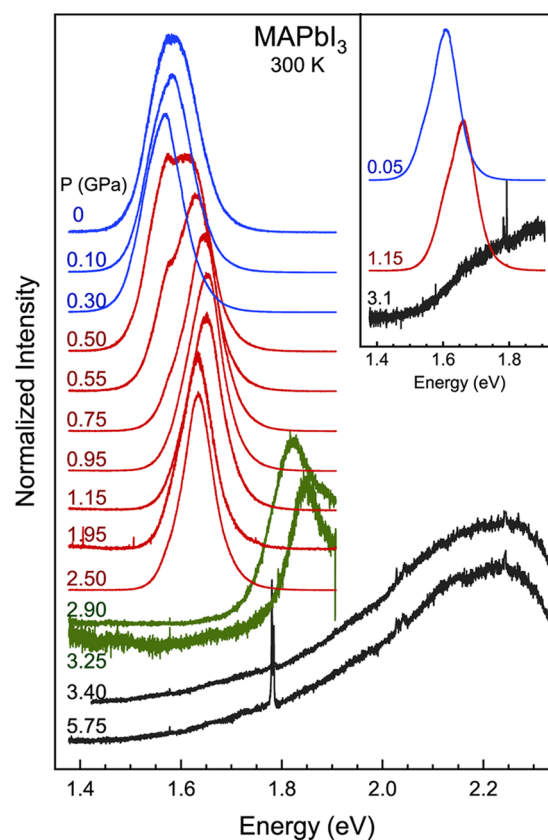
pressure using a Petri dish of weight 120 g applied to substrates. The dimensions of the crystals were found to be 2.0 mm (width) by 32  $\mu\text{m}$  (depth) through parallax measurements taken using secondary electron images from a scanning electron microscope.

**High-Pressure Experiments.** The high-pressure photoluminescence and micro-Raman scattering measurements were performed at room temperature employing a gasketed diamond anvil cell (DAC). Anhydrous propanol was used as pressure transmitting medium, which ensures good hydrostatic conditions (perfectly hydrostatic up to 4.2 GPa<sup>30</sup>) and proved to be chemically inert to MAPbI<sub>3</sub>. Thanks to the growth procedure that directly produced single crystals with a thickness of ca. 30  $\mu\text{m}$  and there was no need to thin down the sample for loading the DAC. This is very important because the thinning procedure employing either mechanical polishing or chemical etching is known to spoil the quality of such soft crystals like MAPbI<sub>3</sub>, introducing large amounts of structural defects, which might have an influence on the behavior of the material under compression. Small pieces cut with a sharp knife of about 100  $\times$  100  $\mu\text{m}^2$  in size were placed into the DAC together with a ruby sphere for pressure calibration.<sup>31</sup> The PL spectra were excited with the 633 nm line of a He–Ne laser and the 514.5 nm line of an Ar<sup>+</sup>-ion laser at pressures lower and higher than 3.5 GPa, respectively, whereas the infrared diode laser emitting at 785 nm was employed for the Raman measurements. The latter turned out most suitable to excite the vibrational modes of the inorganic cage, providing also the highest spectral resolution and stray-light rejection. In all cases, a very low incident light power density below 15 W/cm<sup>2</sup> was used to avoid any photo-degradation of the samples, such that thermal damage by the laser can be safely ruled out. Spectra were collected using a 20 $\times$  long working distance objective with NA = 0.35 and dispersed with a high-resolution LabRam HR800 grating spectrometer equipped with a charge-coupled device detector. PL spectra were corrected for the spectral response of the spectrometer by normalizing each spectrum using the detector and the 600 grooves/mm grating characteristics.

## RESULTS AND DISCUSSION

### Photoluminescence Measurements under Pressure.

Figure 1 shows the evolution of the PL spectra of MAPbI<sub>3</sub> with increasing pressure. All spectra were normalized to their absolute maximum intensity and vertically offset to ease their comparison. It is worth mentioning that we loaded two pieces of MAPbI<sub>3</sub> inside the diamond anvil cell (DAC) and constitutively performed the PL and Raman measurements at the same two points on each piece. The results of the four measurement series are similar; hence, we only show the representative ones. The main PL peak exhibits sudden jumps in the position of its maximum, which are indicative of the occurrence of three phase transitions in the pressure range of the experiment. Different colors correspond to the four observed phases, and the same code will be used throughout the article. At the beginning of the pressure upstroke and before the first phase transition occurs, the PL spectra (blue full lines) exhibit a slight but clear red shift, which indicates that the fundamental band gap of MAPbI<sub>3</sub> in the room-temperature tetragonal phase decreases with pressure. The first phase transition starts at a very low pressure of 0.4 GPa, as signaled by an abrupt blue shift of the main PL peak. This transition is completed at about 0.7 GPa, before which both



**Figure 1.** PL spectra of MAPbI<sub>3</sub> obtained for incremental steps of pressure. The spectra were normalized to their maximum intensity and plotted with a vertical shift for increasing pressure. The different colors indicate the subsequent phases adopted by the material during the pressure upstroke. For pressures lower and higher than 3.4 GPa, the excitation laser wavelengths were 633 and 514 nm, respectively. The inset displays spectra measured by releasing the pressure, demonstrating the full reversibility of the structural changes except for some hysteresis.

phases coexist. The new high-pressure phase is stable up to 2.7 GPa (red solid curves) and should correspond to the cubic phase IV, as reported elsewhere.<sup>16</sup> With increasing pressure and within this phase, the PL emission exhibits first a gradual blue shift and finally a red shift. At about 2.7 GPa, a second phase transformation occurs, which is characterized by an abrupt but stronger blue shift of the PL maximum (green solid curves). As explained in the discussion of the Raman results, this new phase is perfectly crystalline and probably orthorhombic in nature. This result is at odds with the widespread claims of this being the amorphous cubic phase V.<sup>12,16</sup> The PL spectra clearly indicate the occurrence of a third phase transition at about 3.3 GPa, which is again characterized by an abrupt blue shift and a pronounced broadening of the emission peak (black spectra in Figure 1). To properly excite the PL of this phase, we switched to the green laser line. We anticipate that the Raman data indicate again that this phase is crystalline and probably orthorhombic up to the highest pressure of this experiment close to 6 GPa. The broadband emission exhibited by this high-pressure phase, though, speaks for a large heterogeneity in the sample, as far as the electronic states involved in the optical transitions are concerned. It is important to remark that all changes in the PL emission (the Raman too) are fully reversible, even though there is a certain degree of hysteresis, as illustrated by the PL spectra of the inset



to Figure 1, which were taken by releasing the pressure prior to the final opening of the DAC (see also Figure S2 of the Supporting Information).

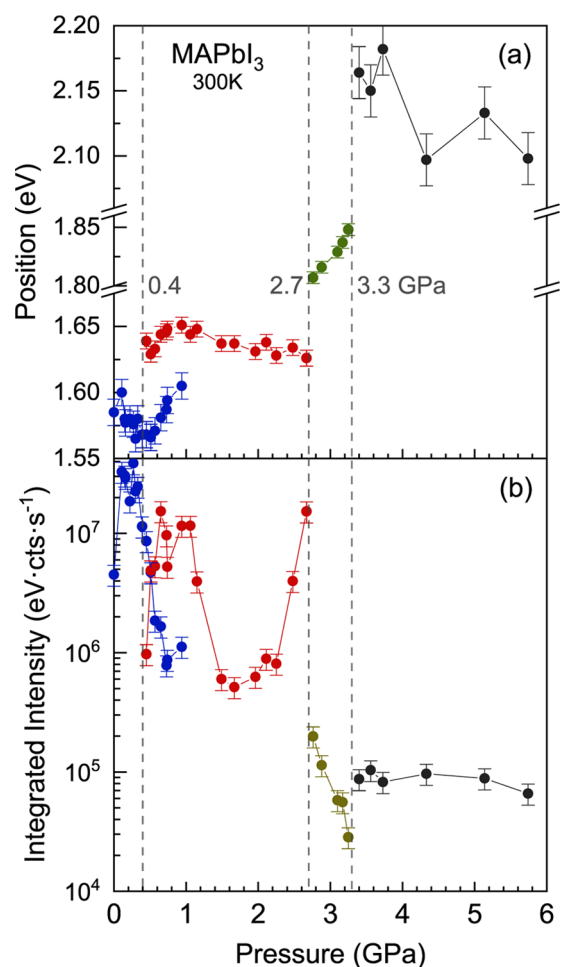
To analyze the PL spectra of MAPbI<sub>3</sub>, we used a Gaussian–Lorentzian cross-product function for describing the main peaks, which are ascribed to free-exciton recombination. We notice that the same fitting protocol was also successfully employed for the analysis of the PL spectra of MAPbI<sub>3</sub> at ambient pressure but as a function of temperature (data will be published elsewhere<sup>32</sup>). The expression for the cross-product function reads as

$$G \times L(\hbar\omega) = A \cdot \frac{\Gamma^2}{4 \cdot s \cdot (E_0 - \hbar\omega)^2 + \Gamma^2} \cdot \exp\left(-4 \ln 2 \frac{(1-s) \cdot (E_0 - \hbar\omega)^2}{\Gamma^2}\right) \quad (1)$$

where  $A$  is the amplitude prefactor,  $E_0$  is the peak energy position,  $\Gamma$  is the full width at half-maximum (FWHM), and  $s$  is a weight parameter that takes the value  $s = 0$  for pure Gaussian lineshape and  $s = 1$  for pure Lorentzian. This function is a useful simplification of a Voigt function, which corresponds to the mathematical convolution of a Lorentzian, taking into account the natural lineshape due to spontaneous emission and whose line width is the inverse of the lifetime, and an inhomogeneously broadened Gaussian, accounting for a normal distribution of exciton energies. Apart from yielding an excellent lineshape fit, the cross-product function has the advantage against the Voigt function of being far less computationally expensive. Representative examples of the lineshape analysis of the PL profiles are depicted in Figure S1 of the Supporting Information.

The assignment of the main emission peak to free-exciton recombination is partly controversial because the reported values for the exciton binding energy in lead halide perovskites span a wide range from a few millielectronvolts<sup>33–40</sup> to several tens of millielectronvolts.<sup>41–44</sup> As suggested,<sup>2</sup> such a difficulty to discern between the free-carrier or correlated electron–hole pair character of the optical properties in these materials might be in direct relation to the particular microstructure of the sample being considered. The reason is that the dielectric screening and consequently the magnitude of the exciton binding energy are largely affected by the presence of grain boundaries, interfaces, and surface defects, where charge can accumulate or dipoles can be induced, all impacting the macroscopic polarization of the medium.<sup>2,34</sup> Furthermore, we point out that claims for the absence of exciton states based on a steplike absorption edge with no peaklike feature at its edge are partly incorrect.<sup>2,33,38,45</sup> A steplike profile is the evidence of Coulomb-interaction-mediated correlations between electrons and holes in the states pertaining to the excitonic energy continuum.<sup>33,46</sup> The absence of a peak just means the absence of bound excitonic states corresponding to the discrete energy spectrum, most probably because the exciton binding energy is on the order of or smaller than the thermal energy. This, in contrast, does not hinder bound exciton states in playing a main role in emission because their optical recombination is favored against that of continuum states due to the much shorter lifetime of the latter.<sup>47</sup> We thus use the Gaussian–Lorentzian cross-product function of eq 1 to describe the lineshape of the PL emission, which we ascribe to free-exciton recombination.

The values of the fitting parameters corresponding to the energy  $E_0$  of the peak maximum and the integrated intensity, given by the product  $A \cdot \Gamma$ , are plotted as a function of pressure in Figure 2. Again, the abrupt changes in the parameters clearly

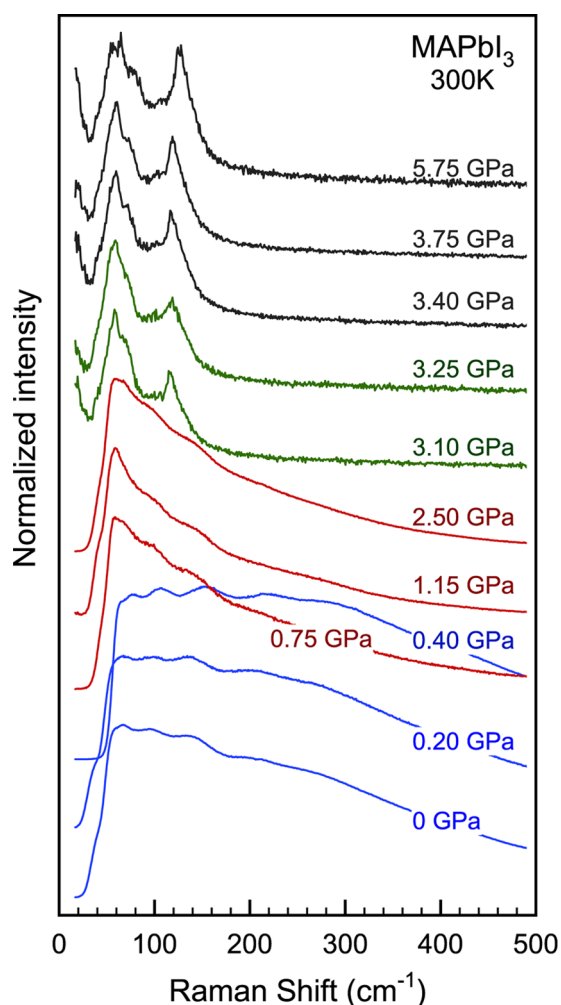


**Figure 2.** (a) Maximum peak position and (b) integrated intensity plotted as a function of pressure, obtained from the PL lineshape fits using eq 1. The pressures at which the phase transitions occur are indicated by vertical dashed lines.

indicate the pressures at which the phase transitions occur (marked by dashed vertical lines).<sup>48</sup> Although we cannot tell the absolute values of band gap and/or exciton binding energy from the lineshape fits, the shift of the PL peak energy  $E_0$  with pressure is to a large extent dictated by the pressure dependence of the gap. In particular, we analyze the pressure-induced red shift of the gap in the tetragonal phase of MAPbI<sub>3</sub>, stable at ambient conditions, which is apparently at odds with the well-established systematics on the pressure dependence of direct band gaps in tetrahedrally bonded semiconductors.<sup>46</sup> In brief, for semiconductors with predominantly  $sp^3$  hybridization, it holds that (i) states with bonding p-orbital character are almost insensitive to pressure. The best example is the top of the valence band at the  $\Gamma$  point of the Brillouin zone (BZ), which is bonding pure p-type. (ii) On the contrary, antibonding s-states exhibit a strong blue shift with pressure. In most of the cases, the bottom of the conduction band also at  $\Gamma$  comprises states with antibonding pure s-orbital character. In consequence, direct gaps at the BZ center increase with pressure at a rate on the order of 100 meV/

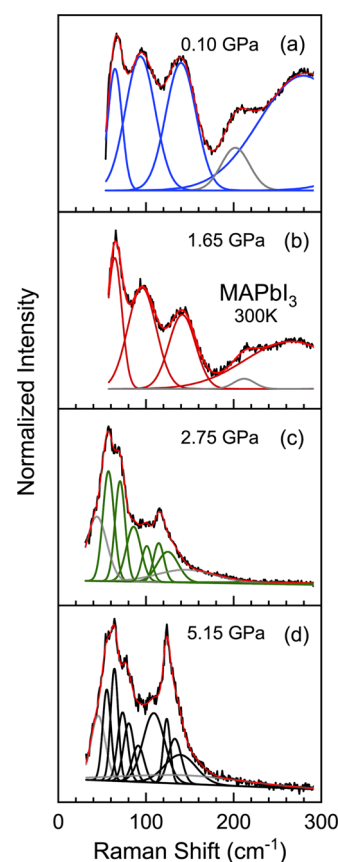
GPa.<sup>46</sup> (iii) Antibonding p-orbitals are characterized by a much smaller but negative deformation potential as compared with s-states. Antibonding p-like states contribute the most to the X-valleys at the BZ edge. As a result, the indirect  $\Gamma$ -X gap decreases with pressure at a lower pace of typically  $-15$  meV/GPa.<sup>46</sup> Relativistic band-structure calculations<sup>35,49,50</sup> for a pseudo-cubic phase of MAPbI<sub>3</sub> predict a direct fundamental gap at the R-point of the BZ. The peculiarity of lead halide perovskites is that due to the huge spin-orbit interaction present in heavy atoms like Pb and I there is a so-called band inversion such that the top of the valence band is predominantly composed by antibonding Pb 6s orbitals hybridized with I 5p orbitals and the bottom of the conduction band is formed by the antibonding split-off Pb 6p-orbitals. Assuming that a similar atomic orbital behavior to that of conventional semiconductors holds for these perovskites, one would expect that the top of the valence band shifts up and the bottom of the conduction band shifts down slightly with applied pressure, leading to a reduction of the fundamental gap, as experimentally observed (linear pressure coefficient of  $-60(10)$  meV/GPa).

**Raman Measurements under Pressure.** Figure 3 summarizes the Raman results obtained on single-crystalline



**Figure 3.** Room temperature Raman spectra of MAPbI<sub>3</sub> measured at different pressures. The spectra were normalized to their maximum intensity and shifted vertically for clarity. The different colors of the spectra indicate the changes in phase after every transition.

MAPbI<sub>3</sub> as a function of hydrostatic pressure. Once more, to ease the comparison, the spectra were normalized to their maximum intensity and plotted with a vertical offset with increasing pressure. The colors of the curves correspond to the different phases, as determined from the PL measurements, because the occurrence of the pressure-induced structural transitions cannot always be clearly established from the occasionally subtle changes in the Raman spectra. For a quantitative assessment of the effect of pressure on the vibrational spectrum of MAPbI<sub>3</sub> we have decomposed it in its different mode components by a lineshape analysis, as illustrated in Figure 4, with a representative example of the

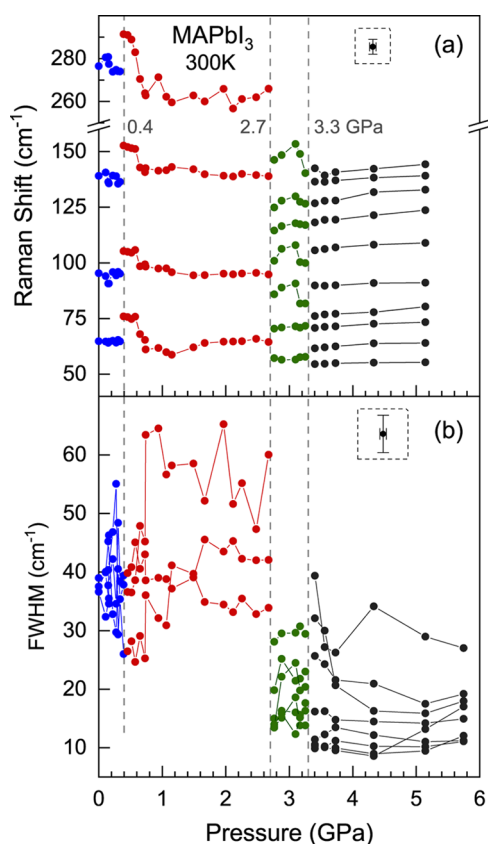


**Figure 4.** Examples of the performed lineshape fits to the Raman spectra using Gaussian functions for different pressures: (a) 0.10 GPa, (b) 1.65 GPa, (c) 2.75 GPa, and (d) 5.15 GPa, each one representing a different high-pressure phase of the material. We point out that the number of Gaussians used for the fits is compatible with the Raman active modes predicted by theory (out of 18 cage eigenmodes)<sup>22</sup> and those observed at low temperature for the orthorhombic phase of MAPbI.<sup>23</sup> The gray solid curves are auxiliary peaks used to improve the fits and are not discussed further. Spectra shown in panels (a) and (b) were obtained by subtracting the broad PL peak from the Raman raw data (see the text for details).

fits for each of the observed phases. We note that for the first two phases ( $P < 2.7$  GPa) all Raman peaks appear on top of a very broad but intense peak, which is ascribed to the main excitonic emission (Figure 3). In fact, the qualitative changes in the Raman spectra of the first two phases are principally due to the shift of this broad background, which varies under compression in exactly the same way as the main excitonic PL peak. For completeness, we refer to a possible alternative explanation in which this broadband is interpreted as a broad

central Raman peak originating from local polar fluctuations intrinsic to the perovskite structure.<sup>51</sup> The strong PL background, however, does not hamper the observation of the Raman features because the latter become resonantly enhanced (outgoing resonance), when the 785 nm line is used for excitation. As for the PL analysis, the background was described by a Gaussian–Lorentzian cross-product function, which has been subtracted from the Raman spectra of the two lowest-pressure phases (see Figure 4a,b) for a better visualization of the phonon modes. All Raman bands/peaks have been fitted using Gaussian functions. On the basis of a previous full assignment of Raman<sup>22,23</sup> and far-infrared spectra,<sup>52</sup> all Raman peaks with frequency lower than 200  $\text{cm}^{-1}$  correspond to optical phonons of the inorganic cage, whereas the broad peak centered at around 280  $\text{cm}^{-1}$  is assigned to the so-called isolated mode associated with a torsional deformation of the MA molecules.

The results of the Raman lineshape fits for the mode frequencies and full widths at half-maximum are depicted in Figure 5 as a function of pressure. The first transition from the



**Figure 5.** (a) Frequency and (b) full width at half-maximum (FWHM) of the Raman peaks, as obtained from the lineshape fits, as a function of pressure up to ca. 6 GPa. The pressures at which the phase transitions occur are marked with vertical dashed lines. Representative error bars are indicated by the symbols inside the dashed squares.

tetragonal to cubic phase<sup>16</sup> can be inferred from the subtle but abrupt changes in the mode frequencies observed at 0.4 GPa, coinciding with the pressure at which the different PL contributions start to change. In contrast, the occurrence of the second phase transition at 2.7 GPa is clearly revealed by the abrupt reduction of the width of all Raman peaks. It is very

difficult to discern if each of the broad bands observed in the Raman spectra of the cubic high-pressure phase splits into several sharp peaks, indicating a reduction of crystal symmetry, or the different components are simply spectrally resolved above 2.7 GPa due to the much smaller widths. Hence, we cannot tell with any degree of confidence if the third phase is cubic, tetragonal, or orthorhombic. Finally, at 3.3 GPa, a third phase transition takes place. An abrupt blue shift of the main PL band occurs, whereas in Raman spectra, the transition can only be assessed by closer inspection of the fitting results (see Figure 5). Above 3.3 GPa, the Raman peaks sharpen further but gradually and some of the peaks split into two. Thus, additional Gaussians ought to be included in the fitting function to describe the Raman lineshape accurately. Such a contrasting behavior of the radiative recombination and the vibrational properties of  $\text{MAPbI}_3$  under high pressure speaks for a transition to a phase that exhibits a slight lattice distortion concomitant with a strong alteration of the electronic properties. Are we being confronted with a kind of “dimerization” of the lattice or the appearance of a superstructure of the organic cations, similarly to the pressure-induced, magnetically driven Peierls transition in  $\text{CuGeO}_3$ ,<sup>53</sup> to give just one example? Clearly more experimental as well as theoretical work is needed to answer this question.

We now turn to the discussion of one of the main results of this work, which concerns the pronounced sharpening of all Raman features taking place at the second phase transition at 2.7 GPa. Such a behavior of the line widths is totally similar to the one observed for decreasing temperature at the tetragonal-to-orthorhombic transition.<sup>22,23</sup> On the basis of this similarity, we propose that the line width reduction of the Raman peaks has the same origin as for the low-temperature orthorhombic phase of  $\text{MAPbI}_3$ . The reduced symmetry of the structure in the high-pressure phase together with a smaller void volume leads to the locking of the MA molecules inside the inorganic cage voids in certain crystalline directions. This causes a sudden and marked reduction of the inhomogeneous broadening of the Raman modes, as a consequence of the vanishing dynamical disorder of the organic cations when locked. This is an important result implying that the suppression of dynamical disorder, which is entropically favorable at low temperatures, is also achieved at room temperature through pure mechanical deformation of the single crystal. Irrespective of its origin, the reduction of the dynamical disorder should have the same positive impact on the thermal conductivity of the material.<sup>28</sup> On the contrary, in an amorphous or highly disordered phase, the thermal conductivity would remain constant or even decrease.

At this point, we would like to call attention to a striking result, namely, the fact that, in our case,  $\text{MAPbI}_3$  does not seem to transform isostructurally into another cubic but amorphous phase at around 3.0 GPa.<sup>16</sup> The sharp peaks we observe in Raman spectra up to 10 GPa, the highest pressure in our experiment, clearly speak against amorphization, defying the claims of the literature.<sup>14–19</sup> Although we cannot tell the symmetry of the lattice by inspection of just the Raman data, as explained below, we found an unexpectedly strong parallel with the structural behavior of  $\text{PbI}_2$  under pressure. We truly believe that the different behaviors observed for  $\text{MAPbI}_3$  under pressure strongly depend on the crystal quality of the sample loaded into the DAC and, of course, of the hydrostatic conditions provided by the particular pressure transmitting medium being used, if any. Regarding the former issue, we

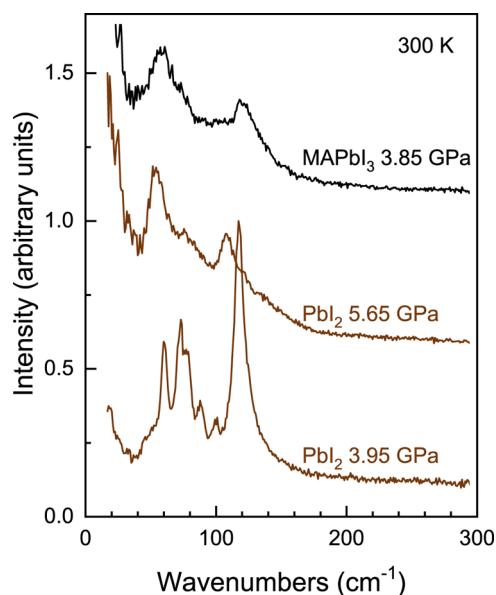


emphasize that the single crystals used here are unique because they were specifically grown with the desired final thickness to fit into the DAC. In this sense, except for the mild cutting into smaller pieces, our crystals have not suffered any mistreatment concerning the necessary thinning of the samples to be loaded into the DAC. It is likely that mechanical polishing or chemical etching might introduce structural defects in a soft material like MAPbI<sub>3</sub>, which under compression would stabilize other phases, leading to a different structural path as a function of pressure.

There is, however, another possibility to explain the apparent discrepancy between our high-pressure Raman results and the X-ray diffraction data of the literature. The crystallographic information extracted from the diffraction patterns depends much on having high long-range order in the structure. On the contrary, Raman scattering is much less sensitive to disorder because even vibrations with an extremely short coherence length are detected. Good examples are the sharp features observed in Raman spectra of semiconductor alloys<sup>54</sup> or the molecular vibrations of the MA cations,<sup>23</sup> for instance. Hence, it could be that the high-pressure phase of MAPbI<sub>3</sub> above 3 GPa corresponds to one in which the pre-existing dynamical disorder of the MA cations is “frozen” at the phase transition. This results in a kind of polycrystal regarding the strain inhomogeneity with nanometric-size domains with different deformation directions such that the long-range order of the inorganic lattice is sufficiently disturbed to affect the X-ray patterns but not the Raman features.

A few words about the pressure-induced structural effects on MAPbI<sub>3</sub> are in place here. We have run further pressure experiments up to 10 GPa and observed that the degree of structural disorder, as indicated by the magnitude of the line broadening of the Raman peaks of the phase setting at above 2.7 GPa, which is sometimes taken for amorphization, depends on how fast pressure is increased. When approaching the phase transition pressure, a rapid increase of pressure leads to broader Raman features, indicating a more disordered structure. If the sample is left overnight at a pressure slightly higher than 2.7 GPa, the Raman spectra measured the next day are as sharp as the ones shown in Figure 3. This clearly indicates that the structural disorder in MAPbI<sub>3</sub>, as well as the occurrence of the fourth phase transition at ca. 3.3 GPa, is a kinetically limited process.

At this point, we would like to report on an accidental finding that might have implications for the understanding of the high-pressure structural behavior of MAPbI<sub>3</sub>. In another experiment, we loaded the DAC using the usual 4:1 methanol/ethanol mixture. Most likely due to the presence of water traces in the mixture,<sup>55</sup> MAPbI<sub>3</sub> unequivocally transformed into PbI<sub>2</sub> under compression at a moderate pressure of about 1 GPa. In Figures S3 and S4 of the Supporting Information, we display all of the Raman spectra as taken in a chronological order and compare them with Raman results for 2H-PbI<sub>2</sub> under pressure.<sup>56</sup> The similarity of the Raman spectra is so striking that leaves no doubts that the crystal had already transformed into PbI<sub>2</sub> when pressure was released to almost ambient after the first upstroke. Moreover, during the second upstroke and at around 0.6 GPa, the phase transition from the two-dimensional (layered) form of 2H-PbI<sub>2</sub> into a three-dimensional crystal structure is clearly observed, exactly as reported.<sup>56</sup> Above 5.5 GPa, however, we find another phase transformation of PbI<sub>2</sub>, not previously reported. As illustrated in Figure 6, the Raman spectra of PbI<sub>2</sub> at such high pressures



**Figure 6.** Raman spectrum of MAPbI<sub>3</sub> at 3.85 GPa compared to the spectra of PbI<sub>2</sub> (transformed from MAPbI<sub>3</sub> under pressure) at 3.95 and 5.65 GPa, corresponding to two different high-pressure phases of the latter. The resemblance of the Raman spectra of the highest-pressure phases of MAPbI<sub>3</sub> and the one of PbI<sub>2</sub> is astonishing.

and those of MAPbI<sub>3</sub> in the phase where the MA molecules are locked in the cage voids are astonishingly similar. Although both materials are certainly different (see Supporting Information for details), we are led to the conclusion that they must share similar structural units in these high-pressure phases. On the one hand, the full reversibility of the structural changes in MAPbI<sub>3</sub> provides evidence that the sixfold coordination of the Pb atoms to the iodides is preserved and the high-pressure phases differ from each other only in the degree of tilting and deformation of the corner-shared PbI<sub>6</sub> octahedra. Furthermore, due to the observed locking of the MA molecules in the voids, the phase setting at above 2.7 GPa is likely to be orthorhombic. On the other hand, recent searching simulations performed through the swarm-intelligence CALYPSO method<sup>57</sup> predict for 2H-PbI<sub>2</sub> a series of phase transformations from the layered  $P\bar{3}m1$  structure to an orthorhombic  $Pnma$  and a tetragonal  $I4/mmm$  one at 2.5 and 27 GPa, respectively. Precisely, the tetragonal phase, which is characterized by a 10-fold coordination of PbI<sub>10</sub> dodecahedral units, is a good candidate for the high-pressure phase we found above 5.5 GPa in PbI<sub>2</sub>, in spite of the large discrepancy in the calculated and measured transition pressures. Hence, the similar shape of the Raman spectra of both materials displayed in Figure 6 might be due to the similarity of the structural building blocks, whereas the red shift of the mode frequencies (even for a much higher pressure) of PbI<sub>2</sub> compared to that of MAPbI<sub>3</sub> is a consequence of the lengthening of the Pb–I bonds imposed by a higher coordination of the structure of the former material.

Finally, we would like to comment on results of a structural search of the high-pressure phases of MAPbI<sub>3</sub>, performed with the minima-hopping method and a classical force-field model, which appeared very recently in the literature.<sup>58</sup> The search revealed that at least two structures are denser and lower in energy than the experimentally observed low-temperature orthorhombic phase. The calculations further show that

particularly a phase type called double-delta could be thermodynamically stabilized under compression in the pressure range of 2–3 GPa, i.e., the range where we observe the second and third phase transitions in MAPbI<sub>3</sub> (at room temperature, though). Double-delta phases contain a pillarlike structure of edge-sharing PbI<sub>6</sub> octahedra, whereas the MA cations uniformly surround them.<sup>58</sup> Interestingly, these novel phases exhibit a much wider fundamental band gap (larger than 3 eV), similarly to the case of the high-pressure phase we found setting at above 3.3 GPa. From the many issues that remain unclear, the understanding of the outspoken reversibility of the pressure-induced structural changes seems crucial. For example, how reversible would be the transformation from the tetragonal or cubic structures, characterized by corner-shared octahedra, to phases like the double-delta ones? The formation of the pillars of edge-shared octahedra in the latter would necessarily imply massive atom movement and bond breaking, which would render difficult the reverse transformation. Clearly, more experimental as well as theoretical work is necessary to finally pinpoint the pressure–temperature phase diagram of MAPbI<sub>3</sub>.

## CONCLUSIONS

In summary, by combining optical spectroscopy (Raman and photoluminescence) with high-pressure techniques, we were able to study structure–property relationships of the archetypal hybrid lead halide perovskite MAPbI<sub>3</sub>. The high-quality single crystals, explicitly grown by the space-confined method with the desired thickness for high-pressure experiments, exhibit a peculiar structural behavior under compression characterized by a sequence of three structural phase transitions at 0.4, 2.7, and 3.3 GPa. All phases are perfectly crystalline, with more or less dynamical disorder of the MA cations, as evidenced by the Raman data. In addition, two issues of the high-pressure phenomenology are worth to be emphasized: On the one hand, at the second phase transition around 2.7 GPa, MAPbI<sub>3</sub> undergoes a transformation into a phase that is characterized by a pronounced reduction of the inhomogeneous broadening of the Raman lines. This is interpreted as evidence of a significant decrease in lattice dynamical disorder because of the locking of the organic cations inside the inorganic cage voids.<sup>23</sup> This behavior is at odds with the previously reported smearing of X-ray diffraction patterns above 3 GPa, interpreted as amorphization. This is, however, an apparent contradiction. Concomitant with the pressure-induced locking of the MA cations, there is a local, orthorhombic distortion of the inorganic cage structure, which on a macroscopic length scale occurs randomly in different directions. At last, this inhomogeneity disturbs the long-range order of the crystal structure, leading to the smearing of the X-ray patterns. Further investigation revealed that the degree of pressure-induced disorder not only depends on crystal quality but also is a kinetically limited process, which is prevented when pressure is slowly raised in the pressure range close to the second phase transition but favored by fast compression (see the discussion in the Supporting Information). On the other hand, the third phase transition at 3.3 GPa involves only a slight structural change, apparent in the Raman spectra only as an additional but small decrease in the line widths and splitting of some peaks, which in turn has associated a marked widening of the fundamental gap. Consequently, the main emission peaks at a much higher energy of 2.15 eV (577 nm) and broadens significantly to a FWHM of ca. 450 meV. The

latter points to large inhomogeneities in the electronic and optical properties of this high-pressure phase of MAPbI<sub>3</sub>. Our findings provide further fundamental insight into the underlying physics of this kind of organic–inorganic hybrid materials, which are causing a change in paradigm in photovoltaic and light-emitting device technology and, possibly, for their by far less explored application in thermoelectricity.

## ASSOCIATED CONTENT

### Supporting Information

The Supporting Information is available free of charge on the ACS Publications website at DOI: 10.1021/acs.jpcc.8b05188.

Details of the lineshape fits performed to PL spectra that are representative of each of the high-pressure phases found in the experiments; brief discussion on reversibility issues as well as a comparative study of the effects of pressure on MAPbI<sub>3</sub> and PbI<sub>2</sub> (PDF)

## AUTHOR INFORMATION

### Corresponding Author

\*E-mail: goni@icmab.es.

### ORCID

Mark T. Weller: 0000-0002-7475-0379

Alejandro R. Goñi: 0000-0002-1193-3063

### Notes

The authors declare no competing financial interest.

## ACKNOWLEDGMENTS

The Spanish Ministerio de Economía, Industria y Competitividad, is gratefully acknowledged for its support through Grant No. SEV-2015-0496 in the framework of the Spanish Severo Ochoa Centre of Excellence program and through Grants MAT2015-70850-P (HIBRI2) and CSD2010-00044 (Consolider NANOTHERM). A.F.-L. acknowledges a FPI fellowship from the Spanish Ministerio co-financed by the European Social Fund. B.C. and O.J.W. thank the EPSRC for Ph.D. studentship funding via the CSCT CDT (EP/G03768X/1, EP/L016354/1). Financial support is also acknowledged from the European Research Council through project ERC CoG648901.

## REFERENCES

- (1) Yang, W. S.; Park, B.-W.; Jung, E. H.; Jeon, N. J.; Kim, Y. C.; Lee, D. U.; Shin, S. S.; Seo, J.; Kim, E. K.; Noh, J. H.; et al. Iodide management in formamidinium-lead-halide-based perovskite layers for efficient solar cells. *Science* **2017**, *356*, 1376–1379.
- (2) Grancini, G.; Kandada, A. R. S.; Frost, J. M.; Barker, A. J.; De Bastiani, M.; Gandini, M.; Marras, S.; Lanzani, G.; Walsh, A.; Petrozza, A. Role of microstructure in the electron-hole interaction of hybrid lead halide perovskites. *Nat. Photonics* **2015**, *9*, 695–700.
- (3) Wang, T.; Daiber, B.; Frost, J. M.; Mann, S. A.; Garnett, E. C.; Walsh, A.; Ehrler, B. Indirect to direct bandgap transition in methylammonium lead halide perovskite. *Energy Environ. Sci.* **2017**, *10*, 509–515.
- (4) Faghihnasiri, M.; Izadifard, M.; Ghazi, M. E. DFT study of mechanical properties and stability of cubic methylammonium lead halide perovskites (CH<sub>3</sub>NH<sub>3</sub>PbX<sub>3</sub>, X = I, Br, Cl). *J. Phys. Chem. C* **2017**, *121*, 27059–27070.
- (5) Domanski, K.; Roose, B.; Matsui, T.; Saliba, M.; Turren-Cruz, S.-H.; Correa-Baena, J.-P.; Carmona, C. R.; Richardson, G.; Foster, J. M.; De Angelis, F.; et al. Migration of cations induces reversible



performance losses over day/night cycling in perovskite solar cells. *Energy Environ. Sci.* **2017**, *10*, 604–613.

(6) Liu, J.; Yin, X.; Liu, X.; Que, M.; Que, W. Multi-influences of ionic migration on illumination-dependent electrical performances of inverted perovskite solar cells. *J. Phys. Chem. C* **2017**, *121*, 16051–16057.

(7) Li, C.; Guerrero, A.; Zhong, Y.; Huettnner, S. Origins and mechanisms of hysteresis in organometal halide perovskites. *J. Phys.: Condens. Matter* **2017**, *29*, No. 193001, and references therein.

(8) Gottesman, R.; Gouda, L.; Kalanoor, B. S.; Haltzi, E.; Tirosh, S.; Rosh-Hodesh, E.; Tischler, Y.; Zaban, A.; et al. Photoinduced reversible structural transformations in free standing  $\text{CH}_3\text{NH}_3\text{PbI}_3$  films. *J. Phys. Chem. Lett.* **2015**, *6*, 2332–2338.

(9) Lang, F.; Shargaieva, O.; Brus, V. V.; Neitzert, H. C.; Rappich, J.; Nickel, N. H. Influence of radiation on the properties and the stability of hybrid perovskites. *Adv. Mater.* **2018**, No. 1702905.

(10) Leguy, A. M. A.; Hu, Y.; Campoy-Quiles, M.; Alonso, M. I.; Weber, O. J.; Azarhoosh, P.; van Schilfgaarde, M.; Weller, M. T.; Bein, T.; Nelson, J.; et al. Reversible hydration of  $\text{CH}_3\text{NH}_3\text{PbX}_3$  in films, single crystals, and solar cells. *Chem. Mater.* **2015**, *27*, 3397–3407.

(11) Wang, Q.; Chen, B.; Liu, Y.; Deng, Y.; Bai, Y.; Dong, Q.; Huang, J. Scaling behavior of moisture-induced grain degradation in polycrystalline hybrid perovskite thin films. *Energy Environ. Sci.* **2017**, *10*, 516–522.

(12) Postorino, P.; Malavasi, L. Pressure-induced effects in organic-inorganic hybrid perovskites. *J. Phys. Chem. Lett.* **2017**, *8*, 2613–2622.

(13) Jaffe, A.; Lin, Y.; Karunadasa, H. I. Halide perovskites under pressure: Accessing new properties through lattice compression. *ACS Energy Lett.* **2017**, *2*, 1549–1555.

(14) Jaffe, A.; Lin, Y.; Beavers, C. M.; Voss, J.; Mao, W. L.; Karunadasa, H. I. High-pressure single-crystal structures of 3D lead-halide hybrid perovskites and pressure effects on their electronic and optical properties. *ACS Cent. Sci.* **2016**, *2*, 201–209.

(15) Kong, L.; Liu, G.; Gong, J.; Hu, Q.; Schaller, R. D.; Dera, P.; Zhang, D.; Liu, Z.; Yang, W.; Tang, Y.; et al. Simultaneous band-gap narrowing and carrier-lifetime prolongation of organic-inorganic trihalide perovskites. *Proc. Natl. Acad. Sci. U.S.A.* **2016**, *113*, 8910–8915.

(16) Szafranski, M.; Katrusiak, A. Mechanism of pressure-induced phase transitions, amorphization, and absorption-edge shift in photovoltaic methylammonium lead iodide. *J. Phys. Chem. Lett.* **2016**, *7*, 3458–3466.

(17) Capitani, F.; Marini, C.; Caramazza, S.; Postorino, P.; Garbarino, G.; Hanfland, M.; Pisanu, A.; Quadrelli, P.; Malavasi, L. High-pressure behavior of methylammonium lead iodide ( $\text{MAPbI}_3$ ) hybrid perovskite. *J. Appl. Phys.* **2016**, *119*, No. 185901.

(18) Jiang, S.; Fang, Y.; Li, R.; Xiao, H.; Crowley, J.; Wang, C.; White, T. J.; Goddard, W. A., III; Wang, Z.; Baikie, T.; et al. Pressure-dependent polymorphism and band-gap tuning of methylammonium lead iodide perovskite. *Angew. Chem., Int. Ed.* **2016**, *55*, 6540–6544.

(19) Ou, T.; Yan, J.; Xiao, C.; Shen, W.; Liu, C.; Liu, X.; Han, Y.; Ma, Y.; Gao, C. Visible light response, electrical transport, and amorphization in compressed organo lead iodine perovskites. *Nanoscale* **2016**, *8*, 11426–11431.

(20) Wang, L.; Wang, K.; Xiao, G.; Zeng, Q.; Zou, B. Pressure-induced structural evolution and band gap shifts of organometal halide perovskite-based methylammonium lead chloride. *J. Phys. Chem. Lett.* **2016**, *7*, 5273–5279.

(21) Wang, L.; Wang, K.; Zou, B. Pressure-induced structural and optical properties of organometal halide perovskite-based formamidinium lead bromide. *J. Phys. Chem. Lett.* **2016**, *7*, 2556–2562.

(22) Brivio, F.; Frost, J. M.; Skelton, J. M.; Jackson, A. J.; Weber, O. J.; Weller, M. T.; Goñi, A. R.; Leguy, A. M. A.; Barnes, P. R. F.; Walsh, A. Lattice dynamics and vibrational spectra of the orthorhombic, tetragonal, and cubic phases of methylammonium lead iodide. *Phys. Rev. B* **2015**, *92*, No. 144308.

(23) Leguy, A. M. A.; Goñi, A. R.; Frost, J. M.; Skelton, J.; Brivio, F.; Rodríguez-Martínez, X.; Weber, O. J.; Pallipurath, A.; Alonso, M. I.; Campoy-Quiles, M.; et al. Dynamic disorder, phonon lifetimes, and

the assignment of modes to the vibrational spectra of methylammonium lead halide perovskites. *Phys. Chem. Chem. Phys.* **2016**, *18*, 27051–27066.

(24) Onoda-Yamamuro, N.; Matsuo, T.; Suga, H. Calorimetric and IR spectroscopic studies of phase transitions in methylammonium trihalogenoplumbates. *J. Phys. Chem. Solids* **1990**, *51*, 1383–1395.

(25) Weller, M. T.; Weber, O. J.; Henry, P. F.; Di Pumpo, A. M.; Hansen, T. C. Complete structure and cation orientation in the perovskite photovoltaic methylammonium lead iodide between 100 and 352 K. *Chem. Commun.* **2015**, *51*, 4180–4183.

(26) Leguy, A. M. A.; Frost, J. M.; McMahon, A. P.; Sakai, V. G.; Kochelmann, W.; Law, C.-H.; Li, X.; Foglia, F.; Walsh, A.; O'Regan, B. C.; et al. The dynamics of methylammonium ions in hybrid organic-inorganic perovskite solar cells. *Nat. Commun.* **2015**, *6*, No. 7124.

(27) Bakulin, A. A.; Selig, O.; Bakker, H. J.; Rezus, Y. L. A.; Müller, C.; Glaser, T.; Lovrincic, R.; Sun, Z.; Chen, Z.; Walsh, A.; et al. Real-time observation of organic cation reorientation in methylammonium lead iodide perovskites. *J. Phys. Chem. Lett.* **2015**, *6*, 3663–3669.

(28) Pisoni, A.; Jacimovic, J.; Barisic, O. S.; Spina, M.; Gaal, R.; Forro, L.; Horvath, E. Ultra-low thermal conductivity in organic-inorganic hybrid perovskite  $\text{CH}_3\text{NH}_3\text{PbI}_3$ . *J. Phys. Chem. Lett.* **2014**, *5*, 2488–2492.

(29) Chen, Y.-X.; Ge, Q.-Q.; Shi, Y.; Liu, J.; Xue, D.-J.; Ma, J.-Y.; Ding, J.; Yan, H.-J.; Hu, J.-S.; Wan, L.-J. General space-confined on-substrate fabrication of thickness-adjustable hybrid perovskite single-crystalline thin films. *J. Am. Chem. Soc.* **2016**, *138*, 16196–16199.

(30) Angel, R. J.; Bujak, M.; Zhao, J.; Gatta, G. D.; Jacobsen, S. D. Effective hydrostatic limits of pressure media for high-pressure crystallographic studies. *J. Appl. Crystallogr.* **2007**, *40*, 26–32.

(31) Mao, H.-K.; Xu, J.; Bell, P. M. Calibration of the ruby pressure gauge to 800 kbar under quasi-hydrostatic conditions. *J. Geophys. Res.* **1986**, *91*, 4673–4676.

(32) Francisco-López, A.; Charles, B.; Weber, O. J.; Alonso, M. I.; Garriga, M.; Campoy-Quiles, M.; Weller, M. T.; Goñi, A. R. On the Structure-Optical-Properties Relationship of Organic-Cation Solid Solutions of Lead Iodide Perovskites as a Function of Temperature, unpublished work, 2018.

(33) Saba, M.; Cadelano, M.; Marongiu, D.; Chen, F.; Sarritzu, V.; Sestu, N.; Figus, C.; Aresti, M.; Piras, R.; Geddo Lehmann, A.; et al. Correlated electron-hole plasma in organometal perovskites. *Nat. Commun.* **2014**, *5*, No. 5049.

(34) Even, J.; Pedesseau, L.; Katan, C. Analysis of multivalley and multibandgap absorption and enhancement of free carriers related to exciton screening in hybrid perovskites. *J. Phys. Chem. C* **2014**, *118*, 11566–11572.

(35) Frost, J. M.; Butler, K. T.; Brivio, F.; Hendon, C. H.; van Schilfgaarde, M.; Walsh, A. Atomistic origins of high-performance in hybrid halide perovskite solar cells. *Nano Lett.* **2014**, *14*, 2584–2590.

(36) Miyata, A.; Mitioglu, A.; Plochocka, P.; Portugall, O.; Wang, J. T.-W.; Stranks, S. D.; Snaith, H. J.; Nicholas, R. J. Direct measurement of the exciton binding energy and effective masses for charge carriers in organic-inorganic tri-halide perovskites. *Nat. Phys.* **2015**, *11*, 582–587.

(37) Fang, H.-H.; Raissa, R.; Abdu-Aguye, M.; Adjokatse, S.; Blake, G. R.; Even, J.; Loi, M. A. Photophysics of organic-inorganic hybrid lead iodide perovskite single crystals. *Adv. Funct. Mater.* **2015**, *25*, 2378–2385.

(38) Shi, D.; Adinolfi, V.; Comin, R.; Yuan, M.; Alarousu, E.; Buin, A.; Chen, Y.; Hoogland, S.; Rothenberger, A.; Katsiev, K.; et al. Low trap-state density and long carrier diffusion in organolead trihalide perovskite single crystals. *Science* **2015**, *347*, 519–522.

(39) Patel, J. B.; Lin, Q.; Zadvorna, O.; Davies, C. L.; Herz, L. M.; Johnston, M. B. Photocurrent spectroscopy of perovskite solar cells over a wide temperature range from 15 to 350 K. *J. Phys. Chem. Lett.* **2018**, *9*, 263–268.

(40) Jha, A.; Duan, H.-G.; Tiwari, V.; Nayak, P. K.; Snaith, H. J.; Thorwart, M.; Miller, R. J. D. Direct observation of ultrafast exciton

dissociation in lead-iodide perovskite by 2D electronic spectroscopy. *ACS Photonics* **2018**, *5*, 852–860.

(41) D'Innocenzo, V.; Grancini, G.; Alcocer, M. J.-P.; Kandada, A. R. S.; Stranks, S. D.; Lee, M. M.; Lanzani, G.; Snaith, H. J.; Petrozza, A. Excitons versus free charges in organo-lead tri-halide perovskites. *Nat. Commun.* **2014**, *5*, No. 3486.

(42) Wu, K.; Bera, A.; Ma, C.; Du, Y.; Yang, Y.; Li, L.; Wu, T. Temperature-dependent excitonic photoluminescence of hybrid organometal halide perovskite films. *Phys. Chem. Chem. Phys.* **2014**, *16*, 22476–22481.

(43) Dong, Q.; Fang, Y.; Shao, Y.; Mulligan, P.; Qiu, J.; Cao, L.; Huang, J. Electron-hole diffusion lengths  $>175 \mu\text{m}$  in solution-grown  $\text{CH}_3\text{NH}_3\text{PbI}_3$  single crystals. *Science* **2015**, *347*, 967–970.

(44) Galkowski, K.; Mitioglu, A. A.; Surrente, A.; Yang, Z.; Maude, D. K.; Kossaki, P.; Eperon, G. E.; Wang, J. T.-W.; Snaith, H. J.; Plochocka, P.; et al. Spatially resolved studies of the phases and morphology of methylammonium and formamidinium lead tri-halide perovskites. *Nanoscale* **2017**, *9*, 3222–3230.

(45) Wu, X.; Trinh, M. T.; Niesner, D.; Zhu, H.; Norman, Z.; Owen, J. S.; Yaffe, O.; Kudisch, B. J.; Zhu, X.-Y. Trap states in lead iodide perovskites. *J. Am. Chem. Soc.* **2015**, *137*, 2089–2096.

(46) Goñi, A. R.; Syassen, K. Chapter 4 Optical Properties of Semiconductors under Pressure. *Semicond. Semimetals* **1998**, *54*, 247–425 and references therein.

(47) Klingshirn, C. F. *Semiconductor Optics*; Springer: Berlin, 1997.

(48) We note that the sharp increase in PL intensity before the second phase transition as well as the abrupt intensity reduction in the third high pressure phase is systematically observed for all four measurement series. Although the reason for this behavior is elusive to us, we speculate that it could be due to pressure-induced changes in absorption at the excitation wavelength.

(49) Giorgi, G.; Fujisawa, J.-I.; Segawa, H.; Yamashita, K. Small photocurrent effective masses featuring ambipolar transport in methylammonium lead iodide perovskite: A density functional analysis. *J. Phys. Chem. Lett.* **2013**, *4*, 4213–4216.

(50) Even, J.; Pedesseau, L.; Katan, C.; Kepenekian, M.; Lauret, J.-S.; Saponi, D.; Deleporte, E. Solid-state physics perspective on hybrid perovskite semiconductors. *J. Phys. Chem. C* **2015**, *119*, 10161–10177.

(51) Yaffe, O.; Guo, Y.; Tan, L. Z.; Egger, D. A.; Hull, T.; Stoumpos, C. C.; Zheng, F.; Heinz, T. F.; Kronik, L.; Kanatzidis, M. G.; et al. Local polar fluctuations in lead halide perovskite crystals. *Phys. Rev. Lett.* **2017**, *118*, No. 136001.

(52) Sendner, M.; Nayak, P. K.; Egger, D. A.; Beck, S.; Müller, C.; Epding, B.; Kowalsky, W.; Kronik, L.; Snaith, H. J.; Puccia, A.; et al. Optical phonons in methylammonium lead halide perovskites and implications for charge transport. *Mater. Horiz.* **2016**, *3*, 613–620.

(53) Goñi, A. R.; Zhou, T.; Schwarz, U.; Kremer, R. K.; Syassen, K. Pressure-temperature phase diagram of the spin-Peierls compound  $\text{CuGeO}_3$ . *Phys. Rev. Lett.* **1996**, *77*, 1079–1082.

(54) Yu, P. Y.; Cardona, M. *Fundamentals of Semiconductors*; Springer: Berlin, 1995.

(55) Charles, B.; Dillon, J.; Weber, O. J.; Islam, M. S.; Weller, M. T. Understanding the stability of mixed A-cation lead iodide perovskites. *J. Mater. Chem. A* **2017**, *5*, 22495–22499.

(56) Jayaraman, A.; Maines, R. G.; Chattopadhyay, T. Pressure-induced structural transitions in  $\text{PbI}_2$ : A high-pressure Raman and optical absorption study. *Pramana* **1986**, *27*, 449–457.

(57) Yang, L.; Zhang, Y.; Wang, J.; Wang, Y.; Yu, W. W. Pressure-induced phase transitions of lead iodide. *RSC Adv.* **2016**, *6*, 84604–84609.

(58) Flores-Livas, J. A.; Tomerini, D.; Amsler, M.; Boziki, A.; Rothlisberger, U.; Goedecker, S. Emergence of Hidden Phases of Methylammonium Lead-Iodide ( $\text{CH}_3\text{NH}_3\text{PbI}_3$ ) upon Compression. 2018, arXiv:1806.05858v1 [cond-mat.mtrl-sci]. arXiv.org e-Print archive. <https://arxiv.org/abs/1806.05858> (accessed June 15, 2018).

## Supporting Information

# Pressure-Induced Locking of Methylammonium Cations versus Amorphization in Hybrid Lead Iodide Perovskites

Adrián Francisco-López,<sup>†</sup> Bethan Charles,<sup>‡</sup> Oliver J. Weber,<sup>‡</sup> M. Isabel  
Alonso,<sup>†</sup> Miquel Garriga,<sup>†</sup> Mariano Campoy-Quiles,<sup>†</sup> Mark T. Weller,<sup>‡</sup> and  
Alejandro R. Goñi<sup>\*,†,¶</sup>

<sup>†</sup>*Institut de Ciència de Materials de Barcelona (ICMAB-CSIC), Campus UAB, 08193 Bellaterra,  
Spain*

<sup>‡</sup>*Dept. of Chemistry & Centre for Sustainable Chemical Technologies, University of Bath,  
Claverton Down, Bath BA2 7AY, UK*

<sup>¶</sup>*ICREA, Passeig Lluís Companys 23, 08010 Barcelona, Spain*

E-mail: goni@icmab.es

## Lineshape fits of PL spectra

Figure S1 shows representative PL spectra of MAPbI<sub>3</sub> for different pressures to illustrate the lineshape analysis of the PL profiles. Different colors correspond to the four phases observed as a

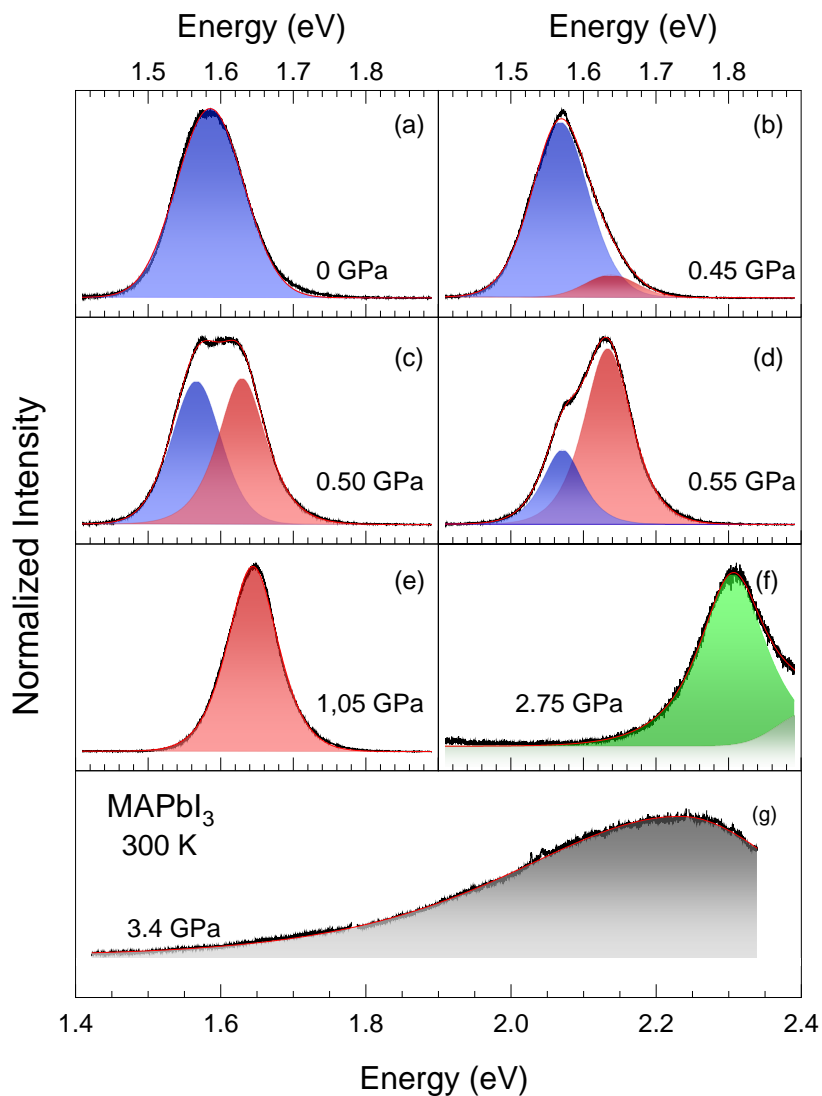


Figure S 1: PL spectra of MAPbI<sub>3</sub> obtained for different pressures. The spectra were normalized to their maximum intensity to ease their comparison. The different colors indicate the subsequent phases adopted by the material during the pressure upstroke (Blue: tetragonal, red: cubic, green: probably orthorhombic, grey: unknown). For pressures lower and higher than 3.4 GPa the excitation laser wavelength was 633 nm and 514 nm, respectively.

function of pressure and the same code was used throughout the manuscript. The main emission peak of MAPbI<sub>3</sub> at room temperature was assigned to free-exciton recombination.<sup>2-5</sup> Thus, for the lineshape fitting of the PL spectra we used a Gaussian-Lorentzian cross-product function.<sup>1</sup> Its expression reads as:

$$G \times L(\hbar\omega) = A \cdot \frac{\Gamma^2}{4 \cdot s \cdot (E_0 - \hbar\omega)^2 + \Gamma^2} \cdot \exp\left(-4 \cdot \ln 2 \frac{(1-s) \cdot (E_0 - \hbar\omega)^2}{\Gamma^2}\right) \quad (1)$$

where  $A$  is the amplitude prefactor,  $E_0$  is the peak energy position,  $\Gamma$  in the full width at half maximum and  $s$  is a weight parameter which takes the value  $s = 0$  for pure Gaussian lineshape and  $s = 1$  for pure Lorentzian. The values of these four adjustable parameters were obtained as a function of pressure from lineshape fits to the measured PL spectra using Eq. (1), as exemplified in Fig. S1. For the cases where there is a coexistence of two phases ( $0.4 \text{ GPa} \leq P \leq 1.0 \text{ GPa}$ ) we used two cross-product functions with independent variable parameter sets.

## Reversibility issues

The reversibility of the structural as well as the related pressure-induced changes in the optical and vibrational properties is certainly a matter of concern for a soft material such as MAPbI<sub>3</sub>. Figure S2 displays Raman and PL spectra measured at two different pressures during the first pressure upstroke (black solid lines) and with decreasing pressure after reaching the highest value of the experiment (green solid lines). Whereas the Raman spectra are almost identical, the PL spectra agree well with each other, besides for small discrepancies in the peak position (probably due to small deviations in the pressure). We remark, though, that the intensity of the PL emission fully recovers after decompression. This is very important because the PL signal is very sensitive to the appearance of structural defects which usually cause its quenching. Altogether, both Raman and

PL spectra demonstrate the full reversibility of the structural changes in MAPbI<sub>3</sub> under hydrostatic pressure.

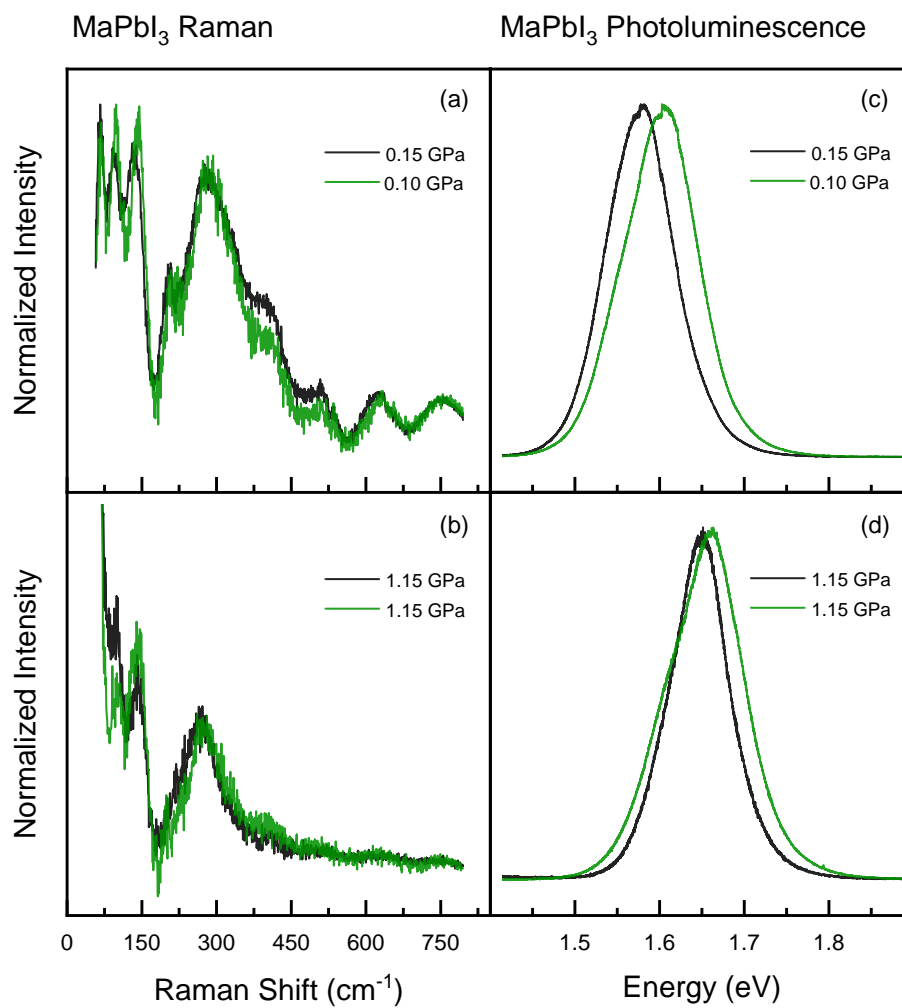


Figure S 2: (a,b) Raman and (c,d) PL spectra of MAPbI<sub>3</sub> obtained for the pressure upstroke (black) and subsequent downstroke (green), demonstrating the high degree of reversibility of the structural/optical changes induced by pressure.

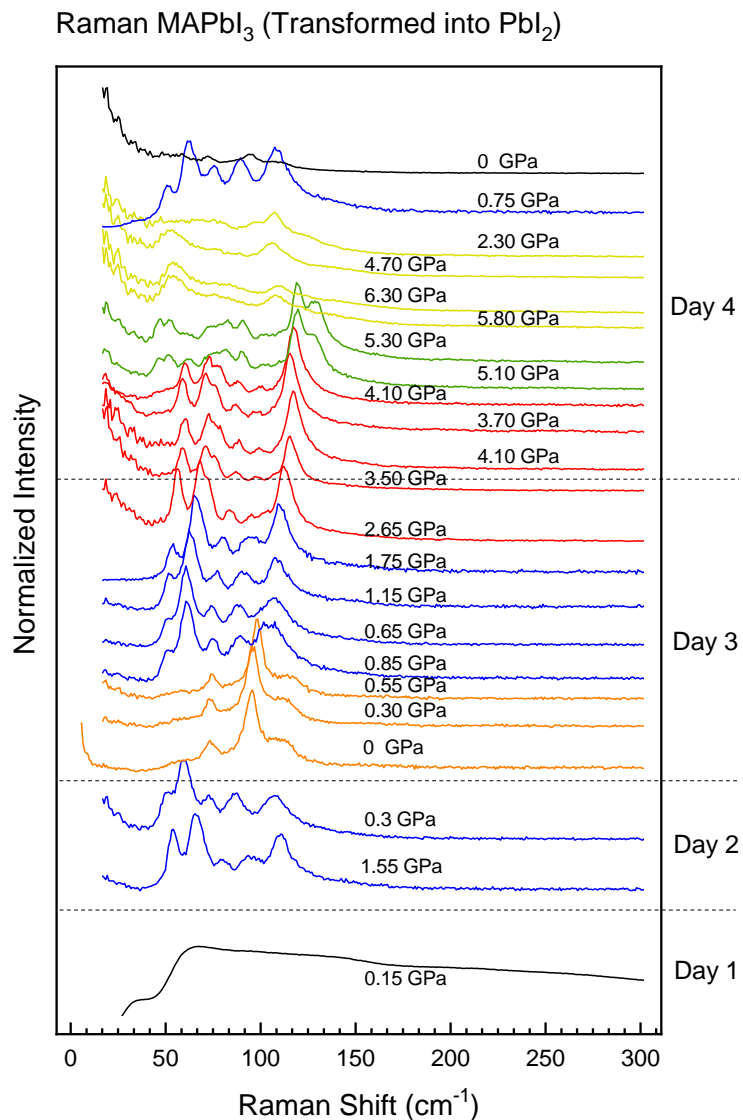


Figure S 3: Raman spectra obtained when applying pressure on a MAPbI<sub>3</sub> sample using a different pressure medium (4:1 methanol-ethanol mixture possibly with traces of water) rather than propanol. After an initial cycle of pressurization, the Raman spectra of the sample coincide with those obtained by for PbI<sub>2</sub>. The horizontal dotted lines mark the different days at which the measurements were performed.

## **A comparative of the effects of pressure on MAPbI<sub>3</sub> and PbI<sub>2</sub>**

Here we report on an accidental finding with implications for the understanding of the high-pressure structural behavior of MAPbI<sub>3</sub>. In another experiment, we loaded the DAC using the usual 4:1 methanol/ethanol mixture. Most likely due to the presence of traces of water in the mixture, MAPbI<sub>3</sub> unequivocally transformed into PbI<sub>2</sub> under compression at a moderate pressure of about 1 GPa. The evidence of this transformation is seen in Figs. S3 and S4. In the former, we display all the Raman spectra as taken chronologically during this separate experiment, whereas in the latter we compare side-by-side the Raman results obtained for 2H-PbI<sub>2</sub> under pressure<sup>6</sup> with spectra measured in the present experiment at similar pressures. The direct comparison clearly indicates, for example, that on day 2, MAPbI<sub>3</sub> had already transformed into PbI<sub>2</sub>, for the similitude of the Raman spectra is just striking. We point out that the PL signal is completely lost once the sample underwent the pressure-induced transition from MAPbI<sub>3</sub> to PbI<sub>2</sub>, i.e., we are not able to record any spectrum similar to the ones reported by Saitoh et al. for PbI<sub>2</sub> single crystals measured under pressure but at low temperature.<sup>7</sup> Moreover, during the second upstroke and at around 0.6 GPa, the phase transition from the 2D (layered) form of 2H-PbI<sub>2</sub> into a 3D crystal structure is observed in Raman scattering, exactly as reported.<sup>6</sup> This phase transition was also observed at the same pressure but a much lower temperature of 77 K.<sup>7</sup> Jayaraman et al.<sup>6</sup> further reported two subsequent phase transitions of 2H-PbI<sub>2</sub>, one at 3 GPa to a phase with a less symmetric structure and another at around 4 GPa to an amorphous phase. Above 5.5 GPa, in contrast, we find an additional phase transformation of PbI<sub>2</sub>, not previously reported. In our case, we emphasize that the structural changes were only partially reversible upon depressurization. As indicated by the Raman spectrum taken by decreasing pressure to 0.75 GPa of Fig. S3, the sample recovered the signature of the 3D crystalline phase of PbI<sub>2</sub>. Nevertheless, when the DAC was finally opened, the sample decomposed completely and became a dark reddish paste, exhibiting the featureless Raman



spectrum of Fig. S3 (0 GPa spectrum at the top). The strong PL of MAPbI<sub>3</sub> also disappeared as soon as the Raman spectra corresponded to the ones of lead iodide.

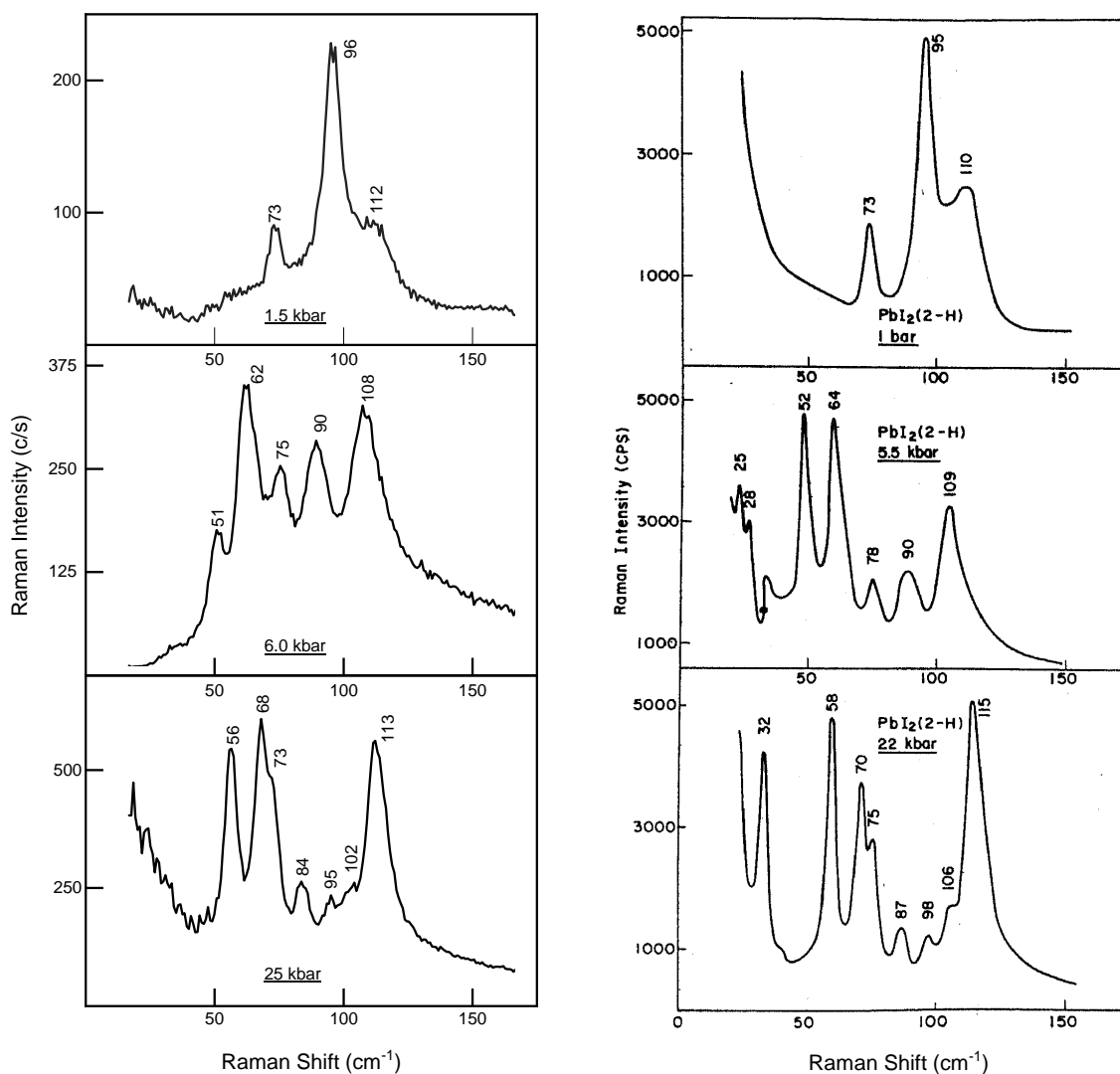


Figure S 4: The panels on the right hand side correspond to a reproduction of Fig. 1 of the work by Jayaraman et al.,<sup>6</sup> which shows Raman spectra of 2H-PbI<sub>2</sub> measured at the pressures where three different phases were stable. The panels on the left hand side display Raman spectra of the MAPbI<sub>3</sub> sample after its presumable transformation into lead iodide measured at similar pressures as by Jayaraman et al.<sup>6</sup> The similitude of the spectra, regarding lineshape as well as the position of the Raman peaks, is so high that there is no doubt that the full pressure-induced transformation of MAPbI<sub>3</sub> into PbI<sub>2</sub> has taken place.

As mentioned in the manuscript, the Raman spectra of  $\text{PbI}_2$  at pressures above 5.5 GPa, as determined in the present experiment, and those of  $\text{MAPbI}_3$  in the phases where the MA molecules are locked in the cage voids are astonishingly similar (see also Fig. 6 of the manuscript). We are thus lead to the conclusion that both materials share similar structural units in these high pressure phases. Hybrid organic-metal-halide perovskites are described by the general formula  $(\text{R-NH}_3)_n\text{MX}_m$ , where R is an organic group, X is a halogen atom (X=I, Br, Cl), and M is a metal (M=Pb, Sn, Ge). The pair of indices  $(n, m)$  control the stoichiometry and charge neutrality of the compound. They also determine crystal packing and dimensionality of the structure, ranging from three-dimensional (3D) corner-shared perovskite structures for  $(n, m)=(1, 3)$ , 2D layered perovskites for  $(n, m)=(2, 4)$  to 0D structures with isolated inorganic octahedra. In this sense, 2H- $\text{PbI}_2$ , a 2D layered semiconductor, can be thought as pertaining to this family of compounds having indices  $(n, m)=(0, 2)$ . In addition, the application of high hydrostatic pressure usually leads to structural phase transformations, where phases exhibiting a higher metal-halogen atom coordination are increasingly favored for higher compression. Hence, it is likely that certain correlation exists between the pressure-induced structural changes of different members of the compound family.

On the one hand, the fact that the structural changes in  $\text{MAPbI}_3$  are fully reversible is evidence that the sixfold coordination of the Pb atoms to the iodides is preserved under pressure and that the high pressure phases differ from each other only in the degree of tilting and deformation of the corner-shared  $\text{PbI}_6$  octahedra (see sketch in Fig. S5). Furthermore, due to the observed locking of the MA molecules in the voids, the phase setting in above 2.7 GPa is likely to be orthorhombic. On the other hand, recent simulations performed through searching algorithms like the swarm-intelligence CALYPSO method<sup>8</sup> predict for 2H- $\text{PbI}_2$  a series of phase transformations from the layered  $P\bar{3}m1$  structure to an orthorhombic  $Pnma$  and a tetragonal  $I4/mmm$  one at 2.5 and 27 GPa, respectively. Precisely the tetragonal phase, which is characterized by a tenfold coordination

of  $\text{PbI}_{10}$  dodecahedral units, is a good candidate for the high-pressure phase we found above 5.5 GPa in  $\text{PbI}_2$ , in spite of the large discrepancy in the calculated and measured transition pressures. The similar shape of the Raman spectra of both materials displayed in Fig. S3 and Fig. 6 of the manuscript might be due to the similarity of the structural building blocks, as depicted in Fig. S5. Another interesting observation is that the Raman mode frequencies of  $\text{PbI}_2$  are redshifted compared to those of  $\text{MAPbI}_3$  even though the Raman spectra of the latter were measured at lower pressures (see Fig. 6 of the manuscript). We believe that this is a consequence of the lengthening of the Pb-I bonds imposed by a higher coordination of the structure having dodecahedral structural units rather than octahedral ones.

In summary, the main conclusion from the results of this section is that the high-pressure phase

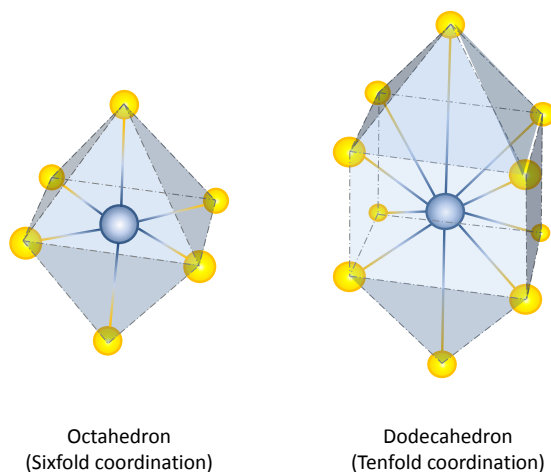


Figure S 5: Sketch of the structural units corresponding to  $\text{PbI}_6$  octahedra and  $\text{PbI}_{10}$  dodecahedra from which the crystalline structure of the high pressure phases of  $\text{MAPbI}_3$  and  $\text{PbI}_2$  might be constructed. The grey central atom is Pb and the yellow balls represent the I atoms. The pb-I bonds are necessarily longer in the dodecahedron due to the higher coordination.

of MAPbI<sub>3</sub> above 3.3 GPa and the one of PbI<sub>2</sub> above 5.5 GPa, reported here for the first time, do share similar structural units, making the Raman spectra to look alike. Though, by no means can be inferred that MAPbI<sub>3</sub> has transformed into PbI<sub>2</sub> at those high pressures. In spite of the (accidental) similarity of the PL emission from PbI<sub>2</sub> at around 2 GPa<sup>7</sup> and that of MAPbI<sub>3</sub> in the fourth high pressure phase, there are unambiguous facts that rule out such a transformation. The strongest one is the full reversibility of the pressure-induced changes in the vibrational as well as optical properties of MAPbI<sub>3</sub> as compared to the complete irreversibility of its humidity-related degradation into PbI<sub>2</sub>.<sup>9</sup>

## References

- (1) Wojdyr, M. Fityk: A general-purpose peak fitting program. *J. Appl. Crystallogr.* **2010**, 43, 1126-1128.
- (2) D'Innocenzo, V.; Grancini, G.; Alcocer, M. J.-P.; Kandada, A. R. S.; Stranks, S. D.; Lee, M. M.; Lanzani, G.; Snaith, H. J.; Petrozza, A. Excitons versus free charges in organo-lead tri-halide perovskites. *Nature Commun.* **2014**, 5, 3486-3492.
- (3) Wu, K.; Bera, A.; Ma, C.; Du, Y.; Yang, Y.; Li, L.; Wu, T. Temperature-dependent excitonic photoluminescence of hybrid organometal halide perovskite films. *Phys. Chem. Chem. Phys.* **2014**, 16, 22476-22481.
- (4) Dong, Q.; Fang, Y.; Shao, Y.; Mulligan, P.; Qiu, J.; Cao, L.; Huang, J. Electron-hole diffusion lengths >175 μm in solution-grown CH<sub>3</sub>NH<sub>3</sub>PbI<sub>3</sub> single crystals. *Sci.* **2015**, 347, 967-970.
- (5) Galkowski, K.; Mitioglu, A. A.; Surrante, A.; Yang, Z.; Maude, D. K.; Kossaki, P.; Eperon, G. E.; Wang, J. T.-W.; Snaith, H. J.; Plochocka, P.; et al. Spatially resolved studies of the

phases and morphology of methylammonium and formamidinium lead tri-halide perovskites. *Nanoscale* **2017**, 9, 3222-3230.

- (6) Jayaraman, A.; Maines, R. G.; Chattopadhyay, T. Pressure-induced structural transitions in  $\text{PbI}_2$ : A high-pressure Raman and optical absorption study. *Pramana-J. Phys.* **1986**, 27, 449-457.
- (7) Saitoh, A.; Komatsu, T.; Karasawa, T. Hydrostatic pressure effects on Raman spectra and the fundamental absorption edge in  $2\text{H-PbI}_2$  crystals. *Phys. Rev. B* **2000**, 62, 398-404.
- (8) Yang, L.; Zhang, Y.; Wang, J.; Wang, Y.; Yu, W. W. Pressure-induced phase transitions of lead iodide. *RSC Adv.* **2016**, 6, 84604-84609.
- (9) Charles, B.; Dillon, J.; Weber, O. J.; Islam, M. S.; Weller, M. T. Understanding the stability of mixed A-cation lead iodide perovskites. *J. Mater. Chem. A* **2017**, 5, 22495-22499.



# Equal Footing of Thermal Expansion and Electron–Phonon Interaction in the Temperature Dependence of Lead Halide Perovskite Band Gaps

Adrián Francisco-López,<sup>†</sup> Bethan Charles,<sup>‡</sup> Oliver J. Weber,<sup>‡</sup> M. Isabel Alonso,<sup>†</sup> Miquel Garriga,<sup>†</sup> Mariano Campoy-Quiles,<sup>†</sup> Mark T. Weller,<sup>‡,§</sup> and Alejandro R. Goñi<sup>\*,†,§</sup>

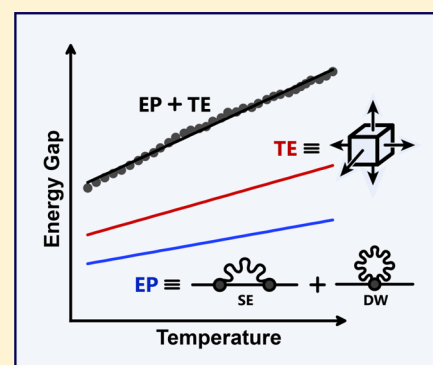
<sup>†</sup>Institut de Ciència de Materials de Barcelona (ICMAB-CSIC), Campus UAB, 08193 Bellaterra, Spain

<sup>‡</sup>Department of Chemistry & Centre for Sustainable Chemical Technologies, University of Bath, Claverton Down, Bath BA2 7AY, U.K.

<sup>§</sup>ICREA, Passeig Lluís Companys 23, 08010 Barcelona, Spain

## Supporting Information

**ABSTRACT:** Lead halide perovskites, which are causing a paradigm shift in photovoltaics, exhibit an atypical temperature dependence of the fundamental gap: it decreases in energy with decreasing temperature. Reports ascribe such a behavior to a strong electron–phonon renormalization of the gap, neglecting contributions from thermal expansion. However, high-pressure experiments performed on the archetypal perovskite MAPbI<sub>3</sub> (MA stands for methylammonium) yield a negative pressure coefficient for the gap of the tetragonal room-temperature phase, which speaks against the assumption of negligible thermal expansion effects. Here we show that for MAPbI<sub>3</sub>, the temperature-induced gap renormalization due to electron–phonon interaction can only account for about 40% of the total energy shift, thus implying thermal expansion to be more if not as important as electron–phonon coupling. Furthermore, this result possesses general validity, holding also for the tetragonal or cubic phase, stable at ambient conditions, of most halide perovskite counterparts.



Hybrid lead halide perovskites of the type APbX<sub>3</sub> with organic A-site cation and halide substitution on the X site are the focus of attention of photovoltaic research and to a lesser extent as light emitters. These materials, which can be cost-effectively deposited from solution, experienced a rash improvement in solar-energy conversion efficiency, recently reaching a remarkable value of 23.7%.<sup>1</sup> For a solar cell as well as for a light emitting device, the band gap and its temperature dependence are fundamental properties of the active material. A peculiarity of the tetragonal and cubic phases of hybrid lead halide perovskites, which are stable at ambient conditions, is that they exhibit an *atypical* dependence on temperature of the fundamental direct gap: it decreases in energy with decreasing temperature. This temperature dependence of the gap is almost ubiquitous in halide perovskites, as it can be found, for example, in MAPbI<sub>3</sub>,<sup>2–6</sup> MAPbBr<sub>3</sub>,<sup>4,5,7</sup> MAPbCl<sub>3</sub>,<sup>8</sup> FAPbI<sub>3</sub>,<sup>5</sup> FAPbBr<sub>3</sub>,<sup>4,5</sup> FA<sub>x</sub>MA<sub>1-x</sub>PbI<sub>3</sub>,<sup>9</sup> CsPbI<sub>3</sub>,<sup>10</sup> CsPbBr<sub>3</sub>,<sup>10,11</sup> MASnI<sub>3</sub><sup>12</sup> and CsSnI<sub>3</sub>.<sup>13</sup> By atypical it is meant opposite to the temperature behavior of the gaps exhibited by most of covalent bonded semiconductors, for which the gap increases with decreasing temperature (see, for instance, refs.<sup>14–18</sup> and references therein).

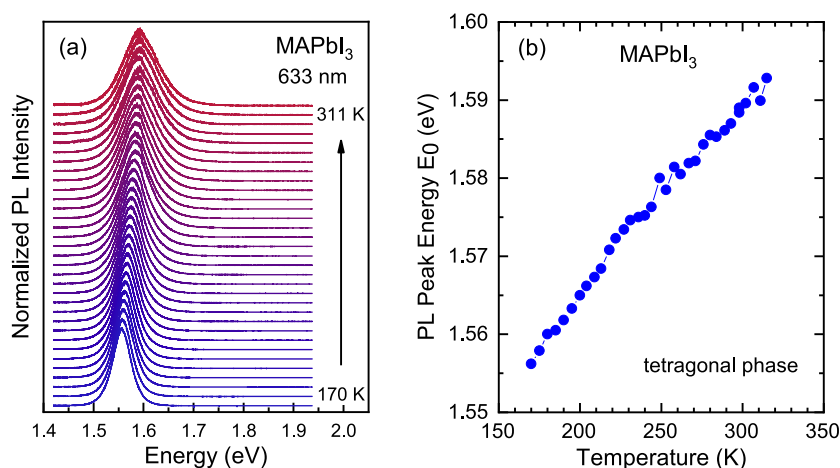
The theoretical framework for describing the variation of band gaps with temperature was set by V. Heine and P. B. Allen<sup>19</sup> and further developed by M. Cardona and co-workers

using the empirical pseudopotential method at an early stage<sup>14,15,17,20</sup> and ab initio techniques afterward.<sup>18,21,23</sup> The changes of the semiconductor band structure with temperature arise essentially from the effect of thermal expansion (TE) due to the anharmonicity of the crystal potential and from electron–phonon interaction. The renormalization of the band energies due to electron–phonon coupling, when considered to second order in the atomic displacements, consists of two terms: The Debye–Waller (DW) and the self-energy (SE) corrections. Usually, for the direct gaps of most semiconductors both terms cause a reduction with increasing temperature. The decrease caused by thermal expansion is mainly due to a positive hydrostatic pressure coefficient of the gaps, whereas the gap reduction arising from electron–phonon interaction is proportional to the Bose–Einstein phonon occupation number. There are, however, exceptions to the mentioned rule. The first reported material that appeared to show an abnormal temperature dependence of the fundamental gap was CuCl, which exhibits a slight sublinear increase of the gap with increasing temperature.<sup>21</sup> Other cuprous halides<sup>22</sup> and several silver chalcopyrites like AgGaS<sub>2</sub> and AgGaSe<sub>2</sub> also

Received: March 27, 2019

Accepted: May 15, 2019

Published: May 15, 2019



**Figure 1.** (a) PL spectra of MAPbI<sub>3</sub> measured at different temperatures in the range of stability of the tetragonal phase (ca. 170–311 K) using the red line (633 nm) for excitation. The spectra were normalized to their maximum intensity and plotted with a vertical shift for increasing temperature. (b) Plot of the temperature dependence of the maximum peak position  $E_0$  of the spectra displayed in part (a).

display abnormal behavior but at low temperatures.<sup>23</sup> A common characteristic of copper halides and silver chalcopyrites is that the pressure coefficient of the gap is very small, such that the thermal expansion contribution to the gap renormalization becomes almost irrelevant. As a consequence, in these cases, the temperature dependence of the gap is mainly determined by electron–phonon interaction. As far as halide perovskites are concerned, thermal expansion effects were indeed considered at an early stage<sup>24</sup> and even taken as the only cause of band gap renormalization.<sup>13</sup> However, probably misled by the copper halide results, researchers adopted lately the point of view of interpreting the atypical temperature dependent renormalization of the fundamental gap of lead halide perovskites exclusively as due to a particularly strong electron–phonon coupling.<sup>7,10</sup> Recent results from first principle calculations also seem to indicate that lattice expansion has negligible effects on the band structure of MAPbI<sub>3</sub> in comparison to the electron–phonon coupling.<sup>25</sup> Here we show this is not the case.

In this Letter, we demonstrate that the role of the electron–phonon interaction in the temperature-induced renormalization of the gap of lead halide perovskites has been widely overestimated. Using available data for the hydrostatic pressure coefficient of the gap, we show for the archetypal perovskite compound MAPbI<sub>3</sub> that the thermal expansion contribution is the leading term in the temperature dependence of the direct gap, whereas electron–phonon interaction effects account for ca. 40% of the total energy shift. Moreover, we provide arguments in favor of an interpretation of the sign and magnitude of the electron–phonon renormalization terms, which holds also for other halide perovskites. On the basis of the results of previous empirical pseudopotential calculations, we infer that the electron–phonon coupling affects electronic states in different ways, depending on their bonding/antibonding and atomic orbital character.

The MAPbI<sub>3</sub> samples used for the high-pressure experiments are high-quality single crystals grown by the space-confined on-substrate fabrication method, as reported elsewhere,<sup>26</sup> having a suitable final thickness of ca. 30 μm. Otherwise, for the experiments as a function of temperature we used large and thick single crystals of about 2 × 2 × 1 mm<sup>3</sup> synthesized from aqueous solution by a similar procedure.<sup>27</sup> The high-pressure photoluminescence (PL) measurements were performed at

room temperature by employing a gasketed diamond anvil cell (DAC) with anhydrous propanol as pressure transmitting medium,<sup>26</sup> whereas the temperature dependent PL measurements were carried out in vacuum using a gas-flow cryostat.<sup>9</sup> The PL spectra were excited with the 633 nm line of a He–Ne laser using a very low incident light power of ca. 1 μW (a power density below 15 W/cm<sup>2</sup>) to avoid photodegradation of the samples. Spectra were collected using a 20× long working distance objective with NA = 0.35 and dispersed with a high-resolution LabRam HR800 grating spectrometer equipped with a charge-coupled device detector. PL spectra were corrected for the spectral response of the spectrometer by normalizing each spectrum using the detector and the 600 grooves/mm grating characteristics.

Figure 1a shows the evolution of the PL spectra with temperature in the stability range of the tetragonal phase of MAPbI<sub>3</sub>. All spectra were normalized to its absolute maximum intensity and vertically offset for clarity. The main PL peak exhibits a gradual red shift and sharpening with decreasing temperature. To analyze the PL spectra of MAPbI<sub>3</sub>, we used a Gaussian–Lorentzian cross-product function for describing the main peak, which is ascribed to free-exciton recombination.<sup>26</sup> The values of the fitting parameter corresponding to the energy  $E_0$  of the PL peak maximum are plotted as a function of temperature in Figure 1b. Although we cannot tell the absolute values of bandgap and/or exciton binding energy from the line shape fits, the shift of the PL peak energy  $E_0$  with temperature (or pressure) is to a large extent dictated by the shift of the gap which for MAPbI<sub>3</sub> exhibits a fairly linear decrease with decreasing temperature.

As mentioned before, the derivative of the gap over temperature contains two terms; one accounts for thermal expansion effects (TE), and the other corresponds to the renormalization directly caused by electron–phonon interaction (EP), which includes the Debye–Waller and self-energy corrections:<sup>14,15,21</sup>

$$\frac{dE_g}{dT} = \left[ \frac{\partial E_g}{\partial T} \right]_{TE} + \left[ \frac{\partial E_g}{\partial T} \right]_{EP} \quad (1)$$

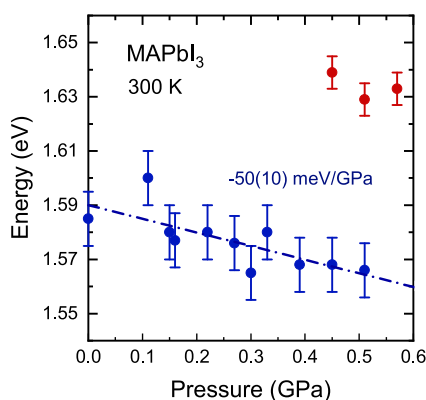
The effect on the gap due to the contraction of the lattice with decreasing temperature is intimately related to the



response of the electronic band structure upon application of external hydrostatic pressure. It thus holds<sup>14,15,18</sup>

$$\left[ \frac{\partial E_g}{\partial T} \right]_{TE} = -\alpha_V \cdot B_0 \cdot \frac{dE_g}{dP} \quad (2)$$

where  $-\alpha_V$  is the volumetric expansion coefficient,  $B_0$  is the bulk modulus, i.e., the inverse of the compressibility, and  $\frac{dE_g}{dP}$  is the pressure coefficient of the gap, which can be determined from high-pressure experiments. The last two factors depend only weakly on temperature. As shown in the Supporting Information, the strongest temperature variation comes from  $\alpha_V$  (also including zero-point vibrations<sup>18</sup>). At room temperature  $\alpha_V$  is positive and the sign of eq 2 for the thermal expansion contribution is determined by the sign of the pressure coefficient. For most semiconductor direct gaps  $\frac{dE_g}{dP}$  is positive as well. Hence, thermal expansion causes a gap reduction. The lead halide perovskites are an exception. Figure 2 shows the variation with pressure of the energy position of



**Figure 2.** Energy  $E_0$  of the PL peak maximum (blue symbols) plotted as a function of pressure in the stability range of the tetragonal phase of MAPbI<sub>3</sub>. The dot-dashed line represents a fit to the data points using a linear function (its slope is indicated). The red symbols correspond to PL emission from regions of the sample that had already undergone the phase transition into the high-pressure cubic phase (see ref 26 for details).

the PL peak measured in MAPbI<sub>3</sub> single crystals with the DAC in the short stability range of the tetragonal phase. A linear fit to the data points (dot-dashed line) yields an unusually large but negative pressure coefficient, as indicated. The negative sign of  $\frac{dE_g}{dP}$  arises from the inverted atomic orbital character of the states at the top and bottom of the valence and conduction band of MAPbI<sub>3</sub>, respectively, as explained elsewhere.<sup>26</sup> This implies that for MAPbI<sub>3</sub> the expansion of the lattice with increasing temperature leads to a gradual opening of the gap, as displayed in Figure 1b. The magnitude of this effect will be discussed later together with the gap renormalization due to electron–phonon interaction.

Gopalan et al.<sup>15</sup> derived an expression for the shift and broadening induced by temperature, through electron–phonon interaction, of any electronic state  $E_{nk}$  with band index  $n$  and wavevector  $\mathbf{k}$ , for which all phonon modes of the branch  $j$ , wavevector  $\mathbf{q}$ , and frequency  $\omega_{jq}$  contribute:

$$\Delta E_{nk}(T) = \sum_{jq} \frac{\partial E_{nk}}{\partial n_{jq}} \left( n_{jq}(T) + \frac{1}{2} \right) \quad (3)$$

where  $n_{jq} = (e^{\beta \hbar \omega_{jq}} - 1)^{-1}$  is the Bose–Einstein phonon occupation factor with  $\beta = \frac{1}{k_B T}$ . The real part of the complex interaction coefficients  $\frac{\partial E_{nk}}{\partial n_{jq}}$  contribute to the energy shift of the bands and contain both the DW and SE parts, whereas the imaginary part leads to a lifetime broadening of the electronic states. Obviously, the sign of the renormalization of a gap is thus determined by the difference in magnitude and sign of the respective energy shift of valence and conduction band.

Invoking energy conservation transforms the summation in eq 3 into an integral over the phonon frequencies:<sup>15</sup>

$$\Delta E_{nk}(T) = \int_0^\infty d\omega g^2 F(n, \mathbf{k}, \omega) \cdot \left( n_{jq}(T) + \frac{1}{2} \right) \\ g^2 F(n, \mathbf{k}, \omega) = \sum_{jq} \frac{\partial E_{nk}}{\partial n_{jq}} \delta(\omega - \omega_{jq}) \quad (4)$$

The function  $g^2 F(n, \mathbf{k}, \omega)$  is the so-called electron–phonon spectral function and is essentially the phonon density of states (DOS) appropriately weighted by electron–phonon matrix elements. As such, the spectral function is temperature independent, which means that the temperature dependence of the electron–phonon contribution to the gap shift arises solely from the Bose–Einstein occupation factor  $n_{jq}(T)$ .

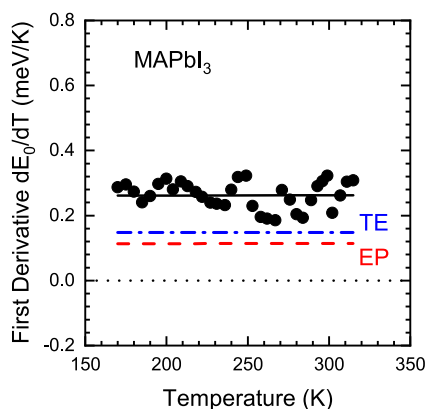
This is an important result because eqs 3 and 4 clearly indicate that the main contributions to the electron–phonon renormalization of the gap arise from peaks in the phonon density of states. In fact, this is at the origin of the Einstein–oscillator model introduced by Cardona and co-workers,<sup>21–23</sup> which approximate the  $\frac{\partial E_{nk}}{\partial n_{jq}}$  coefficients by effective electron–phonon interaction parameters  $A_i$  for phonons with average frequency  $\omega_i$ , inferred from the peaks in the phonon DOS. The EP correction to the gap then reads

$$[\Delta E_g(T)]_{EP} = \sum_i A_i \cdot \left( n_B(\omega_i, T) + \frac{1}{2} \right) \quad (5)$$

where  $n_B$  again stands for the Bose–Einstein factor. In special cases of materials with two atoms per unit cell with markedly different masses like the cuprous halides,<sup>21,22</sup> it is allowed to use a two-oscillator model with a modified effective EP coefficient that explicitly accounts for its dependence on the average phonon frequency and atomic species mass ( $A_i \rightarrow \frac{A'_i}{\omega_i \cdot M_i}$ ). This is justified because the phonon DOS exhibits two peaks, one at the average frequency of the acoustic phonon branches at the Brillouin zone edges, corresponding to vibrations of the heavier mass specie, and another oscillator accounting for the optical phonon contribution, corresponding to vibrations of the lighter mass atomic specie. For exactly the same reason, each of the two oscillators is identified with the contribution from acoustic and optical phonons to the electron–phonon renormalization. We point out that this model cannot be simply transferred to the case of the halide perovskites,<sup>7,10</sup> because perovskites have many atoms per unit cell and the vibrations cannot be classified as lead only or halide only. In fact, an inspection of the phonon DOS for the three methylammonium lead halide compounds<sup>28</sup> indicates

that the DOS exhibits up to four well-defined peaks or bands, not two, with partial intermixing of optical and acoustical branches.

In this respect, we show here that the electron–phonon renormalization can be well accounted for using a single Einstein oscillator with a *positive* effective coefficient  $A_{\text{eff}}$ , so as to reproduce the linear decrease of the gap with decreasing temperature of MAPbI<sub>3</sub>. Since we do not know the absolute magnitude of the gap renormalization at room temperature (or at any other temperature), we decided to circumvent this handicap by evaluating instead the derivative with respect to temperature of the gap renormalization. The closed black symbols in Figure 3 represent the first derivative over



**Figure 3.** First derivative of the PL peak energy  $E_0$  with respect to temperature (closed black symbols), numerically calculated from the data of Figure 1b. The solid black line represents a fit to the data points, corresponding to the sum of the contribution of thermal expansion (blue dot-dashed curve) and electron–phonon interaction (red dashed curve). See text for details.

temperature of the bandgap, numerically calculated point-by-point from the data set of  $E_0$  versus  $T$  shown in Figure 1b. Despite the dispersion of the values, in the temperature range of stability of the tetragonal phase of MAPbI<sub>3</sub>, the first derivative of the gap over temperature is, as expected, essentially constant. The contribution from thermal expansion can be directly obtained from eq 2, using the values of  $\alpha_V = 1.57 \times 10^{-4} \text{ K}^{-1}$ <sup>29</sup> and  $B_0 = 18.8 \text{ GPa}$ <sup>30</sup> from the literature and the linear pressure coefficient determined by us from high-pressure experiments, indicated in Figure 2. The result is the constant contribution represented by the blue dot-dashed line in Figure 3. In order to calculate the contribution from electron–phonon interaction, we have derived eq 5 with respect to temperature, considering a single oscillator with coupling constant  $A_{\text{eff}}$  and oscillator frequency  $\omega_{\text{eff}}$ :

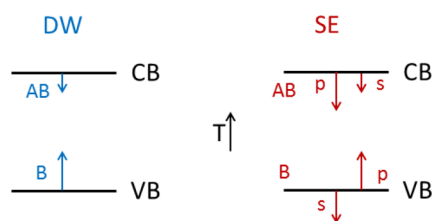
$$\left[ \frac{\partial E_g}{\partial T} \right]_{\text{EP}} = \frac{A_{\text{eff}}}{4T} \cdot \frac{\hbar\omega_{\text{eff}}}{k_B T} \cdot \frac{1}{\sinh^2\left(\frac{\hbar\omega_{\text{eff}}}{2k_B T}\right)} \quad (6)$$

This function together with the constant contribution from TE given by eq 2 were fitted to the data points of Figure 3 using only the electron–phonon coupling constant and the average phonon frequency as adjustable parameters. The resulting values for these parameters are  $A_{\text{eff}} = 8.0(8) \text{ meV}$  and  $\hbar\omega_{\text{eff}} = 5.8(6) \text{ meV}$ , where the numbers in parentheses are the error bars (uncertainty of the last digits). The solid black curve and the dashed red curve in Figure 3 represent the resulting

total rate of gap renormalization per Kelvin and the EP contribution to it, respectively. We emphasize that without further information apart from the data of Figure 1b the only way to ensure uniqueness of the fitting results is to use one Einstein oscillator. Addition of further oscillators would just introduce strong correlations between oscillators parameters, leading to multivalued solutions. In summary, at 300 K we obtain from the fitting results a total renormalization rate of 0.26(5) meV/K, corresponding to the sum of the contribution from thermal expansion (0.15(5) meV/K) and that from electron–phonon interaction (0.11(5) meV/K). This is a clear indication that thermal expansion effects ( $\sim 60\%$ ), rather than being negligible,<sup>7,10,25</sup> are even more important than electron–phonon coupling effects ( $\sim 40\%$ ). We show below that this situation also holds for most, if not all, lead halide perovskites investigated so far.

By accounting for the thermal expansion effects, we obtain within the Einstein-oscillator model a value of ca. 6 meV for effective phonon frequency involved in the gap renormalization, which is in excellent agreement with the frequency of 1 THz (approximately 4 meV) of the specific phonon mode which strongly couples to the gap in terahertz transient transmission experiments<sup>6</sup> and with the frequency of 4.2(8) meV of the phonons leading to exciton broadening,<sup>31</sup> both in MAPbI<sub>3</sub>, although the latter holds for the orthorhombic phase. In contrast, if the two-oscillator model is applied without thermal expansion consideration, unrealistically large average phonon frequencies for the optical branches of approximately 16 meV<sup>7</sup> or even 40–50 meV<sup>10</sup> are found for the best fit to the gap-versus-temperature data. We recall that the maximum cutoff frequency of the phonon modes of the inorganic cages of lead halide perovskites is  $200 \text{ cm}^{-1}$  (ca. 25 meV)<sup>32</sup> but the most intense Raman modes have frequencies below  $100 \text{ cm}^{-1}$  (ca. 12.5 meV).<sup>28</sup> For comparison we show in the Supporting Information results from a literature survey containing a comprehensive list of available band gap pressure and temperature coefficients for different halide perovskite materials.

The calculation by ab initio methods of the magnitude of the electron–phonon interaction in materials like the hybrid halide perovskites, characterized by soft and strongly anharmonic vibrational modes, constitutes a real challenge.<sup>8,24,33,34</sup> Despite their relevance, we prefer to make use of the semiempirical pseudopotential calculations that provided a detailed, though qualitative, picture of the electron–phonon interaction in covalent,  $\text{sp}^3$ -bonded semiconductors<sup>14,15,17,20</sup> (for further details see the Supporting Information). The Debye–Waller correction represents two-phonon processes for which the lattice vibrations perturb the electronic band structure in the same way as in the case of X-ray diffraction patterns, i.e., by smearing the pseudopotential *structure factor*. In this sense, the DW correction mainly depends on the spatial distribution of the electronic charge around the lattice atoms. As illustrated in the sketch of Figure 4, valence-band states with mostly bonding character increase in energy with increasing temperature, whereas the antibonding conduction-band states slightly decrease in energy. Hence, the DW term always cause a gap reduction with increasing temperature for  $\text{sp}^3$ -bonded semiconductors. In contrast, the sign and magnitude of the self-energy term would depend on how the pseudopotential *form factors* react to the different phonon eigenvectors corresponding to the modes leading to the peaks in the phonon DOS. It turns out that the acoustic-phonon SE contribution almost



**Figure 4.** Sketch of the sign and magnitude (arrows) of the Debye–Waller (DW) and self-energy (SE) contributions to the electron–phonon renormalization of valence and conduction-band states of  $sp^3$ -bonded semiconductors, depending on the bonding (B) or antibonding (AB) and atomic orbital character (s or p) of the involved states for the case of increasing temperature ( $T$ ).

cancels out the DW correction,<sup>15</sup> which implies that for  $sp^3$  bonding only optical phonons contribute to the gap renormalization. The remaining SE interaction matrix elements are large and positive for p-like and moderate but negative for s-like bonding valence-band states, whereas for antibonding conduction-band states the SE interaction parameters are negative for s- and p-like states but larger for the latter (see Figure 4). As a consequence, a single Einstein oscillator with a negative coupling constant  $A_{\text{eff}}$  provides a good description of the gap reduction induced by an increase in temperature in conventional semiconductors.

A common feature of the materials showing an abnormal temperature dependence of their gap, like certain cuprous halide<sup>21,22</sup> and Ag chalcopyrite<sup>23</sup> compounds, is the presence of d-states in the valence band. The Cu 3d-like and Ag 4d-like valence electrons hybridize with the usual p-like counterparts, reverting the sign of the electron–phonon interaction and so leading to a strong downshift of the valence band with increasing temperature. The d-state hybridization also has important consequences for the pressure coefficient of the gap,<sup>35</sup> which is largely reduced, because the AB d-states push up the top of the valence band with pressure at a similar pace as for the upshift of the bottom of the conduction band. On the contrary, the unusual temperature-induced gap renormalization in lead halide perovskites possesses a different origin, since there is no hybridization with d-states whatsoever. It is the huge spin–orbit interaction that causes a so-called band inversion. Relativistic band-structure calculations<sup>36–39</sup> for a pseudocubic phase of  $\text{MAPbI}_3$  predict that for the direct gap at the R-point of the Brillouin zone the top of the valence band is predominantly composed by Pb 6s orbitals slightly hybridized with I 5p orbitals, whereas the bottom of the conduction band is formed by the split-off Pb 6p-orbitals. Hence, one expects the EP interaction to lead to a gap increase with increasing temperature (see Supporting Information for details). This is supported by ultraviolet photoemission spectroscopy combined with optical gap measurements, which for  $\text{MAPbI}_3$  show a stronger lowering of the valence-band maximum with respect to the conduction-band minimum, as the temperature is raised.<sup>2</sup> We note that in tin halide perovskites,<sup>12,13</sup> despite the weaker spin–orbit coupling as for lead-based compounds, a similar band inversion occurs, leading to a totally similar atomic orbital character of the electronic states at the conduction and valence-band extrema<sup>40,41</sup> like in  $\text{MAPbI}_3$ . Furthermore, such band inversion also explains the negative pressure coefficient observed in halide perovskites (see Supporting Information for a complete survey of literature data). The pressure coefficient determines the sign of the

thermal expansion contribution, which thus adds up to the effects of electron–phonon interaction as far as the gap renormalization is concerned. Since all arguments presented here are valid for all halide perovskites crystallizing in the tetragonal and/or cubic phases, the same behavior of the gap with temperature, which is ubiquitous in this material system, has a similar explanation.

In conclusion, we have shown that the importance of the electron–phonon interaction in the *abnormal* temperature dependence of the fundamental gap of the tetragonal or cubic phases of halide perovskites has been widely overestimated in previous work. This was the result of totally neglecting the effects of thermal expansion. As a consequence, disproportionately large electron–phonon coupling constants and average phonon frequencies were needed to explain the variation of the gap with temperature in halide perovskites. Using  $\text{MAPbI}_3$  as a representative example, we showed that the thermal expansion effects can be readily quantified from the measured (also unusual) negative pressure coefficient of the gap. Our findings, which have general validity for halide perovskites, clearly indicate that thermal expansion has to be treated on equal footing with the electron–phonon interaction for the correct interpretation of temperature effects on their electronic structure. Given the relevance of the electron–phonon interaction for a variety of physical phenomena apart from the temperature dependence of the gap (charge transport, exciton lifetimes, nonradiative relaxation processes, thermoelectric properties, etc.), its correct assessment is fundamental for further scientific and/or technological developments with halide perovskites.

## ■ ASSOCIATED CONTENT

### 📄 Supporting Information

The Supporting Information is available free of charge on the ACS Publications website at DOI: 10.1021/acs.jpclett.9b00876.

Details of the theoretical discussion, based on the empirical pseudopotential method, of the effects of thermal expansion and electron–phonon interaction on the renormalization of gaps with temperature for conventional semiconductors, a table with the gap pressure and temperature coefficients of the PL peak energy  $E_0$  for the phase of different halide perovskites stable at ambient conditions and a plot showing the smoothing procedure of the data set  $E_0$ -vs-temperature for the calculation of the first derivative (PDF)

## ■ AUTHOR INFORMATION

### Corresponding Author

\*E-mail: goni@icmab.es.

### ORCID

Mark T. Weller: 0000-0002-7475-0379

Alejandro R. Goñi: 0000-0002-1193-3063

### Notes

The authors declare no competing financial interest.

## ■ ACKNOWLEDGMENTS

We gratefully acknowledge fruitful discussions with H. Míguez, M. Calvo, and A. Rubino from the Institute of Materials Science of Seville, Spain. The Spanish Ministerio de Ciencia, Innovación y Universidades, is gratefully acknowledged for its



support through Grant No. SEV-2015-0496 in the framework of the Spanish Severo Ochoa Centre of Excellence program and through Grant MAT2015-70850-P (HIBRI2). A.F.L. acknowledges a FPI fellowship (BES-2016-076913) from the Spanish Ministerio cofinanced by the European Social Fund and the Ph.D. programme in Materials Science from Universitat Autònoma de Barcelona in which he is enrolled. B.C. and O.J.W. thank the EPSRC for Ph.D. studentship funding via the CSCT CDT (EP/G03768X/1, EP/L016354/1). Financial support from is also acknowledged from the European Research Council through project ERC CoG648901.

## REFERENCES

- (1) *Best Research-Cell Efficiency Chart*; National Renewable Energy Laboratory (NREL): Golden, Colorado, USA; [www.nrel.gov/pv/cell-efficiency.html](http://www.nrel.gov/pv/cell-efficiency.html) (2019).
- (2) Foley, B. J.; Marlowe, D. L.; Sun, K.; Saidi, W. A.; Scudiero, L.; Gupta, M. C.; Choi, J. J. Temperature Dependent Energy Levels of Methylammonium Lead Iodide Perovskite. *Appl. Phys. Lett.* **2015**, *106*, 243904.
- (3) Milot, R. L.; Eperon, G. E.; Snaith, H. J.; Johnston, M. B.; Herz, L. M. Temperature-Dependent Charge-Carrier Dynamics in  $\text{CH}_3\text{NH}_3\text{PbI}_3$  Perovskite Thin Films. *Adv. Funct. Mater.* **2015**, *25*, 6218–6227.
- (4) Dar, M. I.; Jacopin, G.; Meloni, S.; Mattoni, A.; Arora, N.; Boziki, A.; Zakeeruddin, S. M.; Rothlisberger, U.; Grätzel, M. Origin of Unusual Gap Shift and Dual Emission in Organic-Inorganic Lead Halide Perovskites. *Sci. Adv.* **2016**, *2*, e1601156.
- (5) Wright, A. D.; Verdi, C.; Milot, R. L.; Eperon, G. E.; Pérez-Osorio, M. A.; Snaith, H. J.; Giustino, F.; Johnston, M. B.; Herz, L. M. Electron-Phonon Coupling in Hybrid Lead Halide Perovskites. *Nat. Commun.* **2016**, *7*, 11755.
- (6) Kim, H.; Hunger, J.; Cánovas, E.; Karakus, M.; Mics, Z.; Grechko, M.; Turchinovich, D.; Parekh, S. H.; Bonn, M. Direct Observation of Mode-Specific Phonon-Band Gap Coupling in Methylammonium Lead Halide Perovskites. *Nat. Commun.* **2017**, *8*, 687.
- (7) Tilchin, J.; Dirin, D. N.; Maikov, G. I.; Sashchiuk, A.; Kovalenko, M. V.; Lifshitz, E. Hydrogen-Like Wannier-Mott Excitons in Single Crystal of Methylammonium Lead Bromide Perovskite. *ACS Nano* **2016**, *10*, 6363–6371.
- (8) Wu, K.; Bera, A.; Ma, C.; Du, Y.; Yang, Y.; Li, L.; Wu, T. Temperature-Dependent Excitonic Photoluminescence of Hybrid Organometal Halide Perovskite Films. *Phys. Chem. Chem. Phys.* **2014**, *16*, 22476–22481.
- (9) Francisco López, A.; Charles, B.; Weber, O. J.; Alonso, M. I.; Garriga, M.; Campoy-Quiles, M.; Weller, M. T.; Goñi, A. R. Phase Diagram of Methylammonium/Formamidinium Lead Iodide Perovskite Solid Solutions from Temperature Dependent Photoluminescence and Raman Spectroscopy, unpublished.
- (10) Saran, R.; Heuer-Jungemann, A.; Kanaras, A. G.; Curry, R. J. Giant Bandgap Renormalization and Exciton-Phonon Scattering in Perovskite Nanocrystals. *Adv. Opt. Mater.* **2017**, *5*, 1700231.
- (11) Shinde, A.; Gahlaut, R.; Mahamuni, S. Low-Temperature Photoluminescence Studies of  $\text{CsPbBr}_3$  Quantum Dots. *J. Phys. Chem. C* **2017**, *121*, 14872–14878.
- (12) Parrott, E. S.; Milot, R. L.; Stergiopoulos, T.; Snaith, H. J.; Johnston, M. B.; Herz, L. M. Effect of Structural Phase Transition on Charge-Carrier Lifetimes and Defects in  $\text{CH}_3\text{NH}_3\text{SnI}_3$  Perovskite. *J. Phys. Chem. Lett.* **2016**, *7*, 1321–1326.
- (13) Yu, C.; Chen, Z.; Wang, J. J.; Pfenninger, W.; Vockic, N.; Kenney, J. T.; Shum, K. Temperature Dependence of the Band Gap of Perovskite Semiconductor Compound  $\text{CsSnI}_3$ . *J. Appl. Phys.* **2011**, *110*, 063526.
- (14) Lautenschlager, P.; Allen, P. B.; Cardona, M. Temperature Dependence of Band Gaps in Si and Ge. *Phys. Rev. B: Condens. Matter Mater. Phys.* **1985**, *31*, 2163–2171.
- (15) Gopalan, S.; Lautenschlager, P.; Cardona, M. Temperature Dependence of the Shifts and Broadenings of the Critical Points in GaAs. *Phys. Rev. B: Condens. Matter Mater. Phys.* **1987**, *35*, 5577–5584.
- (16) Lautenschlager, P.; Garriga, M.; Logothetidis, S.; Cardona, M. Interband Critical Points of GaAs and their Temperature Dependence. *Phys. Rev. B: Condens. Matter Mater. Phys.* **1987**, *35*, 9174–9189.
- (17) Cardona, M.; Gopalan, S. Temperature Dependence of the Band Structure of Semiconductors: Electron-Phonon Interaction. In *Progress on Electron Properties of Solids*; Girlanda, R., Ed.; et al.; Kluwer, 1989; pp 51–64.
- (18) Cardona, M. Electron-Phonon Interaction in Tetrahedral Semiconductors. *Solid State Commun.* **2005**, *133*, 3–18.
- (19) Allen, P. B.; Heine, V. Theory of the Temperature Dependence of Electronic Band Structures. *J. Phys. C: Solid State Phys.* **1976**, *9*, 2305–2312.
- (20) Allen, P. B.; Cardona, M. Theory of the Temperature Dependence of the Direct Gap of Germanium. *Phys. Rev. B: Condens. Matter Mater. Phys.* **1981**, *23*, 1495–1505.
- (21) Göbel, A.; Ruf, T.; Cardona, M.; Lin, C. T.; Wrzesinski, J.; Steube, M.; Reimann, K.; Merle, J.-C.; Joucla, M. Effects of the Isotopic Composition on the Fundamental Gap of CuCl. *Phys. Rev. B: Condens. Matter Mater. Phys.* **1998**, *57*, 15183–15190.
- (22) Serrano, J.; Schweitzer, Ch.; Lin, C. T.; Reimann, K.; Cardona, M.; Fröhlich, D. Electron-Phonon Renormalization of the Absorption Edge of the Cuprous Halides. *Phys. Rev. B: Condens. Matter Mater. Phys.* **2002**, *65*, 125110.
- (23) Bhosale, J.; Ramdas, A. K.; Burger, A.; Muñoz, A.; Romero, A. H.; Cardona, M.; Lauck, R.; Kremer, R. K. Temperature Dependence of Band Gaps in Semiconductors: Electron-Phonon Interaction. *Phys. Rev. B: Condens. Matter Mater. Phys.* **2012**, *86*, 195208.
- (24) Saidi, W. A.; Poncé, S.; Monserrat, B. Temperature Dependence of the Energy Levels of Methylammonium Lead Iodide Perovskite from First-Principles. *J. Phys. Chem. Lett.* **2016**, *7*, 5247–5252.
- (25) Saidi, W. A.; Kachmar, A. Effects of Electron-Phonon Coupling on Electronic Properties of Methylammonium Lead Iodide Perovskites. *J. Phys. Chem. Lett.* **2018**, *9*, 7090–7097.
- (26) Francisco López, A.; Charles, B.; Weber, O. J.; Alonso, M. I.; Garriga, M.; Campoy-Quiles, M.; Weller, M. T.; Goñi, A. R. Pressure-Induced Locking of Methylammonium Cations Versus Amorphization in Hybrid Lead Iodide Perovskites. *J. Phys. Chem. C* **2018**, *122*, 22073–22082.
- (27) Poglitsch, A.; Weber, D. Dynamic Disorder in Methylammoniumtrihalogenoplumbates (II) Observed by Millimeter-Wave Spectroscopy. *J. Chem. Phys.* **1987**, *87*, 6373–6378.
- (28) Leguy, A. M. A.; Goñi, A. R.; Frost, J. M.; Skelton, J.; Brivio, F.; Rodríguez-Martínez, X.; Weber, O. J.; Pallipurath, A.; Alonso, M. I.; Campoy-Quiles, M.; Weller, M. T.; Nelson, J.; Walsh, A.; Barnes, P. R. F. Dynamic Disorder, Phonon Lifetimes, and the Assignment of Modes to the Vibrational Spectra of Methylammonium Lead Halide Perovskites. *Phys. Chem. Chem. Phys.* **2016**, *18*, 27051–27066.
- (29) Jacobsson, T. J.; Schwan, L. J.; Ottosson, M.; Hagfeldt, A.; Edvinsson, T. Determination of Thermal Expansion Coefficients and Locating the Temperature-Induced Phase Transition in Methylammonium Lead Perovskites using X-ray diffraction. *Inorg. Chem.* **2015**, *54*, 10678–10685.
- (30) Szafranski, M.; Katrusiak, A. Mechanism of Pressure-Induced Phase Transitions, Amorphization, and Absorption-Edge Shift in Photovoltaic Methylammonium Lead Iodide. *J. Phys. Chem. Lett.* **2016**, *7*, 3458–3466.
- (31) Diab, H.; Trippé-Allard, G.; Lédée, F.; Jemli, K.; Vilar, Ch.; Bouchez, G.; Jacques, V. L. R.; Tejada, A.; Even, J.; Laurent, J.-S.; Deleporte, E.; Garrot, D. Narrow Linewidth Excitonic Emission in Organic-Inorganic Lead Iodide Perovskite Single Crystals. *J. Phys. Chem. Lett.* **2016**, *7*, 5093–5100.
- (32) Brivio, F.; Frost, J. M.; Skelton, J. M.; Jackson, A. J.; Weber, O. J.; Weller, M. T.; Goñi, A. R.; Leguy, A. M. A.; Barnes, P. R. F.; Walsh, A. Lattice Dynamics and Vibrational Spectra of the Orthorhombic,

Tetragonal, and Cubic Phases of Methylammonium Lead Iodide. *Phys. Rev. B: Condens. Matter Mater. Phys.* **2015**, *92*, 144308.

(33) Whalley, L. D.; Skelton, J. M.; Frost, J. M.; Walsh, A. Phonon Anharmonicity, Lifetimes, and Thermal Transport in  $\text{CH}_3\text{NH}_3\text{PbI}_3$  from Many-Body Perturbation Theory. *Phys. Rev. B: Condens. Matter Mater. Phys.* **2016**, *94*, 220301R.

(34) Whalley, L. D.; Frost, J. M.; Jung, Y.-K.; Walsh, A. Perspective: Theory and Simulation of Hybrid Halide Perovskites. *J. Chem. Phys.* **2017**, *146*, 220901.

(35) Wei, S.-H.; Zunger, A.; Choi, I.-H.; Yu, P. Y. Trends in Band-Gap Pressure Coefficients in Chalcopyrite Semiconductors. *Phys. Rev. B: Condens. Matter Mater. Phys.* **1998**, *58*, R1710–R1713.

(36) Giorgi, G.; Fujisawa, J.-I.; Segawa, H.; Yamashita, K. Small Photocurrent Effective Masses Featuring Ambipolar Transport in Methylammonium Lead Iodide Perovskite: A Density Functional Analysis. *J. Phys. Chem. Lett.* **2013**, *4*, 4213–4216.

(37) Frost, J. M.; Butler, K. T.; Brivio, F.; Hendon, C. H.; van Schilgaarde, M.; Walsh, A. Atomistic Origins of High-Performance in Hybrid Halide Perovskite Solar Cells. *Nano Lett.* **2014**, *14*, 2584–2590.

(38) Even, J.; Pedesseau, L.; Katan, C.; Kepenekian, M.; Lauret, J.-S.; Saponi, D.; Deleporte, E. Solid-State Physics Perspective on Hybrid Perovskite Semiconductors. *J. Phys. Chem. C* **2015**, *119*, 10161–10177.

(39) Borriello, I.; Cantele, G.; Ninno, D. Ab Initio Investigation of Hybrid Organic-Inorganic Perovskites Based on Tin Halides. *Phys. Rev. B: Condens. Matter Mater. Phys.* **2008**, *77*, 235214.

(40) Umari, P.; Mosconi, E.; De Angelis, F. Relativistic GW Calculations on  $\text{CH}_3\text{NH}_3\text{PbI}_3$  and  $\text{CH}_3\text{NH}_3\text{SnI}_3$  Perovskites for Solar Cell Applications. *Sci. Rep.* **2015**, *4*, 4467.

(41) Huang, Y. Q.; Su, J.; Li, Q. F.; Wang, D.; Xu, L. H.; Bai, Y. Structure, Optical and Electrical Properties of  $\text{CH}_3\text{NH}_3\text{SnI}_3$  Single Crystal. *Phys. B* **2019**, *563*, 107–112.



## Supporting Information

# The Equal Footing of Thermal Expansion and Electron-Phonon Interaction in the Temperature Dependence of Lead Halide Perovskite Band Gaps

Adrián Francisco-López,<sup>†</sup> Bethan Charles,<sup>‡</sup> Oliver J. Weber,<sup>‡</sup> M. Isabel  
Alonso,<sup>†</sup> Miquel Garriga,<sup>†</sup> Mariano Campoy-Quiles,<sup>†</sup> Mark T. Weller,<sup>‡</sup> and  
Alejandro R. Goñi<sup>\*,†,¶</sup>

<sup>†</sup>*Institut de Ciència de Materials de Barcelona (ICMAB-CSIC), Campus UAB, 08193 Bellaterra,  
Spain*

<sup>‡</sup>*Dept. of Chemistry & Centre for Sustainable Chemical Technologies, University of Bath,  
Claverton Down, Bath BA2 7AY, UK*

<sup>¶</sup>*ICREA, Passeig Lluís Companys 23, 08010 Barcelona, Spain*

E-mail: goni@icmab.es

## Relation between thermal expansion (TE) and Einstein oscillator model

From thermodynamical arguments<sup>1,2</sup> it is possible to relate the volumetric thermal expansion with the Grüneisen parameter  $\gamma_{j\mathbf{q}} = -\frac{\partial \ln \omega_{j\mathbf{q}}}{\partial \ln V}$  and Bose-Einstein phonon occupation number  $n_{j\mathbf{q}}(T)$  as

$$\begin{aligned} \frac{\Delta V(T)}{V_0} &= \alpha_V \cdot \Delta T \\ &= \frac{1}{B_0 \cdot V_0} \cdot \sum_{j\mathbf{q}} \hbar \omega_{j\mathbf{q}} \gamma_{j\mathbf{q}} \left( n_{j\mathbf{q}}(T) + \frac{1}{2} \right), \end{aligned} \quad (1)$$

where the summation runs over all phonon modes of the branch  $j$ , wavevector  $\mathbf{q}$  and frequency  $\omega_{j\mathbf{q}}$ . Two important results might be surmised from Eq. (1). On the one hand, we note that the electron-phonon coupling is somehow indirectly contained in the thermal expansion (TE) contribution through the phonon Grüneisen parameters. On the other hand, the temperature dependence of the TE gap renormalization is given by the Bose-Einstein occupation factor. This is the same dependence as for the Debye-Waller (DW) and self-energy (SE) contributions, directly accounting for electron-phonon interaction effects. Thus, if the TE contribution is neglected, i.e. not taken explicitly into consideration, an Einstein-oscillator model would nevertheless provide a good description of the temperature dependence of the bandgap, although at the expense of yielding unphysical values of the mean phonon frequency and/or electron-phonon coupling constant.



## The electron-phonon (EP) interaction and the empirical pseudopotential method

For the discussion of the electron-phonon interaction it is strictly necessary to count with a satisfactory description of the electronic states as well as the spectrum of vibrations of the solid. In the former case, the empirical pseudopotential method has demonstrated to be a powerful tool for the calculation and understanding of the temperature dependence of direct band gaps in covalent semiconductors.<sup>3-6</sup> Within the pseudopotential approximation, the electronic states correspond to the eigenvectors  $\Psi_{n\mathbf{k}}$  with band index  $n$  and wavevector  $\mathbf{k}$ , obtained from the following secular equations:<sup>5</sup>

$$\sum_{\mathbf{G}'} \left[ \left( \frac{\hbar^2}{2m} \cdot (\mathbf{k} + \mathbf{G})^2 - E_{n\mathbf{k}} \right) \cdot \delta_{\mathbf{G}\mathbf{G}'} + \sum_{\kappa} V_{\kappa}(\mathbf{G} - \mathbf{G}') \cdot S_{\kappa}(\mathbf{G} - \mathbf{G}') \right] \cdot C_{n\mathbf{k}}(\mathbf{G}') = 0 \quad (2)$$

$$\Psi_{n\mathbf{k}} \propto \sum_{\mathbf{G}} C_{n\mathbf{k}}(\mathbf{G}) e^{i(\mathbf{k} + \mathbf{G}) \cdot \mathbf{r}},$$

where  $\mathbf{G}, \mathbf{G}'$  are reciprocal-lattice vectors,  $C_{n\mathbf{k}}(\mathbf{G})$  are the properly normalized Fourier coefficients of  $\Psi_{n\mathbf{k}}$  and  $V_{\kappa}(\mathbf{G})$  and  $S_{\kappa}(\mathbf{G})$  are the pseudopotential form and structure factors, respectively, of the atom  $\kappa$  in the unit cell. Rather than performing explicit matrix-element calculations, our aim is to attain a qualitative insight into the problem of the electron-phonon interaction that would allow us to draw general conclusions from a careful inspection of the empirical pseudopotential results available in the literature. In addition to the electronic states, a description of the vibrational properties of the solid are needed. Cardona and coworkers<sup>5,6</sup> employed the rigid-ion model to calculate the phonon spectrum of semiconductors to obtain an expression for the electron-phonon (EP) renormalization of the electronic band-state energies as a function of temperature. All phonon modes of the branch  $j$  and with wavevector  $\mathbf{q}$  and frequency  $\omega_{j\mathbf{q}}$  contribute to the renormalization

of the electronic energies, which then reads as:

$$\Delta E_{n\mathbf{k}}(T) = \sum_{j\mathbf{q}\kappa} \frac{A(n, \mathbf{k}, j, \mathbf{q}, \kappa)}{\omega_{j\mathbf{q}} \cdot M_{\kappa}} \left( n_{j\mathbf{q}}(T) + \frac{1}{2} \right), \quad (3)$$

where  $n_{j\mathbf{q}} = \left( e^{\beta \hbar \omega_{j\mathbf{q}}} - 1 \right)^{-1}$  is the Bose-Einstein phonon occupation factor with  $\beta = \frac{1}{k_B T}$ . In Eq. (3) we have explicitly written the dependence of the EP matrix element on the frequency  $\omega_{j\mathbf{q}}$  of the phonon mode involved and the mass  $M_{\kappa}$  of the vibrating atom (an average mass for modes with more than one atom vibrating). Equation (3) can be rewritten by transforming the summation into an integral over the phonon frequencies:<sup>5</sup>

$$\Delta E_{n\mathbf{k}}(T) = \int_0^{\infty} d\omega \cdot g^2 F(n, \mathbf{k}, \omega) \cdot \left( n_{j\mathbf{q}}(T) + \frac{1}{2} \right). \quad (4)$$

The function  $g^2 F(n, \mathbf{k}, \omega)$  is the so-called electron-phonon spectral function and is essentially the phonon density of states (DOS) appropriately weighted by electron-phonon matrix elements. These matrix elements pick up contributions from two terms: The Debye-Waller (DW) and self-energy (SE) term (the electron-phonon Feynman diagrams, corresponding to second order perturbation in atomic displacements, are shown in Fig. 1 of Ref.,<sup>5</sup> for instance).

## The Debye-Waller (DW) correction

The DW term accounts for the coupling between the lattice vibrations and the electronic band states through thermal fluctuations of the atoms around their equilibrium positions, which in turn induce a smearing of the pseudopotential structure factor  $S_{\kappa}(\mathbf{G})$ . In a totally similar way as for x-ray diffraction patterns, such a smearing is easily taken into account by introducing a Debye-Waller

factor in the structure factor:<sup>2</sup>

$$S_{\kappa}(\mathbf{G}) \cdot e^{-\frac{1}{2}\langle u^2 \rangle_{\kappa} \cdot |\mathbf{G}|^2} \simeq S_{\kappa}(\mathbf{G}) \cdot \left[ 1 - \frac{1}{2}\langle u^2 \rangle_{\kappa} \cdot |\mathbf{G}|^2 + \dots \right], \quad (5)$$

where  $\langle u^2 \rangle_{\kappa}$  is the mean-square thermal amplitude of the displacements of the atomic specie  $\kappa$ . As illustrated in Fig. S1, the effect of temperature is twofold: i) The static structure factor  $S(\mathbf{G})$  is reduced in magnitude by the Debye-Waller factor which contains the mean thermal amplitude of the atomic displacements in the exponent. ii) The lost weight of the peak in  $S(\mathbf{G})$  is redistributed forming side tails, corresponding to diffuse scattering processes.

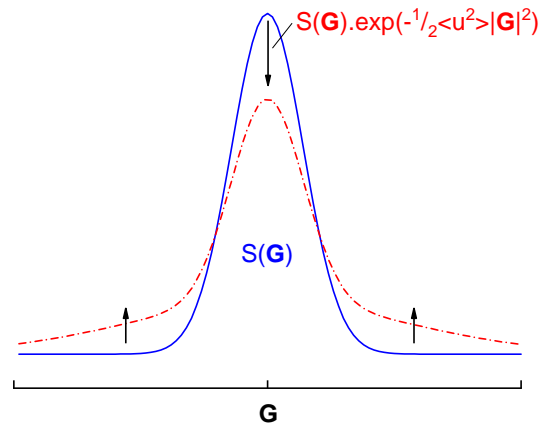


Figure S 1: Sketch showing the pseudopotential structure factor  $S(\mathbf{G})$  (blue curve) in reciprocal space and the effect of the Debye-Waller factor upon it (red curve).

A careful inspection of the empirical pseudopotential results for several  $sp^3$  bonded semiconductors<sup>3,5,6</sup> led us to the following conclusions<sup>3</sup> regarding the DW term of the electron-phonon interaction: i) For conduction band states which are mostly antibonding in nature, i.e., the wavefunction is mainly distributed around the lattice ions, the DW correction is moderate and negative. This means that the DW term causes a moderate downshift in energy of the conduction band with increasing temperature, corresponding to the reduction of the static structure factor at the recipro-

cal lattice vectors due to the DW factor. ii) For valence band states which possess mostly bonding character and concentrate the valence charge in the interatomic regions, the DW correction is large and positive. This means that the valence band shifts up in energy with increasing temperature, as a consequence of the increased structure factor weight in the regions between reciprocal lattice vectors due to the appearance of the diffuse-scattering structure-factor tails.

### **The self-energy (SE) correction**

The self-energy correction can be viewed as a change in the effective mass of valence and conduction electrons due to their interaction with the lattice vibrations. The effective mass can be incremented or reduced, for which the electron energy decreases or increases, respectively, depending on the bonding/antibonding character of the states as well as their atomic orbital character. At last, the SE correction depends on how the pseudopotential form factors  $V_{\kappa}(\mathbf{G})$  of each atomic specie react to the different phonon eigenvectors.

From the empirical pseudopotential calculations we infer following trends for the temperature renormalization of gaps in  $sp^3$  covalently bonded semiconductors: i) For conduction band electrons the SE correction is always negative, pretty weak for acoustic and strong for optical phonons, and larger for  $p$ -like states as compared to  $s$ -like states. This means that conduction band electrons become "heavier" due to their interaction with the lattice vibrations; a coupling that then causes a downshift in energy of the conduction band. ii) For the valence band the sign of the SE correction does depend on the particular phonon modes involved in the interaction. The SE correction is always negative for acoustical phonons but it accidentally almost cancels out with the DW contribution. As a consequence, electron-acoustic-phonon interaction plays a minor role for the gap renormalization in conventional semiconductors. The SE contribution from coupling with optical phonons, in contrast, is negative for  $s$ -like atomic orbitals but positive (twice as large, though)

for  $p$ -like states. Hence, for conventional semiconductors, for which the top of the valence band and the bottom of the conduction band at the Brillouin zone center has exclusively  $p$  and  $s$ -atomic orbital character, respectively, the fundamental gap decreases with increasing temperature. This is a general trend and as such is considered the *normal* temperature dependence of the gap, in frank contrast to that observed for halide perovskites.

## Survey of band-gap pressure and temperature coefficients

Table 1: Linear pressure  $\frac{dE_g}{dP}$  and temperature  $\frac{dE_g}{dT}$  coefficient of the fundamental band gap of the tetragonal or cubic phase, stable at ambient conditions, measured for a series of halide perovskite materials. The notation SC, PC, TF and NC stands for single crystal, polycrystal, thin film and nanocrystal, respectively, indicating the structural quality of the studied samples. Numbers in parentheses are error bars. The asterisk denotes slope values obtained from only three data points available.

| Material           |    | $\frac{dE_g}{dP}$ (meV/GPa) | $\frac{dE_g}{dT}$ (meV/K) | Reference                     |
|--------------------|----|-----------------------------|---------------------------|-------------------------------|
| MAPbI <sub>3</sub> | SC | -50(10)                     | 0.26(5)                   | this work & Ref. <sup>7</sup> |
|                    | SC | -65(10)*                    |                           | Ref. <sup>8</sup>             |
|                    | PC | -210(50)*                   |                           | Ref. <sup>9</sup>             |
|                    | SC | -50(15)*                    |                           | Ref. <sup>10</sup>            |
|                    | SC | -70(10)*                    |                           | Ref. <sup>11</sup>            |

|                     |    |           |          |                    |
|---------------------|----|-----------|----------|--------------------|
|                     | PC | -62(5)    |          | Ref. <sup>12</sup> |
|                     | TF |           | 0.29(5)  | Ref. <sup>13</sup> |
|                     | TF |           | 0.24(5)  | Ref. <sup>14</sup> |
|                     | TF |           | 0.1(1)   | Ref. <sup>15</sup> |
| MAPbBr <sub>3</sub> | PC | -52(8)    |          | Ref. <sup>11</sup> |
|                     | SC | -210(20)* |          | Ref. <sup>16</sup> |
|                     | TF |           | 0.14(6)  | Ref. <sup>14</sup> |
|                     | TF |           | 0.15(8)  | Ref. <sup>15</sup> |
| MAPbCl <sub>3</sub> | PC | -77(5)    |          | Ref. <sup>17</sup> |
| FAPbI <sub>3</sub>  | TF |           | 0.55(5)  | Ref. <sup>15</sup> |
| FAPbBr <sub>3</sub> | TF |           | 0.44(6)  | Ref. <sup>14</sup> |
|                     | TF |           | 0.40(5)  | Ref. <sup>15</sup> |
| CsPbI <sub>3</sub>  | NC |           | 0.06(5)  | Ref. <sup>18</sup> |
| CsPbBr <sub>3</sub> | NC |           | 0.05(5)  | Ref. <sup>18</sup> |
| CsPbCl <sub>3</sub> | NC |           | -0.07(5) | Ref. <sup>18</sup> |

### Calculation of the first derivative of $E_0$ over temperature

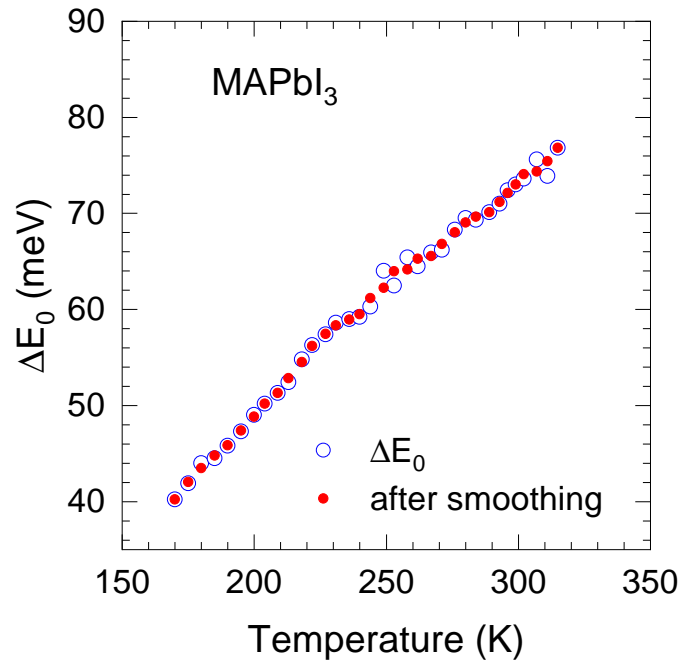


Figure S 2: The values of the change in PL peak energy  $E_0$  as a function of temperature. Open blue symbols correspond to the raw data, whereas the closed red symbols were obtained after smoothing. The latter were used to calculate the point-by-point first derivative with respect to temperature, plotted in Fig. 3 of the main manuscript.

## References

- (1) Ashcroft, N. W.; Mermin, N. D. *Solid State Physics* **1976** (Holt, Rinehart & Winston, Philadelphia) p. 492.
- (2) Cardona, M. Electron-Phonon Interaction in Tetrahedral Semiconductors. *Solid State Commun.* **2005**, 133, 3-18.
- (3) Allen, P. B.; Cardona, M. Theory of the Temperature Dependence of the Direct Gap of Germanium. *Phys. Rev. B* **1981**, 23, 1495-1505.
- (4) Lautenschlager, P.; Allen, P. B.; Cardona, M. Temperature Dependence of Band Gaps in Si and Ge. *Phys. Rev. B* **1985**, 31, 2163-2171.

- (5) Gopalan, S.; Lautenschlager, P.; Cardona, M. Temperature Dependence of the Shifts and Broadenings of the Critical Points in GaAs. *Phys. Rev. B* **1987**, *35*, 5577-5584.
- (6) Cardona, M.; Gopalan, S. Temperature Dependence of the Band Structure of Semiconductors: Electron-Phonon Interaction. *Progress on Electron Properties of Solids*, ed. Girlanda, R.; et al. (Kluwer, 1989), p. 51-64.
- (7) Francisco López, A.; Charles, B.; Weber, O. J.; Alonso, M. I.; Garriga, M.; Campoy-Quiles, M.; Weller, M. T.; Goñi, A. R. Pressure-Induced Locking of Methylammonium Cations Versus Amorphization in Hybrid Lead Iodide Perovskites. *J. Phys. Chem. C* **2018**, *122*, 22073-22082.
- (8) Szafranski, M.; Katrusiak, A. Mechanism of Pressure-Induced Phase Transitions, Amorphization, and Absorption-Edge Shift in Photovoltaic Methylammonium Lead Iodide. *J. Phys. Chem. Lett.* **2016**, *7*, 3458-3466.
- (9) Jiang, S.; Fang, Y.; Li, R.; Xiao, H.; Crowley, J.; Wang, C.; White, T. J.; Goddard III, W. A.; Wang, Z.; Baikie, T.; Fang, J. Pressure-Dependent Polymorphism and Band-Gap Tuning of Methylammonium Lead Iodide Perovskite. *Angew. Chem. Int. Ed.* **2016**, *55*, 6540-6544.
- (10) Jaffe, A.; Lin, Y.; Beavers, C. M.; Voss, J.; Mao, W. L.; Karunadasa, H. I. High-Pressure Single-Crystal Structures of 3D Lead-Halide Hybrid Perovskites and Pressure Effects on Their Electronic and Optical Properties. *ACS Cent. Sci.* **2016**, *2*, 201-209.
- (11) Kong, L.; Liu, G.; Gong, J.; Hu, Q.; Schaller, R. D.; Dera, P.; Zhang, D.; Liu, Z.; Yang, W.; Tang, Y.; Wang, C.; Wei, S.-H.; Xu, T.; Mao, H.-K. Simultaneous Band-Gap Narrowing and Carrier-Lifetime Prolongation of Organic-Inorganic Trihalide Perovskites. *PNAS* **2016**, *113*, 8910-8915.



- (12) Wang, T.; Daiber, B.; Frost, J. M.; Mann, S. A.; Garnett, E. C.; Walsh, A.; Ehrler, B. Indirect to Direct Bandgap Transition in Methylammonium Lead Halide Perovskite. *Energy Environ. Sci.* **2017**, 10, 509-515.
- (13) Milot, R. L.; Eperon, G. E.; Snaith, H. J.; Johnston, M. B.; Herz, L. M. Temperature-Dependent Charge-Carrier Dynamics in CH<sub>3</sub>NH<sub>3</sub>PbI<sub>3</sub> Perovskite Thin Films. *Adv. Funct. Mater.* **2015**, 25, 6218-6227.
- (14) Dar, M. I.; Jacopin, G.; Meloni, S.; Mattoni, A.; Arora, N.; Boziki, A.; Zakeeruddin, S. M.; Rothlisberger, U.; Grätzel, M. Origin of Unusual Gap Shift and Dual Emission in Organic-Inorganic Lead Halide Perovskites. *Sci. Adv.* **2016**, 2, e1601156/1-9.
- (15) Wright, A. D.; Verdi, C.; Milot, R. L.; Eperon, G. E.; Pérez-Osorio, M. A.; Snaith, H. J.; Giustino, F.; Johnston, M. B.; Herz, L. M. Electron-Phonon Coupling in Hybrid Lead Halide Perovskites. *Nature Commun.* **2016**, 7, 11755/1-9.
- (16) Wang, L.; Wang, K.; Zou, B. Pressure-Induced Structural and Optical Properties of Organometal Halide Perovskite-Based Formamidinium Lead Bromide. *J. Phys. Chem. Lett.* **2016**, 7, 2556-2562.
- (17) Wang, L.; Wang, K.; Xiao, G.; Zeng, Q.; Zou, B. Pressure-Induced Structural Evolution and Band Gap Shifts of Organometal Halide Perovskite-Based Methylammonium Lead Chloride. *J. Phys. Chem. Lett.* **2016**, 7, 5273-5279.
- (18) Saran, R.; Heuer-Jungemann, A.; Kanaras, A. G.; Curry, R. J. Giant Bandgap Renormalization and Exciton-Phonon Scattering in Perovskite Nanocrystals. *Adv. Optical Mater.* **2017**, 5, 1700231/1-9.



# Spectroscopic ellipsometry study of $\text{FA}_x\text{MA}_{1-x}\text{PbI}_3$ hybrid perovskite single crystals

Maria Isabel Alonso,<sup>1,a)</sup> Bethan Charles,<sup>2</sup> Adrián Francisco-López,<sup>1</sup> Miquel Garriga,<sup>1</sup> Mark T. Weller,<sup>2</sup> and Alejandro R. Goñi<sup>1,3</sup>

<sup>1</sup>Institut de Ciència de Materials de Barcelona, ICMA-B-CSIC, Campus de la UAB, 08193 Bellaterra, Spain

<sup>2</sup>Department of Chemistry and Centre for Sustainable Chemical Technologies, University of Bath, Claverton Down, Bath BA2 7AY, United Kingdom

<sup>3</sup>ICREA, Passeig Lluís Companys 23, 08010 Barcelona, Spain

(Received 26 July 2019; accepted 9 September 2019; published 30 September 2019)

Organic-inorganic hybrid perovskites have the generic formula  $\text{ABX}_3$ , where X denotes a halide anion and A and B stand for an organic and a metal cation, respectively. These hybrid compounds are semiconductors with highly interesting and tunable properties. They are the subject of intense research for several applications, mainly in solar cells but also as light-emitting diodes and lasers. Tunability of the optical properties may be accomplished by site-substituted solid solutions in A, B, or X sites. In particular, some mixed-cation systems show increased stability for these applications. In this work, the authors report on the variation of the optical constants in mixed A-site cation methylammonium/formamidinium (MA/FA) lead iodide perovskites  $\text{FA}_x\text{MA}_{1-x}\text{PbI}_3$  evaluated by spectroscopic ellipsometry in single crystal samples. The two main polymorphs of  $\text{FAPbI}_3$  are measured. The study is complemented by photoluminescence measurements to gain a better insight into observed spectroscopic features related to the electronic interband transitions of the crystals and their structural integrity. The main result is a continuous variation of the pseudocubic perovskite band structure of the solid solutions between the two end compounds  $\text{MAPbI}_3$  and  $\alpha\text{-FAPbI}_3$ . Published by the AVS. <https://doi.org/10.1116/1.5121604>

## I. INTRODUCTION

Hybrid perovskites  $\text{ABX}_3$ , where X denotes a halide anion and A and B stand for an organic and a metal cation, respectively, are semiconductors that show promise for several optoelectronic applications. The most widespread research is in the field of photovoltaics motivated by the quick improvements in efficiency<sup>1,2</sup> with a record efficiency at present<sup>3</sup> above 25%. Materials of this class also display excellent properties suitable for other applications such as light emitters or detectors.<sup>4-7</sup> For all these applications, knowledge of the optical properties is both of fundamental and practical interest. Spectroscopic ellipsometry (SE) provides detailed experimental knowledge of electronic transitions which can be related to specific aspects of band structure calculations. In addition, values of the optical constants determined by SE enable the design and optimization of light harvesting and out-coupling in solar cells and other devices.<sup>8</sup> One of the main drawbacks of hybrid perovskites are structural changes due to degradation or crystalline phase instabilities.<sup>9,10</sup> Although for applications thin films are employed, studies on single crystals allow for an improved understanding of many properties, among them the optical constants, due to the better quality of samples for structural and optical studies.<sup>11</sup>

Here, we focus on the optical spectra of  $\text{FA}_x\text{MA}_{1-x}\text{PbI}_3$  solid solution single crystals by SE. The improved stability of some of these mixed organic-cation crystals compared to the workhorse compound methylammonium lead iodide ( $\text{MAPbI}_3$ )

makes them interesting. The detailed structural phase behavior of the solid solutions and the near-bandgap absorption have been well determined.<sup>12,13</sup> In contrast, the optical spectra at higher energies have not been studied and, in particular, that of the end compound formamidinium lead iodide ( $\text{FAPbI}_3$ ) is not well established. One possible cause for this is the difficulty to stabilize its perovskite *black* phase at room temperature,  $\alpha\text{-FAPbI}_3$ , versus the hexagonal *yellow* phase  $\delta\text{-FAPbI}_3$ .<sup>12,14,15</sup> Three previous investigations by SE of thin films of  $\text{FAPbI}_3$  have reported on the optical constants of the  $\alpha$  phase<sup>16-18</sup> showing differing results in terms of both observed higher electronic transitions and absolute values of the optical constants. In contrast, only one of these SE investigations<sup>17</sup> reports on the measurement on a thin film of the stable  $\delta$  phase, probably because of its wide bandgap and limited practical interest for applications.

In this work, we study the variation of the optical constants in single crystal samples of mixed A-site cation  $\text{FA}_x\text{MA}_{1-x}\text{PbI}_3$  perovskites as measured and evaluated by SE. We analyze the observed electronic transitions as a function of organic-cation composition  $x$ , obtained by fitting the numerically built second derivatives of the dielectric function. We discuss the results in combination with photoluminescence measurements. In particular, we examine the spectra of the two pure organic cation end compounds in comparison with previous reports.<sup>16-19</sup>

## II. EXPERIMENTAL DETAILS

### A. Sample preparation

The samples used in this study were single crystals with dimensions large enough for ellipsometry measurements, at

Note: This paper is part of the Conference Collection: 8th International Conference on Spectroscopic Ellipsometry 2019, ICSE.

<sup>a)</sup>Electronic mail: isabel@icmab.es

least in millimeter range, grown by inverse solubility crystallization in  $\gamma$ -butyrolactone.<sup>20</sup> Reference 12 contains full details of the precursor synthesis and the reaction compositions. The resultant crystal sizes tended to decrease in solid solutions with large FA contents and some compositions ( $x = 0.8, 0.9$ ) could not be measured. Special effort was made for  $x = 1$  to obtain good quality large FAPbI<sub>3</sub> crystals, since the corresponding optical functions of this pure end compound are not well known.

## B. SE measurements and fitting

Ellipsometric spectra were measured at several angles of incidence with a Sopralab GESSE rotating polarizer ellipsometer using the microspot option. We attempted to detect optical anisotropy in some noncubic crystals (e.g., MAPbI<sub>3</sub> and the MA-rich alloys are tetragonal at room temperature) by measuring the SE data at different orientations of the single crystals, including different in-plane azimuths and different faces. The detected differences were rather small and of the order of differences also seen even at different points of the same large crystal. These variations could be likely originated in irregular surface conditions, in any case, we could not reliably establish any optical anisotropy within our experimental error. Therefore, all the samples were considered as optically isotropic in the analysis regardless of their crystal symmetry. The *true* dielectric functions of the bulk crystals were deduced by considering a roughness overlayer calculated by a standard effective medium approximation of 50% material and 50% voids.<sup>21</sup> More details about the effect of the roughness and a comparison with the typical surface morphology of the crystals is given as supplementary material.<sup>34</sup> The dielectric functions were obtained by regression analysis without imposing any analytical model, the only structural unknown parameter was the surface roughness layer thickness. The numerical inversion result was smoothed by cubic splines.<sup>22</sup> The SE data and regression analysis results are included in the SI as well. The electronic transition parameters were analyzed by numerically building second derivatives of the dielectric function and fitting the observed features by critical point lineshapes.<sup>9,23</sup>

## C. Photoluminescence measurements

The PL spectra were excited with the 633 nm line of a He-Ne laser at very low incident light power density below 15 W/cm<sup>2</sup> to avoid any photodegradation or thermal damage of the samples by the laser. Spectra as a function of temperature from 10 to 365 K were measured using a gas-flow cryostat from CryoVac that fits under the microscope using a 20 $\times$  long working distance objective with NA = 0.35 and dispersed with a high-resolution LabRam HR800 grating spectrometer equipped with a charge-coupled device detector. PL spectra were corrected for the spectral response of the spectrometer by normalizing each spectrum using the detector and the 600 grooves/mm grating characteristics.

## III. OPTICAL SPECTRA OF FA<sub>x</sub> MA<sub>1-x</sub>PbI<sub>3</sub>

In this section, we discuss the measured values of optical constants in the solid solution series and their variation with the organic-cation composition  $x$ . The advantage of measuring single crystals is that the bulk structure is well determined, whereas thin films are polycrystalline and prone to contain some porosity, which affects the value of the optical constants, as is known from the case of MAPbI<sub>3</sub> (Ref. 9) and other hybrid perovskites.<sup>24</sup> Even in bulk single crystals, there is uncertainty in the absolute values due to the correction of surface imperfections, i.e., roughness or overlayers of the as-grown crystal facets. In any case, by now the values for MAPbI<sub>3</sub> are rather well established,<sup>19</sup> whereas, in contrast, those for FAPbI<sub>3</sub> are more uncertain.

Furthermore, formamidinium lead iodide has two main polymorphs<sup>12,14,15</sup> with very different optical properties: The photoactive *black*  $\alpha$ -FAPbI<sub>3</sub> phase and the nonperovskite hexagonal *yellow* phase  $\delta$ -FAPbI<sub>3</sub>. The black phase is metastable at room temperature and depending on the sample environment it transforms slower or faster to the yellow phase.<sup>25</sup> We measured SE spectra of both phases using the same crystal. The transformation from yellow to black could be quickly induced by heating the crystal on a hotplate to about 80 °C for several minutes. After removing it from the hotplate, SE measurements were immediately performed. In fact, no spectral changes could be detected for several hours in the clean room environment at 23 °C ambient temperature and 28% relative humidity in agreement with previous observations of large thermal hysteresis of the cubic-to-hexagonal phase transition.<sup>25</sup> Figure 1 shows

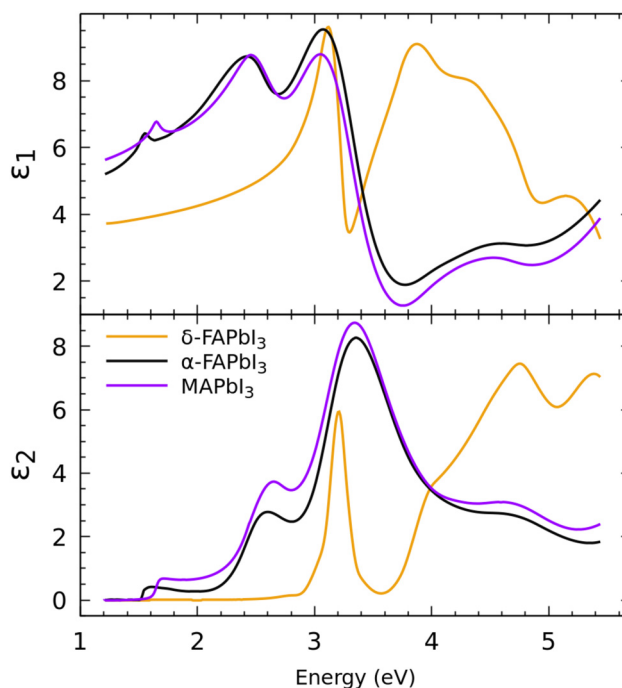


Fig. 1. Real ( $\epsilon_1$ ) and imaginary ( $\epsilon_2$ ) parts of the dielectric functions at room temperature determined for the two pure organic cation compositions. Both perovskite crystals (MAPbI<sub>3</sub> and  $\alpha$ -FAPbI<sub>3</sub>) display very similar spectra in contrast to that of the hexagonal phase  $\delta$ -FAPbI<sub>3</sub>.

the obtained dielectric functions of the pure end compositions. The roughness correction was chosen to render the minimum possible values of the imaginary part  $\epsilon_2$  at low energies, in the transparency region of the materials. The thickness of the rough layers needed for the analysis were 9 nm for the yellow phase and 12 nm for the black phase. These relatively large roughnesses are in the range of those previously found for MAPbI<sub>3</sub> and which produced valid results, also plotted for comparison. The slight roughness parameter increase from the initial crystal to the phase-transformed one correlates with a real worsening of the as-grown surfaces when the crystals undergo a phase transformation.

Compared with previous determinations of  $\alpha$ -FAPbI<sub>3</sub> optical functions in thin films, our results are most similar in value (somewhat higher) and spectral dependence to those reported by Ndione *et al.*<sup>16</sup> The values reported by Kato *et al.*<sup>17</sup> and Subedi *et al.*<sup>18</sup> were not very different but their spectra contained more transitions. In particular, Kato *et al.*<sup>17</sup> assigned the transitions based on a density functional theory (DFT) calculation. These authors also reported the  $\delta$ -FAPbI<sub>3</sub> optical functions, in their case, each phase was a different film deposited in different conditions. In this regard, the largest difference with our data is the refractive index that they determine for both films: they obtain about the same value for the  $\alpha$  and the  $\delta$  phase, whereas we obtain a much lower value for the  $\delta$  phase, as is evident from Fig. 1. This lower value of the real part  $\epsilon_1$  is more consistent in view of the much higher bandgap of  $\delta$ -FAPbI<sub>3</sub>, clearly seen as a pronounced excitonic peak at about 3.2 eV.

Except for the  $\delta$ -FAPbI<sub>3</sub>, all other measured single crystals were perovskite phases. The dielectric functions of the solid solutions determined from the measurements are presented in Fig. 2. No large differences in the optical spectra are observed as the composition varies; the most obvious

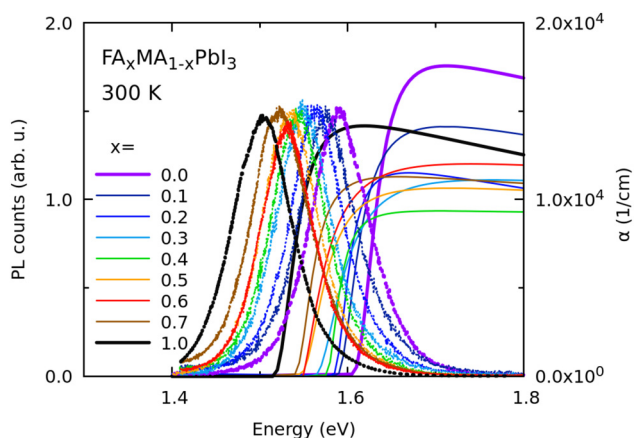


Fig. 3. Near-bandgap absorption and photoluminescence spectra at room temperature showing the concomitant redshift as FA content increases. The maximum intensities of the PL curves were arbitrarily rescaled to show the shifts more clearly. The curves that correspond to the two pure organic cation end compounds are plotted with thicker lines.

change is the bandgap redshift from low to high FA content, also visible in measurements of photoluminescence shown in Fig. 3 together with the absorption coefficient near the bandgap extracted from SE measurements. The highest absorption coefficients just above the bandgap are those of the pure end perovskite crystals. However, the observed absolute value fluctuations can be influenced by variations in crystalline quality and surface perfection that are difficult to control. Nevertheless, different crystals of the same composition usually lead to very close results. However, two different spectra for the mixed crystal with FA content  $x = 0.7$  are displayed in Fig. 2 that correspond to two crystals from different growth batches. In this case, the difference is intriguing, and thus, we investigated more closely this composition to cross

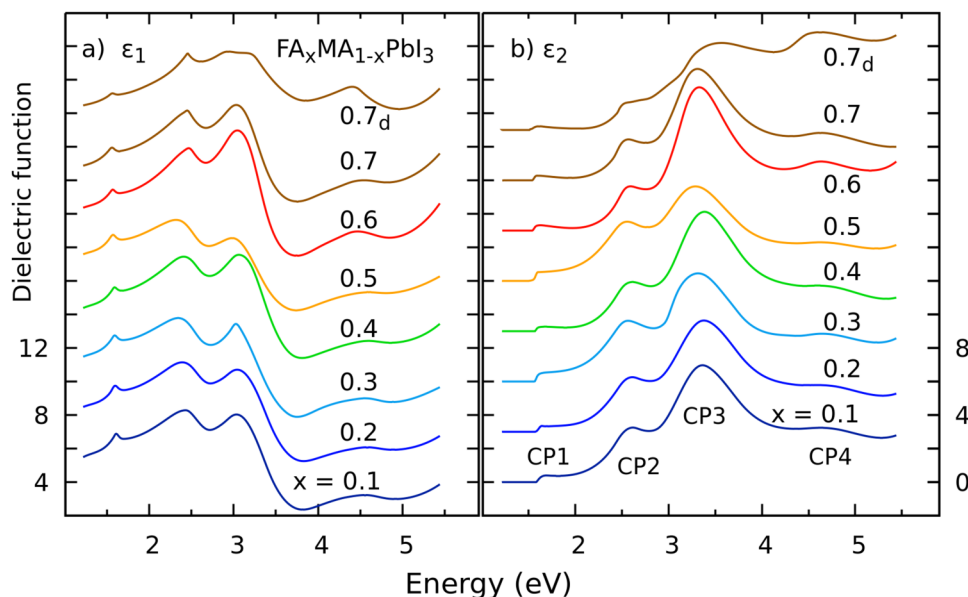


Fig. 2. Dielectric functions at room temperature determined for the measured solid solution  $\text{FA}_x\text{MA}_{1-x}\text{PbI}_3$  perovskites with compositions between  $x = 0.1$  and  $x = 0.7$ . The vertical scales are indicated for the lowest graphs and the rest are displaced for clarity. The two spectra displayed for the highest FA content  $x = 0.7$  correspond to two crystals from different growth batches. The label d stands for *defect* as explained in the text.



check the resulting spectra. Another motivation was that one clear extra peak is apparent near 3 eV in the uppermost spectrum. Note that this composition approximately delimits the region of perovskite phase stability<sup>10</sup> and above this value the FA containing perovskite could transform into the hexagonal phase so that a slight change in stoichiometry could cause the observed difference. We anticipate that we ruled out this possibility as it will be further discussed below.

#### IV. ELECTRONIC TRANSITIONS IN $\text{FA}_x\text{MA}_{1-x}\text{PbI}_3$

In principle, all numerically obtained dielectric functions reported in this work can be parameterized using different analytic models. For  $\text{MAPbI}_3$  different parameterizations have been published. The spectra can be reproduced with the smallest parameter number by using critical point (CP) lineshapes<sup>9</sup> although some authors prefer a sum of Tauc-Lorentz (TL) oscillators<sup>26</sup> to enforce a vanishing value of the absorption coefficient below the bandgap. The drawback of this approach is that not all TL oscillators present in the model correspond to electronic transitions in contrast to the CP oscillators. From the point of view of suppressing the non-physical absorption below the bandgap, the CP model can be improved as shown by Leng *et al.*<sup>27</sup> However, to investigate the bandgap only, the TL model provides a physical representation giving the optical bandgap as well as the peak transition energy.<sup>28</sup> In this work, we apply the TL model to the bandgap region to retrieve the optical bandgap energy value. In addition, to determine the energies of all observed electronic transitions, we used the CP model to analyze the spectra by numerical derivatives.

Derivatives allow a more accurate determination of the CP parameters because the background is eliminated and at the same time CP structures become more pronounced. In this work, we have built numerical second derivatives using the smoothing polynomials method<sup>23,29</sup> to smooth out the experimental noise as much as possible without significant distortion of the spectral features. Therefore, the sharp gap transitions were analyzed separately from the rest of broader upper transitions. From previous study of  $\text{MAPbI}_3$  crystals,<sup>9</sup> it was found that zero-dimensional CPs represented well all transitions. Therefore, we chose 0D CPs for the regression analysis of the experimental numerical derivatives of all samples. The second derivative of the 0D theoretical lineshape is given by

$$\frac{d^2\epsilon(\omega)}{d\omega^2} = 2Ae^{i\varphi}(\hbar\omega - E_g + i\Gamma)^{-3}, \quad (1)$$

where  $A$  is the amplitude,  $\varphi$  is the phase,  $E_g$  is the transition energy, and  $\Gamma$  is the linewidth. Zero-dimensional transitions given by Eq. (1) are characteristic of excitons or localized excitations but also take place in the case of dispersionless electron-hole states, for example, when the effective masses of both electron and hole are large at the transition k-point and its vicinity, as was calculated for  $\text{MAPbI}_3$ .<sup>19</sup>

Figure 4 displays relevant second derivative spectra together with the fit results to illustrate both the similarities and the differences among the investigated samples. In general, the

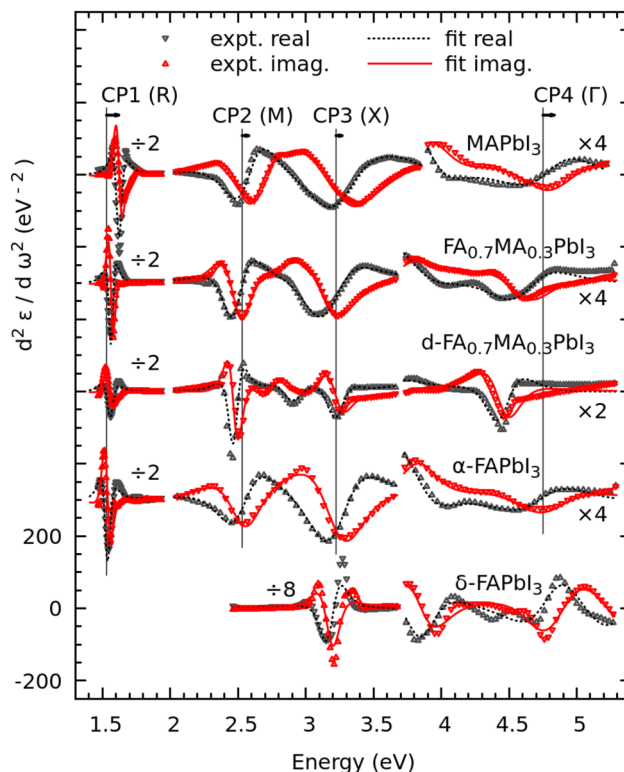


Fig. 4. Second derivative spectra for some relevant samples. One of the solid solution samples is distinguished by the label “d” meaning defect. The vertical scale is indicated for the lowest graph ( $\delta\text{-FAPbI}_3$ ) and the rest are displaced for clarity but keeping the same proportions with the indicated scale factors. Vertical lines are drawn at the main fitted critical point energies for  $\alpha\text{-FAPbI}_3$  and their shifts with respect to  $\text{MAPbI}_3$  are indicated by arrows. These main critical points were assigned in  $\text{MAPbI}_3$  to transitions from the upper valence band to the lower conduction band at different symmetry points of the pseudocubic Brillouin zone<sup>19</sup> noted by labels.

spectra of perovskite phases (in the figure  $\text{MAPbI}_3$ ,  $\alpha\text{-FAPbI}_3$ , and the pristine  $x = 0.7$  crystal) are indeed rather alike. The main critical point energies obtained from the fits are indicated and labeled using the assignments obtained from electronic structure calculations.<sup>19</sup> Four main CPs were identified from the calculations at the four main symmetry points of the pseudocubic Brillouin zone: The fundamental gap, CP1, at the R point, and the upper gaps CP2 at the M point, CP3 at the X point, and CP4 at the  $\Gamma$  point. The dependence with composition of these CPs is plotted in Fig. 5. Our experimental results indicate that the optical spectra of all  $\text{FA}_x\text{MA}_{1-x}\text{PbI}_3$  including  $\alpha\text{-FAPbI}_3$  are very similar although slightly shifted, suggesting that the electronic band structures are basically coincident with some small corrections that progressively evolve to give the continuous redshift as  $x$  increases. The fitted linewidths do not depend on composition, there are some variations but no definite trend. The lowest energy CP1, the fundamental bandgap, is the sharpest and is around 50 meV broad independently of the sample composition. The total energy shift, represented in Fig. 5(a), is about 90 meV. Note that the fitted errors for the energies are much smaller than the linewidth in the range of 3 meV. Different values are plotted for each composition; the highest value is always given by the value CP1 (fit of the second derivative), and the lowest one the optical gap energy

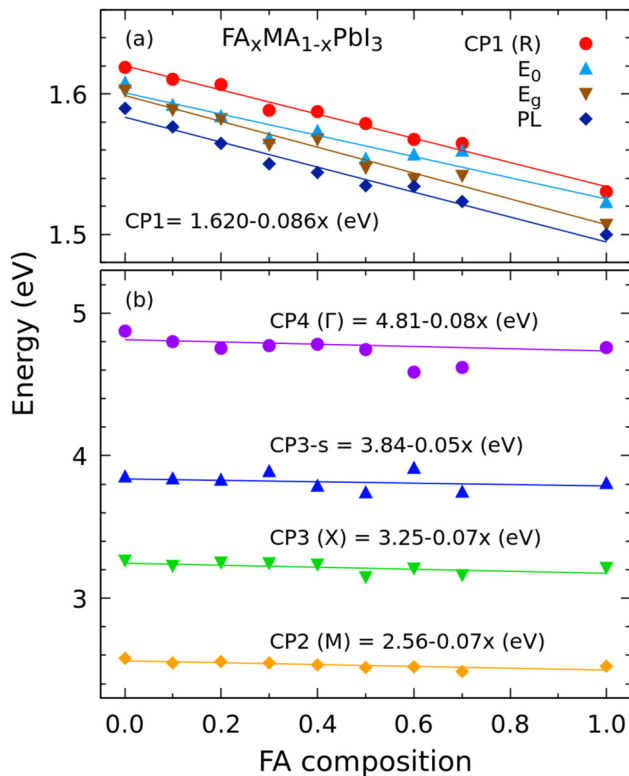


FIG. 5. Electronic interband transitions as a function of composition. (a) Fundamental bandgap energies found from different analyses. Circles display results from fitting the second derivative spectra with 0D CPs. The dielectric function spectra fitted with a TL oscillator give the optical bandgap ( $E_g$ , down-triangles) and the transition energies ( $E_0$ , up-triangles). For comparison, PL peak positions are displayed by squares. The lines are linear fits to the data points. (b) Upper electronic transitions observed in second derivative spectra and fitted with 0D CPs. The assignments to k-points of the Brillouin zone correspond to the mainly identified contributions in band structure calculations.<sup>19</sup> The label CP3-s denotes the shoulder of the CP3 transition. The fitting errors are in all cases smaller than the size of the symbols. The lines are linear fits to the data points.

( $E_g$ ) fitted from the TL lineshape. The difference between these two values is about 20 meV. The PL peak shows an additional Stokes shift of about 10 meV.

The upper transitions plotted in Fig. 5(b) also show a progressive redshift that is between 50 and 90 meV in all cases. For these transitions, the fitted linewidths are much broader and even if there are differences among samples they are also roughly independent of composition. It is worth mentioning that the highest energy part of the UV spectrum is the most affected by the performed roughness correction, cf. Sec. III, and with it, the CP energies of rougher samples (here,  $x = 0.6, 0.7$  and mainly CP4) have an added uncertainty. We also point out that this fact has no effect on the fitted linewidths. Linewidth variations may be indicative of crystal-line quality. In general, sharper transitions are taken to mean better quality. For these samples, this assertion is true referred to the bandgap, CP1. In contrast, we must be aware that this is not necessarily true for the higher energy transitions, in particular, extended defects in the crystals may also lead to sharper higher energy transitions. For good quality crystals, the width for CP2 is about 250 meV and the error in the fitted energies is typically 10 meV. For CP3, the width is

about 400 meV and the error in fitted energies about 20 meV. There is a shoulder to CP3 resolved in the second derivative with a similar width but larger error in its energy determination, about 40 meV. Finally, CP4 is the broadest, about 500 meV but rather well determined, energy fitting errors are about 30 meV. Since the widths of all these electronic transitions do not show definite trends with solid solution composition, we conclude that the electronic structure is mostly given by the inorganic cage structure and the influence of the organic cation is relatively small in the system FA/MA, at least in terms of the electronic structures and their transition energies. In addition, our observations are consistent with a rather continuous change of the band structure and do not support differences in the bandstructures of the end compounds obtained from some calculations.<sup>17</sup>

## V. SIGNATURES OF DEFECTS IN $FA_x MA_{1-x}PbI_3$

From Fig. 4, we can easily compare the two different spectra measured for the mixed crystals with an FA content of  $x = 0.7$ . One of them differs from a typical perovskite sample and we label it accordingly as defect (d- $FA_{0.7}MA_{0.3}PbI_3$ ). In fact, the intensity of the bandgap transition in the derivative is clearly smaller than those of the other perovskites. As already mentioned, the width of all perovskite bandgaps fitted in this work is around 50 meV independently of the sample composition. In the atypical  $x = 0.7$  sample, it is both weaker (smaller amplitude) and broader (70 meV), probably indicating a worse crystal quality of the perovskite in this sample. It is relevant to comment on this because, in contrast, the upper transitions appear stronger and sharper than the ones observed in the perovskites, as is typical of structures with weakly interacting  $[PbI_6]^{4-}$  octahedra, such as  $PbI_2$ , hydrated  $MAPbI_3$ , and  $\delta$ -FAPbI<sub>3</sub>. Note that the energies of the peaks are rather similar in both samples except for the feature near 2.9 eV. Some extra peaks were found in previous reports of the dielectric function of  $\alpha$ -FAPbI<sub>3</sub>.<sup>17,18</sup> In particular, a transition reported at 3.04 eV (Ref. 17) is quite analogous to this extra peak and it does not appear in our  $\alpha$ -FAPbI<sub>3</sub> crystal. This led us to the conclusion that those  $\alpha$ -FAPbI<sub>3</sub> films must have had defects similar to our d- $FA_{0.7}MA_{0.3}PbI_3$  crystal. It is difficult to identify which kind of defect could give rise to such strong features in the upper electronic transition spectrum. In principle, it could correspond to some other component phase or phases. For comparison, the derivative of  $\delta$ -FAPbI<sub>3</sub> is also plotted in Fig. 4. In this case, all transitions are strong and sharp but do not coincide with those observed in our atypical  $x = 0.7$  crystal or the reported  $\alpha$ -FAPbI<sub>3</sub>;<sup>17,18</sup> therefore, we should discard as explanation that some  $\delta$  phase is present in these samples. Actually, it seems clear that the second derivative spectrum of d- $FA_{0.7}MA_{0.3}PbI_3$  is not composed by a perovskite part with additional superimposed peaks from another phase. Instead, the anomalous upper spectrum seems likely to arise from some kind of structural variation that leads to weaker interactions of the  $[PbI_6]^{4-}$  octahedra. We should also mention that the pristine  $x = 0.7$  crystal was quite stable and these peaks did not appear even after several months, in agreement with the fact that the different structure

of the anomalous crystal was formed during growth and was not a degradation product. This stresses the importance of the growth conditions to obtain perfect perovskite samples, either single crystal or films. The main difference in the crystallization processes of both  $x = 0.7$  crystals which we are aware of was a higher temperature heating of the solutions in the case of the d-FA<sub>0.7</sub>MA<sub>0.3</sub>PbI<sub>3</sub> crystal that probably degraded the FA and even more the less stable MA ions in the precursor solution and their incorporation into the structure was affected.

In order to obtain further insight of the defect structure, we have measured PL as a function of temperature. Selected spectra of the d-FA<sub>0.7</sub>MA<sub>0.3</sub>PbI<sub>3</sub> crystal are shown in Fig. 6. The different colors denote two sets of measurements performed at two different spots on the sample, separated by several tens of micrometers (spot diameter ca. 4 μm). At room temperature, a single broad PL peak is observed. However, for one of the series and as temperature is lowered, the sharpening of the linewidth allows one to observe two PL lines with variable intensity, whereas for the other series only one peak remains (see Fig. 6). The ratio of intensities of the peaks is very influenced by the exact point on the sample and by changing the temperature we could not avoid small displacements of the measurement points. Hence, the relative intensities cannot be interpreted. However, the energy positions of these lines are well determined regardless of the measured point and seem to indicate two different compositions. Note that, for a pristine crystal of this composition, only one line is seen at each temperature.<sup>13</sup> These results clearly

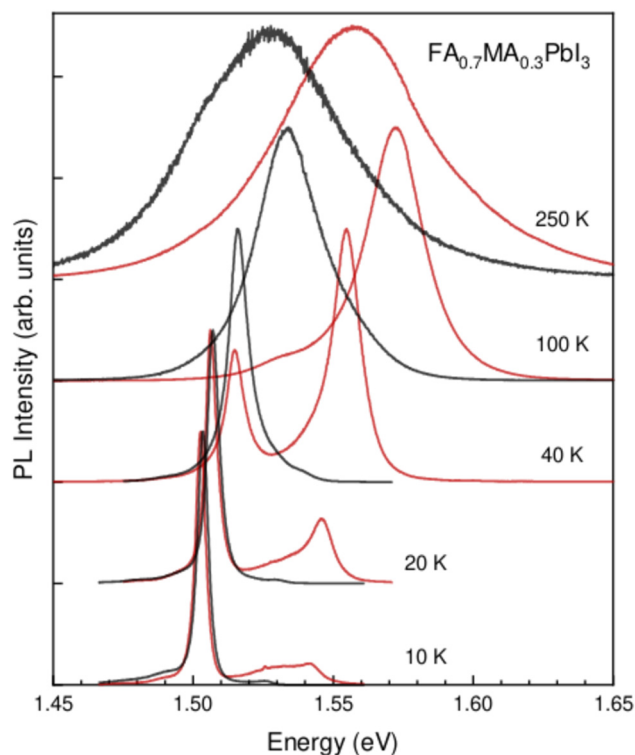


Fig. 6. Photoluminescence spectra as a function of temperature for the d-FA<sub>0.7</sub>MA<sub>0.3</sub>PbI<sub>3</sub> crystal. The two sets of curves are measured by focusing the laser at two different spots on the sample.

show that the crystal is inhomogeneous. On the one side, different spectra can be observed at different points. On the other side, two PL peaks at well determined energies are observed regardless of the point. The difference in energy between the peaks is about 30–40 meV, which can mean a composition change of  $x \sim 0.3$ – $0.4$ . We actually ascribe these two peaks to two compositions, that is, this sample contains segregated FA-richer and MA-richer regions although the average broader bandgap observed by SE corresponds to the nominal  $x = 0.7$  FA content. Note that, for the splitting to be resolved, low temperature measurements are needed and probably a better spatial resolution than that given by the microspot (spot diameter ca. 100 μm) in SE. The exact compositions of the segregated phases cannot be reliably determined because of the strain induced by defects in these regions and the strain-dependence of the PL energy positions.<sup>11</sup> The non-monotonous dependence of the bandgap energy with temperature is influenced by different contributions, in particular, for intermediate  $x$  the change from blue to red-shift observed in Fig. 6 seems to be due to the evolution of tilting of the PbI<sub>6</sub> octahedra in the crystal structure and the changing contribution of the thermal expansion term.<sup>30</sup> This point is still under evaluation and the complete phase diagram with composition and temperature for these alloys will be published elsewhere.<sup>13</sup>

Considering both the PL and the ellipsometry results together, the picture that emerges is that this sample consists of FA/MA segregated perovskite domains that determine the near-bandgap PL and absorption. These domains are spatially separated. However, the presence of these segregated phases does not explain the observation of some sharp higher energy electronic transitions. To understand them, we speculate that between the segregated domains there must be surrounding regions in which internal structural deformations can suppress the interactions of the normal perovskite structure. Such suppression is probably caused by high concentration of vacancies. Local structural changes can be created by both organic-cation (predominantly MA) or iodide vacancies,<sup>31–33</sup> usually present in lower concentrations. This is a possible and most plausible explanation to reconcile all observations in this case, in particular the sharp electronic transitions observed in SE at higher energies.

## VI. CONCLUSIONS

The dielectric functions of FA<sub>*x*</sub>MA<sub>1–*x*</sub>PbI<sub>3</sub> single crystals have been studied in the whole concentration range  $x$ . As-grown crystal facets were measured without further preparation and the measurements were corrected for surface roughness or overlayer effects to determine the true values. Although some compositions crystallize in anisotropic symmetries, no optical anisotropy could be determined and all samples have been considered isotropic. Based on these premises, the results for the best crystals were reported. The two end compositions  $x = 0$  and  $x = 1$  gave rather similar results in terms of values of optical constants for the perovskite structure with values of the absorption coefficient just above the



bandgap slightly larger for MAPbI<sub>3</sub> [ $\alpha \sim 1.8 \times 10^4$  (1/cm)] than for FAPbI<sub>3</sub> [ $\alpha \sim 1.4 \times 10^4$  (1/cm)].

The influence of the organic cation is not only visible as a redshift of the band gap energy from  $x = 0$  to  $x = 1$  but also of all upper transitions. In fact, our observations are consistent with a rather progressive *nearly rigid* shift of the entire band structure.

Also, the complete upper spectrum and specially the second derivative is very sensitive to the presence of structural deformations or other phases. The region of the bandgap shows mainly the normal perovskite regions which are characterized by relatively broad higher energy electronic transitions. Sharper higher energy peaks are more characteristic of crystal structures with weaker interactions in the lead-iodide framework. We believe that the ones we have observed here provide signatures of such suppressed interactions due to internal structural deformations originated in boundary phases between segregated regions which contain numerous vacancies.

## ACKNOWLEDGMENTS

The authors gratefully acknowledge Oliver J. Weber and Mariano Campoy-Quiles for their helpful comments. The Spanish Ministerio de Ciencia, Innovación y Universidades is acknowledged for its support through Grant No. SEV-2015-0496 in the framework of the Spanish Severo Ochoa Centre of Excellence program and through Grant Nos. MAT2015-70850-P (HIBRI2) and PGC2018-095411-B-I00 (RAINBOW). The authors also acknowledge the AGAUR for Grant No. 2017-SGR-00488. B.C. acknowledges the Engineering and Physical Sciences Research Council (EPSRC) for Ph.D. studentship funding via the CSCT CDT (No. EP/G03768X/1). A.F.L. acknowledges the Ph.D. program in Materials Science from Universitat Autònoma de Barcelona in which he is enrolled and an FPI fellowship (No. BES-2016-076913) from the Spanish Ministerio, co-financed by the European Social Fund.

<sup>1</sup>M. Grätzel, *Acc. Chem. Res.* **50**, 487 (2017).

<sup>2</sup>J. J. Yoo et al., *Energy Environ. Sci.* **12**, 2192 (2019).

<sup>3</sup>*Best Research-Cell Efficiency Chart*, National Renewable Energy Laboratory (NREL), Golden, Colorado, 2019, see [www.nrel.gov/pv/cell-efficiency.html](http://www.nrel.gov/pv/cell-efficiency.html).

<sup>4</sup>Z.-K. Tan et al., *Nat. Nanotechnol.* **9**, 687 (2014).

<sup>5</sup>S. D. Stranks and H. J. Snaith, *Nat. Nanotechnol.* **10**, 391 (2015).

<sup>6</sup>B. R. Sutherland and E. H. Sargent, *Nat. Photon.* **10**, 295 (2016).

<sup>7</sup>F. P. Garcia de Arquer, A. Armin, P. Meredith, and E. H. Sargent, *Nat. Rev. Mater.* **2**, 16100 (2017).

<sup>8</sup>H. Fujiwara, N. J. Podraza, M. I. Alonso, M. Kato, K. Ghimire, T. Miyadera, and M. Chikamatsu, "Organic-inorganic hybrid perovskite solar cells," in *Spectroscopic Ellipsometry for Photovoltaics. Volume 1: Fundamental Principles and Solar Cell Characterization*, edited by H. Fujiwara and R. W. Collins (Springer, Cham, 2018), pp. 463–507.

<sup>9</sup>A. M. A. Leguy et al., *Chem. Mater.* **27**, 3397 (2015).

<sup>10</sup>B. Charles, J. Dillon, O. J. Weber, M. S. Islam, and M. T. Weller, *J. Mater. Chem. A* **5**, 22495 (2017).

<sup>11</sup>A. Francisco-López, B. Charles, O. J. Weber, M. I. Alonso, M. Garriga, M. Campoy-Quiles, M. T. Weller, and A. R. Goñi, *J. Phys. Chem. C* **122**, 22073 (2018).

<sup>12</sup>O. J. Weber, B. Charles, and M. T. Weller, *J. Mater. Chem. A* **4**, 15375 (2016).

<sup>13</sup>A. Francisco-López, B. Charles, M. I. Alonso, M. Garriga, M. T. Weller, and A. R. Goñi, "Complete phase diagram of methylammonium/formamidinium lead iodide perovskite solid solutions from temperature dependent photoluminescence and Raman spectroscopy" (unpublished).

<sup>14</sup>A. Binek, F. C. Hanusch, P. Docampo, and T. Bein, *J. Phys. Chem. Lett.* **6**, 1249 (2015).

<sup>15</sup>Q. Han et al., *Adv. Mater.* **28**, 2253 (2016).

<sup>16</sup>P. F. Ndione, Z. Li, and K. Zhu, *J. Mater. Chem. C* **4**, 7775 (2016).

<sup>17</sup>M. Kato, T. Fujiseki, T. Miyadera, T. Sugita, S. Fujimoto, M. Tamakoshi, M. Chikamatsu, and H. Fujiwara, *J. Appl. Phys.* **121**, 115501 (2017).

<sup>18</sup>B. Subedi, L. Guan, Y. Yu, K. Ghimire, P. Uprety, Y. Yan, and N. J. Podraza, *Sol. Energ. Mater. Sol. Cells* **188**, 228 (2018).

<sup>19</sup>A. M. A. Leguy et al., *Nanoscale* **8**, 6317 (2016).

<sup>20</sup>M. I. Saidaminov et al., *Nat. Commun.* **6**, 7586 (2015).

<sup>21</sup>D. E. Aspnes, "The accurate determination of optical properties by ellipsometry," in *Handbook of Optical Constants of Solids*, edited by E. D. Palik (Academic, New York, 1985), Vol. 1, Chap. 5, pp. 89–112.

<sup>22</sup>M. Garriga, M. I. Alonso, and C. Domínguez, *Phys. Stat. Sol. B* **215**, 247 (1999).

<sup>23</sup>M. I. Alonso and M. Garriga, "Optical properties of semiconductors," in *Spectroscopic Ellipsometry for Photovoltaics: Volume 1: Fundamental Principles and Solar Cell Characterization*, edited by H. Fujiwara and R. W. Collins (Springer, Cham, 2018), pp. 89–113.

<sup>24</sup>M. S. Alias, I. Dursun, M. I. Saidaminov, E. M. Diallo, P. Mishra, T. K. Ng, O. M. Bakr, and B. S. Ooi, *Opt. Express* **24**, 16586 (2016).

<sup>25</sup>T. Chen et al., *Sci. Adv.* **2**, e1601650 (2016), see <https://advances.sciencemag.org/content/2/10/e1601650.full.pdf>.

<sup>26</sup>M. Shirayama et al., *Phys. Rev. Appl.* **5**, 014012 (2016).

<sup>27</sup>J. Leng, J. Opsal, H. Chu, M. Senko, and D. E. Aspnes, *Thin Solid Films* **313–314**, 132 (1998).

<sup>28</sup>G. E. Jellison and F. A. Modine, *Appl. Phys. Lett.* **69**, 371 (1996).

<sup>29</sup>P. Lautenschlager, M. Garriga, S. Logothetidis, and M. Cardona, *Phys. Rev. B* **35**, 9174 (1987).

<sup>30</sup>A. Francisco-López, B. Charles, O. J. Weber, M. I. Alonso, M. Garriga, M. Campoy-Quiles, M. T. Weller, and A. R. Goñi, *J. Phys. Chem. Lett.* **10**, 2971 (2019).

<sup>31</sup>M. Pazoki, M. Wolf, T. Edvinsson, and J. Kullgren, *Nano Energy* **38**, 537 (2017).

<sup>32</sup>A. Oranskaia, J. Yin, O. M. Bakr, J.-L. Brédas, and O. F. Mohammed, *J. Phys. Chem. Lett.* **9**, 5474 (2018).

<sup>33</sup>D. Meggiolaro and F. De Angelis, *ACS Energy Lett.* **3**, 2206 (2018).

<sup>34</sup>See supplementary material at <http://dx.doi.org/10.1116/1.5121604> for details on surface roughness including an evaluation by AFM, the ellipsometric data and regression analysis results for all measured compositions, and different dielectric function parameterizations for the end compositions.



**Supplementary Information for: Spectroscopic Ellipsometry Study of  
FA<sub>x</sub>MA<sub>1-x</sub>PbI<sub>3</sub> Solid Solution Hybrid Perovskite Single Crystals:**

Maria Isabel Alonso,<sup>1</sup> Bethan Charles,<sup>2</sup> Adrián Francisco-López,<sup>1</sup> Miquel Garriga,<sup>1</sup>  
Mark T. Weller,<sup>2</sup> and Alejandro R. Goñi<sup>1,3</sup>

<sup>1</sup>*Institut de Ciència de Materials de Barcelona, ICMA-B-CSIC, Campus de la UAB,  
08193 Bellaterra, Spain<sup>a)</sup>*

<sup>2</sup>*Department of Chemistry and Centre for Sustainable Chemical Technologies,  
University of Bath, Claverton Down, Bath, UK*

<sup>3</sup>*ICREA, Passeig Lluís Companys 23, 08010 Barcelona, Spain*

---

<sup>a)</sup>Electronic mail: isabel@icmab.es.

## I. FIGURE LIST

### Figs. S1 – S3 :

Effect of roughness on the determination of the optical constants and roughness evaluation by AFM.

### Figs. S4 – S14 :

Ellipsometric data and regression analysis results for all measured compositions.

### Figs. S15 – S17 :

Different dielectric function parameterizations for the main end compositions.

## II. TABLE LIST

### Table SI :

Roughness parameters evaluated from Atomic Force Microscopy in a MAPbI<sub>3</sub> crystal .

### Tables SII – SIV :

Values of parameters related to the dielectric function of MAPbI<sub>3</sub> and the observed critical points.

### Tables SV – SVII :

Values of parameters related to the dielectric function of  $\alpha$ -FAPbI<sub>3</sub> and the observed critical points.

### Tables SVIII – SX :

Values of parameters related to the dielectric function of  $\delta$ -FAPbI<sub>3</sub> and the observed critical points.

## III. ELLIPSOMETRY SPECTRA OF FA<sub>x</sub>MA<sub>1-x</sub>PBI<sub>3</sub>

The measurements were made in a rotating-polarizer type ellipsometer in which the signal is given by:

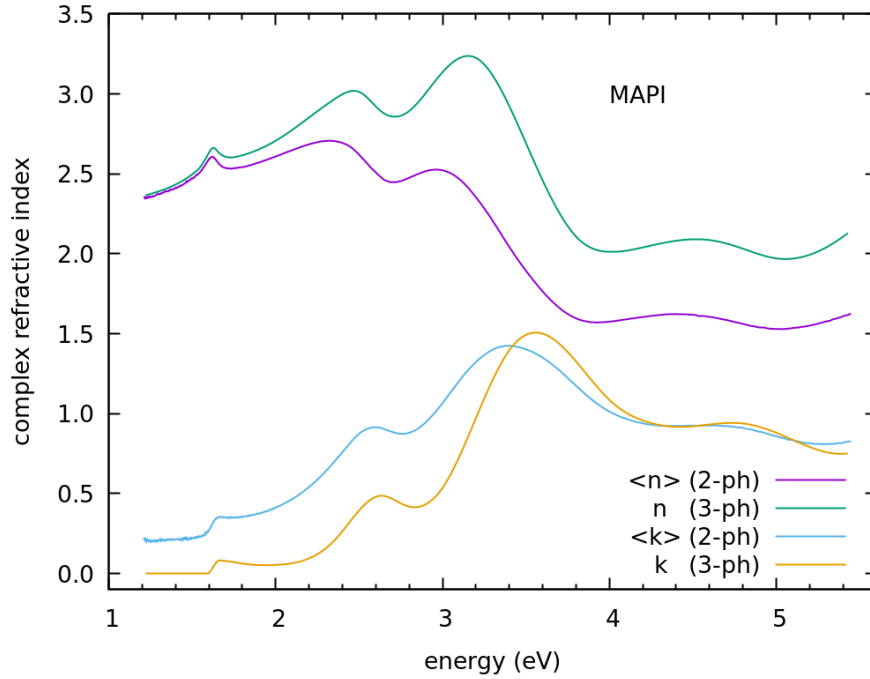
$$I = I_0(1 + \alpha \cos 2\omega_p t + \beta \sin 2\omega_p t), \quad (1)$$

where  $\omega_p$  is the polarizer rotation frequency and  $\alpha$  and  $\beta$  are the Fourier coefficients. These coefficients are the measured magnitudes that we chose to fit in this work.

The frequently used ellipsometric parameters  $\tan \psi$  and  $\cos \Delta$  that are related to the complex reflectance ratio  $\tilde{\rho} = \tan \psi \exp(i\Delta)$  can be calculated from the Fourier coefficients according to:

$$\tan \psi = |\tan A| \sqrt{\frac{1 + \alpha}{1 - \alpha}}, \quad \cos \Delta = \frac{\beta}{\sqrt{1 - \alpha^2}}, \quad (2)$$

where  $A$  is the angle of the fixed analyzer used in the measurement. All presented spectra are measured with  $|A| = 20^\circ$  and at least three angles of incidence ( $65^\circ$ ,  $67.5^\circ$ , and  $70^\circ$ ).



**Figure S1:** Effect of the roughness on the complex refractive index components of  $\text{MAPbI}_3$  as evaluated in this work. The two-phase values are the pseudorefractive index  $\langle \tilde{n} \rangle = \langle n \rangle + i\langle k \rangle$  and the three-phase values or "true" values  $\tilde{n} = n + ik$  take into account the roughness layer.

The dielectric function of an isotropic bulk sample in air using the two-phase model (air/sample) is given by:

$$\langle \tilde{\epsilon} \rangle = \langle \tilde{n} \rangle^2 = \left( \frac{1 - \tilde{\rho}}{1 + \tilde{\rho}} \right)^2 \tan^2 \phi \sin^2 \phi + \sin^2 \phi, \quad (3)$$

where  $\phi$  is the angle of incidence. The optical quantities written in brackets are referred to as "pseudovalues" for which no roughness or overlayer is taken into account. To stress the importance of considering the correction or three-phase model (air/overlayer/sample) we show in Fig. S1 the effect of the roughness layer on the complex refractive index. In the region where the bulk is transparent, that is, below the band gap, the effect of a transparent overlayer on the measured spectra is essentially the appearance of a spurious absorption, whereas the measured refractive index is almost unaffected.<sup>1</sup> This is obviously the case as illustrated in Fig. S1. We use this fact to determine an overlayer thickness in this region by trying to minimize the fitted value of  $k$ . We assume that the overlayer is a roughness layer but it could also be of another nature, the

**Table SI:** Roughness average ( $R_a$ ) and root mean square roughness ( $R_q$ ) for the surface of MAPbI<sub>3</sub> crystal.

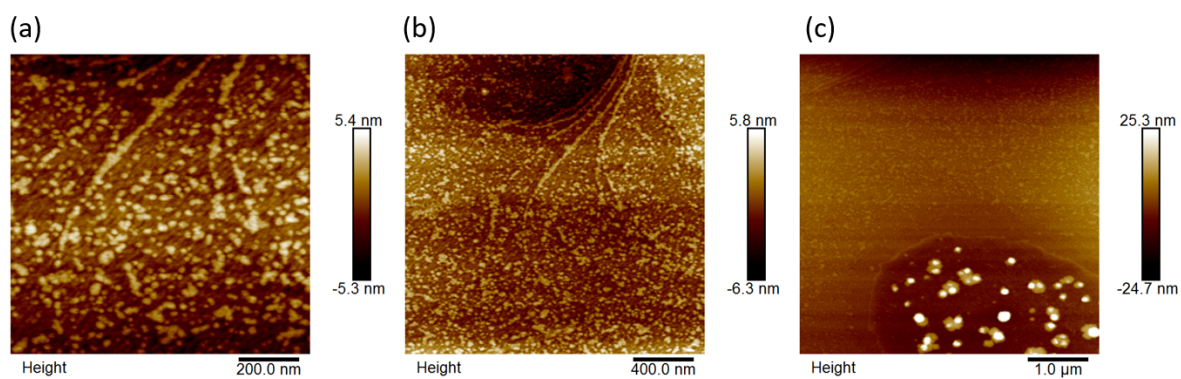
| Area of interest  | $R_a$ (nm) | $R_q$ (nm) |
|-------------------|------------|------------|
| $1 \mu\text{m}^2$ | 1.25       | 1.58       |
| $2 \mu\text{m}^2$ | 1.31       | 1.64       |
| $5 \mu\text{m}^2$ | 4.40       | 6.07       |

obvious example is Silicon and its oxide. However, possible overlayers for hybrid perovskites are usually compounds that show sharp absorption peaks in the visible or near UV. Since no trace of these peaks is seen in Fig. S1, we consider the simplest possibility for the correction, i.e., surface roughness. The assumed roughness model is also the simplest possible: We consider an effective medium model (Bruggeman approximation) and we choose to fix both the geometry (spherical) and the void fraction ( $x = 0.5$ ). Since the thickness of the roughness layer and the mentioned parameters are correlated in a fit, the number we quote as roughness may not be quite reliable because it could vary by changing the roughness model. But this didn't essentially affect the substrate. Hence, we believe that this procedure gives the best dielectric function value which is attainable in the present experiment.

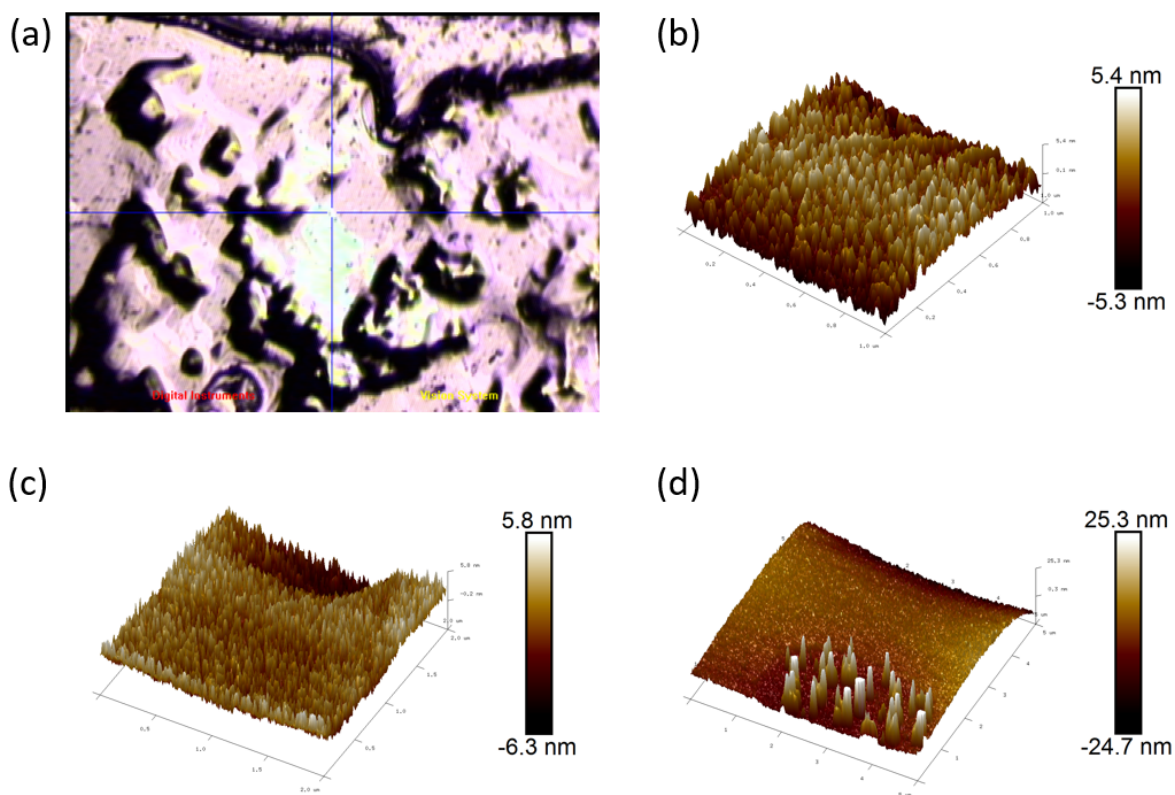
As a comparison for the obtained thickness of the rough layer, Atomic Force Microscopy (AFM) imaging was performed using a Digital Instruments Nanoscope IIIa scanning probe microscope in tapping mode using a Nanoworld soft tapping AFM probe. A typical MAPbI<sub>3</sub> crystal grown by inverse solubility was selected and the surface roughness of three areas ( $1 \mu\text{m}^2$ ,  $2 \mu\text{m}^2$ , and  $5 \mu\text{m}^2$ ) were measured. The roughness average ( $R_a$ ) and root mean square roughness ( $R_q$ ) for the three areas are shown Table SI. The  $5 \mu\text{m}^2$  area image contained larger features (visible in the optical image in Fig. S3(a)) typical of the crystals grown by the inverse solubility method, which significantly increased the surface roughness evaluated in the larger area.

The area measured by SE is much larger in size than the whole area shown in the optical image in Fig. S3(a), which is about  $15 \mu\text{m} \times 15 \mu\text{m}$ . A twice as large roughness obtained from the SE data is conceivable for the larger area illuminated by the microspot (spot diameter ca.  $100 \mu\text{m}$ ). In addition, as explained above, the SE effective roughness value is not necessarily identical with the AFM determination. The successive figures display the different measurements and regression analysis results that lead to the dielectric functions (splines) given in the main text in Figs. 1 and 2.

## Supplementary Information for: Spectroscopic Ellipsometry of FAMAPI Perovskites

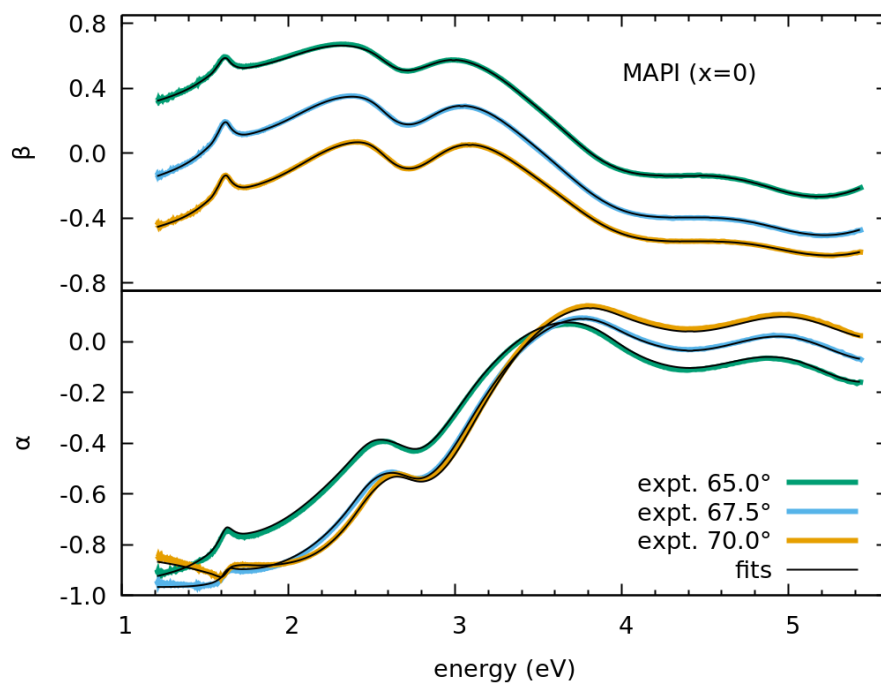


**Figure S2:** AFM images of MAPbI<sub>3</sub> crystal surface of areas (a) 1  $\mu\text{m}^2$ , (b) 2  $\mu\text{m}^2$  and (c) 5  $\mu\text{m}^2$ . Features reaching 25 nm were typical throughout the surface, appearing in clusters and significantly increasing the surface roughness measured.



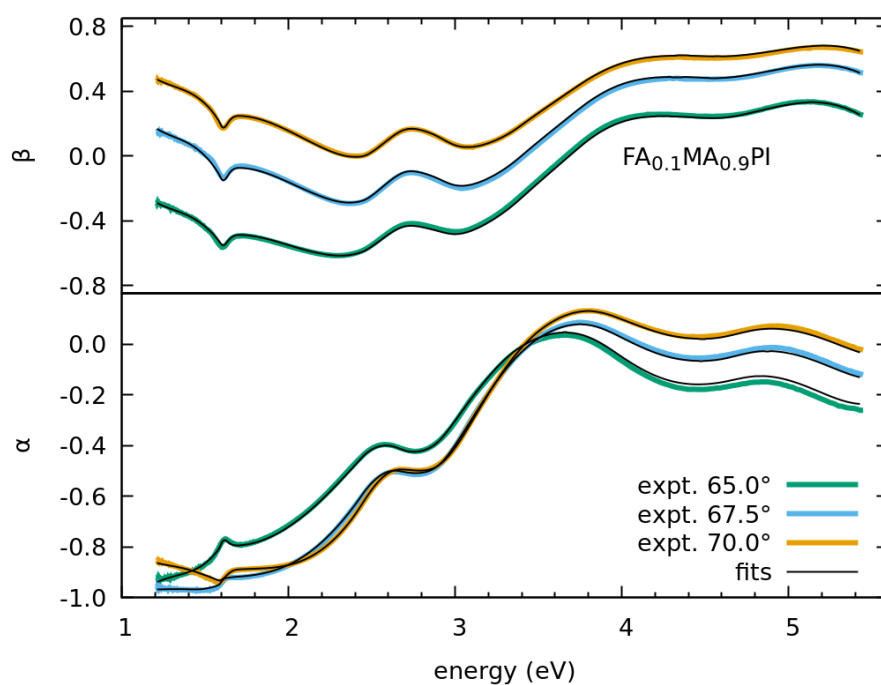
**Figure S3:** (a) Optical image of crystal surface measured in AFM, with 3D images of measurements taken of areas (b) 1  $\mu\text{m}^2$ , (c) 2  $\mu\text{m}^2$  and (d) 5  $\mu\text{m}^2$ .

## Supplementary Information for: Spectroscopic Ellipsometry of FAMAPI Perovskites



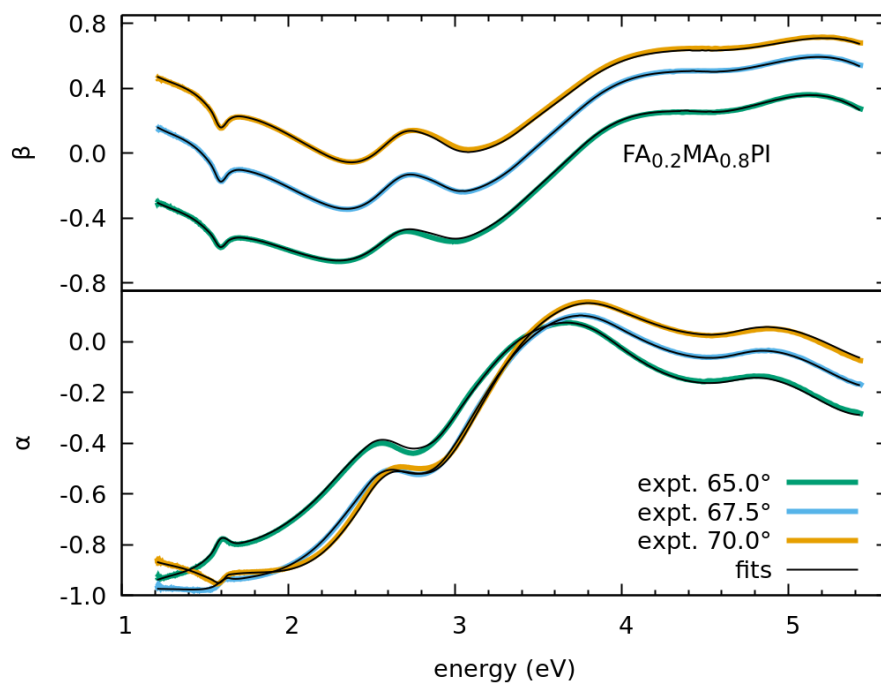
**Figure S4:** Ellipsometry spectra of  $\text{MAPbI}_3$  measured with different angles of incidence given on the plot.

The fitted roughness layer was 12.7 nm and the  $\chi^2 = 0.26$ .

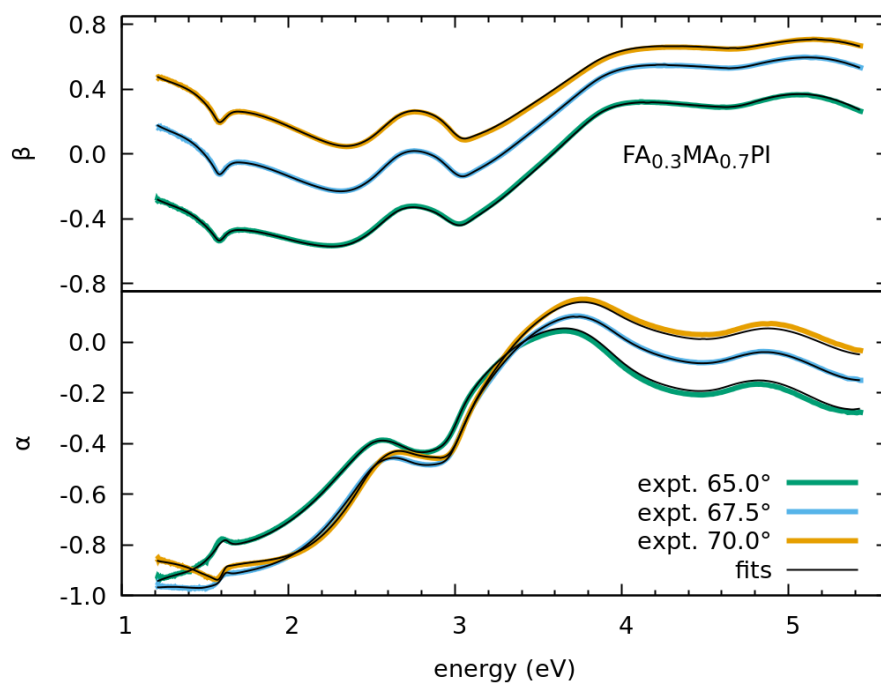


**Figure S5:** Ellipsometry spectra of  $\text{FA}_{0.1}\text{MA}_{0.9}\text{PbI}_3$  measured with different angles of incidence given on the plot. The fitted roughness layer was 11.6 nm and the  $\chi^2 = 0.35$ .

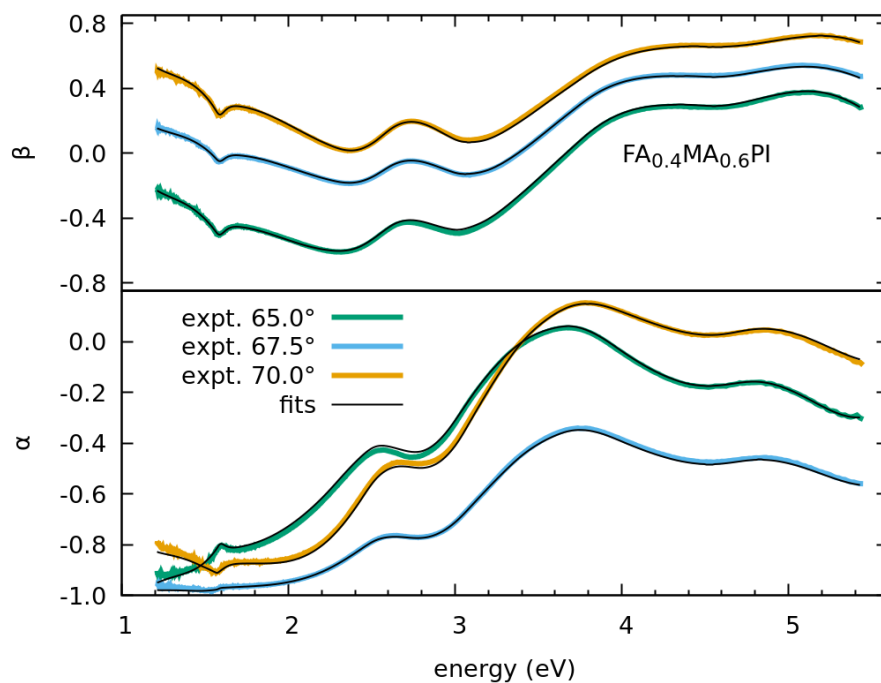




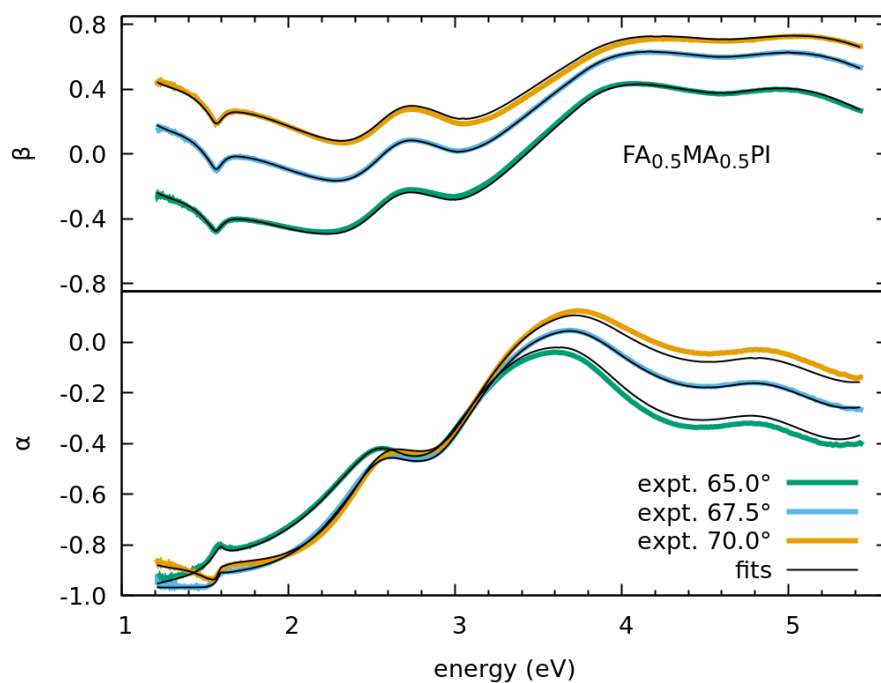
**Figure S6:** Ellipsometry spectra of  $\text{FA}_{0.2}\text{MA}_{0.8}\text{PbI}_3$  measured with different angles of incidence given on the plot. The fitted roughness layer was 9.8 nm and the  $\chi^2 = 0.21$ .



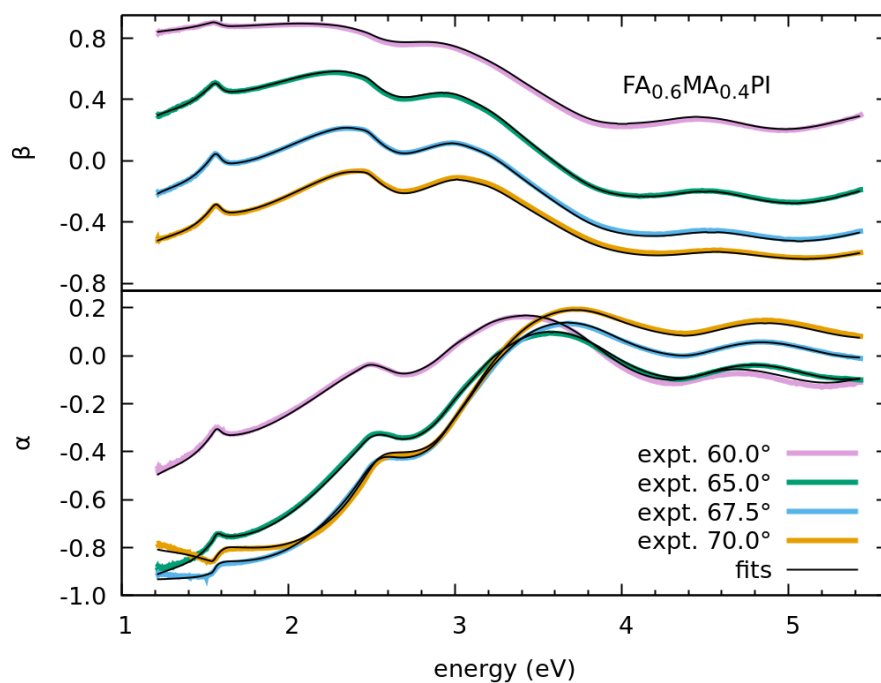
**Figure S7:** Ellipsometry spectra of  $\text{FA}_{0.3}\text{MA}_{0.7}\text{PbI}_3$  measured with different angles of incidence given on the plot. The fitted roughness layer was 11.0 nm and the  $\chi^2 = 0.17$ .



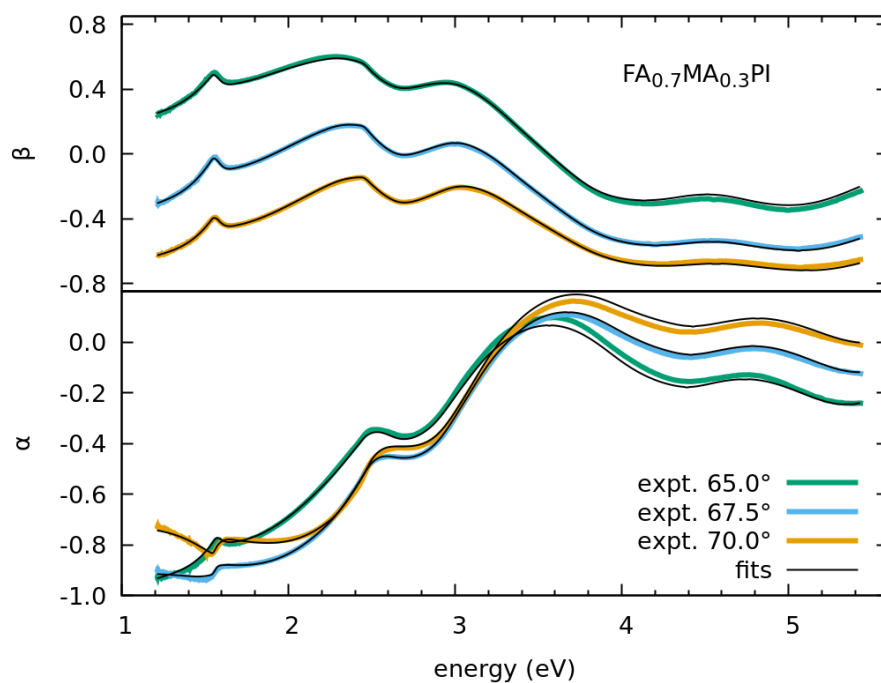
**Figure S8:** Ellipsometry spectra of  $\text{FA}_{0.4}\text{MA}_{0.6}\text{PbI}_3$  measured with different angles of incidence given on the plot. The fitted roughness layer was 13.4 nm and the  $\chi^2 = 0.58$ .



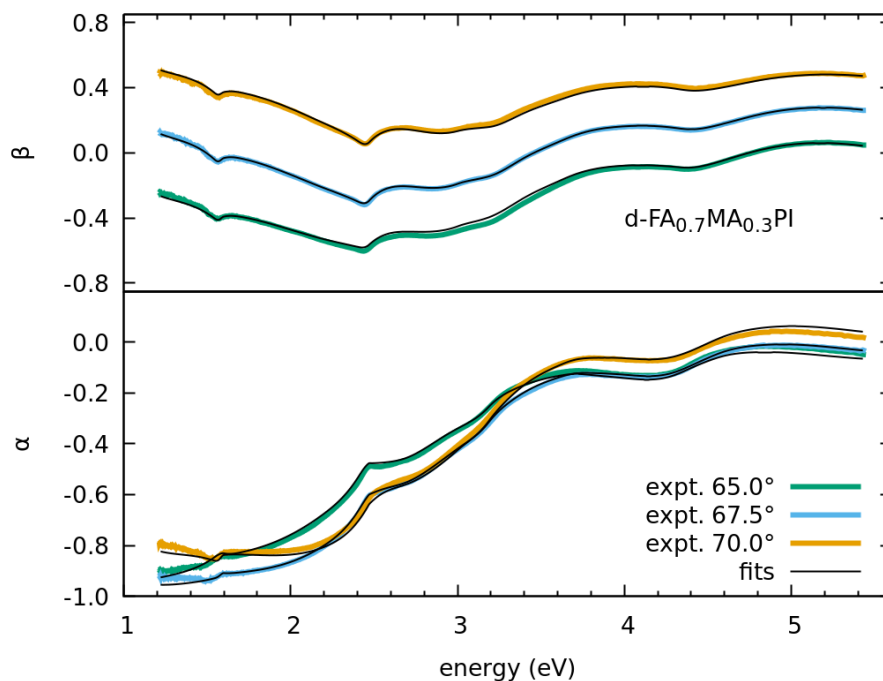
**Figure S9:** Ellipsometry spectra of  $\text{FA}_{0.5}\text{MA}_{0.5}\text{PbI}_3$  measured with different angles of incidence given on the plot. The fitted roughness layer was 11.0 nm and the  $\chi^2 = 0.81$ .



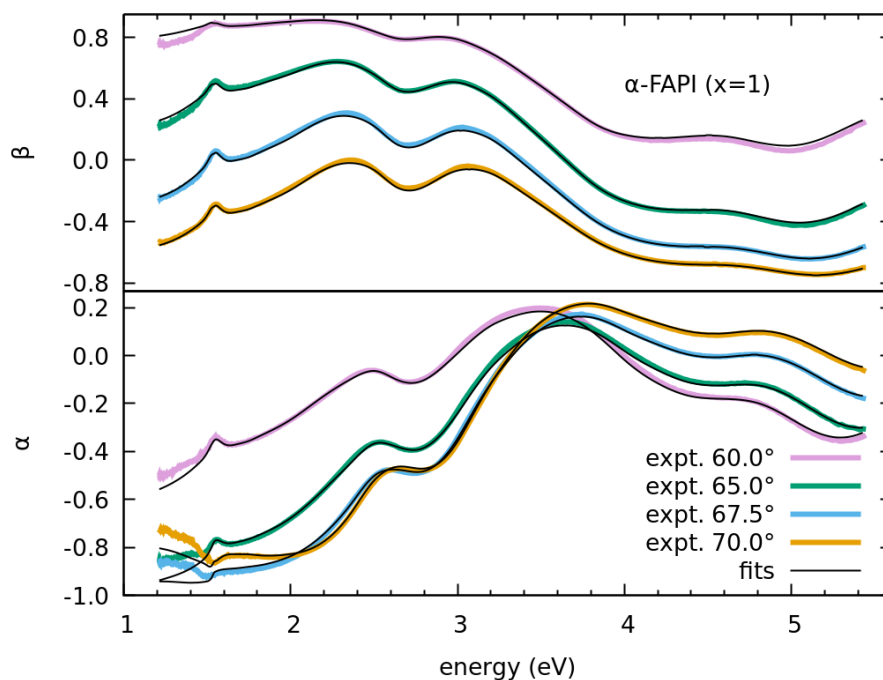
**Figure S10:** Ellipsometry spectra of  $\text{FA}_{0.6}\text{MA}_{0.4}\text{PbI}_3$  measured with different angles of incidence given on the plot. The fitted roughness layer was 18.5 nm and the  $\chi^2 = 0.57$ . (Excluding the angle of incidence at  $60^\circ$ ,  $\chi^2 = 0.39$ .)



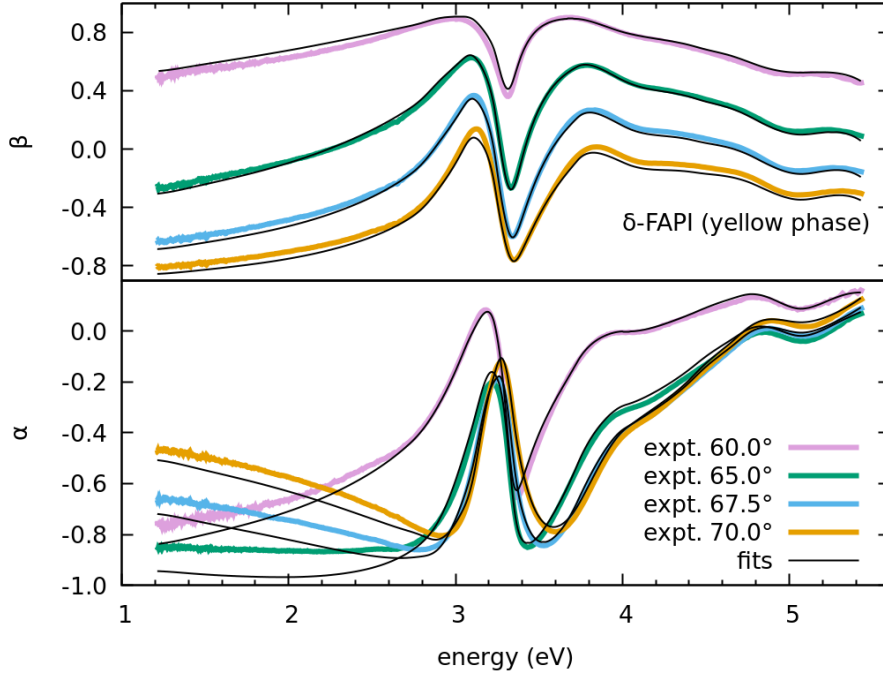
**Figure S11:** Ellipsometry spectra of  $\text{FA}_{0.7}\text{MA}_{0.3}\text{PbI}_3$  measured with different angles of incidence given on the plot. The fitted roughness layer was 18.2 nm and the  $\chi^2 = 0.60$ .



**Figure S12:** Ellipsometry spectra of the defect sample of  $\text{FA}_{0.7}\text{MA}_{0.3}\text{PbI}_3$  measured with different angles of incidence given on the plot. The fitted roughness layer was 15.4 nm and the  $\chi^2 = 1.13$ .



**Figure S13:** Ellipsometry spectra of  $\alpha\text{-FAPbI}_3$  (black phase) measured with different angles of incidence given on the plot. The fitted roughness layer was 15.2 nm and the  $\chi^2 = 5.35$ . (Excluding the angle of incidence at  $60^\circ$ ,  $\chi^2 = 4.14$ ).



**Figure S14:** Ellipsometry spectra of  $\delta$ -FAPbI<sub>3</sub> (yellow phase) measured with different angles of incidence given on the plot. The fitted roughness layer was 9.5 nm and the  $\chi^2 = 20.4$  (Excluding the angle of incidence at 60°,  $\chi^2 = 16.4$ ).

The higher values of  $\chi^2$  obtained for the FAPI samples are mostly due to the worse fits below the band gap due to the imposed constrain  $k \sim 0$  below the band gap. This is especially poor for the yellow phase in which the transparency range spans a large energy interval.

#### IV. DIELECTRIC FUNCTIONS OF MAPbI<sub>3</sub> AND FAPbI<sub>3</sub>

As explained in the main text, the regression analyses were performed without imposing any theoretical lineshape to the dielectric functions. However, some parameterizations were mentioned and are given in the following.

The equations for the lineshape of zero dimensional critical points is:

$$\varepsilon(\omega) = Ae^{i\varphi}(\hbar\omega - E_g + i\Gamma)^{-1}, \quad (4)$$

where  $A$  is the amplitude,  $\varphi$  the phase,  $E_g$  the critical point energy, and  $\Gamma$  the broadening.

**Table SII:** Parameters for the analytic representation of the dielectric function of MAPbI<sub>3</sub> with Critical Points. The 4 first oscillators are CP1 – CP4 and the fifth one represents higher energy contributions and provides the background.

| Oscillator | A      | $\varphi$ (rad) | $E_g$ (eV) | $\Gamma$ (eV) |
|------------|--------|-----------------|------------|---------------|
| 1          | 0.0491 | -1.28           | 1.6538     | 0.0799        |
| 2          | 0.4906 | -0.21           | 2.5809     | 0.1950        |
| 3          | 2.8568 | -0.34           | 3.2839     | 0.3573        |
| 4          | 0.2965 | -0.99           | 4.4644     | 0.3566        |
| 5          | 75.86  | -0.80           | 12.945     | 15.58         |

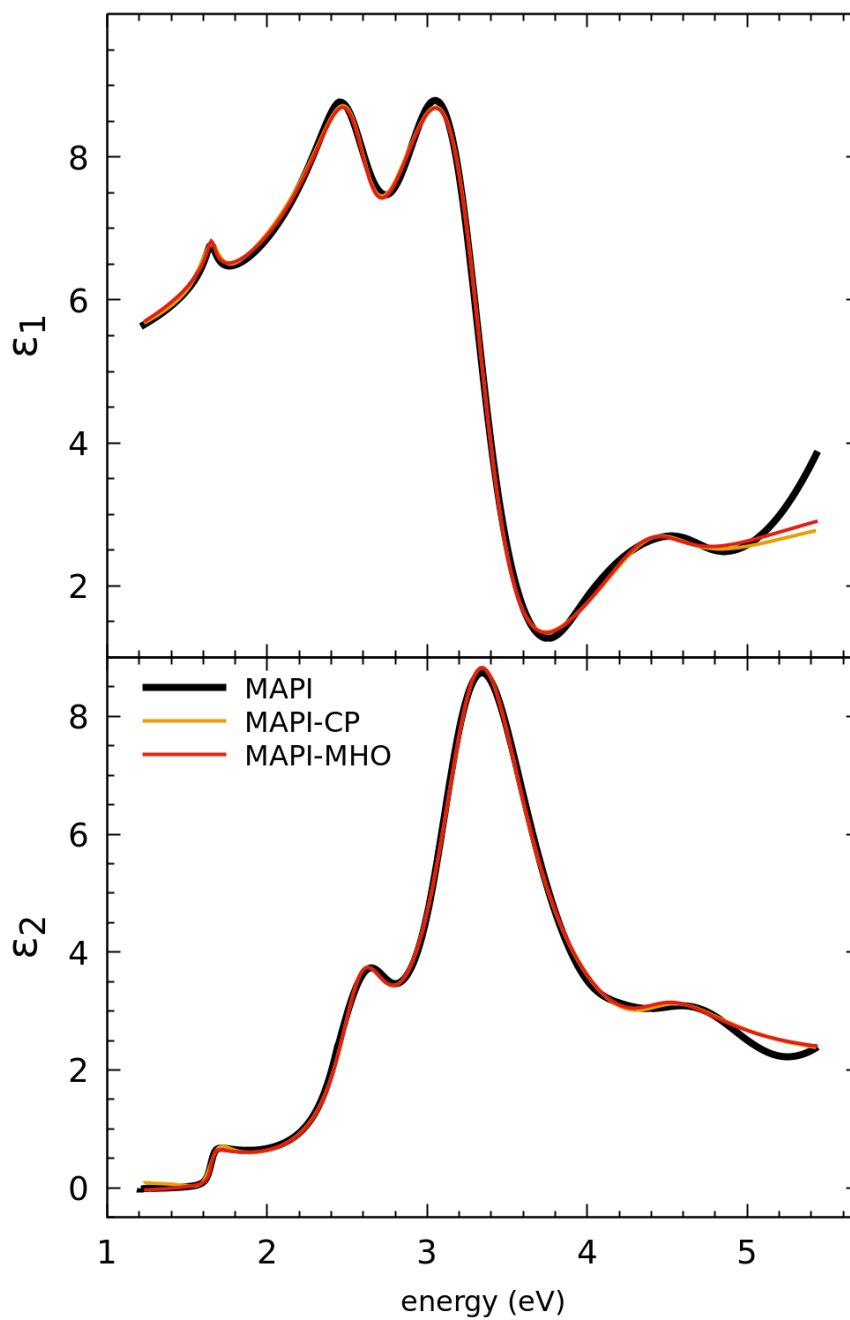
**Table SIII:** Parameters for the analytic representation of the dielectric function of MAPbI<sub>3</sub>. The gap is represented by a modified harmonic oscillator and the rest with Critical Points ( $\mu = -1$ ). The 4 first oscillators are CP1 – CP4 and the fifth one represents all higher energy contributions and provides the background.

| Oscillator | C      | $\varphi$ (rad) | $\mu$ | $E_g$ (eV) | $\Gamma$ (eV) |
|------------|--------|-----------------|-------|------------|---------------|
| 1          | 2.9699 | -0.08           | -0.14 | 1.6525     | 0.0200        |
| 2          | 0.5310 | -0.22           | -1    | 2.5796     | 0.1985        |
| 3          | 2.9109 | -0.36           | -1    | 3.2804     | 0.3603        |
| 4          | 0.2917 | -1.02           | -1    | 4.4353     | 0.3501        |
| 5          | 55.76  | -0.60           | -1    | 13.000     | 9.704         |

The modified harmonic oscillator model equation is:<sup>2</sup>

$$\begin{aligned} \varepsilon(\omega) = & C \left( e^{i\varphi} (E_g - \hbar\omega - i\Gamma)^\mu + e^{-i\varphi} (E_g + \hbar\omega + i\Gamma)^\mu \right) \\ & - 2\text{Re}[e^{-i\varphi} (E_g + i\Gamma)^\mu] - 2i\mu \hbar\omega \text{Im}[e^{-i\varphi} (E_g + i\Gamma)^{\mu-1}] / (\hbar\omega)^2, \end{aligned} \quad (5)$$

where C is related to the amplitude and  $\mu$  is the order of the pole.



**Figure S15:** Dielectric function of MAPbI<sub>3</sub>. The two parameterized fits (up to 5 eV) show the critical point model result and how the bandgap lineshape is improved by the modified harmonic oscillator model.

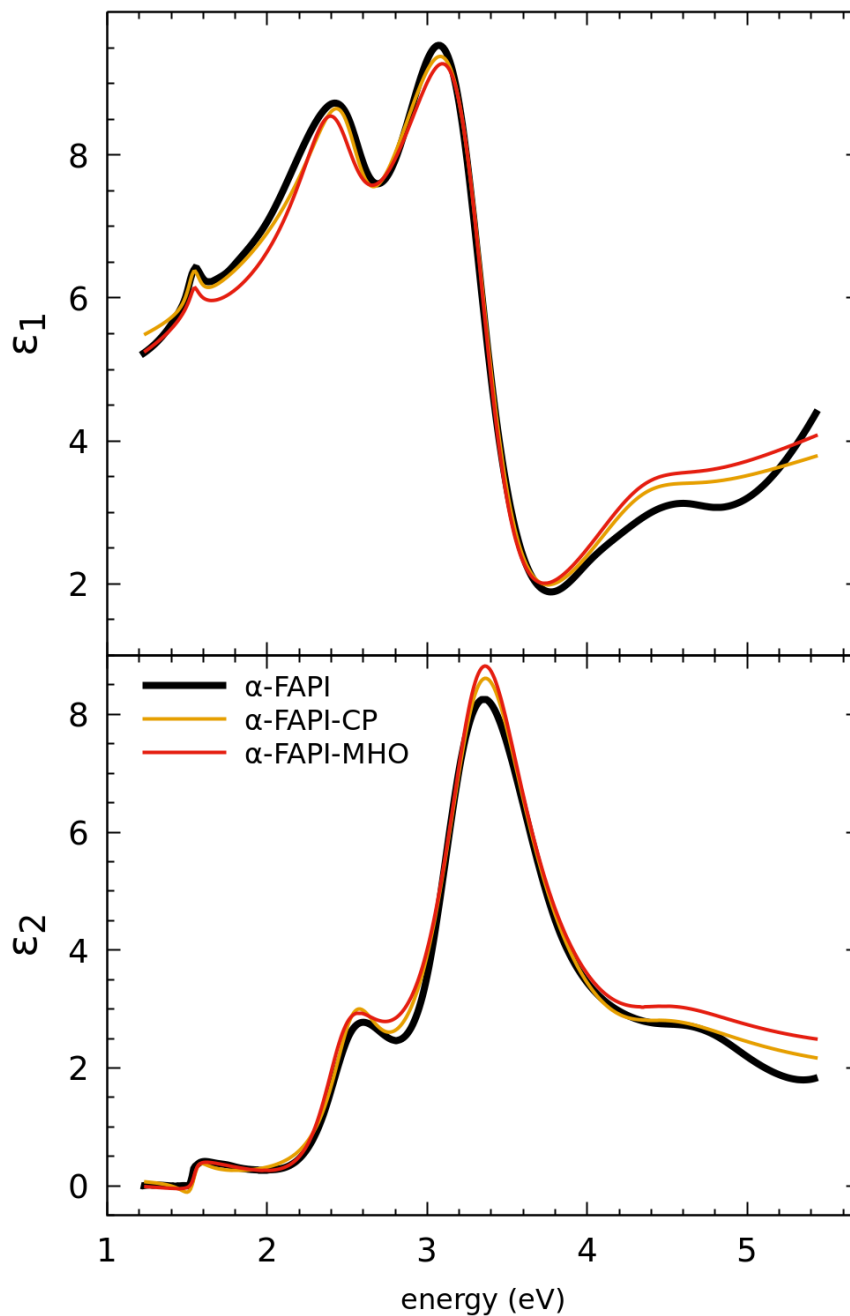
**Table SIV:** Critical Point parameters obtained from fitting the second derivative of the dielectric function of MAPbI<sub>3</sub>. The numbers in parentheses indicate the fitting errors to the last given significant digits. The CP labeled as 3-s is a weak shoulder.

| Oscillator | A        | $\varphi$ (rad) | $E_g$ (eV) | $\Gamma$ (eV) |
|------------|----------|-----------------|------------|---------------|
| CP1        | 0.03(1)  | -1.74(20)       | 1.619(4)   | 0.056(4)      |
| CP2        | 0.81(7)  | -0.17(9)        | 2.576(8)   | 0.258(8)      |
| CP3        | 4.33(29) | -0.77(7)        | 3.265(10)  | 0.453(11)     |
| CP3-s      | 0.44(9)  | 1.22(10)        | 3.689(19)  | 0.406(20)     |
| CP4        | 0.87(9)  | 0.52(13)        | 4.944(24)  | 0.533(24)     |

**Table SV:** Parameters for the analytic representation of the dielectric function of  $\alpha$ -FAPbI<sub>3</sub> with Critical Points. The 4 first oscillators are CP1 – CP4 and the fifth one represents higher energy contributions and provides the background.

| Oscillator | A      | $\varphi$ (rad) | $E_g$ (eV) | $\Gamma$ (eV) |
|------------|--------|-----------------|------------|---------------|
| 1          | 0.0219 | -1.61           | 1.5414     | 0.0456        |
| 2          | 0.4482 | -0.33           | 2.5246     | 0.1926        |
| 3          | 2.8419 | -0.40           | 3.2973     | 0.3502        |
| 4          | 0.3657 | -1.46           | 4.3600     | 0.4500        |
| 5          | 65.26  | -0.01           | 17.96      | 2.9080        |





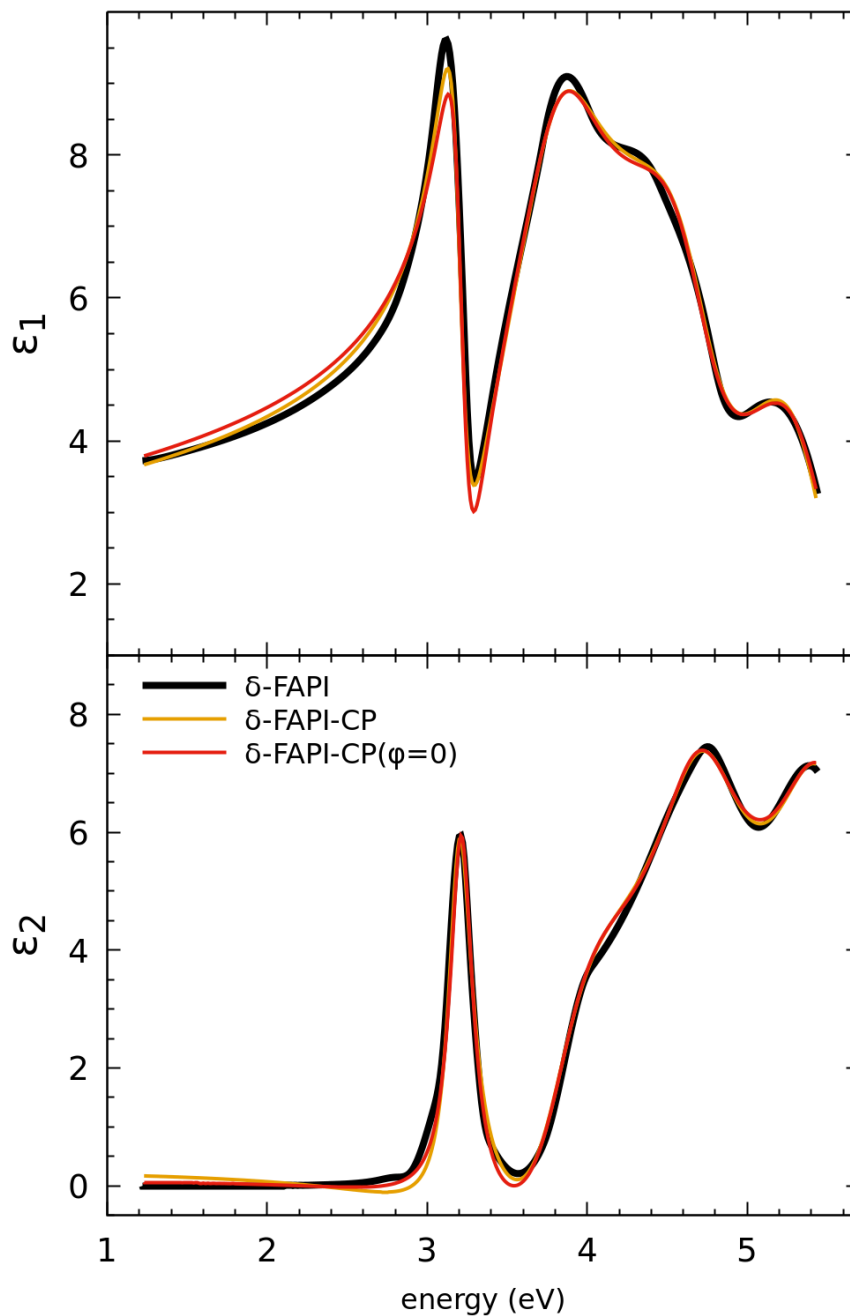
**Figure S16:** Dielectric function of  $\alpha$ -FAPbI<sub>3</sub>. The two parameterized fits (up to 5 eV) show the critical point model result and how the bandgap lineshape is improved by the modified harmonic oscillator model.

**Table SVI:** Parameters for the analytic representation of the dielectric function of  $\alpha$ -FAPbI<sub>3</sub>. The gap is represented by a modified harmonic oscillator and the rest with Critical Points ( $\mu = -1$ ). The 4 first oscillators are CP1 – CP4 and the fifth one represents all higher energy contributions and provides the background.

| Oscillator | C      | $\varphi$ (rad) | $\mu$  | $E_g$ (eV) | $\Gamma$ (eV) |
|------------|--------|-----------------|--------|------------|---------------|
| 1          | 28.54  | -0.13           | -0.016 | 1.5430     | 0.0200        |
| 2          | 0.5600 | -0.83           | -1     | 2.4477     | 0.2262        |
| 3          | 2.5594 | -0.42           | -1     | 3.2971     | 0.3259        |
| 4          | 0.3657 | -1.46           | -1     | 4.3601     | 0.4499        |
| 5          | 40.88  | 0.12            | -1     | 13.074     | 1.031         |

**Table SVII:** Critical Point parameters obtained from fitting the second derivative of the dielectric function of  $\alpha$ -FAPbI<sub>3</sub>. The numbers in parentheses indicate the fitting errors to the last given significant digits. The CP labeled as 3-s is a weak shoulder.

| Oscillator | A        | $\varphi$ (rad) | $E_g$ (eV) | $\Gamma$ (eV) |
|------------|----------|-----------------|------------|---------------|
| CP1        | 0.03(1)  | -1.92(24)       | 1.532(5)   | 0.056(5)      |
| CP2        | 1.06(12) | -0.40(12)       | 2.532(12)  | 0.292(12)     |
| CP3        | 3.23(24) | -0.75(7)        | 3.227(9)   | 0.373(9)      |
| CP3-s      | 0.20(11) | -3.26(10)       | 3.760(22)  | 0.327(52)     |
| CP4        | 0.56(28) | 0.17(35)        | 4.752(78)  | 0.480(86)     |



**Figure S17:** Dielectric function of  $\delta$ -FAPbI<sub>3</sub>. In this case the best fit of the gap is clearly an excitonic lineshape and the two parameterized fits are with critical points. The behavior of  $\epsilon_2$  below bandgap is improved by fixing some of the phases to zero.

**Table SVIII:** Parameters for the analytic representation of the dielectric function of  $\delta$ -FAPbI<sub>3</sub> with Critical Points. The 4 first oscillators are CP1 – CP4 and the fifth one represents higher energy contributions and provides the background. In this fit all phases are free parameters.

| Oscillator | A      | $\varphi$ (rad) | $E_g$ (eV) | $\Gamma$ (eV) |
|------------|--------|-----------------|------------|---------------|
| 1          | 0.5900 | -0.18           | 3.1981     | 0.0913        |
| 2          | 1.3403 | -1.67           | 3.8126     | 0.3531        |
| 3          | 1.4445 | 0.14            | 4.7307     | 0.3490        |
| 4          | 1.6058 | 0.03            | 5.4458     | 0.3535        |
| 5          | 23.27  | 0.20            | 10.041     | 0.1962        |

**Table SIX:** Parameters for the analytic representation of the dielectric function of  $\delta$ -FAPbI<sub>3</sub> with Critical Points. The 4 first oscillators are CP1 – CP4 and the fifth one represents higher energy contributions and provides the background. In this fit some phases have been fixed to zero.

| Oscillator | A      | $\varphi$ (rad) | $E_g$ (eV) | $\Gamma$ (eV) |
|------------|--------|-----------------|------------|---------------|
| 1          | 0.5716 | 0.00            | 3.2129     | 0.0870        |
| 2          | 1.6330 | -0.11           | 3.5748     | 0.3312        |
| 3          | 1.3178 | 0.27            | 4.7561     | 0.3434        |
| 4          | 1.4029 | 0.00            | 5.4458     | 0.3535        |
| 5          | 26.32  | 0.00            | 10.106     | 2.0081        |

**Table SX:** Critical Point parameters obtained from fitting the second derivative of the dielectric function of  $\delta$ -FAPbI<sub>3</sub>. The numbers in parentheses indicate the fitting errors to the last given significant digits.

| Oscillator | A        | $\varphi$ (rad) | $E_g$ (eV) | $\Gamma$ (eV) |
|------------|----------|-----------------|------------|---------------|
| CP1        | 1.08(6)  | -0.47(5)        | 3.187(3)   | 0.137(3)      |
| CP2        | 0.91(8)  | -1.61(12)       | 3.839(3)   | 0.297(3)      |
| CP3        | 2.31(15) | 0.61(10)        | 4.822(4)   | 0.400(6)      |
| CP4        | 1.38(15) | -0.59(22)       | 5.273(30)  | 0.370(7)      |

**REFERENCES**

- <sup>1</sup>D. E. Aspnes, “The accurate determination of optical properties by ellipsometry,” in *Handbook of Optical Constants of Solids*, Vol. 1, edited by E.D.Palik (Academic Press, New York, 1985) Chap. 5, pp. 89–112.
- <sup>2</sup>J. Leng, J. Opsal, H. Chu, M. Senko, and D. Aspnes, “Analytic representations of the dielectric functions of materials for device and structural modeling,” *Thin Solid Films* **313-314**, 132 – 136 (1998).



# Phase Diagram of Methylammonium/Formamidinium Lead Iodide Perovskite Solid Solutions from Temperature-Dependent Photoluminescence and Raman Spectroscopies

Adrián Francisco-López, Bethan Charles, M. Isabel Alonso, Miquel Garriga, Mariano Campoy-Quiles, Mark T. Weller, and Alejandro R. Goñi\*



Cite This: *J. Phys. Chem. C* 2020, 124, 3448–3458



Read Online

ACCESS |



Metrics & More

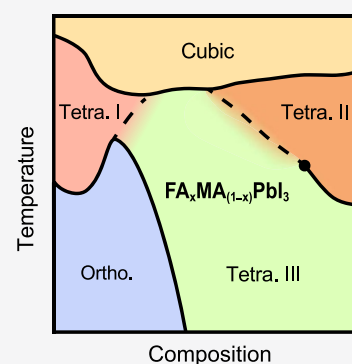


Article Recommendations



Supporting Information

**ABSTRACT:** The complete phase diagram of organic-cation solid solutions of lead iodide perovskites  $[\text{FA}_x\text{MA}_{1-x}\text{PbI}_3]$ , where MA stands for methylammonium,  $\text{CH}_3\text{NH}_3$ , and FA for formamidinium,  $\text{CH}(\text{NH}_2)_2$  with compositions  $x$  ranging from 0 to 1 in steps of 0.1 was constructed in the temperature range from 10 to 365 K by combining Raman scattering and photoluminescence (PL) measurements. The occurrence of phase transitions was inferred from both the temperature-induced changes in the optical emission energies and/or the phonon frequencies and line widths, complementing X-ray and neutron scattering literature data. For MA-rich perovskites ( $x \leq 0.2$ ), the same structural behavior as for  $\text{MAPbI}_3$  was observed with decreasing temperature: cubic  $Pm\bar{3}m \rightarrow$  tetragonal-I  $I4/mcm \rightarrow$  orthorhombic  $Pnma$ . As the FA molecule is larger and more symmetric but less polar than MA, a tetragonal crystal structure is favored at low temperatures and FA compositions  $x > 0.4$ , to the detriment of the orthorhombic phase. As a consequence, with decreasing temperature, the phase transition sequence for FA-rich compounds is cubic  $Pm\bar{3}m \rightarrow$  tetragonal-II  $P4/mbm \rightarrow$  tetragonal-III. The latter presumably belongs to the  $P4bm$  symmetry group, according to neutron scattering data. Strikingly, the isostructural (tetragonal-to-tetragonal) transformation, which occurs between 200 and 150 K, exhibits a kind of critical point for  $x = 0.7$ . For intermediate FA contents, the perovskite solid solution transforms close to 250 K directly from the cubic phase to the tetragonal-III phase. The latter is characterized by a nonmonotonic dependence of the band-gap energy on temperature. We ascribe such behavior to a substantial tilting of the  $\text{PbI}_6$  octahedra in the tetragonal-III phase. In this way, we established important links between crystal-phase stability and the electronic as well as vibrational properties of mixed organic-cation halide perovskites, which might impact the current search for more stable best-performing optoelectronic materials.



## INTRODUCTION

A salient feature of hybrid lead halide perovskites is the peculiar interplay between the organic and inorganic degrees of freedom, which plays a crucial role in their structural, vibrational, optical, and transport properties. In this respect, unraveling the associated structure–property relationships is instrumental for the fundamental understanding of not only the exceptional performance in photovoltaics<sup>1–3</sup> or in light-emitting devices<sup>4–6</sup> but also the in operando stability of this class of materials. In particular, the latter issue is critical for the commercial applicability of halide perovskites, so far hampered by material degradation and/or crystalline phase instabilities.<sup>7–12</sup> Furthermore, the great advantage of this family of materials of being solution processable is somewhat counterbalanced by their mechanical softness<sup>13</sup> and the consequent low energetic barriers for point defect formation and ion migration.<sup>14–16</sup> To seek for the best material among the  $\text{APbX}_3$  lead halide perovskite system that would provide the highest photovoltaic efficiency and simultaneous stability, a fruitful strategy consisted of the systematic exploration of the

compositional space by mainly varying the A-site cation and/or the X halide anion.<sup>9,10,17–20</sup>

Referring to the archetypal hybrid perovskite  $\text{MAPbI}_3$ , where MA stands for methylammonium,  $\text{CH}_3\text{NH}_3$ , the gradual substitution of MA by formamidinium (FA),  $\text{CH}(\text{NH}_2)_2$ , induces a moderate red shift of the fundamental band gap, which amounts to ca. 60 to 100 meV for pure  $\text{FAPbI}_3$ , as extracted from photoluminescence (PL),<sup>18</sup> absorption,<sup>19</sup> diffuse reflectance,<sup>20</sup> or ellipsometry<sup>21</sup> spectra. In this way, the fundamental gap of the mixed organic-cation perovskite becomes closer to the optimum value for a single-junction solar cell, improving its photovoltaic performance.<sup>18,19</sup> In contrast, replacing iodide by bromide causes a strong blue shift of the gap and a simultaneous improvement in crystallinity, thus reducing defect density and boosting photovoltaic action,

Received: October 30, 2019

Revised: January 24, 2020

Published: January 24, 2020



particularly for applications in tandem devices.<sup>18,19</sup> In fact, the latest certified records in the conversion efficiency of hybrid halide perovskite-based solar cells were attained using mixed MA/FA and I/Br materials.<sup>3</sup>

Regarding the structural phase stability, both end-composition materials, MAPbI<sub>3</sub> and FAPbI<sub>3</sub>, have been systematically studied. At ambient conditions, MAPbI<sub>3</sub> crystallizes in a tetragonal phase belonging to the *I4/mcm* space group.<sup>22</sup> This phase will be called Tetra-I, hereafter. The inorganic cage consists of corner-sharing PbI<sub>6</sub> octahedra with straight Pb–I–Pb bonds in the *c*-direction (the bond angle equal to 180°) but being alternately rotated a few tens of degrees along the *c*-direction such that the Pb–I–Pb bond angle in the *a,b*-plane is slightly smaller than 160°.<sup>22</sup> The MA cations, which can freely move inside the cage voids, are dynamically disordered, alternating their orientation in the *a,b*-plane between the four equivalent  $\langle 100 \rangle$  directions every few ps.<sup>22–25</sup> At around 327 K, MAPbI<sub>3</sub> undergoes a second-order phase transition into a cubic phase with *Pm* $\bar{3}$ *m* symmetry, for which all Pb–I–Pb bond angles are necessarily 180°, but the MA cations remain dynamically disordered (now spanning all six equivalent  $\langle 100 \rangle$  directions of the cube).<sup>22</sup> In contrast, at around 165 K, a first-order phase transition occurs, at which MAPbI<sub>3</sub> transforms into an orthorhombic structure pertaining to the *Pnma* space group.<sup>22</sup> Two key features of the low-temperature phase are to be remarked: The lower symmetry and volume of the cage voids induce the locking of the MA cations inside the voids, becoming fully ordered with well-aligned –NH<sub>3</sub> groups,<sup>22–24</sup> and the now somewhat deformed PbI<sub>6</sub> octahedra exhibit a clear tilting in all three spatial directions such that the average Pb–I–Pb bond angle reduces to 154.5°.<sup>22</sup>

The other end-compound FAPbI<sub>3</sub> can be stabilized at room temperature, although with difficulties, in a perovskite phase, the so-called black  $\alpha$ -phase. This phase is cubic and also belongs to the *Pm* $\bar{3}$ *m* space group. The FA cations, being rotationally highly mobile, are dynamically disordered over 24 orientations inside the inorganic cage voids.<sup>26</sup> FAPbI<sub>3</sub> exhibits a different low-temperature behavior than MAPbI<sub>3</sub>, transforming into another tetragonal phase with *P4/mbm* symmetry, hereafter denoted Tetra-II phase, at about 285 K.<sup>17,27</sup> In this tetragonal phase, the FA cations remain dynamically disordered but in the *a,b*-plane.<sup>27</sup> Furthermore, neutron powder diffraction<sup>27</sup> measurements and a combination with X-ray diffraction<sup>28</sup> both indicate that at 140 K FAPbI<sub>3</sub> undergoes an isostructural transition. The low-temperature tetragonal phase, hereafter called Tetra-III, was tentatively indexed as pertaining to the *P4bm* space group,<sup>28</sup> although the neutron diffraction patterns could not be fully indexed using this symmetry for the unit cell.<sup>27</sup> The neutron results are more indicative of a disordered phase, where the FA cations seem to be rotated in increments along the *c*-axis, thus influencing the tilting of the PbI<sub>6</sub> octahedra.

Recently, the different degradation routes and the associated kinetics under atmospheric conditions have been systematically studied for FA<sub>*x*</sub>MA<sub>1–*x*</sub>PbI<sub>3</sub> mixed organic-cation lead iodide thin films over the full compositional range.<sup>10</sup> The main conclusions are the following: MA-rich compounds decompose in air into the precursor iodide salts and (layered) PbI<sub>2</sub>. This degradation is strongly accelerated by ambient humidity but is slowed down with FA incorporation. On the other hand, FA-rich phases are unstable against the formation of a non-perovskitic hexagonal phase, which is the so-called  $\delta$ -phase of FAPbI<sub>3</sub>.<sup>10</sup> This hexagonal phase, which is characterized by

face-sharing PbI<sub>6</sub> octahedra, possesses a much larger band gap,<sup>21</sup> leading to its yellowish appearance.<sup>26,29</sup> Density functional theory calculations predict that the  $\delta$ -phase is more stable by 0.2 eV per formula unit than the perovskite  $\alpha$ -phase.<sup>27</sup> Hence, FA-rich phases convert mainly into this yellow hexagonal structure upon degradation. Importantly, decomposition is strongly inhibited in the intermediate compositional range of *x* = 0.4 to 0.6, where the available routes for degradation of the end-composition materials are highly restricted.<sup>10</sup> Another way of structurally stabilizing the perovskite phases in FA-rich compounds consists of the addition of about 20% of Cs as the A-site cation, which consequently leads to higher crystalline quality and improved photovoltaic properties.<sup>9</sup>

The rotation–libration dynamics of the organic cations inside the cuboctahedral inorganic cage voids plays an important role in the structural and vibrational behavior of lead halide perovskites and vice versa.<sup>30,31</sup> Neutron scattering measurements provided quantitative insights into the rotational dynamics and degree of the dynamic disorder of the MA/FA cations within the inorganic cage in the different phases of hybrid lead halide perovskites.<sup>22,24,27</sup> In addition, time-resolved vibrational spectroscopy<sup>23,31</sup> together with molecular dynamics simulations<sup>30</sup> has identified two time scales for the motion of MA/FA molecules: fast librations (300–600 fs) and slow rotations (2–3 ps). These excitations dominate the dynamics of the MA/FA cations in the cubic and tetragonal high-temperature phases, since the molecules are fully unlocked within the cage voids. In recent temperature-dependent experiments on the three methylammonium lead halides, we found evidence of significant coupling between the vibrations of the anionic (PbX<sub>3</sub><sup>–</sup>)<sub>*n*</sub> (X = I, Br, Cl) network and the CH<sub>3</sub>NH<sub>3</sub><sup>+</sup> cations in the Raman scattering signature.<sup>32,33</sup> As a consequence of the steric interaction between the MA molecules and the halogen atoms of the inorganic cage, the vibrational modes of the latter exhibit a wide statistical distribution of frequencies, which in turn leads to a strong inhomogeneous broadening of the Raman peaks. In contrast, in the low-temperature orthorhombic phase, the reduced volume and symmetry of the cage voids cause the locking of the organic cations, which become well oriented along high-symmetry directions of the perovskite crystal. The result is a pronounced reduction of the inhomogeneous broadening, which is readily observed in low-temperature Raman spectra.<sup>32–34</sup> Interestingly, a similar locking effect of the MA cations and the concomitant reduction in the line width of the inorganic cage phonon modes can be induced at room temperature through the application of high hydrostatic pressure.<sup>35,36</sup> This speaks for the existence of a strain-mediated link between the structural phase behavior of hybrid lead halide perovskites with temperature and/or pressure and the available phase space for the molecular motion of the organic cations.

In this work, we present a systematic study of the structural phase behavior of high-quality single crystals of lead iodide organic-cation solid solutions (FA<sub>*x*</sub>MA<sub>1–*x*</sub>PbI<sub>3</sub>) with compositions *x* ranging from 0 to 1 in steps of 0.1 and in the temperature range from 10 to 365 K. A peculiarity of this work is that the complete phase diagram was obtained solely by optical means, i.e., by monitoring the temperature-induced changes in the fundamental band gap and vibrational spectrum for the different compositions, as observed in PL and Raman experiments, respectively. The transition temperatures deter-



mined here agree very well with the available literature data from X-ray or neutron diffraction experiments. Interestingly, in the high-temperature regime ( $T > 250$  K) and for all compositions, the hybrid perovskites adopt a highly symmetric cubic structure of corner-sharing  $\text{PbI}_6$  octahedra. This is a direct consequence of the full dynamic disorder of the organic cations, moving freely inside the inorganic cage voids, and their strong steric influence on the rigid-body behavior of the  $\text{PbI}_6$  octahedra. By lowering the temperature, a second-order phase transition into up to three different tetragonal structures occurs, depending on composition. In the low-temperature range below ca. 170 K and for MA-rich compounds ( $x \leq 0.4$ ), the solid solution undergoes a first-order phase transition (with discontinuities in several physical properties like fundamental gap or phonon line width) from tetragonal to orthorhombic. Instrumental for this work is the sudden sharpening of the inorganic cage Raman modes due to the locking of the MA molecules within the cage voids of the orthorhombic phase, which allows us to assess with great confidence the occurrence of the phase transition. At the other compositional end, i.e., FA-rich ( $x \geq 0.7$ ) mixed crystals, the phase transition is of the first order but between two tetragonal phases. Both phases are distinguished by the different gaps and, in particular, their distinct temperature dependences. Unexpectedly, this isostructural transition appears to have a kind of critical point for a FA content of  $x = 0.7$ . Below this composition down to  $x = 0.5$ , the tetragonal-to-tetragonal transformation proceeds without any discontinuity in the spectroscopic features such as the band gap.

## EXPERIMENTAL SECTION

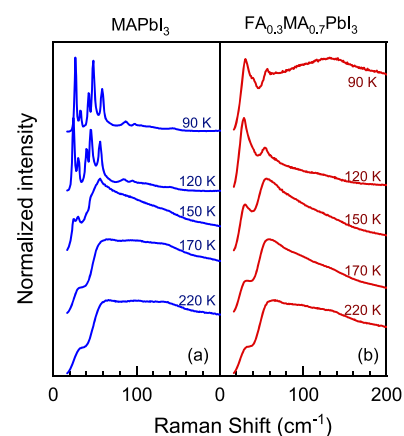
**$\text{FA}_x\text{MA}_{1-x}\text{PbI}_3$  Crystal Growth.** The inverse solubility method of Saidaminov et al.<sup>37</sup> was developed to produce crystals of  $\text{FA}_x\text{MA}_{1-x}\text{PbI}_3$  across the full composition range. Stoichiometric quantities of MAI, FAI (GreatCell Solar), and  $\text{PbI}_2$  (Merck, 99%) were dissolved at 60 °C in dry  $\gamma$ -butyrolactone (Alfa Aesar). Concentrations of the precursor solutions were kept at 1 M, with an exception for the FA-rich materials  $\text{FA}_x\text{MA}_{1-x}\text{PbI}_3$  ( $x \geq 0.8$ ), where concentrations were lowered to 0.9 M to allow the FAI to fully dissolve. When the precursor salts and lead halide powders had completely dissolved, the solutions were quickly filtered using Millex GS filters of pore size 0.22  $\mu\text{m}$  and transferred to clean cylindrical 4 mL glass vials. The solutions were then heated to 110 °C at a rate of 10 °C/h using an oil bath, the temperature of which was carefully controlled and monitored using a Stuart SCT1 controller. Solutions were maintained at 110 °C for 2 h allowing crystallization; the temperature was then raised to 120 °C for a final hour before the remaining solution was filtered and large single crystals were oven-dried at 100 °C overnight.

**Temperature-Dependent Optical Spectroscopy.** The PL spectra were excited with the 633 nm line of a He–Ne laser, whereas an infrared diode laser emitting at 785 nm was employed for the Raman measurements. The latter turned out the most suitable to excite the vibrational modes of the inorganic cage, providing also the highest spectral resolution and stray-light rejection such that the acquisition limit for the Raman spectra at low energies was  $\sim 20$   $\text{cm}^{-1}$ . In all cases, a very low incident light power below 2  $\mu\text{W}$  (power density < 15  $\text{W}/\text{cm}^2$ ) was used to avoid any photodegradation of the samples.<sup>33</sup> Spectra were recorded using a 20 $\times$  long working distance objective with NA = 0.35 (laser spot of ca. 4  $\mu\text{m}$  in diameter) and dispersed with a high-resolution LabRam

HR800 grating spectrometer equipped with a charge-coupled device detector. PL spectra were corrected for the spectral response of the spectrometer by normalizing each spectrum using the detector and the 600 grooves/mm grating characteristics. Raman and PL measurements on large single crystals exhibiting flat surfaces were carried out between 10 and 365 K using a (He) gas flow cryostat from CryoVac with optical access that fits under the microscope of the Raman setup.

## RESULTS AND DISCUSSION

**Temperature-Dependent Raman Measurements.** Figure 1 summarizes the Raman results as exemplified by two



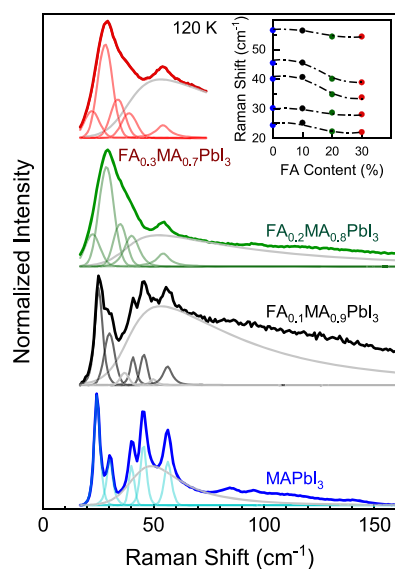
**Figure 1.** Raman spectra in the spectral range of the inorganic cage phonons of (a)  $\text{MAPbI}_3$  single crystal and (b) one with 30% FA content measured at different temperatures, as indicated. The spectra were normalized to their maximum intensities and shifted vertically for clarity.

representative compositions of the  $\text{FA}_x\text{MA}_{1-x}\text{PbI}_3$  series measured as a function of temperature (the complete set of temperature-dependent Raman spectra recorded for different compositions is shown in Figure S1 of the Supporting Information). To ease the comparison, the spectra were normalized to their maximum intensities and plotted with a vertical offset with decreasing temperature. The temperature range shown in Figure 1 was chosen to capture the occurrence of the tetragonal-to-orthorhombic phase transition. For the determination of the transition temperatures, the abrupt change in the line shape of the Raman spectra, mainly the strong narrowing of the cage Raman modes, was employed. We note that such a behavior of the line widths was previously observed for  $\text{MAPbI}_3$  at the temperature of the tetragonal-to-orthorhombic transition at ambient pressure<sup>32–34</sup> and also at room temperature but at a pressure of ca. 3 GPa, corresponding to a transition from a cubic to presumably an orthorhombic phase.<sup>35</sup> The reduced symmetry of the structure in either the low-temperature or the high-pressure phase together with a smaller void volume leads to the locking of the MA molecules inside the inorganic cage voids in certain crystalline directions. This causes a sudden and marked reduction of the inhomogeneous broadening of the Raman modes of the inorganic cage, as a consequence of the vanishing dynamical disorder of the organic cations when locked.<sup>22,23,27,30,31</sup>

The Raman spectra of FA-rich compounds with  $x \geq 0.5$ , however, do not show any of these changes (see the Supporting Information), which is taken as evidence of the

absence of an orthorhombic phase, down to the lowest temperature of the present experiments (ca. 10 K). Moreover, the (Stokes) Raman signal vanishes any time that the main PL peak moves to lower energies and has no overlap with the energy of the scattered Raman photons (see, for instance, Figure S1g,h). This usually happens at low temperatures and high FA content, being most likely the result of a total loss of (outgoing) resonance conditions for excitation with the IR laser (785 nm). We will go back to the Raman results by the discussion of the complete phase diagram.

It is instructive to compare the Raman spectra recorded for different MA-rich compositions in the low-temperature orthorhombic phase to learn about the effect of composition on the cage phonons. For a quantitative assessment of the vibrational spectrum of  $\text{FA}_x\text{MA}_{1-x}\text{PbI}_3$ , we have decomposed the recorded Raman spectra in different mode components by a line shape analysis,<sup>38</sup> as illustrated by the fitting examples displayed in Figure 2 for spectra recorded at 120 K for the four

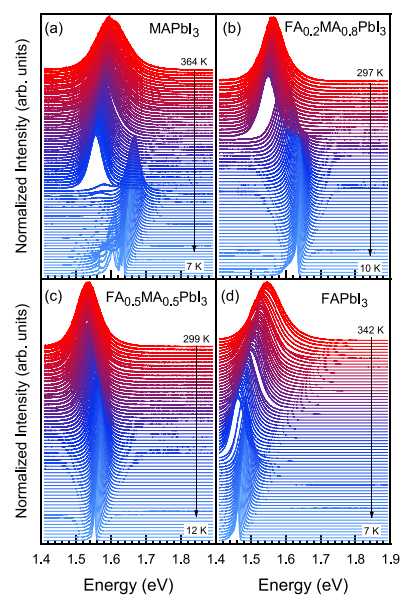


**Figure 2.** Characteristic Raman spectra (strong color curves) of the orthorhombic phase of the four MA-richer solid solution crystals ( $0 \leq x \leq 0.3$ ) recorded at 120 K. The performed line shape fits to the Raman spectra using Lorentzian or Gaussian functions (see the text for details) are also shown as light color curves. The solid gray curves correspond to an edgeline function used for describing the spectral characteristic of the dichroic filter (see the text for details). The inset shows the Raman peak frequencies of the five more pronounced modes as a function of FA content. The dash-dotted lines are just guides to the eye.

samples with  $x$  between 0 and 0.3 (MA rich). The best fits of the Raman band/peaks have been obtained using Lorentzian or Gaussian functions for compositions  $x < 0.2$  or  $x \geq 0.2$ , respectively. Based on a previous assignment of the phonon modes,<sup>32–34,39</sup> all Raman peaks with the frequency lower than  $200 \text{ cm}^{-1}$  correspond to vibrations of the inorganic cage. Here, we restrict ourselves to the five lowest-frequency cage modes, for they are the more pronounced and well-defined ones. The gray edgeline curve accounts for the spectral characteristic of the 785 nm edge filter used to cut the stray laser light in the Raman experiments (the edge center fixed at around  $45 \text{ cm}^{-1}$ ). The inset of Figure 2 shows the plots of the frequency of the five most intense Raman modes obtained from the line shape fits for the four compositions considered. Two conclusions can

be drawn from these data: (i) The line width of the Raman peaks associated with the cage modes increases with increasing FA content. We recall that in the orthorhombic phase, the contribution to the inhomogeneous broadening stemming from the dynamic disorder has vanished due to the locking of the MA molecules in the cage voids. On the contrary, the contribution from the static disorder due to a sort of alloying effect when the MA cations are gradually replaced by FA remains unaltered and becomes apparent in the low-temperature phase. Obviously, the MA/FA mixing disorder increases steadily from zero to a maximum for 50% FA content and then diminishes again (see also the discussion below). (ii) As illustrated by the inset of Figure 2, the frequency of the inorganic cage modes decreases with the increasing FA content. This softening is simply due to the increase in lattice constant as FA, which is a larger cation than MA, is incorporated in the material,<sup>17</sup> leading to a weakening of the covalent metal–halogen bonds.

**Temperature-Dependent Photoluminescence Measurements.** Figure 3 shows the evolution with temperature of



**Figure 3.** PL spectra of  $\text{FA}_x\text{MA}_{1-x}\text{PbI}_3$  single crystals for four selected compositions, namely, (a)  $x = 0$ , (b)  $x = 0.2$ , (c)  $x = 0.5$ , and (d)  $x = 1$ , recorded at different temperatures using the red line (633 nm) for excitation. The spectra were normalized to their maximum intensities and plotted with a vertical shift for increasing temperature. The temperature range is indicated (a temperature step of ca. 5 K).

the PL spectra of four  $\text{FA}_x\text{MA}_{1-x}\text{PbI}_3$  single crystals with different FA contents spanning the whole compositional range ( $x = 0, 0.2, 0.5, 1$ ). All spectra were normalized to their absolute maximum intensities and vertically offset to ease their comparison. The complete set of spectra cascades as a function of temperature for the 11 organic-cation compositions studied here is displayed in Figure S2a–k of the Supporting Information. Depending on the composition, the main PL peak exhibits a nonmonotonic temperature behavior, including sudden jumps in the position of its maximum. As explained further below, the jumps and changes in the tendency of the maximum peak energy are indicative of the occurrence of different phase transitions in the temperature range of the experiment. It is important to remark that all changes in the PL emission (as well as in Raman) are fully reversible, even

though there is a certain degree of hysteresis regarding the precise temperature of the discontinuities.

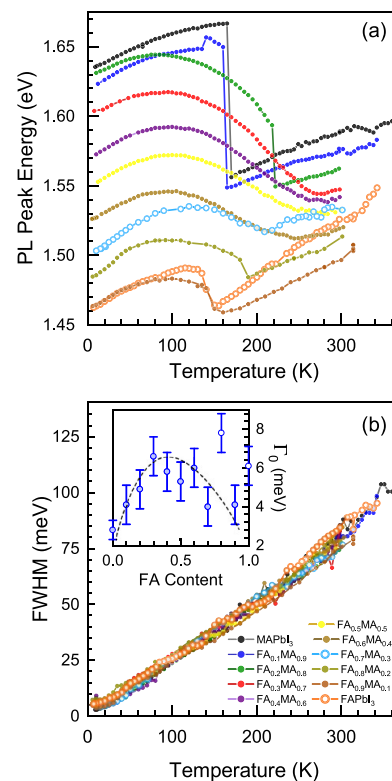
Before discussing the temperature dependence of the PL spectra, we would like to justify the assignment of the main emission peak to free-exciton recombination instead of bimolecular recombination of uncorrelated electron–hole pairs. An inspection of the literature might indicate that this assignment is partly controversial, since the reported values for the exciton binding energy in lead halide perovskites span a wide range from a few meV<sup>40–44</sup> to several tens of meV.<sup>45–49</sup> Nevertheless, recent direct determinations of the exciton binding energy have led to a consensus value of around 15 meV at low temperatures (the orthorhombic phase) in MAPbI<sub>3</sub><sup>50–52</sup> and MAPbBr<sub>3</sub>.<sup>53</sup> Since neither the near band-edge electronic properties like the effective masses nor the dielectric screening changes much in the tetragonal or cubic phases, it is expected that the exciton binding energy also remains unaltered at higher temperatures. In fact, recent ultrafast two-dimensional (2D) electronic spectroscopy investigations yielded for MAPbI<sub>3</sub> a binding energy of about 12 meV at room temperature.<sup>54</sup> With this moderate excitonic binding, the observation of a steplike absorption edge (none or an incipient peaklike feature at the edge) at around ambient temperatures is not surprising, which has been incorrectly interpreted as the absence of excitonic effects.<sup>43,45,55,56</sup> We recall that a steplike profile is the evidence of Coulomb-interaction-mediated correlations between electrons and holes in states of the excitonic energy continuum.<sup>45,57</sup> The absence of a peak just means that bound excitonic states corresponding to the discrete energy spectrum became dissociated because the exciton binding energy is on the order of or smaller than the thermal energy (300 K  $\approx$  26 meV). This, in contrast, does not hinder bound exciton states from playing the main role in emission, since their optical recombination is favored by a much longer lifetime compared to continuum states.<sup>58</sup> Furthermore, our temperature-dependent PL measurements fully support this interpretation.

The PL spectra in Figures 3 and S2 (Supporting Information) thus display the evolution of the free exciton (FE) with decreasing temperature, exhibiting a nonmonotonic shift of its energy and a clear decrease in line width. In view of the relatively small binding energy, the former can be taken as a representative of the temperature dependence of the fundamental band gap of the perovskite solid solutions. The latter is indicative of homogeneously broadened emission peaks, which means a lifetime-limited line width. In high-quality crystals, the homogeneous lifetime broadening is mainly determined by the relaxation channel associated with the scattering of electrons/holes by phonons, thus being strongly temperature dependent. At very low temperatures, the photoexcited carriers can readily form exciton complexes bound to shallow impurities (acceptors and/or donors).<sup>58</sup> In fact, the sharp peaks, which are apparent below the FE energy, become more intense with the decreasing temperature and are ascribed to such bound exciton complexes (see Figures 3a,b and S2a–k). Their properties and the reason for being more pronounced for MA-rich compositions will be discussed in a forthcoming paper.<sup>59</sup>

To analyze the PL spectra of the hybrid perovskites, we used a Gaussian–Lorentzian cross-product function for describing the main emission peak. We notice that the same fitting protocol was also successfully employed for the analysis of the PL spectra of MAPbI<sub>3</sub> as a function of pressure but at ambient

temperature.<sup>35</sup> The expression for the cross-product function, which is given in the Supporting Information, essentially contains three adjustable parameters: the amplitude prefactor  $A$ , the peak energy position  $E_0$ , and the full width at half-maximum (FWHM)  $\Gamma$ . This function is a useful simplification of a Voigt function, which corresponds to the mathematical convolution of a Lorentzian, taking into account the natural line shape due to spontaneous emission, and an inhomogeneously broadened Gaussian, accounting for a normal distribution of exciton energies. There is, actually, a fourth parameter, the so-called line shape-weight parameter  $s$  ( $s = 0$  for pure Gaussian,  $s = 1$  for pure Lorentzian). It turns out that, at temperatures higher than approximately 120 K,  $s$  takes values between 0.5 and 0.75, indicating an almost equal footing of inhomogeneous (Gaussian) and homogeneous (Lorentzian) broadening with a slight preference for the Lorentzian line shape. In contrast, in the low-temperature range,  $s$  adopts much higher values between 0.8 and 0.9, implying that spontaneous emission dominates the low-temperature radiative recombination of excitons in hybrid perovskites.

The values of the fitting parameters corresponding to the peak energy  $E_0$  and the line width  $\Gamma$  are plotted as a function of temperature in Figure 4 for the 11 compositions of the FA<sub>*x*</sub>MA<sub>1–*x*</sub>PbI<sub>3</sub> solid solutions studied here (the PL peak integrated intensities are shown in Figure S3 of the Supporting Information). According to the previous discussion, we consider the shift of the PL peak energy  $E_0$  with temperature



**Figure 4.** (a) Maximum PL peak energy and (b) FWHM plotted as a function of temperature, obtained from the PL line shape fits using a cross-product function (eq 1 of the Supporting Information) for the complete set of compositions of the FA<sub>*x*</sub>MA<sub>1–*x*</sub>PbI<sub>3</sub> series. The inset of part (b) shows the temperature-independent contribution  $\Gamma_0$  to the exciton line width as a function of FA content (eq 1). The dashed line is a guide to the eye.



a representative of the temperature shift of the gap. In this regard, the values of  $E_0$  at room temperature exhibit a clear trend with respect to the organic-cation fraction: the PL emission shifts to the red with the increasing FA content. However, for two compositions, namely, pure FAPbI<sub>3</sub> and the FA<sub>0.7</sub>MA<sub>0.3</sub>PbI<sub>3</sub> mixed crystal (both denoted by open symbols in Figure 4), the red shift of the gap at ambient conditions seems to depart from the overall trend. In both cases, a probable reason is related to the crystal quality of the sample. Concerning the case of the FA content of 70%, a recent study that combines the temperature-dependent PL measurements with spectroscopic ellipsometry<sup>21</sup> indicates that this sample consists of FA- and MA-rich segregated regions separated by regions with high concentration of vacancies (predominantly of MA<sup>60,61</sup>), although maintaining an average stoichiometry of  $x = 0.7$ . Such a spatial segregation, which might be caused by a higher temperature heating of the solutions when growing this particular sample,<sup>17,37</sup> turns out to determine the near band-gap PL and absorption properties of the perovskite mixed crystal. In the case of FAPbI<sub>3</sub>, in contrast, we were not able to study the pristine as-grown sample. For technical reasons, the sample had already transformed into the yellow hexagonal  $\delta$ -phase when received. Although we were able to transform the FAPbI<sub>3</sub> crystal back into the perovskite  $\alpha$ -phase by heating it on a hotplate to about 80 °C for a few minutes,<sup>10</sup> it seems that this treatment was somewhat detrimental for its crystal quality (see also the discussion of the PL FWHM further below).

A careful inspection of the data displayed in Figure 4a indicates the existence of common characteristics in the temperature behavior of  $E_0$ , shared by samples in the whole compositional range. At around room temperature, in the stability range of cubic and tetragonal phases, the gap decreases linearly with decreasing temperature. This at-first-glance atypical behavior has been recently analyzed in MAPbI<sub>3</sub> and ascribed to a roughly equal footing of thermal expansion and electron–phonon renormalization effects.<sup>62</sup> It turns out that this temperature dependence of the gap holds not only for MAPbI<sub>3</sub><sup>62–68</sup> but also for many other halide perovskites like MAPbBr<sub>3</sub>,<sup>53,65,66</sup> MAPbCl<sub>3</sub>,<sup>47</sup> FAPbI<sub>3</sub>,<sup>66,68</sup> FAPbBr<sub>3</sub>,<sup>65,66</sup> CsPbI<sub>3</sub>,<sup>69</sup> CsPbBr<sub>3</sub>,<sup>69,70</sup> MASnI<sub>3</sub>,<sup>71</sup> CsSnI<sub>3</sub>,<sup>72</sup> etc. Moreover, above room temperature, a clear zigzagtype behavior of  $E_0$  is apparent for MAPbI<sub>3</sub> and FA<sub>0.1</sub>MA<sub>0.9</sub>PbI<sub>3</sub> in Figure 4a. According to X-ray diffraction data, the zigzag coincides with the occurrence of the second-order phase transition between the high-temperature cubic phase and the lower-temperature tetragonal phase.<sup>17</sup> For several other compositions, similar behavior can be observed but only after differentiation of the  $E_0$  vs  $T$  curves. For compositions  $x \leq 0.2$ , the energy  $E_0$  exhibits a sudden and abrupt jump to higher values, which, in view of the simultaneous narrowing of the Raman peaks, we ascribe to the occurrence of a first-order tetragonal-to-orthorhombic phase transition. We note that the temperature dependence of  $E_0$  in the orthorhombic phase is almost quadratic. Incidentally, the rigid shift of a group of points of the  $E_0$  vs  $T$  curve just after the phase transition observed for FA<sub>0.1</sub>MA<sub>0.9</sub>PbI<sub>3</sub> is not spurious. On the contrary, the temperature range of the shifted points exactly matches the regime of the coexistence of the tetragonal and orthorhombic phases (see spectra in Figure S2b). We speculate that the energy shift is due to the buildup of inhomogeneous strains in the solid solution, as a consequence of the different unit cell volumes of each phase. At the other compositional end for  $x \geq 0.8$ , in contrast, a less steep jump is observed at temperatures

between 120 and 190 K. We will show that in this case the jump is associated with an isostructural transition between two tetragonal phases. Finally, we point out that for all compositions  $x \geq 0.3$  the phase stable at lower temperatures exhibits a strikingly near-parabolic dependence of the gap. We anticipate here that such behavior is the signature of a third tetragonal phase characteristic of FA/MA mixed crystal perovskites, which displays a peculiar crystal/electronic-structure relationship.

Figure 4b shows the PL peak line width (FWHM) as a function of temperature for the 11 FA<sub>*x*</sub>MA<sub>1-*x*</sub>PbI<sub>3</sub> solid solutions. Essentially, all data points fall onto a common curve, irrespective of FA content, indicating a strong increase of the FWHM with the increasing temperature, as observed for several high-quality perovskite single crystals,<sup>51,73</sup> thin films,<sup>66</sup> and nanocrystals.<sup>69,74</sup> Such marked temperature dependence of the exciton line width is characteristic of an exciton broadening mechanism mediated by electron–phonon interaction given by<sup>75</sup>

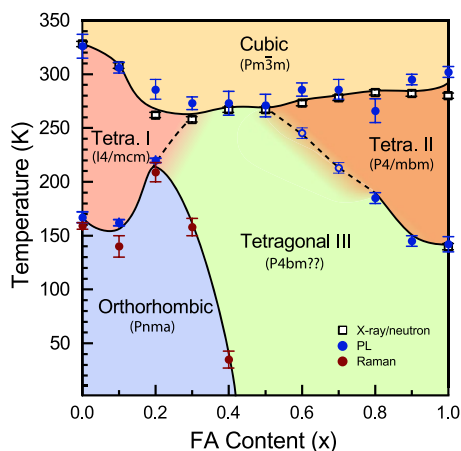
$$\Gamma(T) = \Gamma_0 + \frac{\gamma_{\text{opt}}}{e^{E_{\text{opt}}/k_{\text{B}}T} - 1} \quad (1)$$

where  $\Gamma_0$  is the temperature-independent inhomogeneous broadening, which is mainly determined by the crystal quality;  $\gamma_{\text{opt}}$  is the electron–optical–phonon coupling constant; and  $E_{\text{opt}}$  is the effective optical–phonon energy. Notice that the second term in eq 1 is nothing else than the Bose–Einstein occupation factor for a representative optical mode with an effective frequency, multiplied by an effective coupling strength constant. This is usually referred to as the one-oscillator model of the electron–phonon interaction. In eq 1, we have neglected the contribution stemming from exciton scattering by acoustic phonons because the electron–acoustic–phonon coupling is often several orders of magnitude weaker than for optical phonons.<sup>51,66,73</sup> Using eq 1, we can now proceed to analyze the temperature dependence of the free-exciton line width, looking for correlations between electron–phonon coupling parameters and organic-cation composition. In Figure S4a, we provide for MAPbI<sub>3</sub> an example of a least-squares fit to the FWHM data points with the function of eq 1 and having  $\Gamma_0$ ,  $\gamma_{\text{opt}}$  and  $E_{\text{opt}}$  as adjustable parameters. The values of the parameters yielding the best fit for MAPbI<sub>3</sub> are given in the legend of Figure S4a, whereas the fitting results for  $\gamma_{\text{opt}}$  and  $E_{\text{opt}}$  are plotted as a function of composition in Figure S4b. While the effective phonon energy is almost independent of FA content with an average value of about 5 meV, the electron–phonon coupling strength adopts two different values: ca. 10 meV for the two compositional ends and about 17 meV for intermediate compositions. It is important to note that we have restricted the fit for all compositions to the low-temperature data (as illustrated in Figure S4a for MAPbI<sub>3</sub>), corresponding to either the orthorhombic or the tetragonal phase, where the latter exhibits the parabolic dependence of  $E_0$  on temperature. Despite the fact that eq 1 holds for the high-temperature phases as well, the exponential dependence of the phonon occupation number can be captured by the fitting function only at very low temperatures because of the small value of the effective phonon energy. The values of the fitting parameters are thus no longer uniquely defined for the high-temperature stable phases.

In contrast, the values of the inhomogeneous broadening term  $\Gamma_0$ , depicted in the inset of Figure 4b, do show a dependence on composition. As illustrated by the dashed

curve, this dependence is a bell-shaped function, which roughly correlates with the amount of the disorder introduced in the crystal by mixing MA and FA in different proportions. The two exceptions are the  $\text{FAPbI}_3$  and  $\text{FA}_{0.8}\text{MA}_{0.2}\text{PbI}_3$  samples, which show much stronger residual broadening. This is indicative of a lesser crystal quality, probably due to the instability of FA-rich crystals toward the formation of the hexagonal  $\delta$ -phase. Judging by the sharpness of the exciton peak at low temperatures, the best-quality crystals correspond to pure  $\text{MAPbI}_3$  with a  $\Gamma_0$  value of 2.7(6) meV, which is about half of the best one reported previously.<sup>73</sup>

**Temperature–Composition Phase Diagram of  $\text{FA}_x\text{MA}_{1-x}\text{PbI}_3$ .** Figure 5 displays the temperature–composition



**Figure 5.** Temperature–composition phase diagram of  $\text{FA}_x\text{MA}_{1-x}\text{PbI}_3$  perovskite solid solutions. The symbols represent experimental data (Raman and PL data from this work and X-ray/neutron scattering data from refs 17, 22, 26, 27). The different crystal structures and their symmetry are indicated in the graph. Phase separation lines are a guide to the eye.

tion phase diagram of the  $\text{FA}_x\text{MA}_{1-x}\text{PbI}_3$  solid solutions constructed by optical spectroscopy, employing the temperature-dependent Raman and PL data obtained here combined with literature data from X-ray diffraction and neutron scattering.<sup>17,22,26,27</sup> The identification of the different crystal structures and their assignment to the corresponding space groups are also from the literature and were discussed briefly in the Introduction section. The closed red circles correspond to the transition temperatures determined by Raman scattering. They are obtained from the points at which the strong narrowing of the Raman peaks is observed, as a consequence of the locking of the MA cations inside the cage voids. This occurs when the material transforms into the orthorhombic phase with decreasing temperature. Figure S5 of the Supporting Information illustrates this effect in the case of  $\text{MAPbI}_3$ . In Figure S1a–h, we further show that, apart from the qualitative changes in the Raman spectra line shapes, the transition temperature can also be determined from the Raman data corresponding to either the phonon frequencies or the line widths. Note that for  $x = 0.3$  and  $0.4$  only the Raman technique was able to pinpoint such phase transformations. In addition, the phase transition temperatures denoted by the blue circles were inferred either from abrupt variations of the PL peak energies or from changes in their temperature dependence. Particularly tricky is the determination of the cubic-to-tetragonal-I/II transitions and the transitions into the

tetragonal-III phase. For the former, the transition temperature is taken from the middle point of the zigzag dependence of the  $E_0$  vs  $T$  curve, often visible only in the first derivative curve. For the latter case, the inflection point from a linear to a quadratic temperature dependence of  $E_0$  was considered as the setting-in of the phase transformation. The procedure to determine the different transition temperatures from the PL data is illustrated in Figure S6 of the Supporting Information. When available, the PL data agree well with the phase transition temperatures of the literature (open black squares).

The general picture that emerges from this phase diagram is the following: at room temperature or slightly above as for  $\text{MAPbI}_3$  and  $\text{FA}_{0.1}\text{MA}_{0.9}\text{PbI}_3$ , the most stable phase is a simple cubic one with  $Pm\bar{3}m$  symmetry, which is characterized by straight metal–halogen–metal bonds and fully unlocked organic cations inside the cage voids.<sup>22</sup> Such a highly symmetric structure is stabilized at high temperatures because the entropy reduction of the inorganic cage is overcompensated by the strong dynamic disorder of the MA/FA organic cations, as inferred from molecular dynamics simulations.<sup>27,76</sup> For MA-rich perovskites ( $x \leq 0.2$ ), the same structural behavior as for  $\text{MAPbI}_3$  is observed with decreasing temperature: cubic  $Pm\bar{3}m \rightarrow$  tetragonal-I  $I4/mcm \rightarrow$  orthorhombic  $Pnma$ , with the latter transition being clearly of the first order with a pronounced jump in the PL peak energy. We find out that because the FA molecule is larger and more symmetric but less polar than MA, a tetragonal crystal structure is favored at low temperatures and FA compositions  $x > 0.4$ , to the detriment of the orthorhombic phase. As a matter of fact, the phase transition sequence for FA-rich compounds and decreasing temperature is cubic  $Pm\bar{3}m \rightarrow$  tetragonal-II  $P4/mbm \rightarrow$  tetragonal-III. For the latter structure, which corresponds to  $\gamma$ - $\text{FAPbI}_3$ ,<sup>27</sup> the space-group assignment is uncertain. A unit cell refinement of neutron data indicates that a  $P4bm$  symmetry is plausible but with a certain degree of disorder present in the structure.<sup>27</sup> Strikingly, the isostructural (tetragonal-II to tetragonal-III) transformation, which occurs between 200 and 150 K, exhibits a sort of critical point at  $x = 0.7$ . For FA contents  $x \geq 0.7$ , the transition takes place exhibiting a marked jump in the PL peak energy  $E_0$  (see Figure 4a); the phase separation line is indicated with a solid curve in the phase diagram of Figure 5. In contrast, for FA concentrations lower than 70% (but higher than 20%), the evolution of  $E_0$  with the decreasing temperature is continuous, mimicking supercritical behavior (phase separation thus marked with a dashed line in Figure 5). Finally, for intermediate FA concentrations, the stability range of the tetragonal-III phase extends all the way from very low temperature to more than 250 K, where the  $\text{FA}_x\text{MA}_{1-x}\text{PbI}_3$  mixed crystals transform into the cubic phase. Recent ab initio molecular dynamics calculations have shown that the replacement of FA by a smaller A-site cation like MA causes an increased tilting of the  $\text{PbI}_6$  octahedra to compensate for the reduced space filling offered by the smaller cation.<sup>76</sup> Based on these simulation results and the striking similarity with the orthorhombic phase of the parabolic temperature dependence of the PL peak energy, we speculate that the tetragonal-III structure is also characterized by pronounced tilting of the corner-sharing octahedra. We further expect that the average tilting increases with decreasing temperature and competes with the effect of electron–phonon renormalization,<sup>62</sup> giving rise to the observed nonmonotonic variation of the gap with temperature. Further theoretical and experimental investiga-

tions of this unusual behavior are certainly necessary to unravel its origin.

## CONCLUSIONS

In summary, by combining optical spectroscopy techniques such as Raman and photoluminescence as a function of temperature, we were able to draw the temperature–composition phase diagram for hybrid  $\text{FA}_x\text{MA}_{1-x}\text{PbI}_3$  perovskite solid solutions. Despite the fact that the organic-cation molecules are loosely bonded inside the inorganic cage just by steric interactions, their presence and, in particular, their ability to move, rotate, or librate inside the cage voids turn out to be the determinant for the structural phase stability of the soft skeleton of corner-sharing metal-halide octahedra. At temperatures around ambient and higher, the organic molecules of the A-site cations are freely moving in the inorganic cage voids. The fast molecular dynamics gives rise to almost spherical atomic-density clouds, which favors a cubic environment, hence imposing a cubic symmetry on the labile but heavy arrangement of corner-sharing  $\text{PbI}_6$  octahedra. This holds for the whole compositional range. At temperatures lower than roughly 150 K, the interplay between the cooling of the molecular dynamics and the gradual quenching of the tilting vibrations of the octahedra leads to the mutual locking of the MA/FA cations in different directions in space and of the octahedra at well-defined tilting angles. As a result, the hybrid perovskites transform into crystal structures with lower symmetry but high deformation, at least regarding the tilting angles (metal–halide–metal bonds with angles much lower than  $180^\circ$ ). These are an orthorhombic phase for MA-rich mixed crystals and the disordered Tetra-III phase for FA compositions higher than 40%. At intermediate temperatures, the situation is half way between the high- and low-temperature ones. For both compositional ends, the inorganic cage adopts a tetragonal structure, with the organic molecules freely moving solely in the tetragonal plane and straight metal–halide–metal bonds perpendicular to it. In contrast, for intermediate concentrations, an inhomogeneous strain develops across the mixed crystal. The inhomogeneity is a consequence of the different sizes, polarities, and conformations of the MA and FA molecules, which are translated to the immediate surrounding of the organic molecule, at least to the unit cell in which it is contained. An efficient way to accommodate the inhomogeneous strain is by tilting the octahedra indistinctly in different directions, following the disorderly oriented organic molecules. These are the two main characteristics of the Tetra-III phase: high disorder and tilting. In view of the importance of the link between the crystal structure and the electronic, optical, and vibrational properties of a material, we expect that the knowledge gained here would positively impact the improvement of the optoelectronic performance and longstanding stability of mixed organic-cation hybrid halide perovskites.

## ASSOCIATED CONTENT

### Supporting Information

The Supporting Information is available free of charge at <https://pubs.acs.org/doi/10.1021/acs.jpcc.9b10185>.

Complete set of Raman and PL spectra recorded as a function of temperature in the range 10–365 K for the 11 compositions of the  $\text{FA}_x\text{MA}_{1-x}\text{PbI}_3$  system; details of the fits performed to the exciton line width data points

using a single oscillator model for the electron–phonon interaction contribution (PDF)

## AUTHOR INFORMATION

### Corresponding Author

**Alejandro R. Goñi** – Institut de Ciència de Materials de Barcelona (ICMAB-CSIC), 08193 Bellaterra, Spain; ICREA, 08010 Barcelona, Spain; [orcid.org/0000-0002-1193-3063](https://orcid.org/0000-0002-1193-3063); Email: [goni@icmab.es](mailto:goni@icmab.es)

### Authors

**Adrián Francisco-López** – Institut de Ciència de Materials de Barcelona (ICMAB-CSIC), 08193 Bellaterra, Spain

**Bethan Charles** – Department of Chemistry & Centre for Sustainable Chemical Technologies, University of Bath, Bath BA2 7AY, U.K.

**M. Isabel Alonso** – Institut de Ciència de Materials de Barcelona (ICMAB-CSIC), 08193 Bellaterra, Spain

**Miquel Garriga** – Institut de Ciència de Materials de Barcelona (ICMAB-CSIC), 08193 Bellaterra, Spain

**Mariano Campoy-Quiles** – Institut de Ciència de Materials de Barcelona (ICMAB-CSIC), 08193 Bellaterra, Spain;

[orcid.org/0000-0002-8911-640X](https://orcid.org/0000-0002-8911-640X)

**Mark T. Weller** – Department of Chemistry & Centre for Sustainable Chemical Technologies, University of Bath, Bath BA2 7AY, U.K.; Department of Chemistry, Cardiff University, Wales CF10 3AT, U.K.; [orcid.org/0000-0002-7475-0379](https://orcid.org/0000-0002-7475-0379)

Complete contact information is available at:

<https://pubs.acs.org/doi/10.1021/acs.jpcc.9b10185>

### Notes

The authors declare no competing financial interest.

## ACKNOWLEDGMENTS

The Spanish Ministerio de Ciencia, Innovación y Universidades is gratefully acknowledged for its support through Grant No. SEV-2015-0496 in the framework of the Spanish Severo Ochoa Centre of Excellence program and through Grants MAT2015-70850-P (HIBRI2) and PGC2018-095411-B-I00 (RAINBOW). We also thank the Catalan agency AGAUR for grant 2017-SGR-00488. AFL acknowledges an FPI fellowship (BES-2016-076913) from the Spanish Ministerio co-financed by the European Social Fund and the Ph.D. programme in Materials Science from Universitat Autònoma de Barcelona in which he is enrolled. B.C. thanks the EPSRC for Ph.D. studentship funding via the CSCT CDT (EP/G03768X/1).

## REFERENCES

- (1) Grätzel, M. The Rise of Highly Efficient and Stable Perovskite Solar Cells. *Acc. Chem. Res.* **2017**, *50*, 487–491.
- (2) Yoo, J. J.; Wieghold, S.; Sponseller, M. C.; Chua, M. R.; Bertram, S. N.; Hartono, N. T. P.; Tresback, J. S.; Hansen, E. C.; Correa-Baena, J.-P.; Bulović, V.; et al. An Interface Stabilized Perovskite Solar Cell with High Stabilized Efficiency and Low Voltage Loss. *Energy Environ. Sci.* **2019**, *12*, 2192–2199.
- (3) See Best Research-Cell Efficiency Chart; National Renewable Energy Laboratory (NREL), Golden, Colorado, USA. [www.nrel.gov/pv/cell-efficiency.html](http://www.nrel.gov/pv/cell-efficiency.html), 2019.
- (4) Tan, Z.-K.; Moghaddam, R. S.; Lai, M. L.; Docampo, P.; Higler, R.; Deschler, F.; Price, M.; Sadhanala, A.; Pazos, L. M.; Credgington, D.; et al. Light-Emitting Diodes Based on Organometal Halide Perovskite. *Nat. Nanotechnol.* **2014**, *9*, 687–692.



- (5) Stranks, S. D.; Snaith, H. J. Metal-Halide Perovskites for Photovoltaic and Light-Emitting Devices. *Nat. Nanotechnol.* **2015**, *10*, 391–402.
- (6) Sutherland, B. R.; Sargent, E. H. Perovskite Photonic Sources. *Nat. Photonics* **2016**, *10*, 295–302.
- (7) Leguy, A. M. A.; Hu, Y.; Campoy-Quiles, M.; Alonso, M. I.; Weber, O. J.; Azarhoosh, P.; Van Schilfgaarde, M.; Weller, M. T.; Bein, T.; Nelson, J.; et al. Reversible Hydration of  $\text{CH}_3\text{NH}_3\text{PbX}_3$  in Films, Single Crystals, and Solar Cells. *Chem. Mater.* **2015**, *27*, 3397–3407.
- (8) Gottesman, R.; Gouda, L.; Kalanoor, B. S.; Haltzi, E.; Tirosh, S.; Rosh-Hodesh, E.; Tischler, Y.; Zaban, A.; et al. Photoinduced Reversible Structural Transformations in Free Standing  $\text{CH}_3\text{NH}_3\text{PbI}_3$  Films. *J. Phys. Chem. Lett.* **2015**, *6*, 2332–2338.
- (9) Rehman, W.; McMeekin, D. P.; Patel, J. B.; Milot, R. L.; Johnston, M. B.; Smaith, H. J.; Herz, L. M. Photovoltaic Mixed-Cation Lead Mixed-Halide Perovskites: Links Between Crystallinity, Photo-Stability and Electronic Properties. *Energy Environ. Sci.* **2017**, *10*, 361–369.
- (10) Charles, B.; Dillon, J.; Weber, O. J.; Islam, M. S.; Weller, M. T. Understanding the Stability of Mixed A-Cation Lead Iodide Perovskites. *J. Mater. Chem. A* **2017**, *5*, 22495–22499.
- (11) Wang, Q.; Chen, B.; Liu, Y.; Deng, Y.; Bai, Y.; Dong, Q.; Huang, J. Scaling behavior of moisture-induced grain degradation in polycrystalline hybrid perovskite thin films. *Energy Environ. Sci.* **2017**, *10*, 516–522.
- (12) Dhamaniya, B. P.; Chhillar, P.; Roose, B.; Dutta, V.; Pathak, S. K. Unraveling the Effect of Crystal Structure on Degradation of Methylammonium Lead Halide Perovskite. *ACS Appl. Mater. Interfaces* **2019**, *11*, 22228–22239.
- (13) Faghihnasiri, M.; Izadifard, M.; Ghazi, M. E. DFT Study of Mechanical Properties and Stability of Cubic Methylammonium Lead Halide Perovskites ( $\text{CH}_3\text{NH}_3\text{PbX}_3$ , X = I, Br, Cl). *J. Phys. Chem. C* **2017**, *121*, 27059–27070.
- (14) Domanski, K.; Roose, B.; Matsui, T.; Saliba, M.; Turren-Cruz, S.-H.; Correa-Baena, J.-P.; Carmona, C. R.; Richardson, G.; Foster, J. M.; De Angelis, F.; et al. Migration of cations induces reversible performance losses over day/night cycling in perovskite solar cells. *Energy Environ. Sci.* **2017**, *10*, 604–613.
- (15) Liu, J.; Yin, X.; Liu, X.; Que, M.; Que, W. Multi-Influences of Ionic Migration on Illumination-Dependent Electrical Performances of Inverted Perovskite Solar Cells. *J. Phys. Chem. C* **2017**, *121*, 16051–16057.
- (16) Luo, Y.; Khoram, P.; Brittman, S.; Zhu, Z.; Lai, B.; Ong, S. P.; Garnett, E. C.; Fenning, D. P. Direct Observation of Halide Migration and its Effect on the Photoluminescence of Methylammonium Lead Bromide Perovskite Single Crystals. *Adv. Mater.* **2017**, *29*, No. 1703451.
- (17) Weber, O. J.; Charles, B.; Weller, M. T. Phase Behaviour and Composition in the Formamidinium-Methylammonium Hybrid Lead Iodide Perovskite Solid Solution. *J. Mater. Chem. A* **2016**, *4*, 15375–15382.
- (18) Jacobsson, T. J.; Correa-Baena, J.-P.; Pazoki, M.; Saliba, M.; Schenk, K.; Grätzel, M.; Hagfeldt, A. Exploration of the Compositional Space for Mixed Lead Halogen Perovskites for High Efficiency Solar Cells. *Energy Environ. Sci.* **2016**, *9*, 1706–1724.
- (19) Yang, Z.; Chueh, C.-C.; Liang, P.-W.; Crump, M.; Lin, F.; Zhu, Z.; Jen, A. K.-Y. Effects of Formamidinium and Bromide Ion Substitution in Methylammonium Lead Triiodide Toward High-Performance Perovskite Solar Cells. *Nano Energy* **2016**, *22*, 328–337.
- (20) Pisanu, A.; Ferrara, C.; Quadrelli, P.; Guizzetti, G.; Patrini, M.; Milanese, C.; Tealdi, C.; Malavasi, L. The  $\text{FA}_{1-x}\text{MA}_x\text{PbI}_3$  System: Correlations Among Stoichiometry Control, Crystal Structure, Optical Properties, and Phase Stability. *J. Phys. Chem. C* **2017**, *121*, 8746–8751.
- (21) Alonso, M. I.; Charles, B.; Francisco-López, A.; Garriga, M.; Weller, M. T.; Goñi, A. R. Spectroscopic Ellipsometry Study of  $\text{FA}_{1-x}\text{MA}_x\text{PbI}_3$  Hybrid Perovskite Single Crystals. *J. Vac. Sci. Technol. B* **2019**, *37*, No. 062901.
- (22) Weller, M. T.; Weber, O. J.; Henry, P. F.; Di Pumpo, A. M.; Hansen, T. C. Complete Structure and Cation Orientation in the Perovskite Photovoltaic Methylammonium Lead Iodide Between 100 and 352 K. *Chem. Commun.* **2015**, *51*, 4180–4183.
- (23) Bakulin, A. A.; Selig, O.; Bakker, H. J.; Rezus, Y. L. A.; Müller, C.; Glaser, T.; Lovrincic, R.; Sun, Z.; Chen, Z.; Walsh, A.; et al. Real-Time Observation of Organic Cation Reorientation in Methylammonium Lead Iodide Perovskites. *J. Phys. Chem. Lett.* **2015**, *6*, 3663–3669.
- (24) Leguy, A. M. A.; Frost, J. M.; McMahon, A. P.; Sakai, V. G.; Kochelmann, W.; Law, C.-H.; Li, X.; Foglia, F.; Walsh, A.; O'Regan, J.; et al. The Dynamics of Methylammonium Ions in Hybrid Organic-Inorganic Perovskite Solar Cells. *Nat. Commun.* **2015**, *6*, No. 7124.
- (25) Chen, T.; Foley, B. J.; Ipek, B.; Tyagi, M.; Copley, J. R. D.; Brown, C. M.; Choi, J. J.; Lee, S.-H. Rotational Dynamics of Organic Cations in the  $\text{CH}_3\text{NH}_3\text{PbI}_3$  Perovskite. *Phys. Chem. Chem. Phys.* **2015**, *17*, 31278–31286.
- (26) Weller, M. T.; Weber, O. J.; Frost, J. M.; Walsh, A. Cubic Perovskite Structure of Black Formamidinium Lead Iodide,  $\alpha$ - $[\text{HC}(\text{NH}_2)_2]\text{PbI}_3$ , at 298 K. *J. Phys. Chem. Lett.* **2015**, *6*, 3209–3212.
- (27) Weber, O. J.; Ghosh, D.; Gaines, S.; Henry, P. F.; Walker, A. B.; Islam, M. S.; Weller, M. T. Phase Behavior and Polymorphism of Formamidinium Lead Iodide. *Chem. Mater.* **2018**, *30*, 3768–3778.
- (28) Chen, T.; Foley, B. J.; Park, C.; Brown, C. M.; Harriger, L. W.; Lee, J.; Ruff, J.; Yoon, M.; Choi, J. J.; Lee, S.-H. Entropy-Driven Structural Transition and Kinetic Trapping in Formamidinium Lead Iodide Perovskite. *Sci. Adv.* **2016**, *2*, No. e160165.
- (29) Stoumpos, C. C.; Malliakas, C. D.; Kanatzidis, M. G. Semiconducting Tin and Lead Iodide Perovskites with Organic Cations: Phase Transition, High Mobilities, and Near-Infrared Photoluminescence Properties. *Inorg. Chem.* **2013**, *52*, 9019–9038.
- (30) Frost, J. M.; Walsh, A. What is Moving in Hybrid Halide Perovskite Solar Cells. *Acc. Chem. Res.* **2016**, *49*, 528–535.
- (31) Gallop, N. P.; Selig, O.; Giubertoni, G.; Bakker, H. J.; Rezus, Y. L. A.; Frost, J. M.; Jansen, T. L. C.; Lovrincic, R.; Bakulin, A. A. Rotational Cation Dynamics in Metal Halide Perovskites: Effect on Phonons and Material Properties. *J. Phys. Chem. Lett.* **2018**, *9*, 5987–5997.
- (32) Brivio, F.; Frost, J. M.; Skelton, J. M.; Jackson, A. J.; Weber, O. J.; Weller, M. T.; Goñi, A. R.; Leguy, A. M. A.; Barnes, P. R. F.; Walsh, A. Lattice Dynamics and Vibrational Spectra of the Orthorhombic, Tetragonal, and Cubic Phases of Methylammonium Lead Iodide. *Phys. Rev. B* **2015**, *92*, No. 144308.
- (33) Leguy, A. M. A.; Goñi, A. R.; Frost, J. M.; Skelton, J.; Brivio, F.; Rodríguez-Martínez, X.; Weber, O. J.; Pallipurath, A.; Alonso, M. I.; Campoy-Quiles, M.; Weller, M. T.; Nelson, J.; Walsh, A.; Barnes, P. R. F. Dynamic Disorder, Phonon Lifetimes, and the Assignment of Modes to the Vibrational Spectra of Methylammonium Lead Halide Perovskites. *Phys. Chem. Chem. Phys.* **2016**, *18*, 27051–27066.
- (34) Sharma, R.; Menahem, M.; Dai, Z.; Gao, L.; Brenner, T. M.; Yadgarov, L.; Zhang, J.; Rakita, Y.; Korobko, R.; Pinkas, I.; Rappe, A. M.; Yaffe, O. Halide Perovskites under Polarized Light: Vibrational Symmetry Analysis using Polarized Raman. 2019. arXiv:1912.00363. arXiv.org e-Print archive. <https://arxiv.org/pdf/1912.00363.pdf>.
- (35) Francisco-López, A.; Charles, B.; Weber, O. J.; Alonso, M. I.; Garriga, M.; Campoy-Quiles, M.; Weller, M. T.; Goñi, A. R. Pressure-Induced Locking of Methylammonium Cations Versus Amorphization in Hybrid Lead Iodide Perovskites. *J. Phys. Chem. C* **2018**, *122*, 22073–22082.
- (36) Ghosh, D.; Aziz, A.; Dawson, J. A.; Walker, A. B.; Islam, M. S. Putting the Squeeze on Lead Iodide Perovskites: Pressure-Induced Effects to Tune Their Structural and Optoelectronic Behavior. *Chem. Mater.* **2019**, *31*, 4063–4071.
- (37) Saidaminov, M. I.; Abdelhady, A. L.; Murali, B.; Alarousu, E.; Burlakov, V. M.; Peng, W.; Dursun, I.; Wang, L.; He, Y.; Maculan, G.; et al. High-Quality Bulk Hybrid Perovskite Single Crystals within Minutes by Inverse Temperature Crystallization. *Nat. Commun.* **2015**, *6*, No. 7586.

- (38) Wojdyr, M. Fityk: A General-Purpose Peak Fitting Program. *J. Appl. Crystallogr.* **2010**, *43*, 1126–1128.
- (39) Sendner, M.; Nayak, P. K.; Egger, D. A.; Beck, S.; Müller, C.; Epding, B.; Kowalsky, W.; Kronik, L.; Snaith, H. J.; Puccia, A.; et al. Optical Phonons in Methylammonium Lead Halide Perovskites and Implications for Charge Transport. *Mater. Horiz.* **2016**, *3*, 613–620.
- (40) Even, J.; Pedesseau, L.; Katan, C. Analysis of Multivalley and Multibandgap Absorption and Enhancement of Free Carriers Related to Exciton Screening in Hybrid Perovskites. *J. Phys. Chem. C* **2014**, *118*, 11566–11572.
- (41) Frost, J. M.; Butler, K. T.; Brivio, F.; Hendon, C. H.; van Schilgarde, M.; Walsh, A. Atomistic Origins of High-Performance in Hybrid Halide Perovskite Solar Cells. *Nano Lett.* **2014**, *14*, 2584–2590.
- (42) Fang, H.-H.; Raissa, R.; Abdu-Aguye, M.; Adjokatse, S.; Blake, G. R.; Even, J.; Loi, M. A. Photophysics of Organic-Inorganic Hybrid Lead Iodide Perovskite Single Crystals. *Adv. Funct. Mater.* **2015**, *25*, 2378–2385.
- (43) Shi, D.; Adinolfi, V.; Comin, R.; Yuan, M.; Alarousu, E.; Buin, A.; Chen, Y.; Hoogland, S.; Rothenberger, A.; Katsiev, K.; et al. Low Trap-State Density and Long Carrier Diffusion in Organolead Trihalide Perovskite Single Crystals. *Science* **2015**, *347*, 519–522.
- (44) Patel, J. B.; Lin, Q.; Zadvorna, O.; Davies, C. L.; Herz, L. M.; Johnston, M. B. Photocurrent Spectroscopy of Perovskite Solar Cells Over a Wide Temperature Range from 15 to 350 K. *J. Phys. Chem. Lett.* **2018**, *9*, 263–268.
- (45) Saba, M.; Cadelano, M.; Marongiu, D.; Chen, F.; Sarritzu, V.; Sestu, N.; Figus, C.; Aresti, M.; Piras, R.; Geddo Lehmann, A.; et al. Correlated Electron-Hole Plasma in Organometal Perovskites. *Nat. Commun.* **2014**, *5*, No. 5049.
- (46) D'Innocenzo, V.; Grancini, G.; Alcocer, M. J.-P.; Kandada, A. R. S.; Stranks, S. D.; Lee, M. M.; Lanzani, G.; Snaith, H. J.; Petrozza, A. Excitons Versus Free Charges in Organo-Lead Tri-Halide Perovskites. *Nat. Commun.* **2014**, *5*, No. 3586.
- (47) Wu, K.; Bera, A.; Ma, C.; Du, Y.; Yang, Y.; Li, L.; Wu, T. Temperature-Dependent Excitonic Photoluminescence of Hybrid Organometal Halide Perovskite Films. *Phys. Chem. Chem. Phys.* **2014**, *16*, 22476–22481.
- (48) Dong, Q.; Fang, Y.; Shao, Y.; Mulligan, P.; Qiu, J.; Cao, L.; Huang, J. Electron-Hole Diffusion Lengths >175  $\mu\text{m}$  in Solution-Grown  $\text{CH}_3\text{NH}_3\text{PbI}_3$  Single Crystals. *Science* **2015**, *347*, 967–970.
- (49) Galkowski, K.; Mitioglu, A. A.; Surrante, A.; Yang, Z.; Maude, D. K.; Kossaki, P.; Eperon, G. E.; Wang, J. T.-W.; Snaith, H. J.; Plochocka, P.; et al. Spatially Resolved Studies of the Phases and Morphology of Methylammonium and Formamidinium Lead Tri-Halide Perovskites. *Nanoscale* **2017**, *9*, 3222–3230.
- (50) Miyata, A.; Mitioglu, A.; Plochocka, P.; Portugall, O.; Wang, J. T.-W.; Stranks, S. D.; Snaith, H. J.; Nicholas, R. J. Direct Measurement of the Exciton Binding Energy and Effective Masses for Charge Carriers in Organic-Inorganic Tri-Halide Perovskites. *Nat. Phys.* **2015**, *11*, 582–587.
- (51) Phuong, L. Q.; Nakaike, Y.; Wakamiya, A.; Kanemitsu, Y. Free Excitons and Exciton-Phonon Coupling in  $\text{CH}_3\text{NH}_3\text{PbI}_3$  Single Crystals Revealed by Photocurrent and Photoluminescence Measurements at Low Temperatures. *J. Phys. Chem. Lett.* **2016**, *7*, 4905–4910.
- (52) Liu, Z.; Bhamu, K. C.; Luo, L.; Shah, S.; Park, J.-M.; Cheng, D.; Long, M.; Biswas, R.; Fungara, F.; Shinar, R.; et al. Spatial-Temporal Spectroscopy Characterizations and Electronic Structure of Methylammonium Perovskites. *MRS Commun.* **2018**, 961–969.
- (53) Tilchin, J.; Dirin, D. N.; Maikov, G. I.; Sashchiuk, A.; Kovalenko, M. V.; Lifshitz, E. Hydrogen-Like Wannier-Mott Excitons in Single Crystal of Methylammonium Lead Bromide Perovskite. *ACS Nano* **2016**, *10*, 6363–6371.
- (54) Jha, A.; Duan, H.-G.; Tiwari, V.; Nayak, P. K.; Snaith, H. J.; Thorwart, M.; Miller, R. J. D. Direct Observation of the Ultrafast Exciton Dissociation in Lead-iodide Perovskite by 2D Electronic Spectroscopy. *ACS Photonics* **2018**, *5*, 852–860.
- (55) Grancini, G.; Kandada, A. R. S.; Frost, J. M.; Barker, A. J.; De Bastiani, M.; Gandini, M.; Marras, S.; Lanzani, G.; Walsh, A.; Petrozza, A. Role of Microstructure in the Electron-Hole Interaction of Hybrid Lead Halide Perovskites. *Nat. Photon.* **2015**, *9*, 695–701.
- (56) Wu, X.; Trinh, M. T.; Niesner, D.; Zhu, H.; Norman, Z.; Owen, J. S.; Yaffe, O.; Kudisch, B. J.; Zhu, X.-Y. Trap States in Lead Iodide Perovskites. *J. Am. Chem. Soc.* **2015**, *137*, 2089–2096.
- (57) Goñi, A. R.; Syassen, K. Optical Properties of Semiconductors Under Pressure. *Semicond. Semimetals* **1998**, *54*, 247–425.
- (58) Klingshirn, C. F. *Semiconductor Optics*; Springer, Berlin, 1997.
- (59) Francisco-López, A.; Charles, B.; Alonso, M. I.; Garriga, M.; Campoy-Quiles, M.; Weller, M. T.; Goñi, A. R. *Shallow-Defect Photophysics of Mixed Organic-Cation Lead Iodide Perovskites from Low-Temperature Photoluminescence*. Unpublished.
- (60) Oranskaia, A.; Yin, J.; Bakr, O. M.; Brédas, J.-L.; Mohammed, O. F. Halogen Migration in Hybrid Perovskites: The Organic Cation Matters. *J. Phys. Chem. Lett.* **2018**, *9*, 5474–5480.
- (61) Meggiolaro, D.; De Angelis, F. First-Principle Modeling of Defects in Lead Halide Perovskites: Best Practices and Open Issues. *ACS Energy Lett.* **2018**, *3*, 2206–2222.
- (62) Francisco López, A.; Charles, B.; Weber, O. J.; Alonso, M. I.; Garriga, M.; Campoy-Quiles, M.; Weller, M. T.; Goñi, A. R. Equal Footing of Thermal Expansion and Electron-Phonon Interaction in the Temperature Dependence of Lead Halide Perovskite Band Gaps. *J. Phys. Chem. Lett.* **2019**, *10*, 2971–2977.
- (63) Foley, B. J.; Marlowe, D. L.; Sun, K.; Saidi, W. A.; Scudiero, L.; Gupta, M. C.; Choi, J. J. Temperature Dependent Energy Levels of Methylammonium Lead Iodide Perovskite. *Appl. Phys. Lett.* **2015**, *106*, No. 243904.
- (64) Milot, R. L.; Eperon, G. E.; Snaith, H. J.; Johnston, M. B.; Herz, L. M. Temperature-Dependent Charge-Carrier Dynamics in  $\text{CH}_3\text{NH}_3\text{PbI}_3$  Perovskite Thin Films. *Adv. Funct. Mater.* **2015**, *25*, 6218–6227.
- (65) Dar, M. I.; Jacopin, G.; Meloni, S.; Mattoni, A.; Arora, N.; Boziki, A.; Zakeeruddin, S. M.; Rothlisberger, U.; Grätzel, M. Origin of Unusual Gap Shift and Dual Emission in Organic-Inorganic Lead Halide Perovskites. *Sci. Adv.* **2016**, *2*, No. e1601156.
- (66) Wright, A. D.; Verdi, C.; Milot, R. L.; Eperon, G. E.; Pérez-Osorio, M. A.; Snaith, H. J.; Giustino, F.; Johnston, M. B.; Herz, L. M. Electron-Phonon Coupling in Hybrid Lead Halide Perovskites. *Nat. Commun.* **2016**, *7*, No. 11755.
- (67) Saidi, W. A.; Poncé, S.; Monserrat, B. Temperature Dependence of the Energy Levels of Methylammonium Lead Iodide Perovskite from First-Principles. *J. Phys. Chem. Lett.* **2016**, *7*, 5247–5252.
- (68) Chen, T.; Chen, W.-L.; Foley, B. J.; Lee, J.; Ruff, J. P. C.; Ko, J. Y. P.; Brown, C. M.; Harriger, L. W.; Zhang, D.; Park, C.; et al. Origin of Long Lifetime of Band-Edge Charge Carriers in Organic-Inorganic Lead Iodide Perovskites. *Proc. Natl. Acad. Sci. U.S.A.* **2017**, *114*, 7519–7524.
- (69) Saran, R.; Heuer-Jungemann, A.; Kanaras, A. G.; Curry, R. J. Giant Bandgap Renormalization and Exciton-Phonon Scattering in Perovskite Nanocrystals. *Adv. Opt. Mater.* **2017**, *5*, No. 1700231.
- (70) Shinde, A.; Gahlaut, R.; Mahamuni, S. Low-Temperature Photoluminescence Studies of  $\text{CsPbBr}_3$  Quantum Dots. *J. Phys. Chem. C* **2017**, *121*, 14872–14878.
- (71) Parrott, E. S.; Milot, R. L.; Stergiopoulos, T.; Snaith, H. J.; Johnston, M. B.; Herz, L. M. Effect of Structural Phase Transition on Charge-Carrier Lifetimes and Defects in  $\text{CH}_3\text{NH}_3\text{SnI}_3$  Perovskite. *J. Phys. Chem. Lett.* **2016**, *7*, 1321–1326.
- (72) Yu, C.; Chen, Z.; Wang, J. J.; Pfenninger, W.; Vockic, N.; Kenney, J. T.; Shum, K. Temperature Dependence of the Band Gap of Perovskite Semiconductor Compound  $\text{CsSnI}_3$ . *J. Appl. Phys.* **2011**, *110*, No. 063526.
- (73) Diab, H.; Trippé-Allard, G.; Lédée, F.; Jemli, K.; Vilar, Ch.; Bouchez, G.; Jacques, V. L. R.; Tejada, A.; Even, J.; Lauret, J.-S.; et al. Narrow Linewidth Excitonic Emission in Organic-Inorganic Lead Iodide Perovskite Single Crystals. *J. Phys. Chem. Lett.* **2016**, *7*, 5093–5100.
- (74) Pflugsten, O.; Klein, J.; Protesescu, L.; Bodnarchuk, M. I.; Kovalenko, M. V.; Bacher, G. Phonon Interaction and Phase



Transition in Single Formamidinium Lead Bromide Quantum Dots. *Nano Lett.* **2018**, *18*, 4440–4446.

(75) Rudin, S.; Reinecke, T. L.; Segall, B. Temperature-Dependent Exciton Linewidths in Semiconductors. *Phys. Rev. B* **1990**, *42*, 11218–11231.

(76) Ghosh, D.; Walsh Atkins, P.; Islam, M. S.; Walker, A. B.; Eames, C. Good Vibrations: Locking of Octahedral Tilting in Mixed-Cation Iodide Perovskites for Solar Cells. *ACS Energy Lett.* **2017**, *2*, 2424–2429.



**Supporting Information**

**Phase Diagram of**

**Methylammonium/Formamidinium Lead Iodide**

**Perovskite Solid Solutions from Temperature**

**Dependent Photoluminescence and Raman**

**Spectroscopy**

Adrián Francisco-López,<sup>†</sup> Bethan Charles,<sup>‡</sup> M. Isabel Alonso,<sup>†</sup> Miquel  
Garriga,<sup>†</sup> Mariano Campoy-Quiles,<sup>†</sup> Mark T. Weller,<sup>‡,¶</sup> and Alejandro  
R. Goñi<sup>\*,†,§</sup>

<sup>†</sup>*Institut de Ciència de Materials de Barcelona (ICMAB-CSIC), Campus UAB, 08193 Bellaterra,  
Spain*

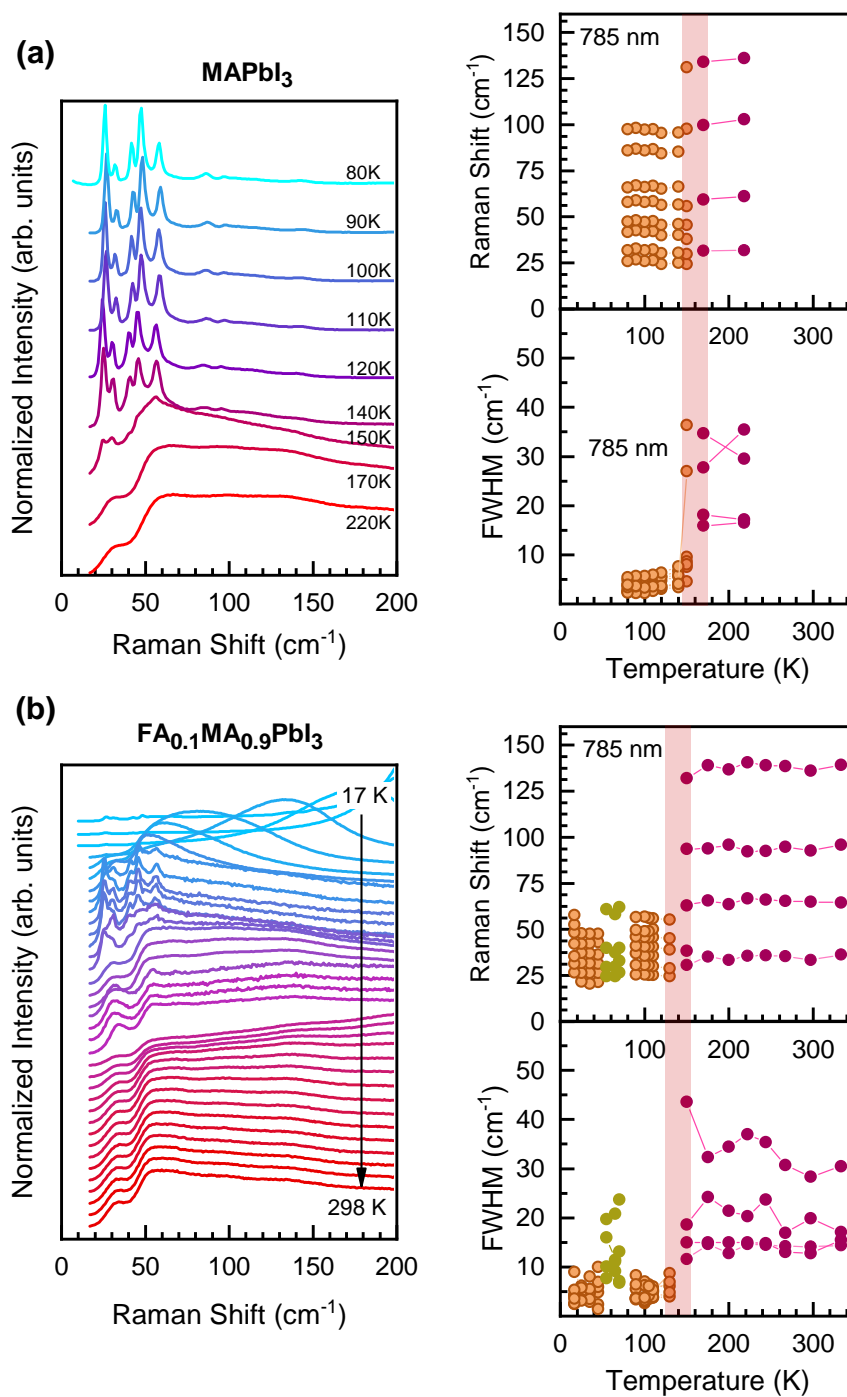
<sup>‡</sup>*Dept. of Chemistry & Centre for Sustainable Chemical Technologies, University of Bath,  
Claverton Down, Bath BA2 7AY, UK*

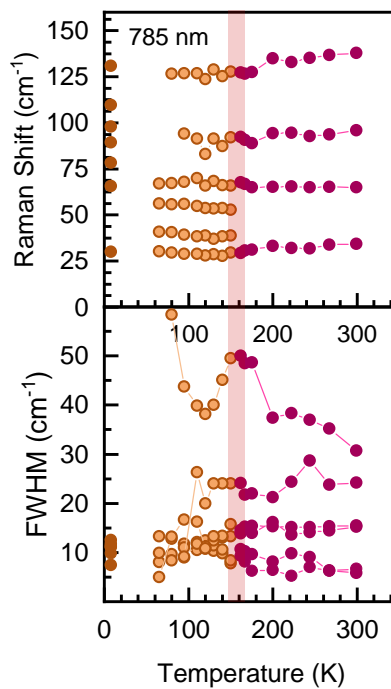
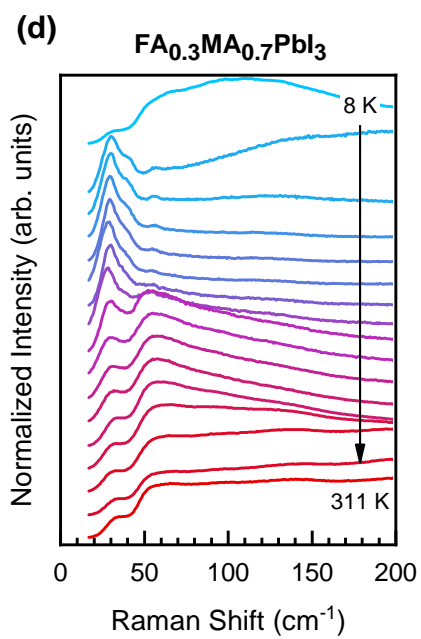
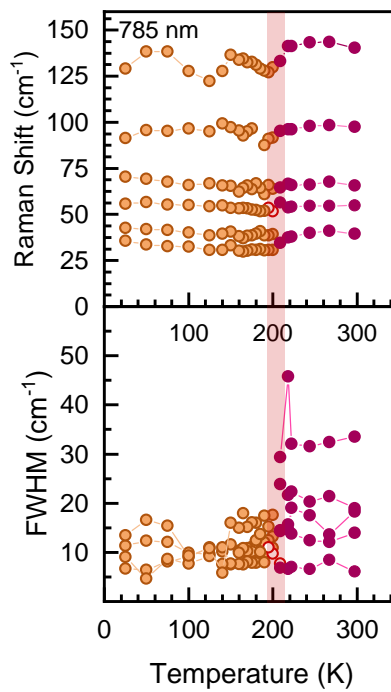
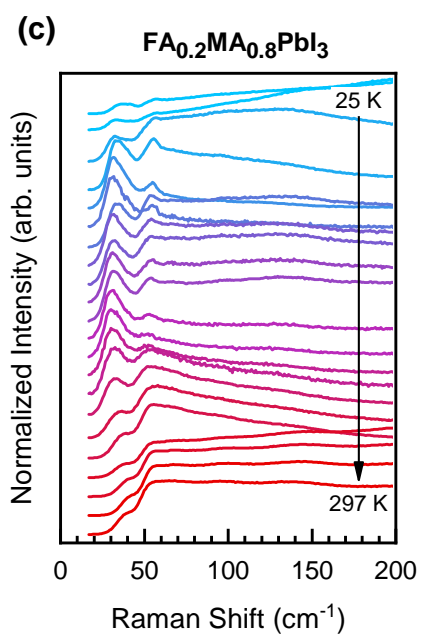
<sup>¶</sup>*Dept. of Chemistry, Cardiff University, Wales CF10 3AT, UK*

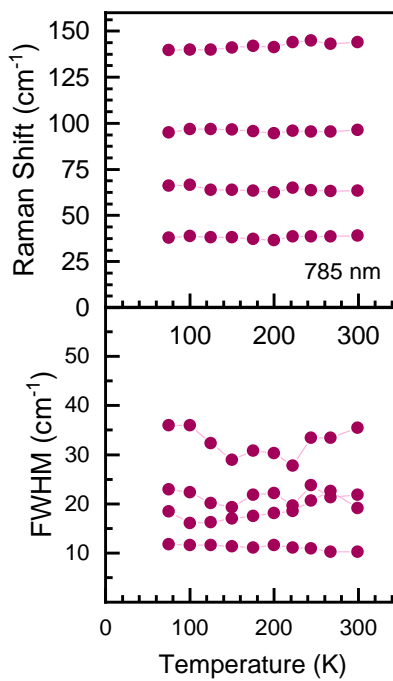
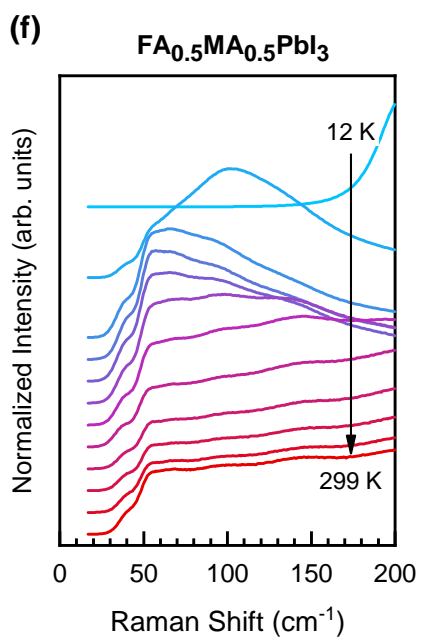
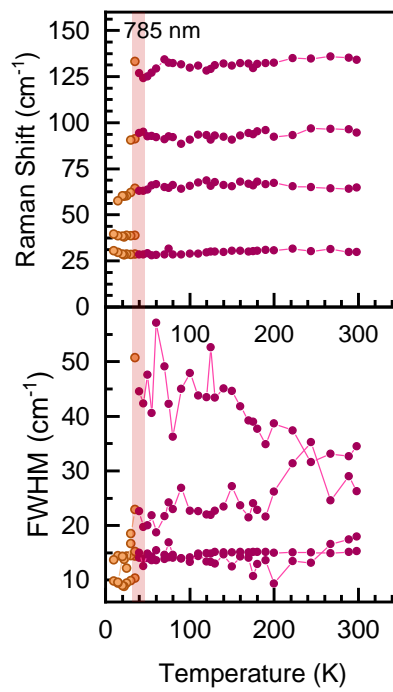
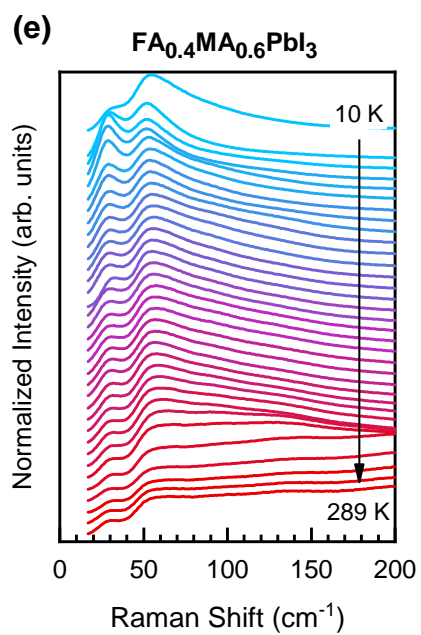
<sup>§</sup>*ICREA, Passeig Lluís Companys 23, 08010 Barcelona, Spain*

E-mail: goni@icmab.es

## Raman spectra of $\text{FA}_x\text{MA}_{1-x}\text{PbI}_3$ solid solutions







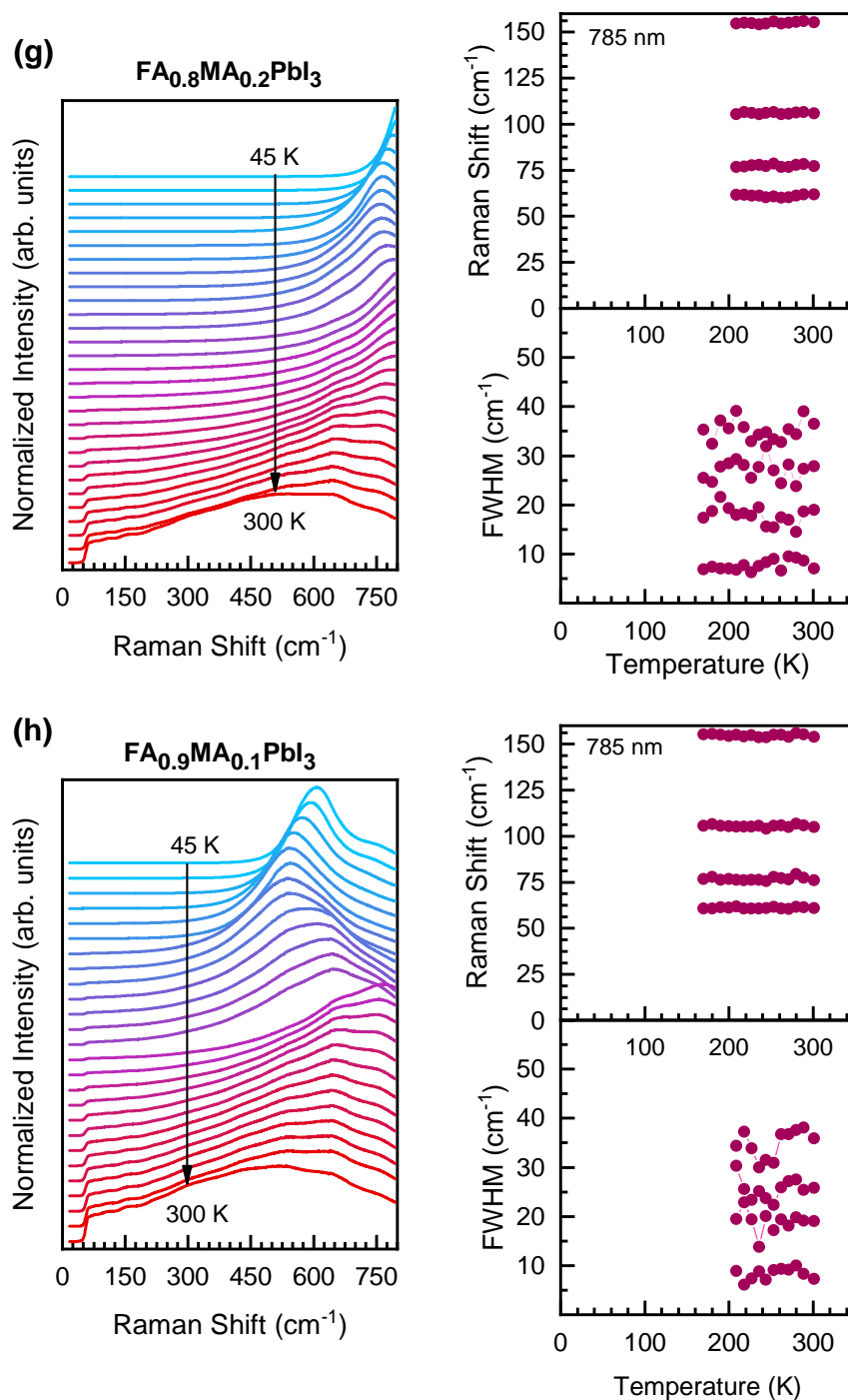


Figure S 1: Raman spectra, the energy position and the linewidth of the main Raman peaks as a function of temperature for (a)  $\text{MAPbI}_3$ , (b)  $\text{FA}_{0.1}\text{MA}_{0.9}\text{PbI}_3$ , (c)  $\text{FA}_{0.2}\text{MA}_{0.8}\text{PbI}_3$ , (d)  $\text{FA}_{0.3}\text{MA}_{0.7}\text{PbI}_3$ , (e)  $\text{FA}_{0.4}\text{MA}_{0.6}\text{PbI}_3$ , (f)  $\text{FA}_{0.5}\text{MA}_{0.5}\text{PbI}_3$ , (g)  $\text{FA}_{0.8}\text{MA}_{0.2}\text{PbI}_3$ , and (h)  $\text{FA}_{0.9}\text{MA}_{0.1}\text{PbI}_3$ . The spectra were normalized to their maximum intensity for clarity.

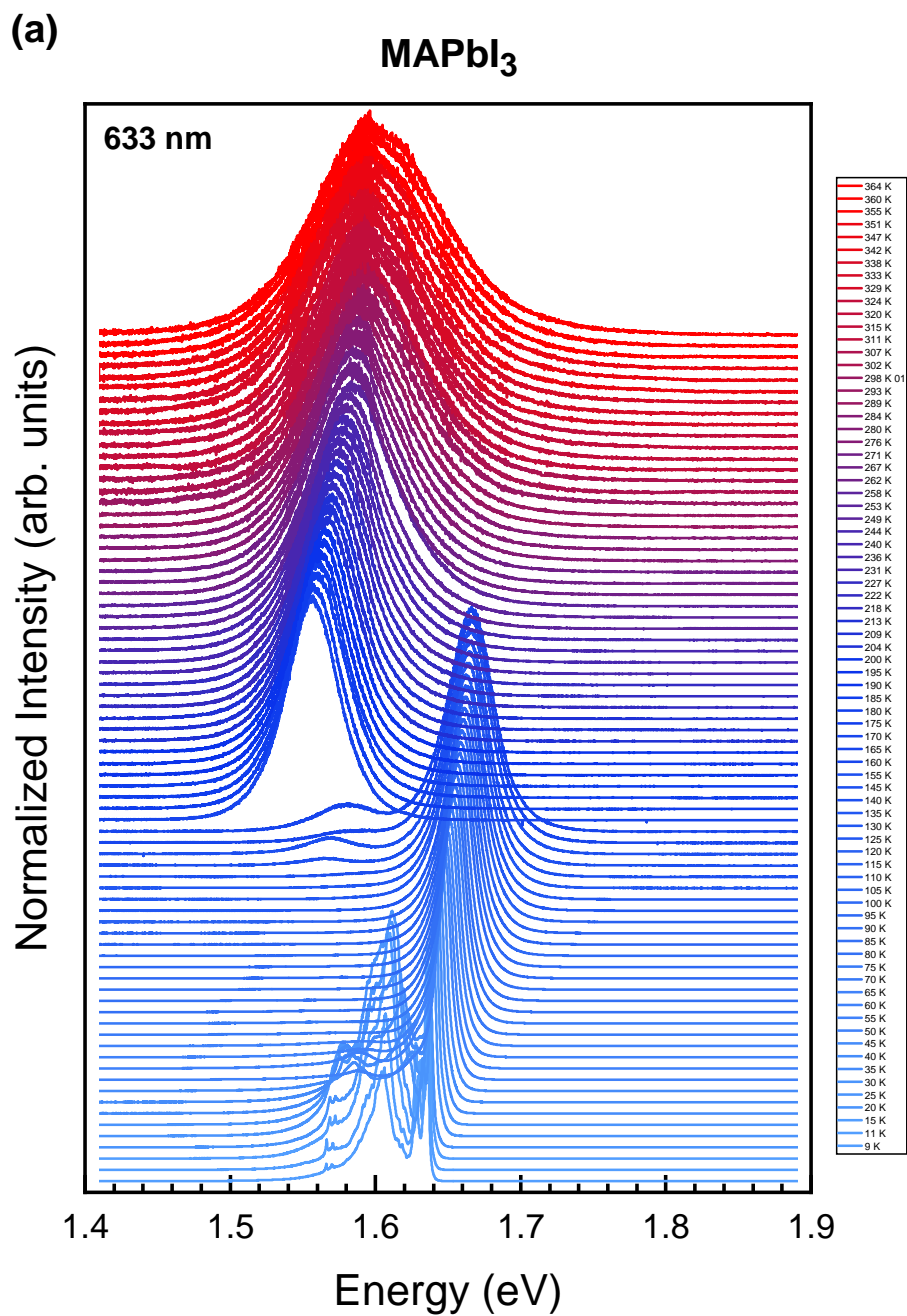


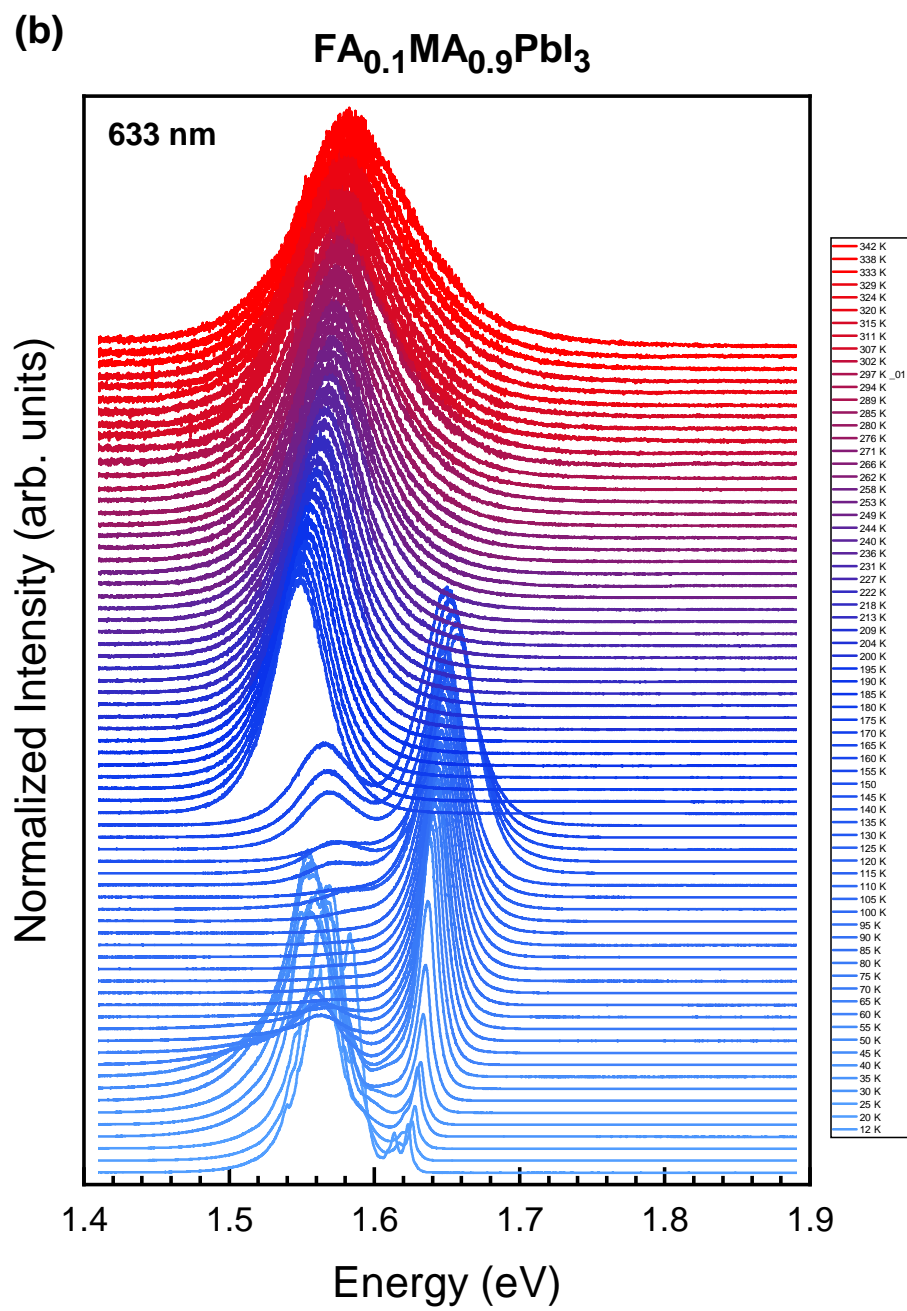
Figures S1(a-h) show the complete set of Raman spectra measured at different temperatures between ca. 10 and 300 K for mixed crystals of the  $\text{FA}_x\text{MA}_{1-x}\text{PbI}_3$  series with different FA content. For FA compositions  $x = 0$  to 0.5 we show only the spectral range up to  $200\text{ cm}^{-1}$  corresponding to the inorganic cage modes. With exception of the sample with  $x = 0.5$ , in all MA-rich crystals, an abrupt change in Raman lineshape, corresponding mainly to a more or less strong reduction of the phonon linewidths, is observed at low temperatures. The temperature at which this sharpening occurs depends on FA composition. This is taken as evidence of the structural phase transition into the low-temperature orthorhombic phase, as discussed in the main text and elsewhere.<sup>1,2</sup> In contrast, for the two FA-rich samples ( $x = 0.8$  and  $0.9$ ) we show a larger wavenumber range to make visible the pronounced PL peak corresponding to the main exciton recombination in the perovskite and how the PL peak moves as temperature changes, crossing the energy region of the scattered Raman photons (see Figs. S1(g-h)). For high FA contents and at low temperatures, the PL peaks become pretty narrow and shift down in energy below that of the scattered Raman photons, such that the overlap between PL and Raman signals vanishes. In this case, the outgoing resonance conditions for Raman scattering are lost and no peaks whatsoever are any longer apparent in Raman spectra.

As discussed in the main text, the Raman spectra were decomposed into their different components by fitting each spectrum using Gaussian or Lorentzian functions (see examples in Fig. 2 of the main manuscript). In Fig. S1, next to each panel with the Raman spectra we show the corresponding plot of the peak energy position and linewidth of the main cage phonon modes as a function of temperature. It is clear from these plots that the occurrence of the phase transition into the orthorhombic phase can be assessed, apart from the linewidth reduction, also from the sudden changes in the phonon frequencies (the shaded pink rectangles indicate the temperature range of the structural transition). In fact, symbols with different colors pertain to different phases: The

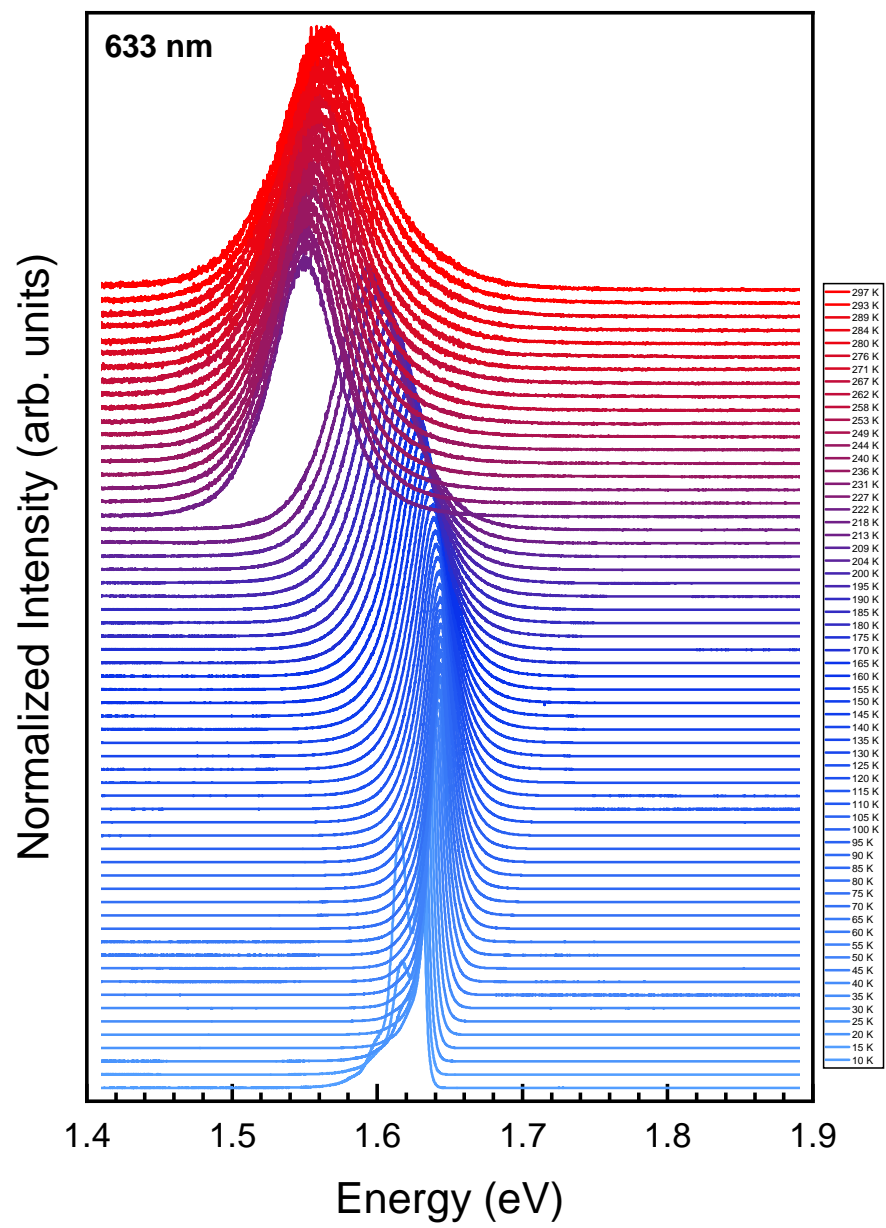
dark purple symbols correspond to the high temperature phases (cubic or tetragonal-I, II, III, we cannot distinguish between them from the Raman data), whereas the dark-orange symbols represent the positions of the Raman peaks in the orthorhombic low-temperature phase. The reduced symmetry of the orthorhombic structure leads to the observed splitting of Raman modes, which are readily observed for the MA-rich samples and are characterized by much smaller linewidths (there is much less or no inhomogeneous broadening of the Raman peaks due to alloying).

## PL spectra of $\text{FA}_x\text{MA}_{1-x}\text{PbI}_3$ solid solutions

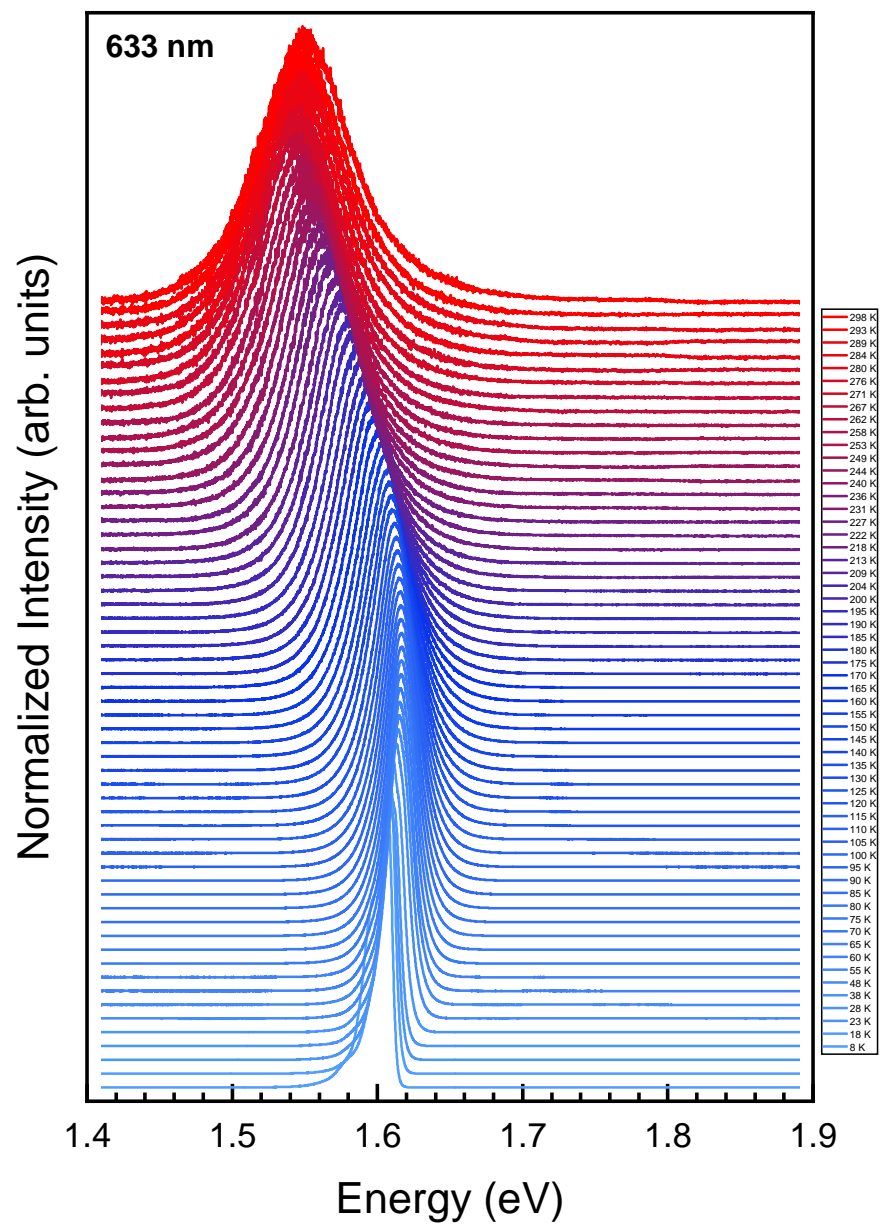




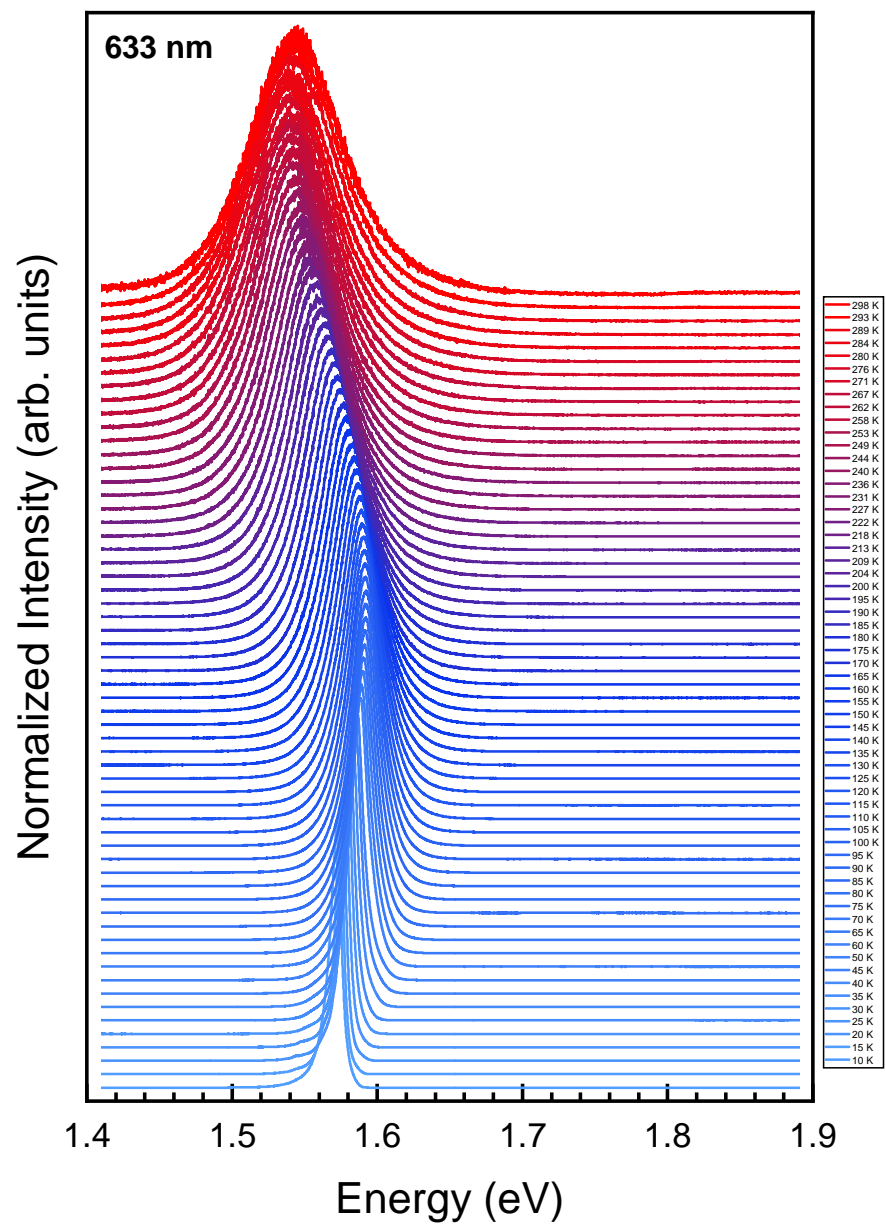
(c)



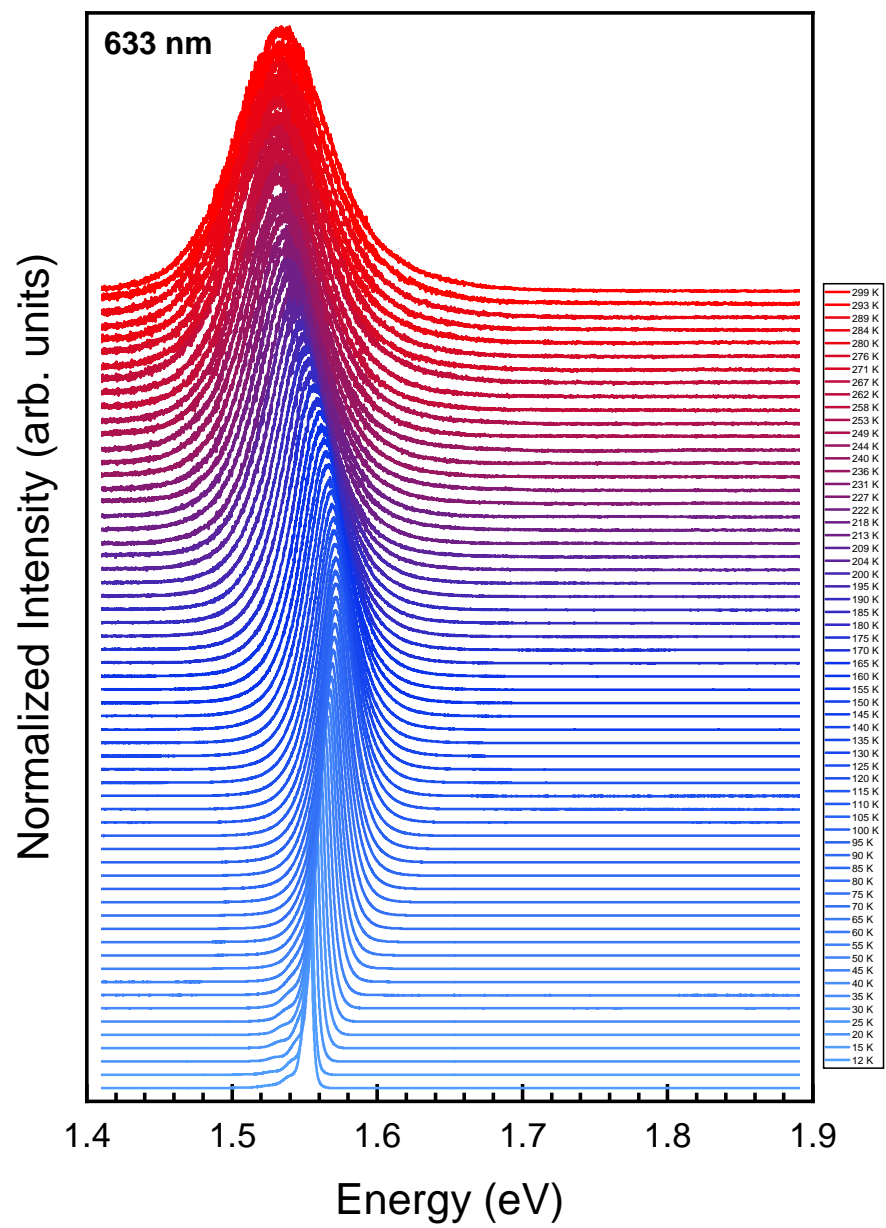
(d)



(e)

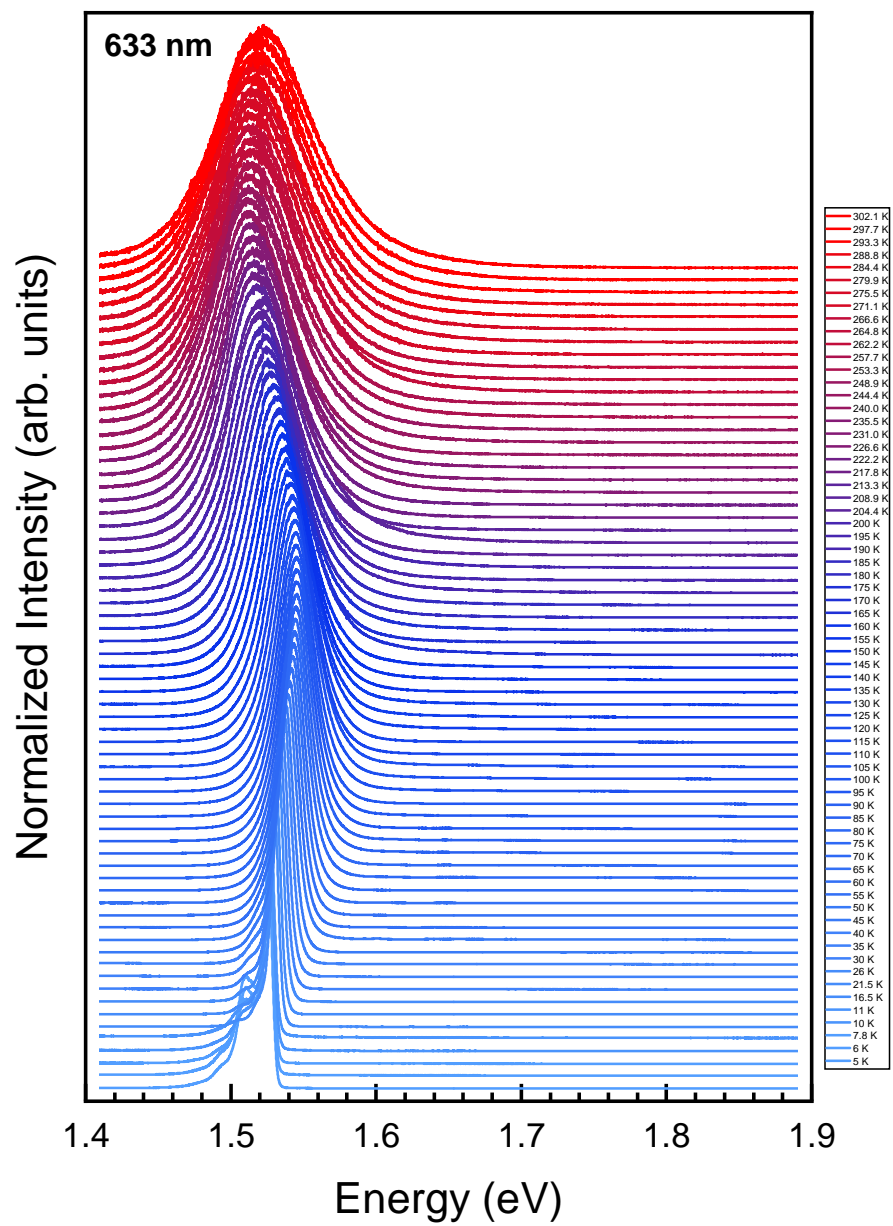


(f)

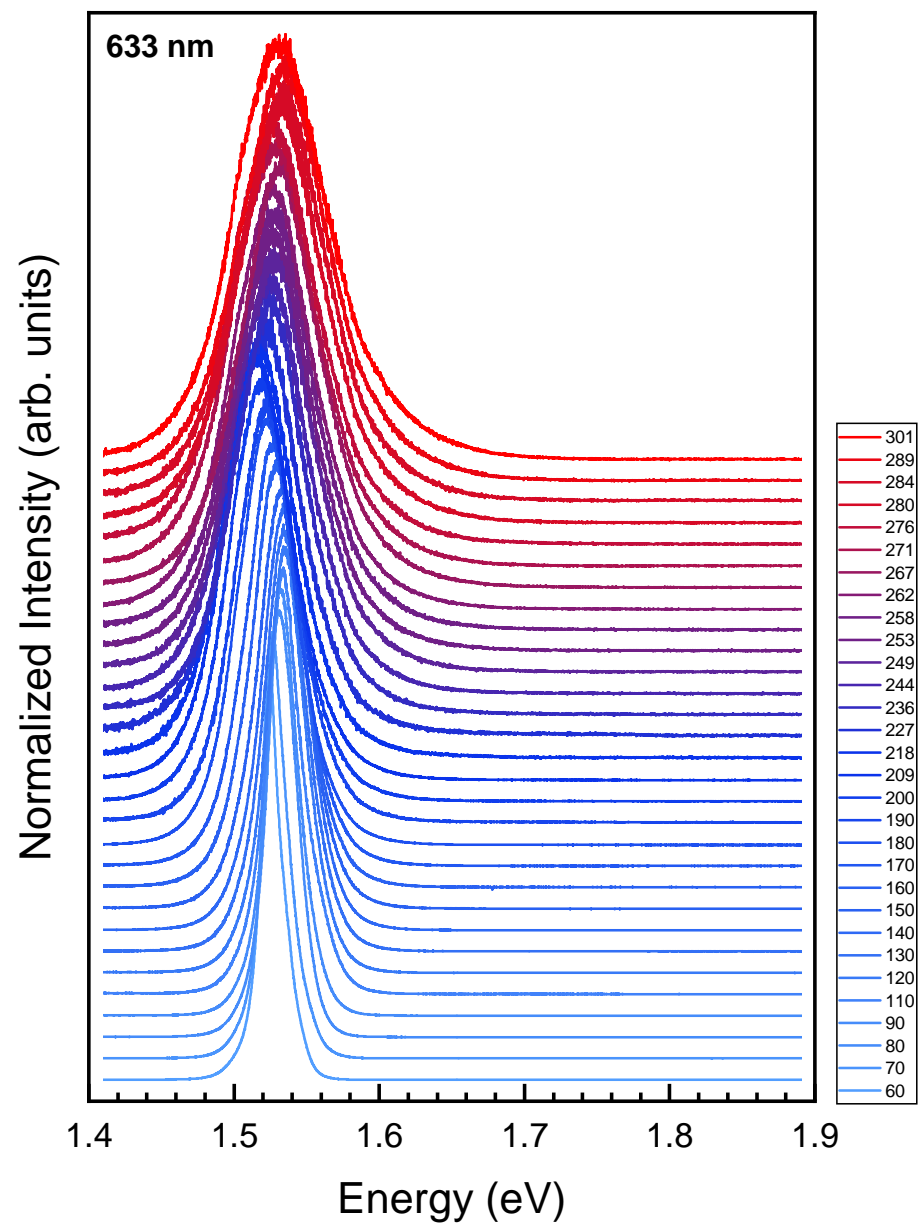
 $\text{FA}_{0.5}\text{MA}_{0.5}\text{PbI}_3$ 



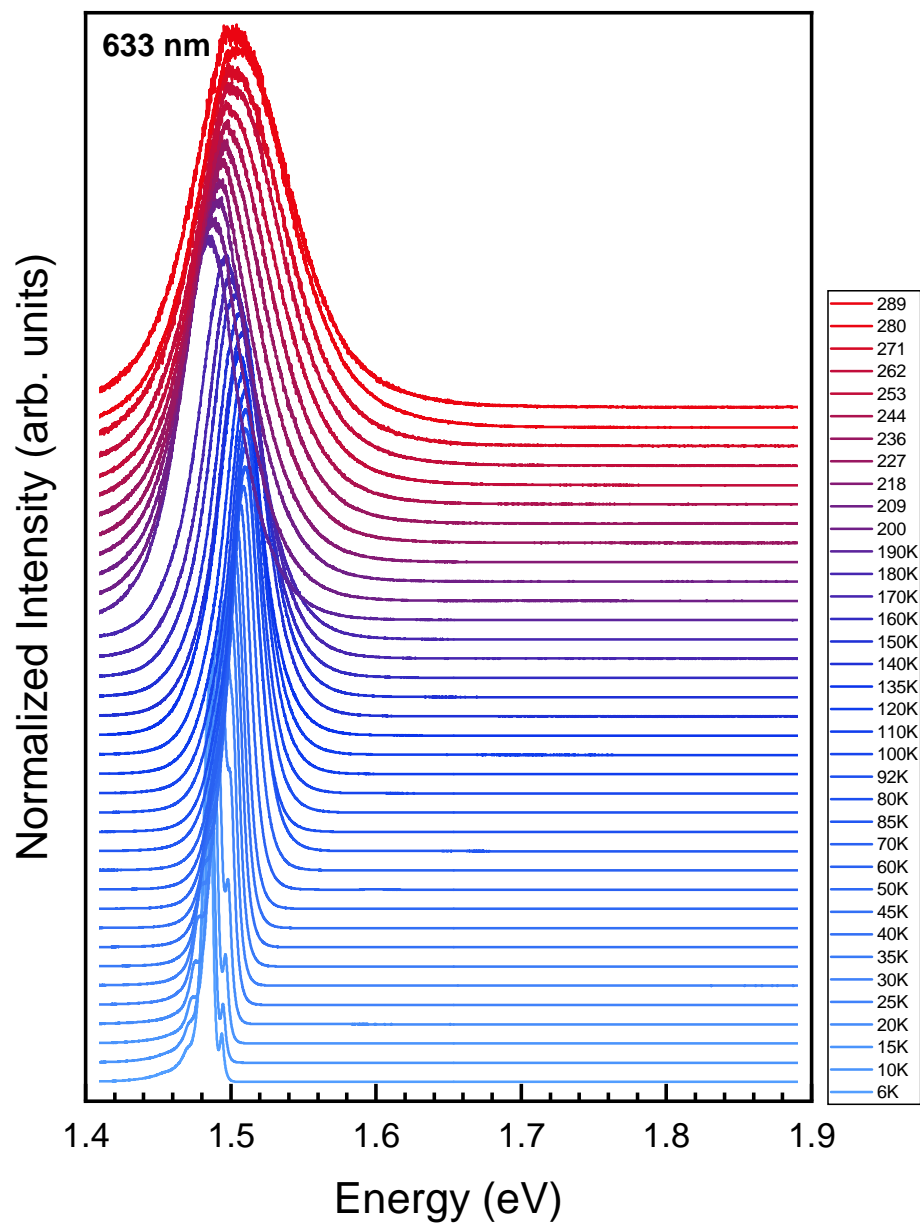
(g)

 $\text{FA}_{0.6}\text{MA}_{0.4}\text{PbI}_3$ 

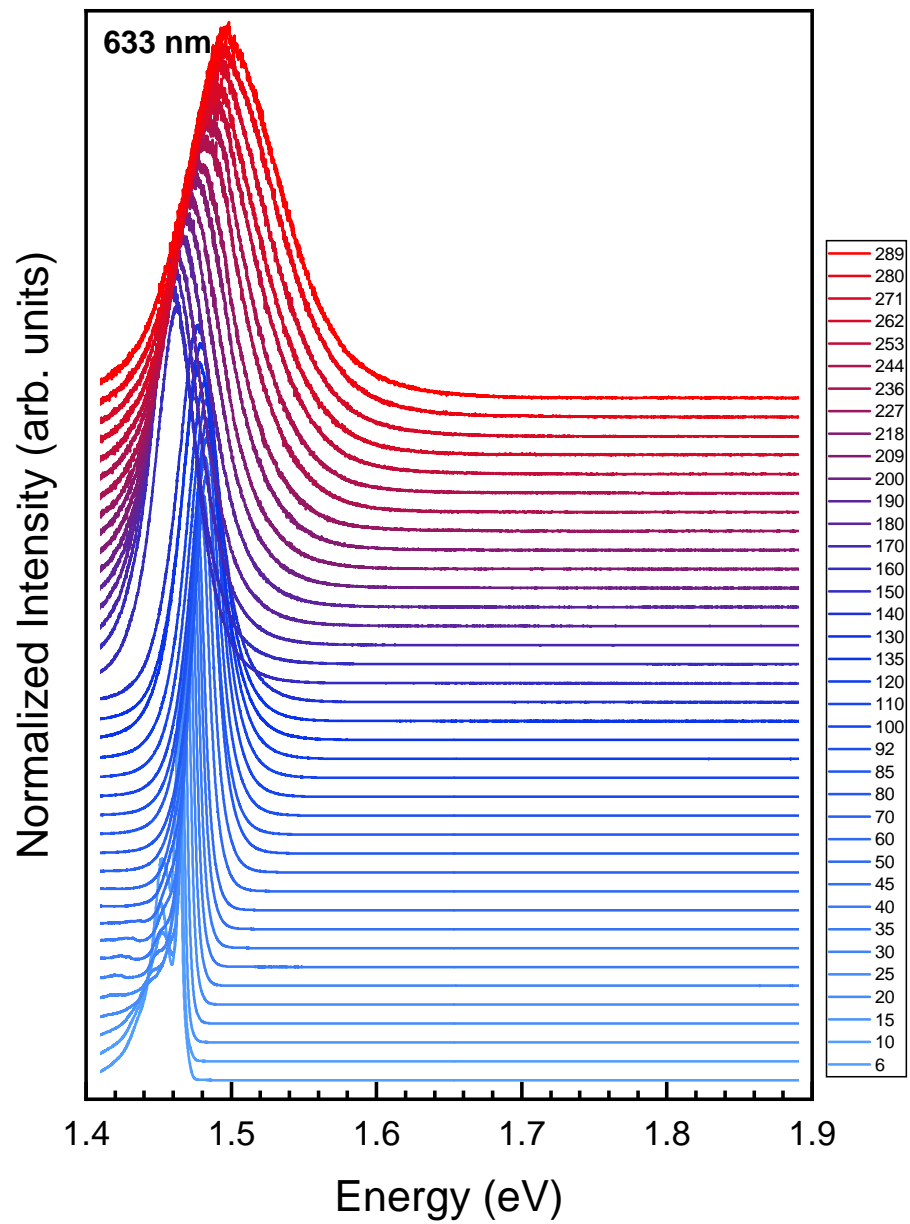
(h)



(i)



(j)

 $\text{FA}_{0.9}\text{MA}_{0.1}\text{PbI}_3$ 

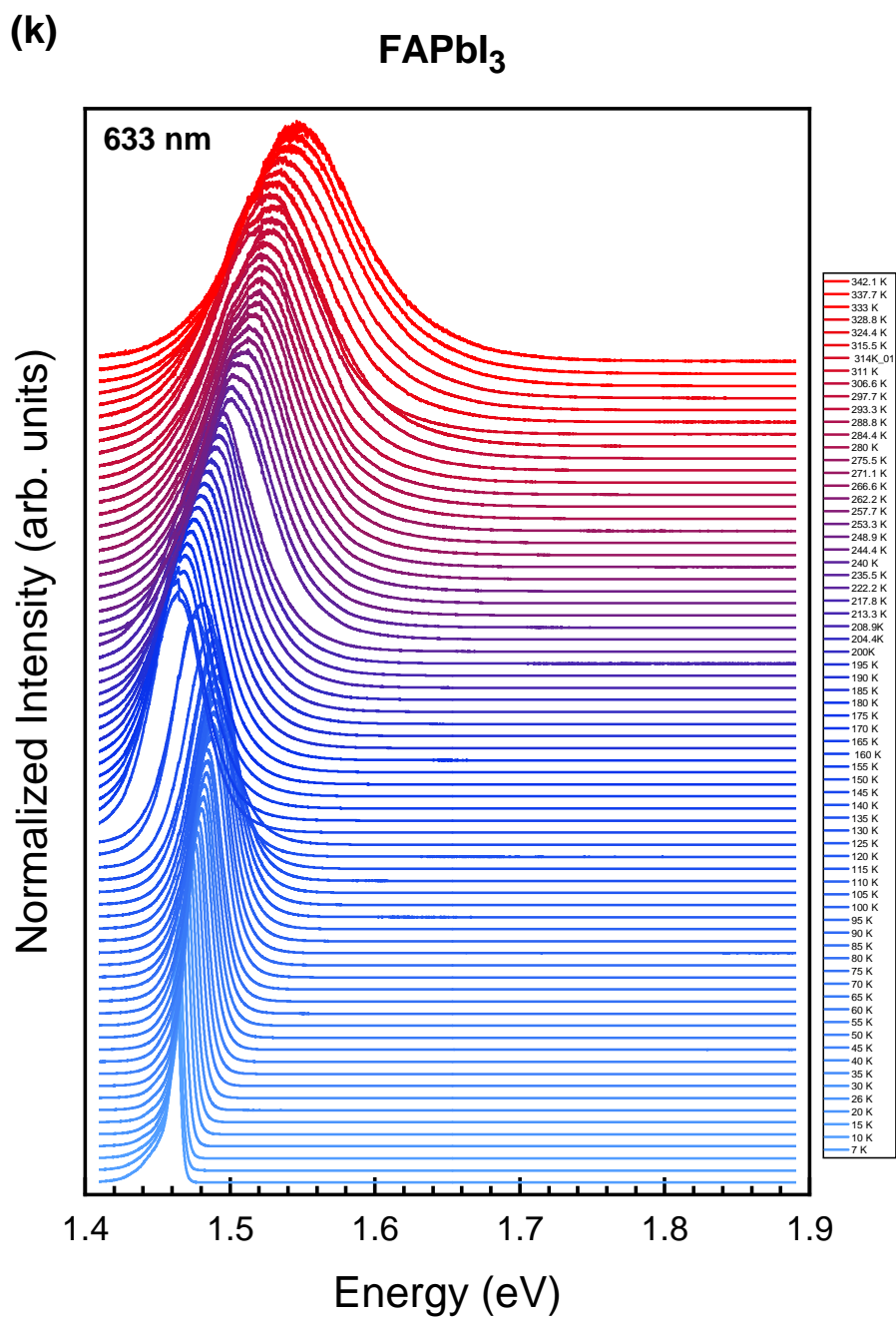


Figure S 2: PL spectra as a function of temperature for (a) MAPbI<sub>3</sub>, (b) FA<sub>0.1</sub>MA<sub>0.9</sub>PbI<sub>3</sub>, (c) FA<sub>0.2</sub>MA<sub>0.8</sub>PbI<sub>3</sub>, (d) FA<sub>0.3</sub>MA<sub>0.7</sub>PbI<sub>3</sub>, (e) FA<sub>0.4</sub>MA<sub>0.6</sub>PbI<sub>3</sub>, (f) FA<sub>0.5</sub>MA<sub>0.5</sub>PbI<sub>3</sub>, (g) FA<sub>0.6</sub>MA<sub>0.4</sub>PbI<sub>3</sub>, (h) FA<sub>0.7</sub>MA<sub>0.3</sub>PbI<sub>3</sub>, (i) FA<sub>0.8</sub>MA<sub>0.2</sub>PbI<sub>3</sub>, (j) FA<sub>0.9</sub>MA<sub>0.1</sub>PbI<sub>3</sub> and (k) FAPbI<sub>3</sub>. The spectra were normalized to their maximum intensity for clarity. Temperatures are indicated in the legends.

Figures S2(a-k) show the complete set of PL spectra measured at different temperatures between ca. 10 and 365 K for all eleven compositions of  $\text{FA}_x\text{MA}_{1-x}\text{PbI}_3$  mixed crystals, spanning the whole compositional range from  $x = 0$  to 1 in steps of 10% FA content. The main emission peak observed for all compositions at higher temperature was assigned to free-exciton (FE) recombination.<sup>3-6</sup> Thus, for the quantitative analysis of the PL spectra we performed a lineshape fitting<sup>7</sup> using a Gaussian-Lorentzian cross-product function (lineshape fitting examples were published elsewhere<sup>2</sup>). Its expression reads as:

$$G \times L(\hbar\omega) = A \cdot \frac{\Gamma^2}{4 \cdot s \cdot (E_0 - \hbar\omega)^2 + \Gamma^2} \cdot \exp\left(-4 \cdot \ln 2 \frac{(1-s) \cdot (E_0 - \hbar\omega)^2}{\Gamma^2}\right) \quad (1)$$

where  $A$  is the amplitude prefactor,  $E_0$  is the peak energy position,  $\Gamma$  in the full width at half maximum (FWHM) and  $s$  is a weight parameter which takes the value  $s = 0$  for pure Gaussian lineshape and  $s = 1$  for pure Lorentzian. The values of these four adjustable parameters were obtained as a function of temperature from lineshape fits to the measured PL spectra using Eq. (1). For the cases where there is a coexistence of two phases we used two cross-product functions with independent variable parameter sets. The much more complicated analysis of the wealth of peaks, apparent at low temperatures (below ca. 70 K) for high MA content and ascribed to radiative recombination of bound (acceptor/donor) exciton complexes, will be published elsewhere.<sup>8</sup>

Figure S3 displays the integrated intensity of the main PL peak, calculated as the product of the peak amplitude  $A$  by the linewidth  $\Gamma$  extracted from the lineshape fits using the cross-product function of Eq. (1), plotted as a function of temperature for the series of  $\text{FA}_x\text{MA}_{1-x}\text{PbI}_3$  mixed crystals. With decreasing temperature down to ca. 100 K the integrated intensity increases for all concentrations between one and two orders of magnitude. This is the typical behavior of free-exciton radiative recombination as compared to bimolecular recombination of uncorrelated electron-hole pairs and is the result of an enhanced optical matrix element due to a reinforced Coulomb at-

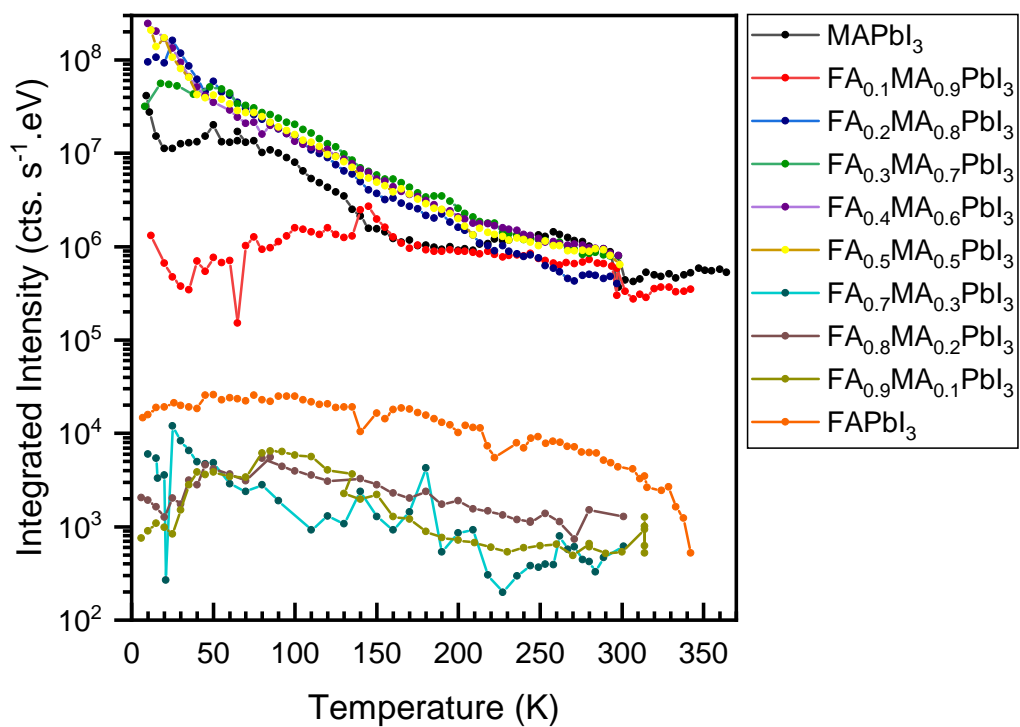


Figure S 3: The PL peak integrated intensity ( $A \times \Gamma$ ) plotted as a function of temperature, obtained from the PL lineshape fits using a cross-product function of Eq. (1) for the complete set of compositions of the  $\text{FA}_x\text{MA}_{1-x}\text{PbI}_3$  series.

traction, i.e. an increased wavefunction overlap between electron and hole forming the exciton. Below 100 K, in many cases the integrated intensity of the free exciton decreases with decreasing temperature. This effect is the consequence of the appearance of the emission bands related to bound-exciton complexes (see low temperature spectra in Figs. S2(a) to S2(k)), which provide a competing radiative recombination channel, thus growing in intensity at the expense of the FE intensity.

Figure S4(a) shows the values of the full width at half maximum (FWHM) of the main PL peak of MAPbI<sub>3</sub> as a function of temperature (closed symbols), as obtained from least-squares fits using Eq. (1). We only show the low temperature range below 160 K corresponding to the orthorhombic phase. The red solid curve represents the result of a fit to the FWHM data points using the function of Eq. (1) of the main manuscript, which accounts for the inhomogeneous and homogeneous broadening contributions to the exciton linewidth, the latter arising from electron-phonon interaction. This function contains three adjustable parameters: The temperature-independent inhomogeneous broadening  $\Gamma_0$  which is mainly determined by the crystal quality, the electron-optical-phonon coupling constant  $\gamma_{opt}$  and the effective optical-phonon energy  $E_{opt}$ . The fitting results for the last two parameters are plotted as a function of FA content in Fig. S4(b). To first approximation, the electron-phonon interaction parameters causing homogeneous line broadening of the free exciton in hybrid halide perovskite solid solutions seem to be fairly independent of organic-cation composition.



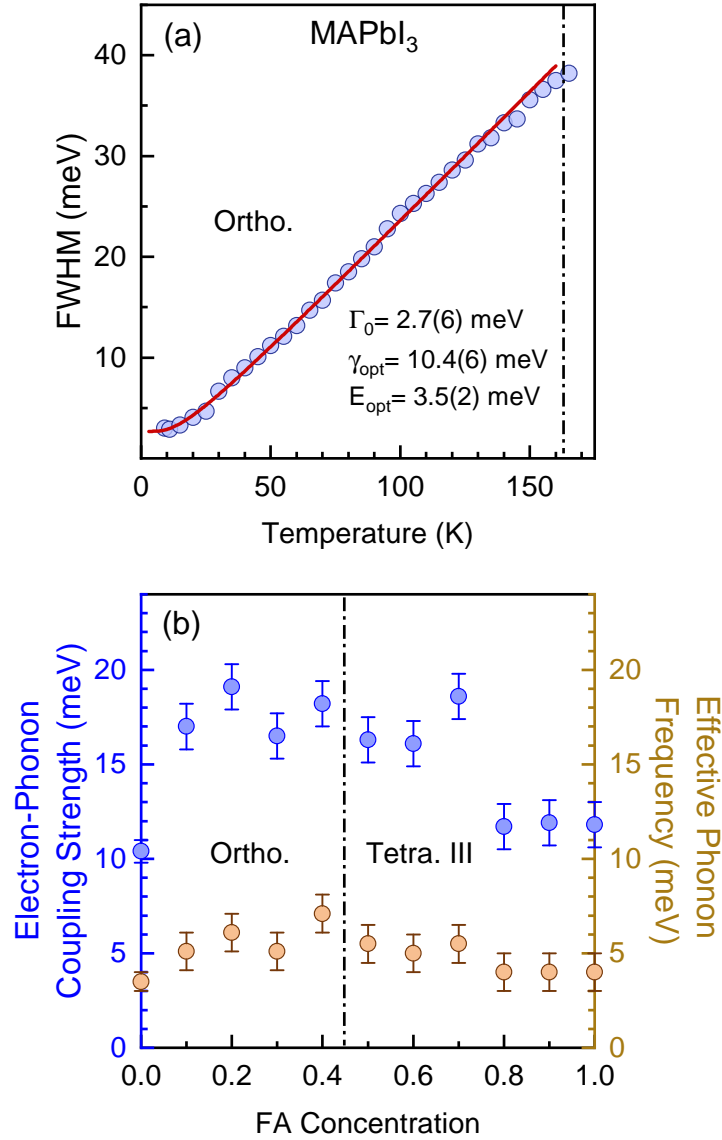


Figure S 4: (a) The full width at half maximum (closed symbols), as obtained from lineshape fits to the PL spectra of MAPbI<sub>3</sub> using Eq. (1), plotted as a function of temperature in the range up to ca. 160 K, corresponding to the stability regime of the orthorhombic phase. The red curve corresponds to a least-squares fit using the expression for the exciton linewidth of Eq. (1) of the main manuscript. The values obtained for three adjustable parameters are given in the legend. (b) The electron-phonon coupling strength  $\gamma_{opt}$  (blue symbols) and the effective phonon frequency  $E_{opt}$  (other symbols) represented as a function of the FA concentration for the whole FA<sub>x</sub>MA<sub>1-x</sub>PbI<sub>3</sub> series. The dot-dashed vertical lines mark off either the temperature or FA-content range of stability of the orthorhombic and the tetragonal phases.

## Procedures to construct the phase diagram of $\text{FA}_x\text{MA}_{1-x}\text{PbI}_3$ from Raman and PL data

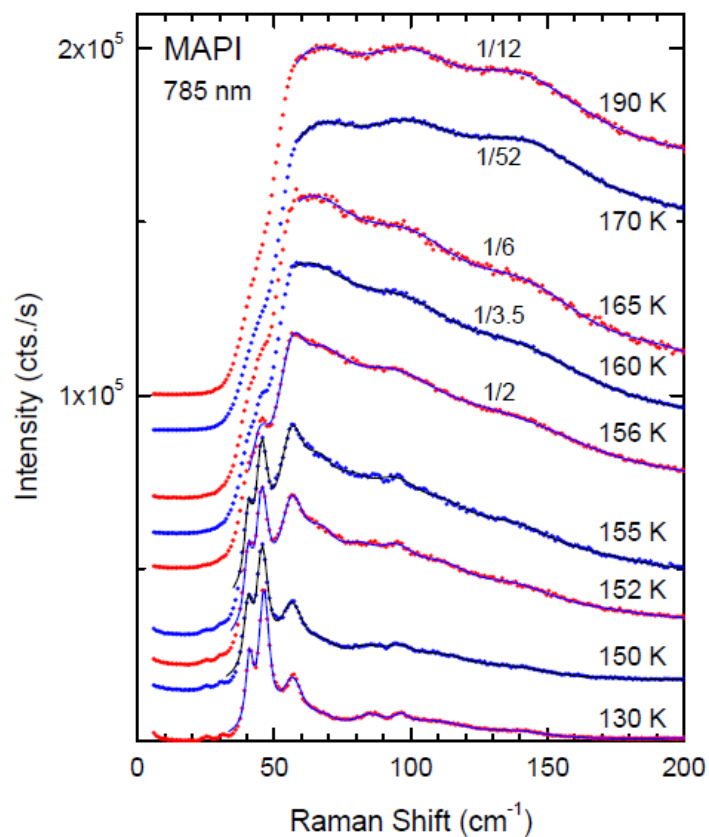


Figure S 5: A series of Raman spectra of  $\text{MAPbI}_3$  taken in small temperature steps in the range of the Tetra-I to Ortho phase transition. The figure illustrates how the transition temperature can be accurately determined from the qualitative changes in the Raman lineshapes.

Figure 5 displays the influence on the Raman lineshape of the structural changes occurring at the transition into the orthorhombic phase in the case of  $\text{MAPbI}_3$ . By screening the temperature range of the phase transformation in small temperature steps, the transition temperature can be readily and accurately determined by inspection of the temperature-induced changes in the Raman

lineshape (mainly the linewidth). Since the "static" inhomogeneous broadening of the Raman peaks increases with increasing FA content, i.e., increasing lattice disorder, for higher  $x$  values such a determination becomes increasingly difficult but remains feasible.

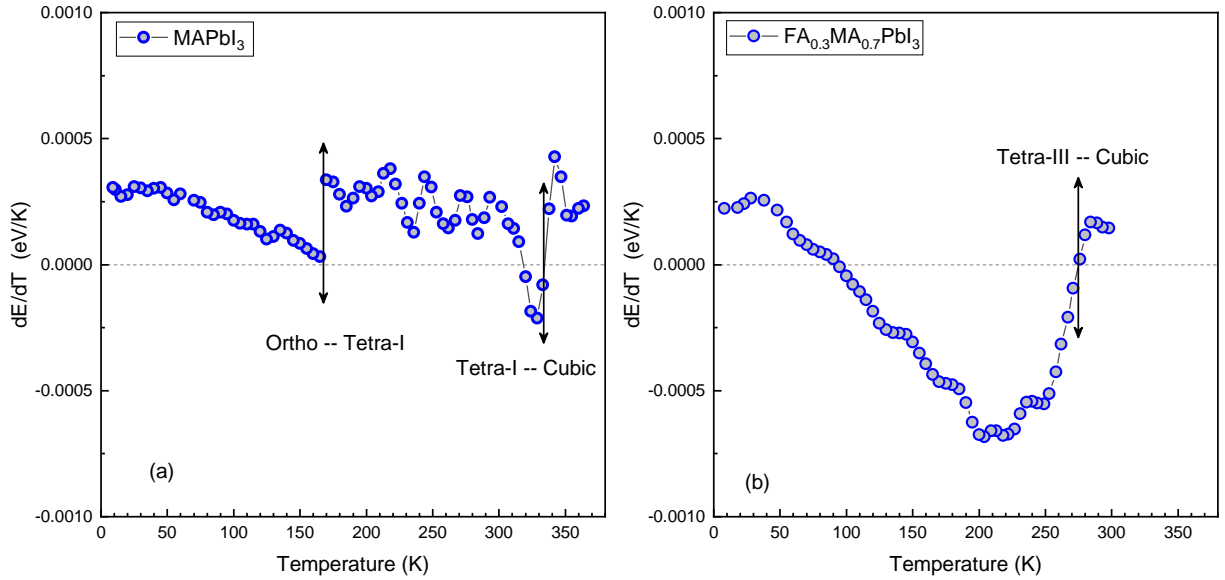


Figure S 6: First derivative of the PL peak energy  $E_0$  with respect to temperature for (a)  $\text{MAPbI}_3$  and (b)  $\text{FA}_{0.3}\text{MA}_{0.7}\text{PbI}_3$  plotted as a function of temperature. The temperatures at which different structural phase transitions occur are indicated by arrows. See text for details.

In Figs. S6(a)-(b) we illustrate the procedure to extract the phase transition temperature from the data of the PL peak energy  $E_0$  as a function of temperature. For that purpose we first construct the graphs of the derivative of  $E_0$  over temperature plotted as a function of temperature for each FA concentration, as shown in Figs. S6(a) and S6(b) for  $\text{MAPbI}_3$  and  $\text{FA}_{0.3}\text{MA}_{0.7}\text{PbI}_3$ , respectively, as examples. In the first case, the temperature of the phase transition between the cubic and the tetra-I phase (the same procedure is valid for the cubic-tetra-II transition for high FA contents), which in the  $E_0$ -vs.- $T$  curve corresponds to a zigzag type behavior, is extracted from the zero of the first derivative curve, as indicated in Fig. S6(a). In the same figure, we also show the determination of the transition temperature for the tetra-I to orthorhombic transformation, which simply corresponds

to the temperature at which the jump in the first derivative occurs. For the smooth transition between the cubic and the tetra-III phase, taking place for intermediate FA concentrations, the transition temperature is obtained again from the crossing point of the first derivative curve and the temperature axis (see example in Fig. S6(b)). This corresponds to the inflection point in the  $E_0$ -vs.- $T$  curve, which is less straightforward to be determined.

## References

- (1) Leguy, A. M. A.; Goñi, A. R.; Frost, J. M.; Skelton, J.; Brivio, F.; Rodríguez-Martínez, X.; Weber, O. J.; Pallipurath, A.; Alonso, M. I.; Campoy-Quiles, M.; Weller, M. T.; Nelson, J.; Walsh, A.; Barnes, P. R. F. Dynamic Disorder, Phonon Lifetimes, and the Assignment of Modes to the Vibrational Spectra of Methylammonium Lead Halide Perovskites. *Phys. Chem. Chem. Phys.* **2016**, 18, 27051-27066.
- (2) Francisco-López, A.; Charles, B.; Weber, O. J.; Alonso, M. I.; Garriga, M.; Campoy-Quiles, M.; Weller, M. T.; Goñi, A. R. Pressure-Induced Locking of Methylammonium Cations Versus Amorphization in Hybrid Lead Iodide Perovskites. *J. Phys. Chem. C* **2018**, 122, 22073-22082.
- (3) D'Innocenzo, V.; Grancini, G.; Alcocer, M. J.-P.; Kandada, A. R. S.; Stranks, S. D.; Lee, M. M.; Lanzani, G.; Snaith, H. J.; Petrozza, A. Excitons Versus Free Charges in Organo-Lead Tri-Halide Perovskites. *Nature Commun.* **2014**, 5, 3486-3492.
- (4) Wu, K.; Bera, A.; Ma, C.; Du, Y.; Yang, Y.; Li, L.; Wu, T. Temperature-Dependent Excitonic Photoluminescence of Hybrid Organometal Halide Perovskite Films. *Phys. Chem. Chem. Phys.* **2014**, 16, 22476-22481.

- (5) Dong, Q.; Fang, Y.; Shao, Y.; Mulligan, P.; Qiu, J.; Cao, L.; Huang, J. Electron-Hole Diffusion Lengths  $>175 \mu\text{m}$  in Solution-Grown  $\text{CH}_3\text{NH}_3\text{PbI}_3$  Single Crystals. *Sci.* **2015**, 347, 967-970.
- (6) Galkowski, K.; Mitioglu, A. A.; Surrente, A.; Yang, Z.; Maude, D. K.; Kossaki, P.; Eperon, G. E.; Wang, J. T.-W.; Snaith, H. J.; Plochocka, P.; et al. Spatially Resolved Studies of the Phases and Morphology of Methylammonium and Formamidinium Lead Tri-Halide Perovskites. *Nanoscale* **2017**, 9, 3222-3230.
- (7) Wojdyr, M. Fityk: A General-Purpose Peak Fitting Program. *J. Appl. Crystallogr.* **2010**, 43, 1126-1128.
- (8) Francisco-López, A.; Charles, B.; Alonso, M. I.; Garriga, M.; Campoy-Quiles, M.; Weller, M. T.; Goñi, A. R. Shallow-Defect Photophysics of Mixed Organic-Cation Lead Iodide Perovskites from Low-Temperature Photoluminescence. Unpublished.

## 7 Conclusions and perspectives

By combining optical spectroscopy with high-pressure and low-temperature techniques, we were able to study fundamental structural and optoelectronic properties of hybrid halide perovskites ( $\text{FA}_x\text{MA}_{1-x}\text{PbI}_3$ ). Their dielectric functions have been studied for the whole concentration range in ref. III, and also the first complete composition-temperature phase diagram for this type of materials was given in ref. IV. It has been shown how the interplay between the semi-rigid inorganic cage and the loosely bound organic molecules plays a fundamental role in the structural behavior of hybrid perovskites. At ambient or higher temperatures, the free rotation and movement of the organic cations inside the cage voids randomly reorient the cations along the three spatial coordinates, favoring a spherical density distribution and, concomitantly, a cubic symmetry. For intermediate temperatures, i.e. above  $\sim 150$  K, the contraction of the lattice entails a tilting of the  $\text{PbI}_6$  octahedra along the Pb-I-Pb bond to accommodate the crystalline structure to the reduced space available. For the compositional ends  $\text{MAPbI}_3$  and  $\text{FAPbI}_3$ , the organic cations see their freedom of movement restricted to the tetragonal plane. For the mixed cation formula, on the other hand, the inhomogeneity induced in the crystal due to the different sizes, polarities and conformations of the MA and FA molecules yields a more disordered phase, characterized by tilting the octahedra indistinctly in different directions. At lower temperatures, further tilting and a distortion of the octahedra induce a transition to an orthorhombic phase, for FA contents lower or equal than 0.4, locking the movement of the organic molecule inside the lead iodide cages. As a result, the Raman features are no longer subjected to the dynamic inhomogeneous broadening related to the free movement and re-orientation of the cations, and accordingly, their line-widths are drastically reduced.

Regarding the high-pressure experiments, in the case of pure  $\text{MAPbI}_3$  we observed three pressure-induced phase transitions at 0.4, 2.7 and 3.3 GPa. The second phase transition, at 2.7 GPa, is characterized by a sudden reduction in the inhomogeneous broadening of the Raman lines, similar to the one observed at low temperatures. Previous studies observed a smearing of the X-ray diffraction patterns after this phase transition, which was assigned to amorphization of the material. Our data, however, shows that the crystallinity of the material is unaffected through all the phases observed. This apparent disagreement is ascribed to the effect of the pressure-induced orthorhombic distortion of the inorganic cage, which in the macroscopic length scale occurs randomly in different directions. This disturbs the long-range order of the crystal structure, leading to the smearing of the X-ray diffraction patterns. Raman spectroscopy, however, is much less sensitive to this type of long-range disorder. The sharpness of the Raman features is evidence of a high degree of order at a microscopic length scale, incompatible with amorphization. The third phase transition, at 3.3 GPa, is reported in ref. I for the first time, and is characterized by a further reduction in the dynamic inhomogeneous broadening of the Raman peaks and the splitting of some of the peaks.

An interesting feature of hybrid halide perovskites is their atypical bandgap dependence on temperature. For instance, at temperatures higher than 150 K, the linear shift in energy with increasing temperature is positive, whereas archetypal semiconductors such as Si, Ge,

GaAs, etc. present a negative slope. This shift depends on two terms; the first one is the thermal expansion contribution, which can be experimentally obtained by studying the gap shift as a function of pressure for a given temperature. The second contribution corresponds to the electron-phonon renormalization of the bandgap. Below 0.4 GPa, we show in ref. II that the bandgap energy also exhibits an inverted dependence with increasing pressure with respect to typical semiconductors. In fact, the thermal expansion contribution to the shift of the bandgap with temperature, that can be derived from this contraction of the lattice, cannot be neglected, as it was previously suggested in the literature, since this contribution is as important as the corresponding to the renormalization of the band-gap due to electron-phonon coupling.

For temperatures lower than roughly 150 K, the bandgap dependence on temperature is even more peculiar, with the magnitude of the energy shift with temperature changing non-monotonically, switching from positive to negative for intermediate FA concentrations. To better understand this atypical behavior, more high-pressure experiments at temperatures lower than 150 K are required. Preliminary attempts have been made for some compositions of the  $\text{FA}_x\text{MA}_{1-x}\text{PbI}_3$  family, and the results are promising, as the gap dependence on pressure also changes with temperature. This suggests that the effect of the contraction of the lattice plays a fundamental role in the behavior of the bandgap. Applying pressure at low temperatures, however, is not an easy task. It involves the cryogenic loading of the pressure cell with liquid helium in its superfluid state, and a careful and precise preparation for several days to obtain just a few experimental points. However, these measurements, together with theoretical calculations, are fundamental to understand the origin of the atypical dependence on temperature of the bandgap of hybrid halide perovskites for the full range of temperatures.

It seems also interesting to study fundamental properties of perovskite nanocrystals (NCs), as new properties and tunability possibilities arise at the nano-scale. Preliminary studies on metal halide perovskite NCs show that the dependence of the bandgap energy with temperature appears to be size-dependent, suggesting a different contribution of the electron-phonon interaction to the overall shift for different nanocrystals. In order to explore this hypothesis further, pressure-dependent, low temperature experiments need to be carried out for different sizes of hybrid halide perovskite nanocrystals.

In summary, our findings provide further fundamental insight into the underlying physics of this kind of organic–inorganic hybrid materials, which are causing a change in paradigm in photovoltaic and light-emitting device technology. Still, more fundamental work needs to be done following the line of this thesis to fully unravel the optoelectronic properties of hybrid halide perovskites as a function of temperature and/or pressure at the macro and nano-scale.